NONLOCAL THERMOELECTRICITY AND ENTANGLEMENT IN TOPOLOGICAL JOSEPHSON JUNCTIONS

PHD PROGRAM
NANOSCIENCE

ACADEMIC YEAR
2020/2021

SCUOLA NORMALE SUPERIORE

CANDIDATE
Gianmichele Blasi

SUPERVISORS
Dr. Fabio Taddei
Dr. Alessandro Braggio
Prof. Vittorio Giovannetti

Except where acknowledged in the customary manner, the material presented in this thesis is, to the best of my knowledge, original and has not been submitted in whole or part for a degree in any university.

Gianmichele Blasi

Acknowledgements

First of all, I would like to thank my supervisors not only for their support and guidance, their patience and perseverance but also for challenging me along the journey making it fruitful and fun. In particular, I would to thank Dr. Fabio Taddei for his unconventional sense of humor, his stoic pragmatism and for teaching me that “less is more”. In the same way, I thank Dr. Alessandro Braggio for his unbreakable passion, unstoppable dedication and for teaching me, instead, that “more is not enough”. A special thanks goes to Prof. Vittorio Giovannetti who put together such a “Research Suicide Squad” with the ambitious aim of reconcile quantum information and condensed matter. Thank you All, for the wonderful opportunities, the useful bits of advice, and for helping me face this Ph.D. challenge with responsibility, serenity, and critical sense.

Further thanks go to my colleagues and collaborators, Daniel Gresta and Dr. Matteo Carrega for the joint efforts, and to Prof. Yuval Gefen for allowing me to collaborate with him as a research fellow in the joint program between Scuola Normale and the Weizmann Institute of Science. A special thanks goes to Prof. Liliana Arrachea for welcoming me to her research group in Buenos Aires. I wish to thank her for her unfailing scientific intuition, the richness of her ideas and connections, and her kindness and professionalism.

These years spent in Pisa would not have been the same without all my “compagni di merende”. In particular, I wish to say thank you to Bibek for teaching me what it means *not to be* a Brahmin; to Vasco, second to none, “sei un Grande!”; to Giulio for his very refined sense of smell; to Farzad who aside from “critical situations” always manages to be relaxed and positive; to Pietro for his elegance and calmness despite the 79’s toxic environment; to Paolo to be the coherent superposition of Greta Thunberg and Dj Franchino; to Marcello whose darkness made everything else shine; to Chessa “MATTO COMPLETO”; to Fanizza who-escaped-from-Foggia-not-for-Foggia-but-for-the-foggians; to Donato who taught me the equivalence between the “torneo della Normale” and the Champions League; to Belliardo for not killing me (yet); to Salvatore to be the Michael Moore of Twitch; to Luis for his ballistic way of living; to Cusumano and Aurelia to be my pandemic-neighboring-shouters; to Paola for having scouted Di Lorenzo and let us win the Euro 2020; to Giorgio for his pessimistic optimism; to Cecilia to be the most enthusiastic party-planner I ever met; to Alessandro for his out-of-the-time kindness and generosity; to Jisu-amuchina-Kim for being overcautious with “stay home” advices; and to Luca who could have shown me “Just Dance” a few kilos ago.

Among all, my most special thanks goes to Anna. Honestly, I didn’t find any valid theorem, approximation, or hidden variable which could explain what on earth allows her to bear with me. Maybe Physics is not ready for such revelations! Luckily, this thesis is not about that.

Last but not least, I want to dedicate a heartfelt thanks to my family. None of this would have been possible without the unconditional support of my loved ones, for whom my gratitude goes beyond *the narrow margin of this page*. In particular, I thank my uncle Donato for the invaluable technical assistance, my brother Giuseppe, my nemesis, and my parents: Maria “la Giano”, my personal coach, and my best supporter and motivator Raffaele. Finally, I dedicate this thesis to the memory of my grandmother Ninetta. You are in my eyes, my hands, and inside my heart.

List of publications

- **G. Blasi**, F. Taddei, V. Giovannetti, and A. Braggio
  Manipulation of Cooper pair entanglement in hybrid topological Josephson junctions
  Phys. Rev. B, **99**(6) 064514 (2019)
  Proceedings **12**(1), 44 (2019).
- **G. Blasi**, F. Taddei, L. Arrachea, M. Carrega, and A. Braggio
  Nonlocal Thermoelectricity in a Superconductor–Topological-Insulator–Superconductor Junction in Contact with a Normal-Metal Probe: Evidence for Helical Edge States
  Phys. Rev. Lett., **124**(22) 227701 (2020).
- **G. Blasi**, F. Taddei, L. Arrachea, M. Carrega, and A. Braggio
  Nonlocal thermoelectricity in a topological Andreev interferometer
  Phys. Rev. B, **102**(24) 241302(R) (2020).
- D. Gresta, **G. Blasi**, F. Taddei, M. Carrega, A. Braggio, and L. Arrachea
  Signatures of Jackiw-Rebbi resonance in the thermal conductance of topological Josephson junctions with magnetic islands
  Phys. Rev. B, **103**(7) 075439 (2021).
- **G. Blasi**, F. Taddei, L. Arrachea, M. Carrega, and A. Braggio
  Nonlocal thermoelectric engines in hybrid topological Josephson junctions
  Phys. Rev. B, **103**, 235434 (2021).
- **G. Blasi**, A. Braggio, V. Giovannetti, and F. Taddei
  Non local topological Josephson jucntion in $\nu = 2$ *quantum Hall effect*
  In preparation (2021).

Contents

1

Introduction

The development of quantum mechanics at the turn of the last century represented a unique intellectual experience, which forced scientists and philosophers to profoundly change the concepts they used to describe the World. After these heroic efforts it was possible to understand the stability of matter, the mechanical and electrical properties of materials, the interaction between radiation and matter and many other characteristics of the microscopic world which, otherwise, were impossible to explain within the elegant but incomplete framework of classical physics. After a few decades, that conceptual revolution made possible a technological shake-up, known as “the first quantum revolution”, which is at the origin of our information society. Indeed, it is with the quantum understanding of the structure and properties of matter that physicists and engineers were able to conceive and develop (inter alia) transistors and lasers - two of the key technologies that today enable broadband information transfer, among many others scientific and commercial applications [Bell2004].

Recently, tremendous advances in nanofabrication techniques have enabled unprecedented preparation and control of quantum systems in a wide range of physical devices. Experiments involving few degrees of freedom can be carried out in several platforms ranging from trapped ions [Friedenauer2008, Blatt2012], to cold bosons loaded into optical lattices [Yukalov2009], to superconducting qubits in microwave cavities [Wallraff2004, Majer2007], to single-electron transistors [Kastner1992]. This experimental breakthrough has opened the path for a “second quantum revolution”. Therefore, whereas the first quantum revolution provided us with the rules that govern the physical reality on the microscopic scale, with the second quantum revolution we will be able to use these rules allowing us to move into a new era of quantum technology [MacFarlane2003].

Evidently a fruitful route towards the development of new quantum technologies is represented by the fertile field of *quantum thermodynamics* [Pekola2015, Binder2019]. The dominant trend of building devices on a smaller and smaller scale, leads to the point that design must inevitably be based on quantum principles. Thus, on the experimental side, the goal of quantum thermodynamics is the development of highly controllable nanoscale devices that operate on length and temperature scales that make a quantum description necessary. It aims to build a new conceptual framework that goes beyond the conventional regime of validity of macroscopic thermodynamics to account for finite size effects such as quantisation, quantum superposition, entanglement and decoherence. At this point, questions arise: Do quantum phenomena, such as coherence and quantum correlations result in thermodynamic advantages or limitations? Do quantum engines and refrigerators perform better or worse compared to their classical counterparts? What is the meaning of heat, work and entropy at the quantum level and how these quantities can be defined in this regime? It was precisely in attempting to address such fundamental questions that, at the threshold of the 21st century, with the pioneering works of Hicks and Dresselhaus [Hicks1993, Hicks1993a] and Mahan and Sofo [Mahan1996], it was realized that nanostructured materials can outperform classical thermoelectric materials [Harman2000, Venkatasubramanian2001, Josefsson2018]. More recently, thermoelectricity in low-dimensional systems also finds applications in heat management at the nano-scale to perform (for example) active cooling on chip [Giazotto2006, Fagas2014] - an urgent problem given the progressive miniuaturization of the electronic components. In this respect, considerable progress has been made with the introduction of the so called phase-coherent caloritronics in superconducting circuits [Sanchez2014, Fornieri2017, Hwang2020]. The key idea here is to control heat fluxes in superconducting hybrid systems by exploiting the macroscopic quantum coherence inherent to the superconducting phase difference in Josephson junctions [Josephson1962]. Moreover, the possibility to master heat currents in thermally biased Josephson junctions with a tunable phase difference also demonstrated remarkable results towards the implementation of the thermal counterparts of interferometers [Giazotto2012, Martinez-Perez2014, Fornieri2016], diodes [Chang2006, Martinez-Perez2015] and solid-state memory devices [Xie2011] for the realization of thermal transistors [Giazotto2014, Fornieri2016] and thermal logic gates [Li2012].

An alternative yet promising route to quantum technologies has been found in the recently emerged field of *quantum topology* [Moore2009, Hasan2010, Bernevig2013a]. Originally developed nearly a hundred years ago, band theory of solids [Bloch1929] - a major pillar of modern physics - has long been thought to be fully understood and lacking in particular revelations. However, starting in the late 1980s with the discovery of the quantum Hall effect [Klitzing1980] and then in the early 2000s with the theorization and discovery of topological insulators [Kane2005, Konig2007], our understanding of crystalline solids underwent an unexpected turn. In fact, topological quantum materials are a class of compounds featuring electronic band structures which are topologically distinct from trivial insulators. Remarkably, topological insulators are characterized by a full insulating gap in the bulk and topologically protected gapless edge states, manifesting spin-momentum locking features and robustness against perturbations with very long decoherence lengths [Roth2009, Chen2012, Wiedenmann2016]. For this reason, in combination with superconductors, topological insulators are anticipated to lead to a new architecture for topological quantum bits exploiting exotic phenomena such as Majorana modes [Kitaev2001, Lutchyn2010, Oreg2010], and fostering advances in the fields of quantum information and quantum computation [Moore2009].

The work presented in this thesis develops themes which connect the two successful fields of quantum thermodynamics and quantum topology. In particular, we focus on the study of the electrical and thermoelectrical properties of hybrid topological superconducting systems [Veldhorst2012, Hart2014], investigating the potential of the intriguing and fruitful marriage between topology and coherent thermodynamics [Scharf2020, Scharf2021]. Through this work, we show how Josephson junctions based on Two Dimensional Topological Insulators (2DTIs) may represent a concrete and fruitful playing ground for fundamental research as well as for potential applications for quantum sensing [Giazotto2015, Heikkila2018], entanglement manipulation [Blasi2019], and thermal engines [Mazza2014, Vischi2019]. On the one hand, in the first part of the thesis, we give an overview of the theoretical framework and formalism necessary to describe these systems. On the other, we fully characterize the thermoelectric response and performances of such hybrid junctions, in different configurations and under a wide range of external tuning parameters. In this regard, we first investigate how the flux and phase biases trigger nonlocal thermoelectric effects in a topological Josephson junction in contact with a normal-metal probe under the application of a thermal difference between the superconducting terminals. Then, we analyze the thermal conductance of a 2DTI Josephson junction hosting a magnetic island showing that it can be used to characterize the topological nature of the junction. In conclusion, we discuss how a hybrid topological Josephson junction, consisting of two planes of topological insulator, can be used as promising platform for the manipulation of spin-entangled electrons in solid-state systems offering the prospect of encoding, transmitting and processing the quantum information in a fault-tolerant, topologically protected manner [Nayak2008, Wu2014].

The outline of the thesis is the following. It consists of two parts: in Part I, entitled "Theoretical Framework", we lay the theoretical foundations necessary to describe hybrid topological Josephson junctions; while Part II, named "Original Results", is devoted to presenting original studies about these systems. For completeness, appendices from A to D, contain complementary results and details of calculations presented in the different chapters. More specifically, in Chaps. 2 and 3 we provide an overview of the basic concepts that underlie the two main constituent materials necessary for the realization of a hybrid topological Josephson junction, namely: topological insulators and superconductors. In particular, in Chap. 2, theoretical models, materials properties, and experimental results on Chern insulators and 2DTIs are reviewed and the emergence of edge states at the boundaries of these materials is discussed. In Chap. 3 we introduce the Bogoliubov-de Gennes (BdG) formalism - which will constitute the framework of the entire thesis - and discuss how the BdG equations can be used to describe one of the most important phenomenon arising in presence of superconductivity: the Andreev reflection.

In Chaps. 4 and 5, we introduce the technical tools necessary for dealing with phase-coherent quantum transport and thermoelectricity in multiterminal mesoscopic hybrid devices. Specifically, in Chap. 4 we start by presenting first the Landauer-Büttiker (or scattering) theory developed for normal metal mesoscopic systems, and then we extend it to include superconducting components. The power of the scattering approach is encoded in a single mathematical object: the scattering matrix. In this respect, in Sec. 4.4, we deduce the foundamental symmetry relations that the scattering matrix has to satisfy depending on the specific symmetry class of the underlying Hamiltonian describing the system. In Chap. 5, we apply the scattering theory to the case of the linear response regime, and use the aforementioned symmetries of the scattering matrix to obtain the Onsager reciprocal relations. The main aspects of the Josephson effect and the constitutive equations governing the behavior of Josephson junctions are reviewed in Chap. 6.

In the remaining chapters we collect original results. In Chaps. 7, 8 and 9 we consider a system consisting of a topological Josephson junction hosting a pair of helical edge states of a quantum spin Hall bar in contact with a normal-metal probe. In Chap. 7, the orbital phase induced by a small magnetic field threading the junction known as Doppler shift (DS), combines with the conventional Josephson phase difference and originates an effect akin to a Zeeman field in the spectrum. As a consequence, when a temperature bias is applied to the superconducting terminals, a thermoelectric current is established in the normal probe. We argue that this purely non-local thermoelectric effect is a unique signature of the helical nature of the edge states coupled to superconducting leads and it can constitute a useful tool for probing the helical nature of the edge states in systems where the Hall bar configuration is difficult to achieve.

In Chap. 8 we show that nonlocal thermoelectricity can be eventually generated by a *purely* Andreev interferometric mechanism. This response can be tuned by imposing a Josephson phase difference, through the application of a dissipationless current between the two superconductors, even *without* the need of applying an external magnetic field. We discuss in detail the origin of this effect and we provide also a realistic estimation of the nonlocal Seebeck coefficient.

While in Chaps. 7 and 8 we assumed equal proximized gaps in the two superconducting terminals, by focusing only on the linear response regime; in Chap 9 we generalize the analysis to the case where we have different gaps which better describes a realistic experimental situation, where the samples have unavoidable imperfections leading to asymmetric pairing potentials in the superconducting leads. In this configuration we point out that the gap asymmetry gives rise to a new intermediate regime where Andreev interference determines a local thermoelectrical effect even without applying a phase bias. Finally, we discuss the power and the efficiency of the topological thermoelectric engine which reaches maximum power at maximal efficiency for a well coupled normal probe.

In Chap. 10 we consider a 2DTI Josephson junction with embedded magnetic domains. These hybrid heterostructures can host a number of topological phases, such as Jackiw-Rebbi solitons and Majorana zero modes. In particular, we show that, configurations hosting soliton magnetic modes lead to a peculiar behavior of the thermal conductance, characterized by a negative slope as a function of the temperature. At low temperatures, these junctions also show characteristic coherence patters in the behavior of the thermal conductance as function of the Josephson phase bias and the angle between the magnetizations of the domains.

In Chap. 11 we investigate the supercurrent in a hybrid topological Josephson junction consisting of two planes of topological insulator in a specific configuration, which allows both local (LAR) and crossed (CAR) Andreev processes at the interfaces with two conventional s-wave superconductors. We describe the effects of gate voltage and magnetic flux controls applied to the edge states of each TI. In particular, we demonstrate that the voltage gating allows the manipulation of the entaglement symmetry of non-local Cooper pairs associated to the CAR process. Remarkably, we find that the critical current of the junction takes a very simple form which reflects the change in the symmetry occurred to the entangled state and allows to determine the microscopic parameters of the junction.

Finally, in Chap. 12, we draw the conclusions of this thesis.

Part I

Theoretical Framework

2

Topological Insulators

A recurring theme in condensed-matter physics has been the discovery and classification of distinctive phases of matter. Classically, we learn of phases such as liquid, crystal, or vapor. However quantum theory has revealed many more fascinating and exotic states of matter, such as superconductors, Bose-Einstein condensates, ferromagnets and antiferromagnets, and etc. Often, these phases can be understood using Landau's approach [Ginzburg1944], which characterizes states in terms of underlying symmetries that are spontaneously broken. However, the major limitation of Landau's theory of phase transitions is that it is related to a local order parameter. Over the past 40 years, it has become clear that a series of phases of matter do not have a local order parameter [Bernevig2013]. For most of them, a nonlocal order parameter can be defined, but it is unclear how a Landau-like theory of this order parameter can be developed. In particular, the study of the quantum Hall effect has led to a different classification paradigm based on the notion of topological order [TKNN1982, Wen1995]. The state responsible for the quantum Hall effect does not break any symmetries, but it defines a topological phase in the sense that certain fundamental properties (such as the quantized value of the Hall conductance and the number of gapless boundary modes) are insensitive to smooth changes in material parameters and cannot change unless the system passes through a quantum phase transition.

In the present chapter we give a review of different topological phases of matter. In particular, we focus on two-dimensional insulating phases, i.e. phases where a bulk energy gap separates the highest occupied electronic states (in the conduction band) from the lowest empty states (in the valence band). The question underlying the topological classification of insulators is whether all insulating phases are equivalent to each other, and in particular whether the ensembles of the valence bands of different insulators can be continuously transformed into each other without closing the energy gap. In contrast to ordinary ("trivial") insulators, one of the most striking features of topological ("non-trivial") insulators is the existence of gapless conducting edge states. As we will discuss along the thesis, these states are predicted to have special properties that could be useful for applications ranging from spintronics to quantum computation to quantum thermodynamics. Among the topologically non-trivial insulating phases we can distinguish Chern insulators (and quantum Hall phases), arising when time-reversal symmetry is broken, and $\mathbb{Z}_2$ topological insulators (or quantum spin Hall phases), whose edge states are protected by time-reversal symmetry [Hasan2010]. The latter, which represent one of the main object of this thesis, are also known simply as 2D topological insulators or 2DTIs, and we will adhere to this naming convention.

2.1 Topological band theory

For crystalline insulating materials whose physical properties are well captured by a one-particle theory, the band theory of solids [Bloch1929] provides a powerful language to describe the electronic structure of such systems. This theory exploits the translational symmetry of the crystal to classify electronic states in terms of their crystal momentum $\boldsymbol{k}$, defined in a periodic Brillouin zone. The Bloch states $|u_m(\boldsymbol{k})\rangle$, defined in a single unit cell of the crystal, are eigenstates of the Bloch Hamiltonian $H(\boldsymbol{k})$. The eigenvalues $\epsilon_m(\boldsymbol{k})$ define energy bands that collectively form the band structure. In an insulator an energy gap separates the occupied valence band states from the empty conduction band states.

Band structures where the eigenvalues of $H(\boldsymbol{k})$ show an energy gap, can be classified topologically by considering the equivalence classes of Bloch Hamiltonians $H(\boldsymbol{k})$ that can be continuously deformed into one another without closing the energy gap. These classes are characterized by a topological invariant $n \in \mathbb{Z}$, called the Chern invariant. The theory of the Chern invariant is rooted in the mathematics of fiber bundles [Nakahara2003], but it can be understood physically in terms of the Berry curvature [Berry1984, Xiao2010] associated with the Bloch wave functions.

The concepts of Berry phase and Berry curvature were introduced by Sir Michael Berry in a seminal paper [Berry1984] concerning the adiabatic evolution of an eigenenergy state when some external parameters are changed slowly and cyclically, i.e. so that they describe a closed path $\mathcal{C}$ in the parameter space. In the absence of degeneracy, the eigenstate $|u_m(\boldsymbol{k})\rangle$ will come back to itself at the end of the loop, but there will be a phase difference equal to the time integral of the energy (divided by $\hbar$) - corresponding to the dynamical phase - plus an extra Berry phase γ_m. Such a phase is given by the line integral over the path $\mathcal{C}$ of the so-called Berry connection $\mathcal{A}_m = i\,\langle u_m(\boldsymbol{k})|\,\nabla_{\boldsymbol{k}}\,|u_m(\boldsymbol{k})\rangle$. This may be equivalently expressed as a surface integral of the Berry curvature (or Berry flux) $\Omega_m = \nabla_{\boldsymbol{k}} \times \mathcal{A}_m$ over an arbitrary surface $\mathcal{S}$ enclosed by the path $\mathcal{C}$ [1]. The Berry curvature is a gauge invariant vector field whose flux through the Brillouin zone gives topological classification of the band structure [Nakahara2003, Xiao2010]. The Chern invariant $n \in \mathbb{Z}$, characterizing classes of equivalence of insulating Bloch Hamiltonians, is given by the following expression

$$n = \sum_{m}^{\star} \frac{1}{2\pi} \int_{BZ} d\boldsymbol{k}\ \Omega_m(\boldsymbol{k}) \tag{2.2}$$

where the apex $\star$ indicates that the summation is taken over occupied bands and the integration is taken for $\boldsymbol{k}$ inside the Brillouin zone (BZ). If the Chern invariant n, defined in Eq. (2.2), is different from zero we talk about topologically non-trivial insulators, otherwise we refer to trivial insulators.

---

[1] The Berry flux $\Omega_m(\boldsymbol{k})$ is related to the gauge-field tensor [Xiao2010]

$$\Omega^m_{\alpha\beta}(\boldsymbol{k}) = i \sum_{m' \neq m} \frac{\langle u_m(\boldsymbol{k})|\,\partial_{k_\alpha} H(\boldsymbol{k})\,|u_{m'}(\boldsymbol{k})\rangle\,\langle u_{m'}(\boldsymbol{k})|\,\partial_{k_\beta} H(\boldsymbol{k})\,|u_m(\boldsymbol{k})\rangle - (\alpha \leftrightarrow \beta)}{(\epsilon_m(\boldsymbol{k}) - \epsilon_{m'}(\boldsymbol{k}))^2}, \tag{2.1}$$

through the relation $\Omega^m_{\alpha\beta} = \varepsilon_{\alpha\beta\xi}(\Omega_m)_\xi$ where where α, β and ξ are cartesian indexes and $\varepsilon_{\alpha\beta\xi}$ is the Levi-Civita antisymmetry tensor.

2.2 Quantum Hall effect and Chern insulators

A first example of a topologically non-trivial insulating state is the integer quantum Hall state. The quantum Hall effect was first reported for the two-dimensional electron gas in the inversion layer of a silicon metaloxide- semiconductor field-effect-transistor at temperature $T = 1.5\ K$ and magnetic field $B = 18\ T$ by Klaus von Klitzing [Klitzing1980], and earned him the Nobel prize in 1985. The quantization of the electrons' circular orbits with cyclotron frequency ω_c leads to quantized Landau levels with energy $\epsilon_m = \hbar\omega_c(m + 1/2)$. If N Landau levels are filled and the rest are empty, then an energy gap separates the occupied and empty states just as in an insulator. Unlike an insulator, though, an electric field causes the cyclotron orbits to drift, leading to a Hall current characterized by the quantized Hall conductivity

$$\sigma_{xy} = N\frac{e^2}{h}, \tag{2.3}$$

which represents the ratio between the electric current density along x and the y-component of the electric field in the sample. The quantization of σ_{xy} has been measured to 1 part in 10^9, making it very appealing for metrological applications.

Quite remarkably, in Ref. [TKNN1982] Thouless *et al.* demonstrated that the Hall conductivity σ_{xy}, computed by using the Kubo formula, is strongly related with the Chern number. More precisely they showed that the number of Landau levels N of Eq. (2.3) exactly coincides with the topological invariant n of Eq. (2.2). The Hall conductivity is therefore proportional to the Chern number, where the proportionality constant depends only on fundamental constants (e and $\hbar$). Let us insist on the observation that any perturbation or disorder added to the Hamiltonian which, however, does not close the energy gap, leaves the Chern number (and so the Hall conductivity) unaltered. This is a clear manifestation of the topological nature of the quantum Hall state which also explains the exceptionally flat plateaus of the Hall conductivity observed in quantum Hall effect experiments [Klitzing1980].

Haldane model

A simple example of the quantum Hall effect in a band theory is provided by the so-called Haldane model Hamiltonian [Haldane1988]. It represents the paradigm for Chern insulators, and has been used as a workhorse in many simulations, providing invaluable insight into topological features of the electronic wavefunction as well as into features of orbital magnetization [Resta2020].

The idea of Haldane is that the quantum Hall effect may result from the broken time-reversal symmetry without any net magnetic flux through the unit cell of a periodic two-dimensional graphene model [Shen2012]. In order to understand that, let us first start by considering the Hamiltonian of a two-dimensional graphene model. The simplest description of graphene employs a two band model for the p_z orbitals on the two equivalent atoms in the unit cell of graphene's honeycomb lattice. The Bloch Hamiltonian takes the following form

$$H(\boldsymbol{k}) = \vec{h}(\boldsymbol{k}) \cdot \vec{\sigma} \tag{2.4}$$

where $\vec{\sigma} = (\sigma_x, \sigma_y, \sigma_z)$ are Pauli matrices and $\vec{h}(\boldsymbol{k}) = (h_x(\boldsymbol{k}), h_y(\boldsymbol{k}), 0)$. The combination of spatial inversion symmetry (SIS) [i. e. $h_z(\boldsymbol{k}) = -h_z(-\boldsymbol{k})$], and time-reversal symmetry (TRS) [i. e. $h_z(\boldsymbol{k}) = h_z(-\boldsymbol{k})$] requires $h_z(\boldsymbol{k}) = 0$. From the eigenspectrum of Eq. (2.4), it turns out that the conduction and valence band touch each other at two distinct points in the Brillouin zone (called Dirac points), namely $\boldsymbol{K_1}$ and $\boldsymbol{K_2} = -\boldsymbol{K_1}$. Near those points, i. e. for small $\boldsymbol{q_i} \equiv \boldsymbol{k} - \boldsymbol{K_i}$ (with $i = 1, 2$), the electronic dispersion resembles the linear dispersion, and Eq. (2.4) splits in the two independent effective Hamiltonians

$$H(\boldsymbol{q_i}) = \hbar v_F \; \boldsymbol{q_i} \cdot \vec{\sigma} \tag{2.5}$$

where v_F is the Fermi velocity. The degeneracy at the Dirac points is protected by the SIS and TRS. In order to lift such a degeneracy, Haldane imagined to break the TRS with a "periodic magnetic field" with opposite orientations on the different atoms of each unit cell such that its cell average vanishes. This perturbation allows nonzero $h_z(\boldsymbol{k})$ and introduces a mass term to the Hamiltonians of Eq. (2.5)

$$H(\boldsymbol{q_i}) = \hbar v_F \boldsymbol{q_i} \cdot \vec{\sigma} + m_i \sigma_z, \tag{2.6}$$

which have dispersions $\epsilon(\boldsymbol{q_i}) = \pm\sqrt{|\hbar v_F \boldsymbol{q_i}|^2 + m_i^2}$ respectively characterized by the energy gaps $2|m_i|$ with $m_i = h_z(\boldsymbol{K_i})$ for each Dirac point $i = 1, 2$. Note that, SIS requires the masses at $\boldsymbol{K_1}$ and $\boldsymbol{K_2}$ have opposite signs, i. e. $m_1 = -m_2$. Haldane showed that this gapped state is not an insulator but rather a quantum Hall state with $\sigma_{xy} = e^2/h$. More precisely, by using Eq. (2.2), it follows that each Dirac point contributes $\pm e^2/2h$ to σ_{xy}. In the insulating state with $m_1 = m_2$ the two cancel, so $\sigma_{xy} = 0$. In the quantum Hall state with $m_1 = -m_2$ they add.

2.3 Two Dimensional Topological Insulator (2DTI)

As we have seen so far, it turns out that a necessary condition for having topologically non-trivial Chern insulators is to have a broken TRS. Indeed, it is easy to show that if the system is time-reversal symmetric, it follows that [Xiao2010] $\Omega_m(-\boldsymbol{k}) = -\Omega_m(\boldsymbol{k})$ and the integral in Eq. (2.2) vanishes trivially. As a consequence, any time-reversal symmetric Bloch insulator is a topologically trivial Chern insulator. For these time-reversal invariant models, however, it exists a different topological classification proposed in 2005 by Kane and Mele [Kane2005, Kane2005a]. The key to understand these new class of topological materials, called $\mathbb{Z}_2$ insulators, or simply Two Dimensional Topological Insulators (2DTIs) is to examine the role of TRS for spin 1/2 particles (see Sec. 4.4 for more details). A time-reversal invariant Bloch Hamiltonian $H(\boldsymbol{k})$ must satisfy

$$\mathcal{T} H(\boldsymbol{k}) \mathcal{T}^{-1} = H(-\boldsymbol{k}), \tag{2.7}$$

where we introduced the time-reversal anti-unitary operator $\mathcal{T} = -i\sigma_y K$, where σ_y is the Pauli matrix acting in the spin-space and K is the complex conjugate operator, such that $\mathcal{T}^2 = -1$. Similarly to the case of Chern insulators, it is possible to distinguish the equivalence classes of Bloch Hamiltonians satisfying this constraint and that can be smoothly deformed without closing the energy gap. When TRS is preserved, the Chern number is $n = 0$, but there is an additional $\mathbb{Z}_2$ topological invariant with two possible values $\nu = \{0, 1\}$ [Kane2005, Kane2005a].

There are several mathematical formulations of the $\mathbb{Z}_2$ invariant ν of 2DTIs. In particular the calculation of the topological invariant ν is quite simple if the 2D system conserves the spin S_z along the z-direction. In this case the up and down spins have independent Chern numbers $n_\uparrow$ and $n_\downarrow$. TRS requires $n_\uparrow + n_\downarrow = 0$, but the difference $n_\uparrow - n_\downarrow$ defines a quantized spin Hall conductivity, and the $\mathbb{Z}_2$ topological invariant ν takes the following simple form

$$\nu = [(n_\uparrow - n_\downarrow)/2] \bmod 2. \tag{2.8}$$

More general definitions of ν are available when S_z nonconserving terms are added to the Bloch Hamiltonian - see Ref. [Hasan2010] for more details.

Quantum spin Hall insulators and HgTe/CdTe quantum wells

Research on spin-orbit coupling in graphene led Kane and Mele [Kane2005, Kane2005a] to propose the first model of a 2DTI consisting of two time-reversed copies of the Haldane model. In the Kane-Mele model the spin degree of freedom is taken into account, and the overall system is time-reversal symmetric. For this reason, 2DTIs are also known as quantum spin Hall insulators (QSHIs) [Hasan2010].

In the simplest picture, the intrinsic spin-orbit interaction commutes with the electron spin S_z, so the Hamiltonian decouples into two independent Hamiltonians for the up and down spins, resulting in two copies of Eq. (2.6), which overall do not violate TRS. The result is that, under an applied electric field E_y, the up and down spins have Hall currents that flow in opposite directions. Thus opposite signs of the conductivity are obtained for each spin, and the total Hall conductivity of the system turns out to be zero. However, even if the Hall conductivity is zero, there is a quantized spin Hall conductivity, defined by $\sigma^s_{xy} = (J^{\uparrow}_x - J^{\downarrow}_x)/E_y$ with $\sigma^s_{xy} = e/2\pi$ - a quantum spin Hall effect.

However, even if the Kane-Mele model provided an interesting theoretical toy model for QSHIs, it was soon shown to be unrealistic since the spin–orbit effect in graphene based systems is extremely small [Konig2008]. Understandably, a better place to look for this physics would be in materials with strong spin-orbit interactions. To this end, Bernevig, Hughes, and Zhang [BHZ2006], paved the way to the experimental discovery of the QSH state in semiconductors with an "inverted" electronic gap, and predicted a quantum phase transition in HgTe/CdTe quantum wells. $\mathrm{Hg}_{1-x}\mathrm{Cd}_x\mathrm{Te}$ is a family of semiconductors with strong spin-orbit interactions. For both HgTe and CdTe, the main bands near the Fermi level are close to the Γ-point in the Brillouin zone, and they are the s-type band (Γ_6) and the p-type band which is split to a $J = 3/2$-band (Γ_8) and a $J = 1/2$-band (Γ_7) by spin–orbit coupling (see Fig. 2.1 (a)). CdTe has a band order with an s-type (Γ_6) conduction band and p-type valence bands (Γ_8, Γ_7) which are separated from the conduction band by a large energy gap of $\sim 1.6\ eV$. HgTe, as a bulk material, can be regarded as a symmetry-induced semi-metal. Its negative energy gap of $\sim 300\ meV$ indicates that the Γ_8 band, which usually forms the valence band, is above the Γ_6 band. Based on this unusual sequence of the states, such a band structure is said to be inverted.

When HgTe-based quantum well structures are grown, the peculiar properties of the well material can be utilized to tune the band structure in a unique way. Heuristically, when the thickness d of the HgTe layer is small, the heterostructure behaves similarly to the bulk CdTe (with normal band ordering). On the other hand, as d is increased, the material behaves more like bulk HgTe (with inverted bands). So as the thickness increases we expect to reach a critical thickness d_c where the Γ_8 and Γ_6 subbands cross and become inverted with the Γ_8 bands becoming conduction subbands and Γ_6 becoming valence subbands - as illustrated in Fig. 2.1 (b). Bernevig *et al.* showed that such an inversion of the bands takes place at the critical thickness $d_c = 6.3\ nm$ at which the gap closes, and the $\mathbb{Z}_2$ invariant changes, passing from $\nu = 0$ (trivial insulator for $d < d_c$) to $\nu = 1$ (quantum spin Hall insulator for $d > d_c$), signaling the occurrence of a quantum phase transition.

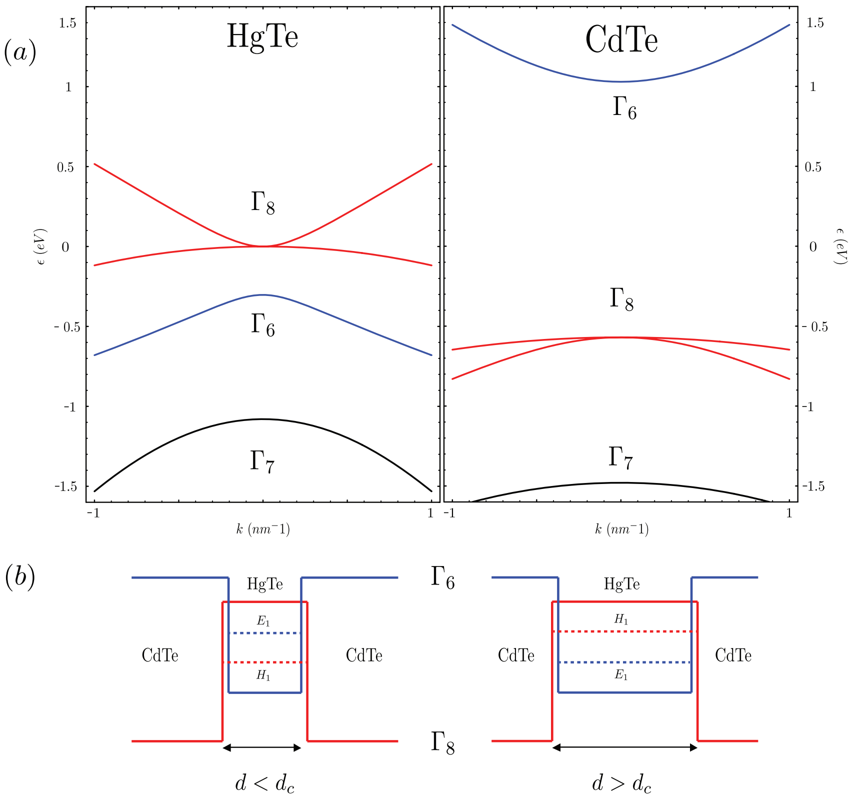

FIGURE 2.1: (a) - Bulk bandstructure for HgTe (top-left panel) and CdTe (top-right panel). (b) - Schematic picture of quantum well geometry and lowest subbands for two different thicknesses. The notation for the heavy-hole-like (H_1) and electron-like (E_1) subbands is according to the properties of the respective wave functions. Figure adapted from Ref. [Konig2008].

2.4 Edge states and bulk-boundary correspondence

A striking consequence of the topological classification of gapped band structures is the existence of gapless conducting states at interfaces where the topological invariant changes. The existence of edge states in topologically non-trivial crystal is readily explained imagining an interface where the Bloch Hamilltonian slowly interpolates between a topologically non-trivial insulator $(n, \nu \neq 0)$ and a trivial insulator $(n, \nu = 0)$. Somewhere along the way the energy gap has to vanish because otherwise it would be impossible for the topological invariant to change. There will therefore be low energy electronic states bound to the region where the energy gap passes through zero. This interplay between the topological structure of bulk crystals and the presence of gapless boundary modes is known as the bulk-boundary correspondence: in a nutshell, even if the system is a bulk insulator, it constitutes an edge Fermi liquid [Bernevig2013].

Chiral edge modes

In the context of Chern insulators, it is well known that edge states emerge at the interface between the integer quantum Hall state and vacuum [Halperin1982]. Naively, they can be understood in terms of the skipping motion electrons execute as their cyclotron orbits bounce off the edge (see Fig. 2.2 (a)). It can be shown [Hasan2010] that the number of edge states at the interface with topologically trivial insulators corresponds to the topological invariant n of Eq. (2.2). Importantly, such edge states of Chern insulators are chiral in the sense that they propagate in one direction only along the edge, as showed in Fig. 2.2 (a). Moreover, these states are insensitive to disorder because there are no states available for backscattering - a fact that underlies the perfectly quantized electronic transport in the quantum Hall effect.

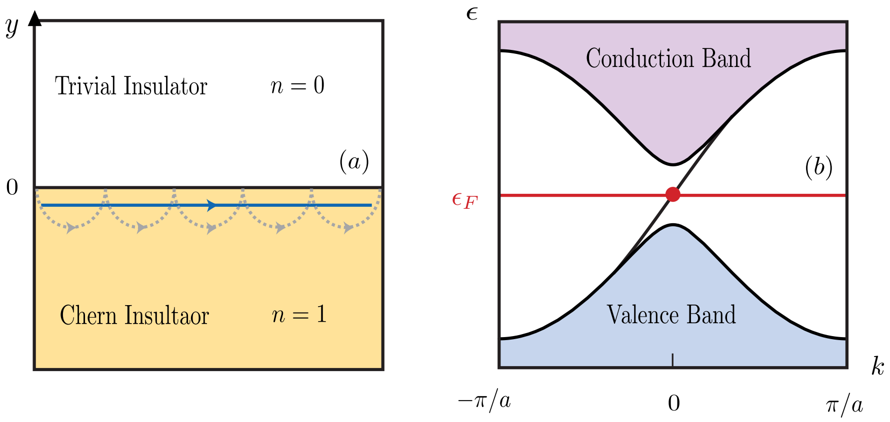

FIGURE 2.2: Pictorial representation of the chiral edge modes of Chern insulators. (a) -A Chern insulator with $n = 1$ is interfaced with a trivial insulator ($n = 0$). At the interface, where the energy gap closes, a chiral edge mode (blue arrow) is established. Dashed gray lines represent the skipping cyclotron orbits executed by electrons bouncing off the edge. (b) - Schematic of the band structure of this system. The bulk conduction and valence bands are joined by an edge mode traversing the energy gap. Figure adapted from Ref. [Hasan2010].

A simple theory of the chiral edge states is based on the Jackiw-Rebbi model, which can be developed using the two band Dirac model [Jackiw-Rebbi1976] introduced in Eq. 2.6 in a semi-infinite geometry with an edge at $y = 0$, as depicted in Fig. 2.2 (a). In this respect, let us consider an interface where the mass at one of the Dirac points (say $\boldsymbol{K_1}$) is fixed and positive, $m_1 = m > 0$, while the mass at the other Dirac point ($\boldsymbol{K_2}$) changes sign as a function of y, namely

$$m_2(y) \equiv \begin{cases} +m & \text{for} \quad y > 0 \\ -m & \text{for} \quad y < 0 \end{cases} . \tag{2.9}$$

In this way we have a trivial insulator for $y > 0$, and the quatum Hall state for $y < 0$. The wave function solution with energy $\epsilon(q_x) = \hbar v_F q_x$ can be written as

$$\Psi(x, y) \propto e^{iq_x x} e^{-|my/\hbar v_F|} \begin{pmatrix} 1 \\ 1 \end{pmatrix}, \tag{2.10}$$

which dominantly distributes near the interface at $y = 0$ and decays exponentially away from it. This band of states intersects the Fermi energy ϵ_F with a positive group velocity $v_F = (1/\hbar)(d\epsilon/dq_x)$ and defines a right moving chiral edge mode, as depicted in Fig. 2.2 (b).

Helical edge modes

Edge states are also present in 2DTIs. Differently from Chern insulators, they always occurs in pairs, and the $\mathbb{Z}_2$ invariant ν indeed corresponds to the number of pairs of the edge states modulo 2. The fact that the eigenstates of a TRS invariant Hamiltonian are at least twofold degenerate is guaranteed by Kramer's theorem, and directly follows from the relation $\mathcal{T}^2 = -1$ valid for spin 1/2 particles. Indeed, suppose that a nondegenerate state $|\varphi\rangle$ existed, then $\mathcal{T}|\varphi\rangle = c|\varphi\rangle$ for some constant c. This would mean $\mathcal{T}^2|\varphi\rangle = |c|^2|\varphi\rangle$, which is not allowed since $|c|^2 \neq -1$. Importantly, the two states, $|\varphi\rangle$ and $\mathcal{T}|\varphi\rangle$, form a Kramers pair whose degeneracy cannot be lifted by any time reversal symmetric perturbation [Kane2005, Kane2005a].

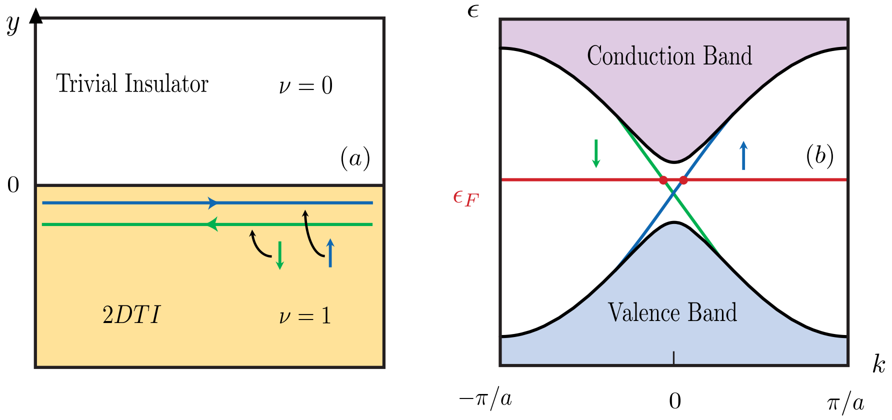

FIGURE 2.3: Pictorial representation of the helical edge modes of 2DTIs. (a) - A 2DTI with $\nu = 1$ is interfaced with a trivial insulator ($\nu = 0$). At the interface, where the energy gap closes, a couple of counter-propagating edge modes is established. (b) - Schematic of the band structure of this system. The bulk conduction and valence bands are joined by the two helical edge modes with opposite spins traversing the energy gap. Opposite slops of the ϵ-k dispersion curves indicate that they have opposite velocity. Figure adapted from Ref. [Hasan2010].

Moreover, since TRS requires that states at momenta k and $-k$ have opposite spin, Kramers pairs with opposite spin-polarization counterpropagate at a given edge, as schematically depicted in Fig. 2.3 (a). This distinctive property of edge states is called "spin-momentum locking" and constitutes one of the main characteristics of 2DTIs that we will be able to discuss extensively throughout the thesis. In contrast to the chiral states of Chern insulators, they are said to be helical in analogy with the correlation between spin and momentum of a particle known as helicity [Wu2006]. The helical edge states can be described by the following low energy 1D Dirac effective Hamiltonian

$$H_{\text{edge}} = \int dx \; \psi_\uparrow^\dagger \left(-i\hbar v_F \partial_x - \mu\right) \psi_\uparrow + \psi_\downarrow^\dagger \left(i\hbar v_F \partial_x - \mu\right) \psi_\downarrow, \tag{2.11}$$

where $\psi_\uparrow$ ($\psi_\downarrow$) is the field operator of spin-↑ (↓) electrons, μ is the chemical potential, and v_F is the propagation Fermi velocity.

Due to their helical property, 2DTI's edge states form a unique 1D conductor that is essentially half of an ordinary 1D conductor. However, while ordinary conductors (which have both spins propagating in both directions) are fragile because the electronic states are susceptible to Anderson localization in the presence of weak disorder [Anderson1958, Lee1985]; the quantum spin Hall edge states cannot be localized even for strong disorder. Indeed, as soon as time-reversal symmetry is ensured, it can be shown (by using the Landauer-Büttiker formalism) that no elastic backscattering can occur at the interface between a disordered and a clean region. As a consequence, the transport along the edge is ballistic at zero temperature and the conductivity will be quantized to $2e/h$. Moreover, recent studies on the impact of electron-phonon [Budich2012] and spin-phonon interaction [Groenendijk2018] in helical edge states support the idea that the transport is ballistic at the operating temperatures of a few kelvin.

Within a year of the theoretical prediction of 2DTIs in HgTe/CdTe quantum wells, the Würzburg group led by Laurens Molenkamp [Konig2007], realized the device and performed transport experiments that convincingly demonstrated the existence of the edge states in quantum spin Hall insulators. In Fig. 2.4 are shown the resistance measurements for a

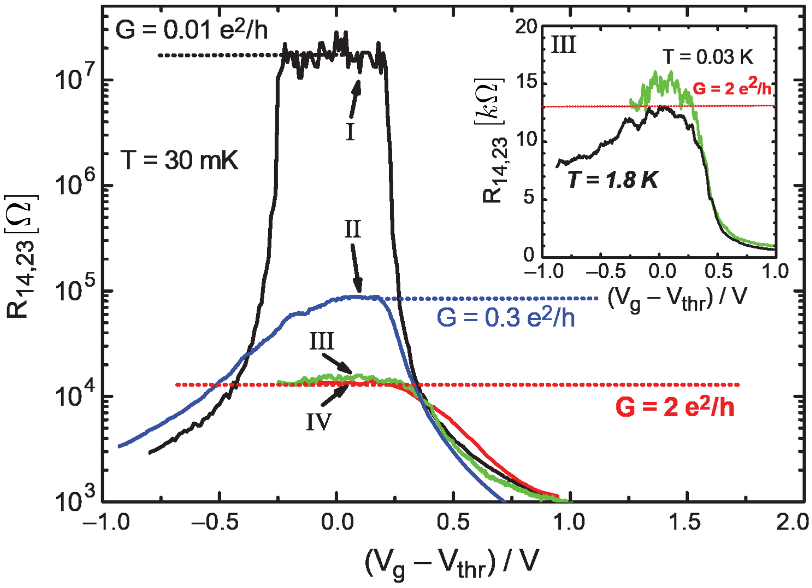

Figure 2.4: Experimental measures of the non-local resistance as a function of the gating voltage in CdTe/HgTe/CdTe quantum wells of different widths. Samples *III* and *IV*, with $d > d_c$, are in the topological regime, and the non-local conductance is $2e^2/h$ (red dashed line). Sample *I*, with $d < d_c$, is in the trivial insulating regime, showing much higher resistances. The inset shows the resistance of the sample *III* at 30 mK (green) and 1.8 K (black). Figure adapted from Ref. [Konig2007].

series of HgTe/CdTe samples as a function of a gate voltage which tunes the Fermi energy through the bulk energy gap. Sample *I* is a narrow quantum well with a thickness of the HgTe layer smaller than the critical thickness $d_c = 6.3\ nm$: the resistance increases to the order of $\approx 10^7\ \Omega$, in agreement with the insulating behavior expected for the topologically trivial regime. Samples *II*–*IV* are wider wells ($d > d_c$) in the inverted regime. In particular, samples *III* and *IV* (with the same length $L = 1\ \mu m$ but different widths $W = 0.5, 1\ \mu m$) exhibit quantized transport associated with edge states with a conductance $2e^2/h$. Sample *II*, much longer ($L = 20\ \mu m$), showed finite temperature scattering effects.

As a final remark, it is important to stress that, the helical nature of the edge states is commonly probed in HgTe quantum wells by means of nonlocal transport measurements in a Hall bar geometry with four or more terminals [Konig2007, Roth2009, Brune2012] and quantum point contacts [Citro2011, Ronetti2016, Ronetti2017]. These kind of measurments can be very hard to implement in other systems, where evidence is shown on the existence of edge states but not yet on their helical nature [Tang2017, Wu2018, Liu2020]. For this reason, one of the main goal of this thesis is to demonstrate that non local thermoelectric effects, obtained in 2DTI based Josephson junctions, can be used to probe the helical nature of the edge states of such a systems.

3

Bogoliubov-de Gennes Formalism

Together with topological insulators (presented so far), superconductors constitute the other important ingredient we need for the realization of a hybrid topological Josephson junction, which represents the main object of investigation of this thesis. This introduction does not aim at a detailed presentation of superconductivity but only introduces the few concepts necessary for the understanding of the rest of this work.

In the first part of this chapter, Sec. 3.1, we present the microscopic theory of the superconductivity in case of spatially inhomogeneous superconducting systems. In this context we introduce the Bogoliubov-de Gennes (BdG) formalism, which will constitute the framework of the entire thesis. As we will see in Sec. 3.2, this formalism artificially doubles the degree of freedom and this redundancy introduces a new “symmetry”: the particle-hole symmetry (PHS). Finally, in Sec. 3.3, we conclude by showing that the BdG equations can be used also to describe one of the most important phenomenon arising in presence of superconductivity: the Andreev reflection.

3.1 BdG formalism

In the framework of the microscopic Bardeen-Cooper-Schrieffer (BCS) theory [BCS1957], one considers only pure materials, in which the momentum $\boldsymbol{k}$ is a good quantum number, and in which $\boldsymbol{k}\uparrow$ and $\boldsymbol{k}\downarrow$ states are occupied in pairs. However, a more general problem arises if the superconducting order parameter $\Delta(\boldsymbol{r})$ varies in space, e. g. at an interface with another material. To cope with these situation and describe spatially inhomogeneous superconducting systems, one may use the Bogoliubov equations, which generalize the ordinary Hartree-Fock equations of the many-electron theory [Tinkham1966].

When there are spatial variations in the Hamiltonian, such as variations in the superconducting pairing potential $\Delta(\boldsymbol{r})$ as well as the ordinary scalar potential $V(\boldsymbol{r})$, the plane-wave momentum eigenfunctions characterized by $\boldsymbol{k}$ (used in the original BCS development) are no longer appropriate. They must be replaced by suitable position-dependent functions [DeGennes1966]. In this respect, the many-particle effective BCS Hamiltonian in the

Hartree-Fock-Bogoliubov mean-field approximation can be written as

$$\mathcal{H} = \sum_{\sigma} \int d\boldsymbol{r}\ \hat{\psi}^{\dagger}_{\sigma}(\boldsymbol{r}) H \hat{\psi}_{\sigma}(\boldsymbol{r}) + \int d\boldsymbol{r}\ \left[\Delta(\boldsymbol{r})\hat{\psi}^{\dagger}_{\uparrow}(\boldsymbol{r})\hat{\psi}^{\dagger}_{\downarrow}(\boldsymbol{r}) + \Delta^{*}(\boldsymbol{r})\hat{\psi}_{\downarrow}(\boldsymbol{r})\hat{\psi}_{\uparrow}(\boldsymbol{r})\right], \tag{3.1}$$

where $\hat{\psi}^{\dagger}_{\sigma}(\boldsymbol{r})$ and $\hat{\psi}_{\sigma}(\boldsymbol{r})$ are the creation and annihilation operators for position eigenfunctions with spin $\sigma = \uparrow\downarrow$ and $H = \boldsymbol{P}^2/2m + eV(\boldsymbol{r}) - \mu$. Here $\boldsymbol{P} = -i\hbar\nabla - (e/c)\boldsymbol{A}$ with $\boldsymbol{A}$ and V the vector and scalar potential respectively, and with μ the chemical potential. The second term in the right-hand side of Eq. (3.1) is responsible for the superconductivity and it is associated with the complex order parameter in the superconductor $\Delta(\boldsymbol{r})$. The Hamiltonian $\mathcal{H}$ can be diagonalized through the generalized Bogoliubov [Bogoliubov1958, Valatin1958] transformation

$$\begin{cases} \hat{\psi}_{\sigma}(x) = \sum_{n} \left[u_n(x)\hat{\gamma}_{n,\sigma} + \text{sign}(\sigma)v^{*}_{n}(x)\hat{\gamma}^{\dagger}_{n,-\sigma}\right] \\ \hat{\psi}^{\dagger}_{\sigma}(x) = \sum_{n} \left[u^{*}_n(x)\hat{\gamma}^{\dagger}_{n,\sigma} + \text{sign}(\sigma)v_{n}(x)\hat{\gamma}_{n,-\sigma}\right] \end{cases}. \tag{3.2}$$

The summation over states n indicates the summation over the discrete spectrum and/or the integration over the continuous spectrum. The operators of free electrons satisfy the standard commutation relations for Fermi particles:

$$\begin{aligned} \left[\hat{\psi}^{\dagger}_{\sigma}(\boldsymbol{r}), \hat{\psi}_{\sigma'}(\boldsymbol{r}')\right] &= \delta_{\sigma,\sigma'}\delta(\boldsymbol{r} - \boldsymbol{r}') \\ \left[\hat{\psi}_{\sigma}(\boldsymbol{r}), \hat{\psi}_{\sigma'}(\boldsymbol{r}')\right] &= 0. \end{aligned} \tag{3.3}$$

Similarly we require that the operators $\hat{\gamma}^{\dagger}_{n,\sigma}, \hat{\gamma}_{n,\sigma}$ also satisfy the commutation relations for Fermi particles reflecting the canonical character of the transformation of Eq. (3.2):

$$\begin{aligned} \left[\hat{\gamma}^{\dagger}_{n,\sigma}, \hat{\gamma}_{n',\sigma'}\right] &= \delta_{\sigma,\sigma'}\delta_{n,n'} \\ \left[\hat{\gamma}_{n,\sigma}, \hat{\gamma}_{n',\sigma'}\right] &= 0. \end{aligned} \tag{3.4}$$

Combining conditions of Eqs. (3.3) and (3.4), the functions $u_n(\boldsymbol{r})$ and $v_n(\boldsymbol{r})$ satisfy the completeness relation

$$\begin{aligned} \sum_{n} \left[u^{*}_n(\boldsymbol{r})u_n(\boldsymbol{r}') + v_n(\boldsymbol{r})v^{*}_n(\boldsymbol{r}')\right] &= \delta(\boldsymbol{r} - \boldsymbol{r}') \\ \sum_{n} \left[u^{*}_n(\boldsymbol{r})v_n(\boldsymbol{r}') - v_n(\boldsymbol{r})u^{*}_n(\boldsymbol{r}')\right] &= 0, \end{aligned} \tag{3.5}$$

and orthogonality relation

$$\begin{aligned} \int d\boldsymbol{r}\ \left[u^{*}_n(\boldsymbol{r})u_{n'}(\boldsymbol{r}) + v_n(\boldsymbol{r})v^{*}_{n'}(\boldsymbol{r})\right] &= \delta_{n,n'} \\ \int d\boldsymbol{r}\ \left[u^{*}_n(\boldsymbol{r})v_{n'}(\boldsymbol{r}) - v_n(\boldsymbol{r})u^{*}_{n'}(\boldsymbol{r})\right] &= 0. \end{aligned} \tag{3.6}$$

Transformation of Eq. (3.2) diagonalizes the Hamiltonian of Eq. (3.1), reducing it to the form

$$\mathcal{H} = U_0 + \sum_{\sigma,n} \epsilon_n \hat{\gamma}^{\dagger}_{n,\sigma}\hat{\gamma}_{n,\sigma} \tag{3.7}$$

in which Bogoliubov quasiparticle operators, given in terms of the wave field operators, take the form

$$\begin{aligned}\hat{\gamma}_{n,\uparrow} &= \int d\boldsymbol{r} \ \left[u_n^*(\boldsymbol{r})\hat{\psi}_\uparrow(\boldsymbol{r}) + v_n^*(\boldsymbol{r})\hat{\psi}_\downarrow^\dagger\right] \\ \hat{\gamma}_{n,\downarrow}^\dagger &= \int d\boldsymbol{r} \ \left[u_n(\boldsymbol{r})\hat{\psi}_\downarrow^\dagger(\boldsymbol{r}) - v_n(\boldsymbol{r})\hat{\psi}_\uparrow\right],\end{aligned} \tag{3.8}$$

and where U_0 plays the role of the ground-state energy of the system

$$U_0 = \int d\boldsymbol{r} \ \sum_n \left[v_n(\boldsymbol{r})Hv_n^*(\boldsymbol{r}) + u_n^*(\boldsymbol{r})Hu_n(\boldsymbol{r})\right] - \sum_n \epsilon_n. \tag{3.9}$$

The diagonalization requires that the functions $u_n(\boldsymbol{r})$ and $v_n(\boldsymbol{r})$ satisfy the so-called Bogoliubov-de Gennes (BdG) equations

$$\begin{pmatrix} H & \Delta \\ \Delta^* & -H^* \end{pmatrix}\begin{pmatrix} u_n(\boldsymbol{r}) \\ v_n(\boldsymbol{r}) \end{pmatrix} = \epsilon_n \begin{pmatrix} u_n(\boldsymbol{r}) \\ v_n(\boldsymbol{r}) \end{pmatrix}. \tag{3.10}$$

The pair potential $\Delta(\boldsymbol{r})$ has to be determined selfconsistently, and is given by

$$\Delta(\boldsymbol{r}) = g\sum_n u_n(\boldsymbol{r})v_n^*(\boldsymbol{r})\left[1 - 2f(\epsilon_n)\right], \tag{3.11}$$

where $g < 0$ is the attractive interaction constant defined by BCS and $f(\epsilon_n)$ is the Fermi function. Because of Eq. (3.11), the determination of the excitation energy spectrum is a non-linear problem, which is further complicated by the fact that the vector potential $\boldsymbol{A}$ has also to be determined self-consistently from the current density, via Maxwell's equations [Bardeen1969]. A straightforward solution of the BdG equations would involve choosing tentative forms for $\Delta(\boldsymbol{r})$, solving the equations, recalculating the pairing potential using Eq. (3.11), and then repeating the procedure until a self-consistent solution is obtained. This can be prohibitively difficult. The superconducting gap can sometimes be specified "manually" and the problem can be solved quite accurately without resorting to self-consistency. For example, in the case of a small normal contact connected to a massive superconductor(s) via tunneling junctions we can assume the superconducting gap to be constant in the superconductor and zero in the normal metal. This approximation takes the name of "rigid boundary condition".

It is important to notice that the BdG equations of Eq. (3.10) are invariant under the transformations $\epsilon_n \to -\epsilon_n$, $u_n(\boldsymbol{r}) \to v_n^*(\boldsymbol{r})$ and $v_n(\boldsymbol{r}) \to -u_n^*(\boldsymbol{r})$. In this sense the set of solutions of Eqs. (3.10) is redundant [Lesovik2011]. This can be simply explained in the case when the superconducting pairing potential is zero. It is clear that, in this case, the same initial electron state (expressed in terms of the Bogoliubov quasiparticles) can be described either by the creation of an electron-like state or by the annihilation of a hole-like state with the opposite energy. This redundancy of the solutions of the BdG equations can be better understood in the light of the intrinsic particle hole symmetry (PHS) of the BdG Hamiltonian, as we will better discuss in the next section.

As a consequence of this redundancy, all quantities of interest (such as the charge density, current density and the self-consistent fields U_0 and Δ) can be expressed in two different but equivalent ways [Datta1996, Datta1999]: (i) within the exitation picture, by using only the solutions of the BdG equation corresponding to positive energies $\epsilon \geq 0$, in which case both the electron-like and hole-like states have to be taken into account; (ii) within the single particle picture, by integrating over all the (positive and negative) energies, in which case only the electron-like states are taken into account. These approaches are equivalent and can be chosen in accordance with their practicality. We notice that in principle other variants are also possible [Lesovik2011]. As far as concern this thesis, all the following results have been obtained within the exitation picture.

3.2 Particle-Hole Symmetry

Particle-hole symmetry appears in the context of superconducting systems described by a mean-field Bogoliubov-De Gennes Hamiltonian. It is a consequence of the fermionic exchange statistics and applies to all quadratic (or mean-field) Hamiltonians of the form

$$\mathcal{H} = \sum_{\alpha\beta} H_{\alpha\beta}\ \hat{c}^{\dagger}_{\alpha}\hat{c}_{\beta} + \frac{1}{2}\sum_{\alpha\beta}\left(\Delta_{\alpha\beta}\ \hat{c}^{\dagger}_{\alpha}\hat{c}^{\dagger}_{\beta} + \Delta^{*}_{\alpha\beta}\ \hat{c}_{\alpha}\hat{c}_{\beta}\right) \tag{3.12}$$

where the operators $\hat{c}^{\dagger}_{\alpha}$ and $\hat{c}_{\alpha}$ denote the creation and annihilation of an electron in second quantization [Altland-Zirnabauer1997]. Importantly, such a Hamiltonian $\mathcal{H}$ does not conserve the number of electrons, but still conserves the parity of the number of electrons, that is whether the number of electrons is even or odd. Here we introduced some generic orthonormal basis of single electron states $|\alpha\rangle$, where α is a multi-index that combines the orbital and spin quantum numbers of the electron. If N is the number of orbital states used, α runs from 1 to $2N$. Furthermore, the anti-commutation relations $\{\hat{c}_{\alpha}, \hat{c}_{\beta}\} = \{\hat{c}^{\dagger}_{\alpha}, \hat{c}^{\dagger}_{\beta}\} = 0$ and $\{\hat{c}_{\alpha}, \hat{c}^{\dagger}_{\beta}\} = \delta_{\alpha\beta}$ imply that the single-particle Hamiltonian $\boldsymbol{H}$ is hermitian (i. e. $H_{\alpha\beta} = H^{*}_{\beta\alpha}$), while the pair potential $\boldsymbol{\Delta}$ is anti-symmetric, i. e. $\Delta_{\alpha\beta} = -\Delta_{\beta\alpha}$. Notice that, in the spin space, the pair potential matrix can be written in the following form [Timm2012]

$$\boldsymbol{\Delta} = \begin{pmatrix} -\boldsymbol{d_x} + i\boldsymbol{d_y} & \boldsymbol{\Delta_s} + \boldsymbol{d_z} \\ -\boldsymbol{\Delta_s} + \boldsymbol{d_z} & \boldsymbol{d_x} + i\boldsymbol{d_y} \end{pmatrix} \tag{3.13}$$

with

$$\boldsymbol{\Delta_s} = \frac{\boldsymbol{\Delta}_{\uparrow\downarrow} - \boldsymbol{\Delta}_{\downarrow\uparrow}}{2} \tag{3.14}$$

$$\boldsymbol{d_x} = \frac{-\boldsymbol{\Delta}_{\uparrow\uparrow} + \boldsymbol{\Delta}_{\downarrow\downarrow}}{2} \tag{3.15}$$

$$\boldsymbol{d_y} = -i\ \frac{\boldsymbol{\Delta}_{\uparrow\uparrow} + \boldsymbol{\Delta}_{\downarrow\downarrow}}{2} \tag{3.16}$$

$$\boldsymbol{d_z} = \frac{\boldsymbol{\Delta}_{\uparrow\downarrow} + \boldsymbol{\Delta}_{\downarrow\uparrow}}{2} \tag{3.17}$$

where we have identified the singlet matrix-component of the gap $\boldsymbol{\Delta_s}$, and the triplet matrix-components collected in the vector $\boldsymbol{d} = (\boldsymbol{d_x}, \boldsymbol{d_y}, \boldsymbol{d_z})$. When $\boldsymbol{d} = 0$ we talk about singlet pairing or s-wave superconductors, otherwise we talk about triplet pairing superconductors. We can now group all the creation and annihilation operators in the vector $\hat{\boldsymbol{C}} = \left(\hat{\boldsymbol{c}}_{\uparrow}, \hat{\boldsymbol{c}}_{\downarrow}, \hat{\boldsymbol{c}}_{\uparrow}{}^{\dagger}, \hat{\boldsymbol{c}}_{\downarrow}{}^{\dagger}\right)^{T}$, where we made explicit the spin degree of freedom. In this way we can write $\mathcal{H}$ in the form "row multiplies matrix multiplies column" [Altland-Zirnabauer1997]

$$\mathcal{H} = \frac{1}{2}\hat{\boldsymbol{C}}^{\dagger} H_{BdG}\hat{\boldsymbol{C}}. \tag{3.18}$$

The $4N \times 4N$ matrix H_{BdG} is known as the Bogoliubov-de Gennes Hamiltonian, and it has the following structure

$$H_{BdG} = \begin{pmatrix} \boldsymbol{H} & \boldsymbol{\Delta} \\ -\boldsymbol{\Delta}^* & -\boldsymbol{H}^* \end{pmatrix}. \tag{3.19}$$

It is important to notice that the eigenvalue problem

$$H_{BdG}\Psi(\boldsymbol{r}) = \epsilon\Psi(\boldsymbol{r}) \tag{3.20}$$

corresponds to the generalized Bogoliubov-de Gennes equations of Eq. (3.10) (notice the different sign of the gap order parameter $\boldsymbol{\Delta}^*$, which in Eq. (3.19) is a matrix). Later in this section we will show how Eq. (3.10) can be obtained from Eq. (3.19) in the case of singlet pairing superconductors with preserved spin-rotation symmetry. Interestingly, Eq. (3.20) can be interpreted as the wave equation for the multi-component wave function

$$\Psi(\boldsymbol{r}) = \begin{pmatrix} \boldsymbol{u}(\boldsymbol{r}) \\ \boldsymbol{v}(\boldsymbol{r}) \end{pmatrix} \tag{3.21}$$

of a quasiparticle with energy ϵ. The wave function $\Psi(\boldsymbol{r})$ describes excitations known as Bogoliubov quasiparticles, formed out of coherent superpositions of electrons $\boldsymbol{u}(\boldsymbol{r})$ and holes $\boldsymbol{v}(\boldsymbol{r})$. This interpretation can be useful, in the consideration of the Andreev scattering [Andreev1964] as we will see in the next Sec. 3.3.

If interpreted as a single particle Hamiltonian in first quantization picture, the operator H_{BdG}, acts in an enlarged space, which takes the name of Nambu space, which is the tensor product of the physical space $\mathbb{C}^{2N}$ (orbitals and spin) with an extra degree of freedom $\mathbb{C}^2$, which we call the "particle-hole space". Note however that the "particles" and "holes" of the BdG formalism are not the particle and hole states of a degenerate Fermi gas. Indeed, the matrix $\boldsymbol{H}$ already acts on all of the single-electron states, which have energies either above or below the chemical potential. The BdG-hole states acted upon by $-\boldsymbol{H}^*$ are identical (and in this sense redundant, or unphysical) copies of the BdG-particle states acted upon by $\boldsymbol{H}$. They are introduced for the convenience of treating the pairing field within the formalism of first quantization [Altland-Zirnabauer1997].

By construction the BdG Hamiltonian anticommutes with the anti-unitary particle-hole (or charge conjugation) operator

$$\mathcal{P} = \tau_x K \tag{3.22}$$

such that $\{H_{BdG}, \mathcal{P}\} = 0$, where K is the complex conjugate operator and τ_x is a Pauli matrix acting on the particle-hole space. In this sense, the BdG-Hamiltonian H_{BdG} is said to obey the particle-hole symmetry (PHS), namely

$$H_{BdG} = -\mathcal{P} H_{BdG} \mathcal{P}^{-1}. \tag{3.23}$$

Because of this symmetry, for every eigenstate $\Psi = (\boldsymbol{u}, \boldsymbol{v})^T$ with energy ϵ, there is a particle-hole conjugate state $\mathcal{P}\Psi = (\boldsymbol{v}^*, \boldsymbol{u}^*)^T$ with opposite energy $-\epsilon$, i. e. $H_{BdG}\mathcal{P}\Psi = -\mathcal{P}\hat{H}_{BdG}\Psi = -\epsilon\mathcal{P}\Psi$. Furthermore, since the action of the complex conjugation in the momentum-space changes k in $-k$, PHS ensures that electron and hole dispersions of the same spin are symmetric with respect to the point $(\epsilon, k) = (0, 0)$. We emphasize that, despite the name, PHS is not a proper symmetry: the relation between the state at energy ϵ and $-\epsilon$ is due to a mathematical artifact to resolve BdG equations and thus it is a redundancy rather than a physical symmetry.

As a final remark, let us consider the case of singlet pairing superconducting systems with preserved spin-rotation symmetry (as that described by the Hamiltonian of Eq. (3.1)). This means that the BdG Hamiltonian satisfy the following relation

$$[H_{BdG}, J_k] = 0; \quad \text{with} \quad J_k \equiv \begin{pmatrix} \sigma_k & 0 \\ 0 & -\sigma_k^T \end{pmatrix}, \tag{3.24}$$

where $k = x, y, z$. In this case it can be shown that, the Hamiltonian $\mathcal{H}$ of Eq. (3.18) can be brought into the form

$$\widetilde{\mathcal{H}} = \frac{1}{2}\left(\hat{\boldsymbol{c}}_\uparrow^\dagger, \hat{\boldsymbol{c}}_\downarrow\right)\widetilde{H}_{BdG}\begin{pmatrix} \hat{\boldsymbol{c}}_\uparrow \\ \hat{\boldsymbol{c}}_\downarrow^\dagger \end{pmatrix} \tag{3.25}$$

up to a term which is proportional to the identity. Here, $\widetilde{H}_{BdG}$ is a $2N \times 2N$ matrix with the following structure

$$\widetilde{H}_{BdG} = \begin{pmatrix} \boldsymbol{h} & \boldsymbol{\delta} \\ \boldsymbol{\delta}^* & -\boldsymbol{h}^* \end{pmatrix} \tag{3.26}$$

which clearly coincide with Eq. (3.10) when $\boldsymbol{h} \equiv H$ and $\boldsymbol{\delta} \equiv \Delta$. In this case it is possible to construct an alternative particle-hole symmetry operator, $\mathcal{P} = \tau_y K$, where τ_y acts in a restricted particle-hole space of states of the form $\Psi = (u_\uparrow, v_\downarrow)^T$ [Schnyder2008].

3.3 Andreev reflection

In the previous sections we have seen that the Bogoliubov-de Gennes equations are used in order to diagonalize the mean-field BCS Hamiltonian and can be interpreted as wave equations for quasiparticle excitations which are mixtures of particles and holes. Here we show that through the BdG equations one can define Andreev reflections at the N-S interface between a normal-metal and an s-wave superconductor, which describe an additional scattering process (with respect to ordinary reflections) taking place in such a system.

The simplest problem of a 1D N-S system was examined by Blonder, Tinkham and Klapwijk in 1982 [BTK1982]. This approach is also valid in higher dimensions, provided that there is translational invariance in the direction perpendicular to the electronic motion [Lambert1998]. To see this, imagine the 3D system of Fig. 3.1, with a finite width in the y-direction, finite high in the z-direction and infinite in the x-direction. The problem is quantized in the y-z-plane, thus we can factorize the wavefunction into

$$\Psi(x, y, z) = \psi(x)\Phi_n(y, z), \tag{3.27}$$

where n denotes the quantum number labeling the transversal modes

$$\left[-\frac{\hbar^2}{2m}\left(\frac{\partial^2}{\partial z^2} + \frac{\partial^2}{\partial y^2}\right) + V_\perp(y, z)\right]\Phi_n(y, z) = \epsilon_n \Phi_n(y, z) \tag{3.28}$$

with transversal energy ϵ_n and $V_\perp$ the transversal confining potential. The energy is the sum of the longitudinal and transversal energies $\epsilon = \epsilon_\parallel + \epsilon_n$, such that, for a given transversal mode n, the effective chemical potential for the longitudinal propagation reads $\mu_n = \epsilon_F - \epsilon_n$, where ϵ_F is the Fermi energy (which already includes the self-consistent potential U_0 of Eq. (3.9)). For a fixed transversal mode n^* (such that $\mu \equiv \mu_{n^*}$), the problem becomes one-dimensional

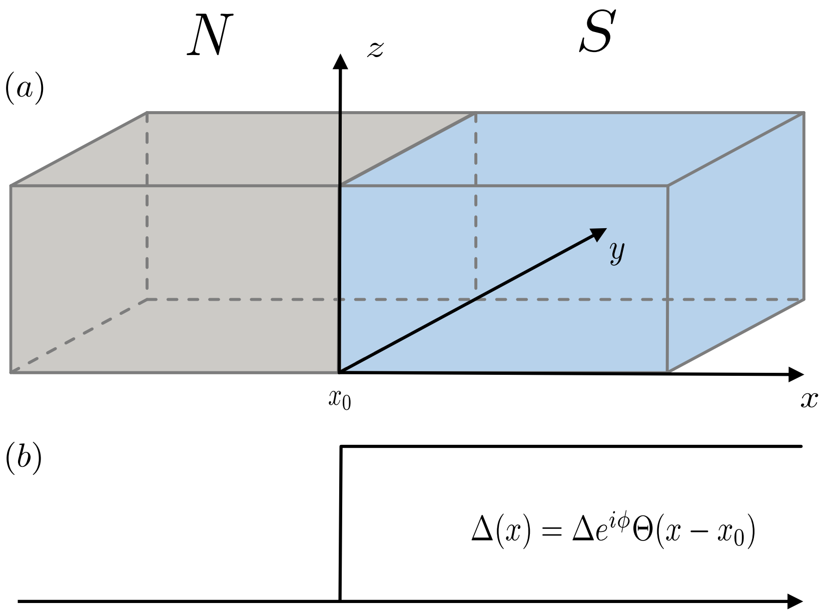

FIGURE 3.1: (a) - Scheme of a 3D N-S junction with finite width in the y-direction, finite high in the z-direction and infinite in the x-direction. The interface is positioned at x_0, the normal region N extends for $x < x_0$ and the superconductor S is located for $x > x_0$. (b) - Profile of the gap order parameter with rigid boundary condition along the x-direction.

and the Bogoliubov–de Gennes equations for a singlet pairing superconducting system reduce to

$$\begin{pmatrix} H & \Delta \\ \Delta^* & -H^* \end{pmatrix} \begin{pmatrix} u(x) \\ v(x) \end{pmatrix} = \epsilon \begin{pmatrix} u(x) \\ v(x) \end{pmatrix} \tag{3.29}$$

with

$$H = -\frac{\hbar^2}{2m}\frac{\partial^2}{\partial x^2} + \Lambda(x) - \mu \tag{3.30}$$

in which we included the contact potential $\Lambda(x) = \Lambda\delta(x - x_0)$ at the interface located in $x = x_0$. This is meant to represent the effect of the barrier in the junction, the localized disorder at the interface, or the intentional oxide barrier in a tunnel junction. Moreover, we consider rigid boundary conditions for the gap order parameter, i. e. $\Delta(x) = \Theta(x - x_0)\Delta e^{i\phi}$.

It is important to stress that here we consider an s-wave superconducting systems with preserved spin-rotation symmetry (as described by the Hamiltonians of Eqs. (3.10) and (3.26)). This means that the superconducting order parameter Δ only couples particles and holes with opposite spin. As a consequence the components of the wave vector of Eq. (3.29), namely $u(x)$ and $v(x)$, should be labeled by opposite spin indices: e. g. $u_\uparrow(x)/v_\downarrow(x)$ or $u_\downarrow(x)/v_\uparrow(x)$ - see the discussion at the end of the previous section. However in the absence of spin-flip processes (such as in the presence of magnetic domains) this only affects normalization, and we can omit the spin label for simplicity.

Such Hamiltonian of Eq. (3.29) was introduced for the first time in Ref. [BTK1982] as a generalized semiconductor model to treat the transmission and reflection of particles at the N-S interface within the scattering theory of transport. This approach goes beyond the usual tunnel limit in which only the superconducting density of states, $N_S(E)$, distinguishes the superconductor from the situation in the normal state [Datta1996]. Indeed, one of the major shortcoming with the tunneling approach is that the density-of-states factor makes no reference to the microscopic nature of the superconducting state by ignoring the presence of condensate and not taking into account the quasiparticle excitations as mixtures of particles and holes. Here instead, we describe a generalized semiconductor model specifically designed to avoid this loss of information.

As prescribed by the excitation picture, in the following, we will be interested in finding only the non-negative energy solutions of Eq. (3.29), i. e. with $\epsilon \geq 0$ (where μ is taken as reference for energies) [Dolcini2009]. We will proceed by computing first the wavefunctions in the normal region N (for $x < x_0$), then in the superconducting region S (for $x > x_0$), and finally we will match the solutions in order to compute the scattering coefficients which describe the interface.

Solutions in N

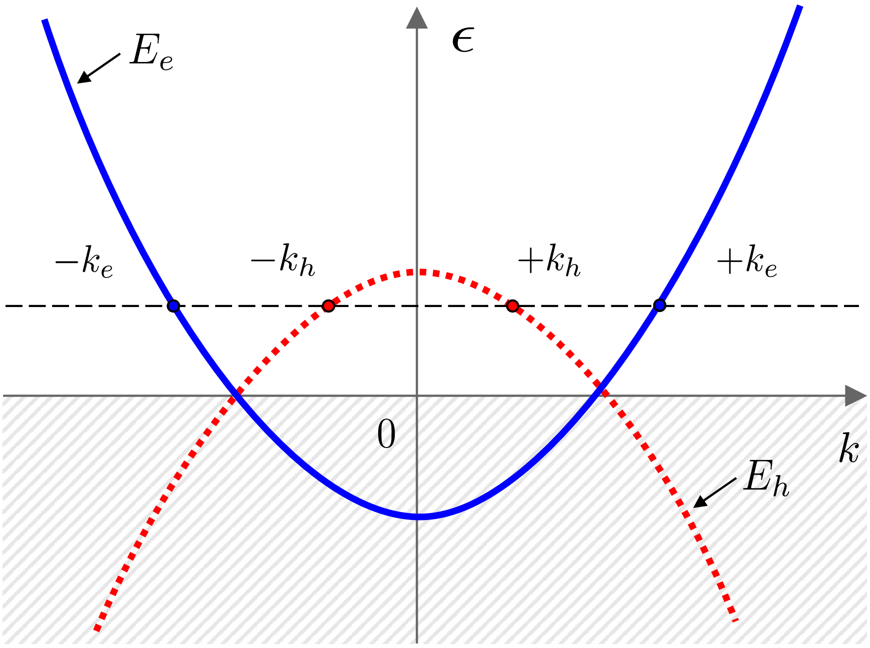

FIGURE 3.2: BdG spectrum in the N region. As ensured by PHS, dispersion curves for electrons (blue solid line) and holes (red dotted line) are redundant copies mirrored with respect the origin. Within the excitation picture, only positive energies are considered (notice that dispersion curves for negative energies have been shaded). The horizontal dashed line, for a fixed $\epsilon > 0$, intercepts the curves at points $\pm k_e$ for electrons and $\pm k_h$ for holes. The slope of the dispersion curves at these points indicate the group velocity of each mover.

In the normal side N the Eq. (3.29) reduces to

$$\begin{pmatrix} -\frac{\hbar^2}{2m}\frac{\partial^2}{\partial x^2} - \mu & 0 \\ 0 & \frac{\hbar^2}{2m}\frac{\partial^2}{\partial x^2} + \mu \end{pmatrix} \begin{pmatrix} u(x) \\ v(x) \end{pmatrix} = \epsilon \begin{pmatrix} u(x) \\ v(x) \end{pmatrix} \tag{3.31}$$

which exhibits the following steady-state plane-wave solutions

$$\psi^N_{e\pm}(x) = \begin{pmatrix}1\\0\end{pmatrix} e^{\pm i k_e x}; \qquad \psi^N_{h\pm}(x) = \begin{pmatrix}0\\1\end{pmatrix} e^{\mp i k_h x} \tag{3.32}$$

Here the upper index N refer to eigenstate solutions inside the normal region, and $\pm$ indicate the direction of propagation along the x-axis ($+$ for right movers, $-$ for left movers) for both electrons (e) and holes (h). In Fig. 3.2 are reported the different branches of the eigenspectrum of the BdG Hamiltonian relative to the eigenstate solutions of Eq. (3.32), which are given by the following relations

$$E_e = \frac{\hbar^2 k_e^2}{2m} - \mu; \qquad E_h = \mu - \frac{\hbar^2 k_h^2}{2m} \tag{3.33}$$

for electrons (blue solid line) and holes (red dotted line) respectively. Notice that, in Eqs. (3.32) and (3.33), we introduced the electron and hole wave vector amplitudes

$$k_e = k_F\sqrt{1+\frac{\epsilon}{\mu}}; \qquad k_h = k_F\sqrt{1-\frac{\epsilon}{\mu}} \tag{3.34}$$

with $k_F = \sqrt{2m\mu}/\hbar$ the Fermi wave vector. As emerges from Fig. 3.2, due to the BdG-formalism and the corresponding introduction of holes, the spectrum is doubled. More precisely, the spectra of electrons and holes are mirrored with respect the point $(\epsilon, k) = (0, 0)$, such that $E_h(k_h) = -E_e(-k_e)$, as ensured by PHS. As already mentioned in the previous section, such a redundancy in the eigenspectrum of the BdG Hamiltonian can be cured within the excitation picture by considering only the solutions corresponding to positive energies $\epsilon \geq 0$.

Solutions in S

In the superconducting side S the Eq. (3.29) reduces to

$$\begin{pmatrix} -\frac{\hbar^2}{2m}\frac{\partial^2}{\partial x^2} - \mu & \Delta e^{i\phi} \\ \Delta e^{-i\phi} & \frac{\hbar^2}{2m}\frac{\partial^2}{\partial x^2} + \mu \end{pmatrix} \begin{pmatrix} u(x)\\ v(x)\end{pmatrix} = \epsilon \begin{pmatrix} u(x)\\ v(x)\end{pmatrix} \tag{3.35}$$

which exhibits two solutions

$$\psi^S_{\tilde{e}\pm}(x) = \begin{pmatrix} u_0 e^{i\frac{\phi}{2}} \\ v_0 e^{-i\frac{\phi}{2}} \end{pmatrix} e^{\pm i q_{\tilde{e}} x}; \qquad \psi^S_{\tilde{h}\pm}(x) = \begin{pmatrix} v_0 e^{i\frac{\phi}{2}} \\ u_0 e^{-i\frac{\phi}{2}} \end{pmatrix} e^{\mp i q_{\tilde{h}} x}. \tag{3.36}$$

Here the upper index S refer to excitations inside the superconductor, and $\pm$ indicate the direction of propagation along the x-axis ($+$ for right movers, $-$ for left movers) for both electron-like solutions ($\tilde{e}$) and hole-like solutions ($\tilde{h}$). Usually, in the literature, one refers to quasiparticles (QPs) for $\psi^S_{\tilde{e}\pm}$ and to quasiholes (QHs) for $\psi^S_{\tilde{h}\pm}$. In this thesis we adopt the same notation. This nomenclature can be rationalized by observing that when the gap closes, i. e. $\Delta \to 0$, QPs continuously evolve into electrons ($\psi^S_{\tilde{e}\pm} \to \psi^N_{e\pm}$) and QHs continuously evolve into holes ($\psi^S_{\tilde{h}\pm} \to \psi^N_{h\pm}$). The different branches of the eigenspectrum of the BdG Hamiltonian are depicted in Fig. 3.3. Within the excitation picture we are concerned with quasiparticles energies above the ground state ($\epsilon \geq 0$), which are given by the following relations

$$E_{\tilde{e}} = \sqrt{\left(\frac{\hbar^2 q_{\tilde{e}}^2}{2m} - \mu\right)^2 + \Delta^2} \qquad E_{\tilde{h}} = \sqrt{\left(\mu - \frac{\hbar^2 q_{\tilde{h}}^2}{2m}\right)^2 + \Delta^2} \tag{3.37}$$

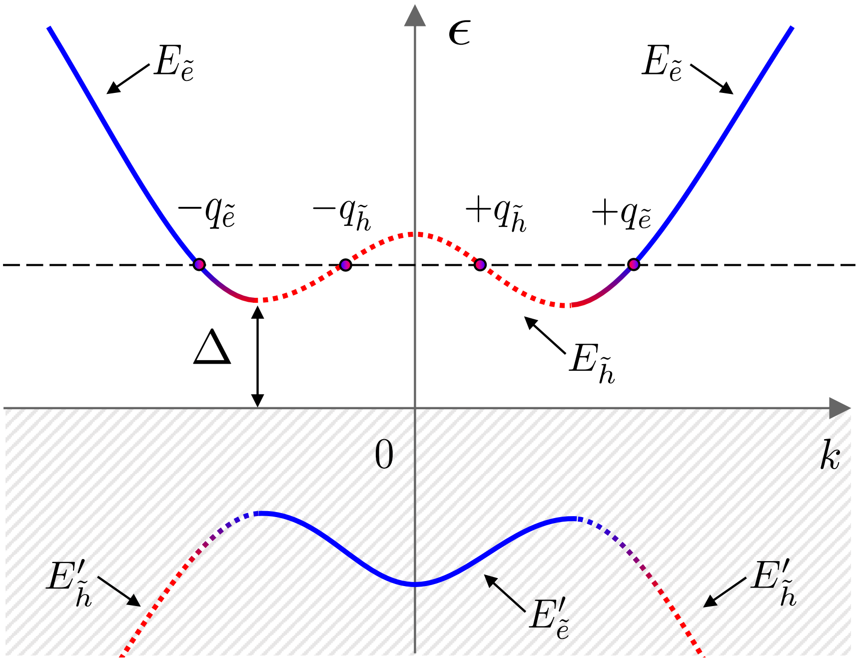

FIGURE 3.3: BdG spectrum in the S region. The presence of the superconductor opens a gap Δ in the eigenspectrum of Fig. 3.2, and hybridizes electron- and hole-states (as indicated by the colored transition). Branches corresponding to QPs are depicted by solid lines, those corresponding to QHs are indicated by dotted lines. $E_{\tilde{e}}$ and $E_{\tilde{h}}$ label branches with positive energy, $E'_{\tilde{e}}$, $E'_{\tilde{h}}$ indicate those with negative energy (the latter are redundant, hence we do not consider them, as indicated by the shaded region). The horizontal dashed line, for a fixed $\epsilon > \Delta$, intercepts the curves at points $\pm q_{\tilde{e}}$ for QPs and $\pm q_{\tilde{h}}$ for QHs. The slope of the dispersion curves at these points indicate the group velocity of each mover.

for QPs (solid line) and QHs (dashed line) respectively. Also in this case, PHS introduces particle-hole conjugated states with negative energies, $E'_{\tilde{e}}$ and $E'_{\tilde{h}}$ (see Fig. 3.3). These eigenenergies, which satisfy the relations $E'_{\tilde{e}}(q_{\tilde{e}}) = -E_{\tilde{h}}(-q_{\tilde{h}})$ and $E'_{\tilde{h}}(q_{\tilde{h}}) = -E_{\tilde{e}}(-q_{\tilde{e}})$, are redundant and therefore we do not consider them. In Eqs. (3.36) and (3.37) we introduced the wave vector amplitudes

$$q_{\tilde{e}} = k_F\sqrt{1+\sqrt{\frac{\epsilon^2-\Delta^2}{\mu^2}}}; \qquad q_{\tilde{h}} = k_F\sqrt{1-\sqrt{\frac{\epsilon^2-\Delta^2}{\mu^2}}} \tag{3.38}$$

for QPs and QHs respectively. Notice that, as depicted in Fig. 3.3, the direction of propagation (corresponding to the sign of the slope of eigenspectrum at a given energy) and the sign of the wave vector are coincident for QPs (namely $+q_{\tilde{e}}$ is related to right moving QPs $\psi^S_{\tilde{e}+}$, and $-q_{\tilde{e}}$ refer to left moving QPs $\psi^S_{\tilde{e}-}$), while are opposite for QHs ($-q_{\tilde{h}}$ is related to right moving QHs $\psi^S_{\tilde{h}+}$, and $+q_{\tilde{h}}$ refer to left moving QHs $\psi^S_{\tilde{h}-}$).

The eigenstate solutions of Eq. (3.36), are expressed in terms of the so-call coherence factors u_0 and v_0 which take the following form

$$u_0(\epsilon) = \sqrt{\frac{1}{2}\left(1 + \sqrt{\frac{\epsilon^2 - \Delta^2}{\epsilon^2}}\right)} \equiv \sqrt{\frac{\Delta}{2\epsilon}} e^{\frac{1}{2}h(\epsilon)};$$

$$v_0(\epsilon) = \sqrt{\frac{1}{2}\left(1 - \sqrt{\frac{\epsilon^2 - \Delta^2}{\epsilon^2}}\right)} \equiv \sqrt{\frac{\Delta}{2\epsilon}} e^{-\frac{1}{2}h(\epsilon)} \tag{3.39}$$

with

$$h(\epsilon) \equiv \begin{cases} \text{arcCosh}\left(\frac{\epsilon}{\Delta}\right) & \text{for} \quad \epsilon > \Delta \\ i\,\text{arccos}\left(\frac{\epsilon}{\Delta}\right) & \text{for} \quad \epsilon < \Delta \end{cases}. \tag{3.40}$$

It is worth to notice that quasiparticles at energy ϵ have charge

$$Q(\epsilon) = \pm e\left[u_0^2(\epsilon) - v_0^2(\epsilon)\right] = \pm e\sqrt{\frac{\epsilon^2 - \Delta^2}{\epsilon^2}} \equiv \pm e N_S(\epsilon)^{-1} \tag{3.41}$$

where ± stay for QPs and QHs respectively and $N_S(\epsilon)$ indicates the density of states of the excitations inside the superconductor. This witnesses the fractional character of quasiparticles charge inside superconductors, which is zero at the energy gap and approaches $\pm e$ for energies well above (below) the gap.

Scattering matrix coefficients

We now want to determine the scattering coefficients. Let us start by considering the case of an incident electron, incoming from the N electrode towards the interface

$$\psi_{\text{in}}(x) = \frac{1}{\sqrt{2\pi\hbar v_e}} \begin{pmatrix} 1 \\ 0 \end{pmatrix} e^{+ik_e x}. \tag{3.42}$$

The incoming wave reflects back into the N region in a left-moving electron or a left-moving hole

$$\psi_{\text{refl}}(x) = \frac{r_{ee}}{\sqrt{2\pi\hbar v_e}} \begin{pmatrix} 1 \\ 0 \end{pmatrix} e^{-ik_e x} + \frac{r_{he}}{\sqrt{2\pi\hbar v_h}} \begin{pmatrix} 0 \\ 1 \end{pmatrix} e^{ik_h x} \tag{3.43}$$

while, inside the superconducting region, it transmits (if the energy is not in the gap, i. e. $\epsilon \geq \Delta$) as a right-moving QP or a right-moving QH

$$\psi_{\text{trans}}(x) = \frac{t_{\tilde{e}e}}{\sqrt{2\pi\hbar w_e}} \begin{pmatrix} u_0 e^{i\frac{\phi}{2}} \\ v_0 e^{-i\frac{\phi}{2}} \end{pmatrix} e^{+iq_{\tilde{e}} x} + \frac{t_{\tilde{h}e}}{\sqrt{2\pi\hbar w_h}} \begin{pmatrix} v_0 e^{i\frac{\phi}{2}} \\ u_0 e^{-i\frac{\phi}{2}} \end{pmatrix} e^{-iq_{\tilde{h}} x}. \tag{3.44}$$

In Eq. (3.43) the coefficient r_{ee} represents an ordinary refelction process in which the incoming electron from the N region is reflected as an electron on the same side. On the contrary, the coefficients r_{he} represents a new scattering process called Andreev reflection, which only emerges in presence of superconductors, and which converts the incoming electron from the N electrode into a hole on the same side. Similarly, in Eq. (3.44), the coefficients $t_{\tilde{e}e}$ and $t_{\tilde{h}e}$ represent the transmission amplitudes for the incoming electron to be transmitted to the S side as a QP and a QH respectively. We have normalized the wavefunctions with their group velocities, which are different in general for particle and holes, and from normal to superconduting side. In this way, each wavefunction carries the same amount of flux of quasiparticle probability current, and therefore the above coefficients describe a unitary scattering matrix. Specifically we have

$$v_e = \frac{1}{\hbar}\left|\frac{\partial E_e}{\partial k_e}\right| = \frac{v_F}{k_F}k_e; \qquad v_h = \frac{1}{\hbar}\left|\frac{\partial E_h}{\partial k_h}\right| = \frac{v_F}{k_F}k_h \tag{3.45}$$

for the N side, and

$$w_{\tilde{e}} = \frac{1}{\hbar}\left|\frac{\partial E_{\tilde{e}}}{\partial q_{\tilde{e}}}\right| = \frac{v_F}{k_F}q_{\tilde{e}}\left(u_0^2 - v_0^2\right); \qquad w_{\tilde{h}} = \frac{1}{\hbar}\left|\frac{\partial E_{\tilde{h}}}{\partial q_{\tilde{h}}}\right| = \frac{v_F}{k_F}q_{\tilde{h}}\left(u_0^2 - v_0^2\right) \tag{3.46}$$

for the S side, with $v_F = \hbar k_F/m$ the Fermi velocity. It is important to stress that the transmitted wave function $\psi_{trans}(x)$ of Eq. (3.44), indicates states which propagate above the energy gap (i. e. $\epsilon \geq \Delta$). In the sub-gap regime (i. e. $\epsilon < \Delta$), instead, the group velocity it is not defined, the wave vector amplitudes $q_{\tilde{e}/\tilde{h}}$ acquire an imaginary part, and the solutions of the Bogoliubov equations become evanescent waves which decay exponentially inside the superconductor

$$\psi_{\text{evan}}(x) = \eta_{\tilde{e}e}\begin{pmatrix} u_0 e^{i\frac{\phi}{2}} \\ v_0 e^{-i\frac{\phi}{2}} \end{pmatrix} e^{+iq_{\tilde{e}}x} + \eta_{\tilde{h}e}\begin{pmatrix} v_0 e^{i\frac{\phi}{2}} \\ u_0 e^{-i\frac{\phi}{2}} \end{pmatrix} e^{-iq_{\tilde{h}}x}. \tag{3.47}$$

Notice, however, that unitary of the scattering matrix only holds for propagating modes, because evanescent waves carry no current and unitarity is related to the conservation of the current. To solve for the scattering coefficients r_{ee}, r_{he}, $t_{\tilde{e}e}$ and $t_{\tilde{h}e}$ one needs matching conditions at the interface. The boundary conditions can be obtained by imposing first the continuity across the interface

$$\begin{cases} u(x_0^-) = u(x_0^+) \\ v(x_0^-) = v(x_0^+) \end{cases} \tag{3.48}$$

where we indicated with $x_0^{\pm} = \lim_{\delta\to 0^{\pm}} x_0 + \delta$, and with x_0 the position of the interface along the x-direction. Similarly, we obtain the boundary conditions for the derivatives by integrating Eq. (3.29) around the point x_0,

$$\begin{cases} \partial_x u(x_0^+) - \partial_x u(x_0^-) = \dfrac{2m\Lambda}{\hbar^2}u(x_0) \\ \partial_x v(x_0^+) - \partial_x v(x_0^-) = \dfrac{2m\Lambda}{\hbar^2}v(x_0) \end{cases}. \tag{3.49}$$

In the last equations we considered $u(x_0) = (u(x_0^+)+u(x_0^-))/2$ and $v(x_0) = (v(x_0^+)+v(x_0^-))/2$. Eqs. (3.42)-(3.44), together with boundary conditions (3.48)-(3.49), completely determines the scattering coefficients. The detailed solution is straightforward, but the resulting expressions look rather cumbersome (see the end of this section for more details). In this regard, it is convenient to resort to the so called Andreev approximation, which consists in envisaging low energies with respect to the Fermi level

$$\epsilon, \Delta \ll \mu, \tag{3.50}$$

and thus retain the lowest order in ϵ/μ and Δ/μ. One can then approximate

$$k_{e/h} \simeq q_{\tilde{e}/\tilde{h}} \simeq k_F. \tag{3.51}$$

It is important to notice that, under such approximation, all the details about the curvature of the BdG eigenspectrum is completely lost. As consequence, no themoelectric effects can arise within the Andreev approximation limit. Instead, for a correct description of the thermoelectric phenomena in hybrid superconducting systems, it is necessary to go beyond the Andreev approximation.
Thus, by exploiting Eq. (3.51), we obtain the following expressions for the reflection and transmission amplitudes

$$r_{ee} = -\frac{Z\,(i+Z)\,(u_0^2-v_0^2)}{u_0^2+Z^2\,(u_0^2-v_0^2)} \tag{3.52a}$$

$$r_{he} = \frac{u_0 v_0}{u_0^2+Z^2\,(u_0^2-v_0^2)}e^{-i\phi} \tag{3.52b}$$

$$t_{\tilde{e}e} = \frac{(1-iZ)\,u_0\sqrt{u_0^2-v_0^2}}{u_0^2+Z^2\,(u_0^2-v_0^2)}e^{-i\frac{\phi}{2}} \cdot \Theta(\epsilon-\Delta) \tag{3.52c}$$

$$t_{\tilde{h}e} = \frac{Zv_0\sqrt{u_0^2-v_0^2}}{u_0^2+Z^2\,(u_0^2-v_0^2)}e^{-i\frac{\phi}{2}} \cdot \Theta(\epsilon-\Delta) \tag{3.52d}$$

(see the end of this section for their computation beyond the Andreev approximation). The amplitudes for the evanescent wave we introduced in Eq. (3.47) in the sub-gap regime (i. e. $\epsilon < \Delta$) read as

$$\eta_{\tilde{e}e} = \frac{(1-iZ)\,u_0}{u_0^2+Z^2\,(u_0^2-v_0^2)}e^{-i\frac{\phi}{2}}; \qquad \eta_{\tilde{h}e} = \frac{Zv_0}{u_0^2+Z^2\,(u_0^2-v_0^2)}e^{-i\frac{\phi}{2}}. \tag{3.53}$$

Similar equations can be found for incoming holes from N or incoming QPs and QHs from S. In this case, the remaining scattering coefficients respect the following relations

$$\begin{cases} r_{\tilde{e}\tilde{e}} = r^*_{\tilde{h}\tilde{h}} = r^*_{hh} = r_{ee} \\ -r_{\tilde{h}\tilde{e}}e^{-i\phi} = -r^*_{\tilde{e}\tilde{h}}e^{-i\phi} = r^*_{eh} = r_{he} \\ t_{e\tilde{e}}e^{-i\phi} = t^*_{h\tilde{h}}e^{-i\phi} = t^*_{\tilde{h}h} = t_{\tilde{e}e} \\ -t_{h\tilde{e}} = -t^*_{e\tilde{h}} = t^*_{\tilde{e}h} = t_{\tilde{h}e} \end{cases} \tag{3.54}$$

Notice that in Eqs. (3.52)-(3.53), we introduced the dimensionless barrier strength

$$Z = \frac{\Lambda}{\hbar v_F}. \tag{3.55}$$

The meaning of such parameter Z becomes clear in the case of a normal junction, i. e. when the gap in the superconductor is set to be zero ($\Delta \to 0$). In this case one can prove that Z is related to the transmission probability

$$T = \frac{1}{1+Z^2}. \tag{3.56}$$

From the above relation, it follows that Z can be interpreted as the transparency of the N-S interface: for $Z \ll 1$ we have a very transparent (or ideal) interface, while for $Z \gg 1$ we have a weakly transparent interface (tunnel limit) [BTK1982].

From Eqs. (3.52), one can easily verify that

$$\left|r_{ee}\right|^2 + \left|r_{he}\right|^2 + \left|t_{\tilde{e}e}\right|^2 + \left|t_{\tilde{h}e}\right|^2 = 1 \tag{3.57}$$

as required by unitarity of the scattering matrix. In particular, it is important to notice that in the subgap regime the transmission coefficients $t_{\tilde{e}e} = t_{\tilde{h}e} = 0$, and thus Eq. (3.57) becomes

$$|r_{ee}|^2 + |r_{he}|^2 = 1 \quad \text{for} \quad \epsilon < \Delta. \tag{3.58}$$

Perfect Andreev reflection

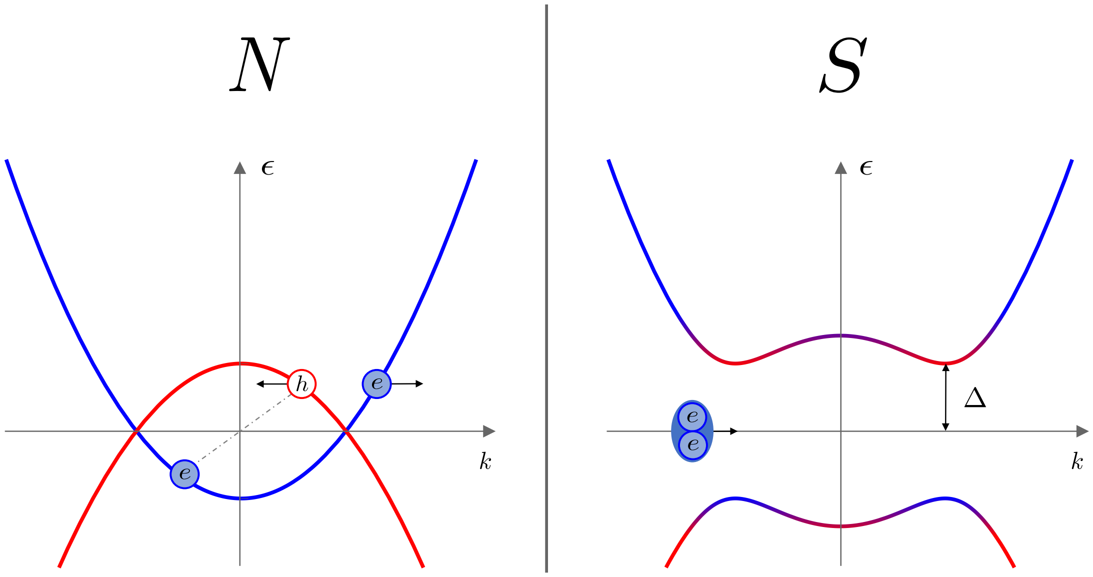

FIGURE 3.4: Andreev reflection: An incident electron with energy $\epsilon < \Delta$ "drags" an electron with energy $-\epsilon$ along with it into the superconductor. This leaves behind an empty state that flows away from the interface. The process corresponds to the injection of a Cooper pair inside the superconductor.

In order to discuss the physical consequences of the coefficients $r_{ee}, r_{he}, t_{\tilde{e}e}$ and $t_{\tilde{h}e}$ found above, it is convenient to consider the special case of an ideal interface ($Z = 0$). In this case the reflection amplitudes of Eqs. (3.52a) and (3.52b), take the form

$$r_{ee} = 0 \tag{3.59}$$

$$r_{he} = e^{-i\phi}\frac{v_0}{u_0} = e^{-i\phi}e^{h(\epsilon)} = e^{-i\phi}\begin{cases} \text{arcCosh}\left(\dfrac{\epsilon}{\Delta}\right) & \text{for} \quad \epsilon > \Delta \\ i\arccos\left(\dfrac{\epsilon}{\Delta}\right) & \text{for} \quad \epsilon < \Delta \end{cases}, \tag{3.60}$$

where we made explicit the expression for the function $h(\epsilon)$ defined in Eq. (3.40). A similar relation can be obtained for an injected hole by simply changing $\phi \to -\phi$. An important consequence of this fact is that, for an ideal N-S interface, an injected electron can only be reflected as a hole with opposite spin. This phenomenon is known as perfect Andreev reflection, and is depicted in Fig. 3.4 [Andreev1964]. In contrast to an ordinary reflection, where momentum is not conserved and charge is conserved, in an Andreev reflection process, momentum is almost conserved (namely in the Andreev approximation limit both the incoming electron and the reflected hole have momentum very close to the same k_F), whereas charge is not conserved. Such a coherent reflection of an incoming electron into an outgoing hole with opposite spin can be effectively interpreted as the injection of a Cooper pair inside the superconducting lead, as schematically represented in Fig. 3.4. In this case, an incident electron with energy ϵ “drags” an electron with opposite energy (with respect the chemical potential μ, here taken as reference) along with it inside the superconductor. This creates a Cooper pair at zero energy in the condensate of the superconductor, and leaves behind an empty state (corresponding to an hole excitation) that flows away from the interface inside the normal region [Datta1996].

Andreev reflection is the predominant scattering mechanism for quasiparticles incoming from the normal side with energies below the superconducting gap. This phenomenon links the transport in normal regions, where the charge is carried by quasi-particles, to the transport in the superconducting region, where the charge is carried by the condensate, thus as far as quantum transport is concerned, it allows electrical currents to flow instead of blocking them as normal reflection does. Moreover, it doubles the conductance with respect to a normal transmission event since the charge in the normal part changes by $2e$ instead of e. As far as energy and heat are concerned, the Andreev reflection blocks their flows since energy is propagated by quasi-particle, but not the condensate.

Current-Supercurrent conversion

As we have just seen, Andreev reflection processes seem to convert discontinuously ordinary charge current into supercurrent at the interface between the N and S region. However, if one examines the problem more deeply one can obtain a more microscopic view of this conversion process. The key point relies on the evanescent wave solutions of the BdG Hamiltonian, which decay exponentially inside the superconductor when $\epsilon < \Delta$ [BTK1982].

In order to see that, it is convenient to consider the time-dependent BdG equation

$$i\hbar\frac{\partial}{\partial t}\begin{pmatrix}u(x,t)\\ v(x,t)\end{pmatrix} = \begin{pmatrix}H & \Delta\\ \Delta^* & -H^*\end{pmatrix}\begin{pmatrix}u(x,t)\\ v(x,t)\end{pmatrix}, \tag{3.61}$$

which is the analog of the Schrödinger equation governing the dynamics of the excitations above the superconducting ground state via the BdG Hamiltonian. Notice that, in the case μ and Δ are all constant, then

$$u(x,t) = u(x)e^{-i\epsilon t/\hbar} \quad \text{and} \quad v(x,t) = v(x)e^{-i\epsilon t/\hbar}, \tag{3.62}$$

where $u(x)$ and $v(x)$ correspond to the electron and hole components of the wave functions of Eqs. (3.32) and (3.36) respectively. By defining $P(x,t) = |u(x,t)|^2 + |v(x,t)|^2$ as the probability density of finding either an electron or a hole at a particular time and place, we can use Eq. (3.61) in order to obtain the following continuity equation

$$\frac{\partial P}{\partial t} + \frac{\partial J_P}{\partial x} = 0, \tag{3.63}$$

where we introduced the probability current

$$J_P = \frac{\hbar}{m}\left[\mathrm{Im}\left(u^*\partial_x u\right) - \mathrm{Im}\left(v^*\partial_x v\right)\right]. \tag{3.64}$$

Notice that the hole current enters with a sign opposite to that of the electron part.

Similarly, we can derive a conservation law for quasiparticle charge. Assigning a unit charge $+e$ to the electron and $-e$ to the hole, the net quasiparticle charge density can be written as $Q(x,t) = e\left(|u(x,t)|^2 - |v(x,t)|^2\right)$. Using again Eq. (3.61), one obtains the continuity equation for the quasiparticle charge Q, which takes the form

$$\frac{\partial Q}{\partial t} + \frac{\partial J_Q}{\partial x} = \frac{4e\Delta}{\hbar}\mathrm{Im}\left(u^* v\right), \tag{3.65}$$

where we introduced the charge current

$$J_Q = \frac{e\hbar}{m}\left[\mathrm{Im}\left(u^*\partial_x u\right) + \mathrm{Im}\left(v^*\partial_x v\right)\right]. \tag{3.66}$$

Differently from the case of the probability current of Eq. (3.64), in Eq. (3.66), both the electron and hole contributions to the quasiparticle current enter with the same sign. By direct inspection, it turns out that, inside the superconductor $J_P \propto w_{\tilde{e}/\tilde{h}} = 0$ at the gap edge (i. e. $\epsilon = \Delta$), while $J_Q = ev_F$. Of course, for the normal region nothing so dramatic occurs, and we always find simply $J_Q = eJ_P$.

Another important thing to notice, is the presence of a non-zero term on the right side of Eq. (3.65). The fact that such a term is different from zero implies that the charge current is not conserved. In fact, it acts as a source (or drain) term connecting the quasiparticles with the condensate inside the superconductor.

As a simple example of quasiparticle current being converted to condensate current, we consider the case of an electron with an energy $\epsilon < \Delta$, coming from the N region and resulting in an evanescent wave inside the superconductor. For an ideal interface, i. e. $Z = 0$, and $\phi = 0$ one can show that (see Eqs. (3.52)-(3.53)) $r_{ee} = \eta_{\tilde{h}e} = 0$, $r_{he} = u_0/v_0$ and $\eta_{\tilde{e}e} = 1/u_0$. In the sub-gap regime, $|r_{he}|^2 = 1$, which means the incident electron is totally Andreev reflected as a hole. Thus, the total charge carried in the normal metal equals $2ev_F$, but in the superconductor J_Q is exponentially suppressed. Explicitly

$$J_Q = \frac{e\hbar}{m}\mathrm{Im}\left[\left(\eta_{\tilde{e}e}e^{iq_{\tilde{e}}x}\right)^*\partial_x\left(\eta_{\tilde{e}e}e^{iq_{\tilde{e}}x}\right)\left(u_0^* u_0 + v_0^* v_0\right)\right]. \tag{3.67}$$

Letting $q_{\tilde{e}} \approx k_F + i\sqrt{\Delta^2 - \epsilon^2}/\hbar v_F$ (in the limit $\mu \gg \epsilon, \Delta$), and being $|u_0|^2 = |v_0|^2$ in the sub-gap regime, we have

$$J_Q = \frac{|u_0|^2 + |v_0|^2}{|u_0|^2} ev_F e^{-\frac{2x}{\hbar v_F}\sqrt{\Delta^2-\epsilon^2}} = 2ev_F e^{-\frac{x}{\lambda}} \tag{3.68}$$

where we introduced the penetration depth

$$\lambda = \frac{\hbar v_F}{2\Delta}\left[1 - \left(\frac{\epsilon}{\Delta}\right)^2\right]^{-\frac{1}{2}}, \tag{3.69}$$

which corresponds to the length that the particle travels inside the superconductor before the current is converted to the supercurrent carried by the condensate. Notice that, although right at the gap edge such a length diverges, the characteristic length scales as the superconducting coherence length $\lambda \sim \xi = v_F\hbar/\Delta$. The "disappearing current" reappears as current carried by the condensate. Indeed, by rewriting the drain term in Eq. (3.65) as

$$-\partial_x J_S \equiv \frac{4e\Delta}{\hbar}\mathrm{Im}\left(u^* v\right) \tag{3.70}$$

then

$$\begin{aligned} J_S &= \frac{4e\Delta}{\hbar}\int_0^x dx'\ \mathrm{Im}\left(\eta^*_{\tilde{e}e} v_0^* e^{-iq_{\tilde{e}}x'} \eta_{\tilde{e}e} u_0 e^{iq_{\tilde{e}}x'}\right) \\ &= \frac{4e\Delta}{\hbar}\mathrm{Im}\left(\frac{v_0^* u_0}{u_0^* u_0}\right)\int_0^x dx'\ e^{-\frac{x}{\lambda}} \\ &= 2ev_F\left(1 - e^{-\frac{x}{\lambda}}\right). \end{aligned} \tag{3.71}$$

This is the desired result, explicitly showing the supercurrent increasing to an asymptotic value as $x \to \infty$, at the same rate as the quasiparticle current dies away.

Beyond the Andreev approximation

We conclude this section by giving the explicit expressions of the scattering coefficients of Eq. (3.52) and similar, obtained beyond the Andreev approximation in the case of an ideal interface $Z = 0$:

$$r_{ee} = \frac{e^{2ixk_e}\left(-\Gamma q_{\tilde{e}} q_{\tilde{h}} + \Gamma k_e k_h + \Xi_1 k_e - \Xi_2 k_h\right)}{\Gamma q_{\tilde{e}} q_{\tilde{h}} + \Gamma k_e k_h + \Xi_1 k_e + \Xi_2 k_h} \qquad r_{eh} = \frac{2u_0 v_0 \sqrt{k_e k_h}\left(q_{\tilde{e}} + q_{\tilde{h}}\right) e^{i(xk_e - xk_h + \phi)}}{\Gamma q_{\tilde{e}} q_{\tilde{h}} + \Gamma k_e k_h + \Xi_1 k_e + \Xi_2 k_h}$$

$$r_{he} = \frac{2u_0 v_0 \sqrt{k_e k_h}\left(q_{\tilde{e}} + q_{\tilde{h}}\right) e^{i(xk_e - xk_h - \phi)}}{\Gamma q_{\tilde{e}} q_{\tilde{h}} + \Gamma k_e k_h + \Xi_1 k_e + \Xi_2 k_h} \qquad r_{hh} = \frac{e^{-2ixk_h}\left(-\Gamma q_{\tilde{e}} q_{\tilde{h}} + \Gamma k_e k_h - \Xi_1 k_e + \Xi_2 k_h\right)}{\Gamma q_{\tilde{e}} q_{\tilde{h}} + \Gamma k_e k_h + \Xi_1 k_e + \Xi_2 k_h}$$

$$t_{\tilde{e}e} = \frac{2u_0\left(q_{\tilde{h}} + k_h\right)\sqrt{\Gamma k_e q_{\tilde{e}}}\, e^{\frac{1}{2}i(-2xq_{\tilde{e}} + 2xk_e - \phi)}}{\Gamma q_{\tilde{e}} q_{\tilde{h}} + \Gamma k_e k_h + \Xi_1 k_e + \Xi_2 k_h} \qquad t_{\tilde{e}h} = -\frac{2v_0\left(k_e - q_{\tilde{h}}\right)\sqrt{\Gamma k_h q_{\tilde{e}}}\, e^{-\frac{1}{2}i(2xq_{\tilde{e}} + 2xk_h - \phi)}}{\Gamma q_{\tilde{e}} q_{\tilde{h}} + \Gamma k_e k_h + \Xi_1 k_e + \Xi_2 k_h}$$

$$t_{\tilde{h}e} = -\frac{2v_0\left(k_h - q_{\tilde{e}}\right)\sqrt{\Gamma k_e q_{\tilde{h}}}\, e^{\frac{1}{2}i(2xq_{\tilde{h}} + 2xk_e - \phi)}}{\Gamma q_{\tilde{e}} q_{\tilde{h}} + \Gamma k_e k_h + \Xi_1 k_e + \Xi_2 k_h} \qquad t_{\tilde{h}h} = \frac{2u_0\left(q_{\tilde{e}} + k_e\right)\sqrt{\Gamma k_h q_{\tilde{h}}}\, e^{ixq_{\tilde{h}} - ixk_h + \frac{i\phi}{2}}}{\Gamma q_{\tilde{e}} q_{\tilde{h}} + \Gamma k_e k_h + \Xi_1 k_e + \Xi_2 k_h}$$

$$r_{e\tilde{e}} = \frac{e^{-2ixq_{\tilde{e}}}\left(\Gamma q_{\tilde{e}} q_{\tilde{h}} - \Gamma k_e k_h - \Xi_3 k_e + \Xi_4 k_h\right)}{\Gamma q_{\tilde{e}} q_{\tilde{h}} + \Gamma k_e k_h + \Xi_1 k_e + \Xi_2 k_h} \qquad r_{e\tilde{h}} = -\frac{2u_0 v_0\left(k_e + k_h\right)\sqrt{q_{\tilde{e}} q_{\tilde{h}}}\, e^{-ix(q_{\tilde{e}} - q_{\tilde{h}})}}{\Gamma q_{\tilde{e}} q_{\tilde{h}} + \Gamma k_e k_h + \Xi_1 k_e + \Xi_2 k_h}$$

$$r_{h\tilde{e}} = -\frac{2u_0 v_0\left(k_e + k_h\right)\sqrt{q_{\tilde{e}} q_{\tilde{h}}}\, e^{-ix(q_{\tilde{e}} - q_{\tilde{h}})}}{\Gamma q_{\tilde{e}} q_{\tilde{h}} + \Gamma k_e k_h + \Xi_1 k_e + \Xi_2 k_h} \qquad r_{h\tilde{e}} = \frac{e^{2ixq_{\tilde{h}}}\left(\Gamma q_{\tilde{e}} q_{\tilde{h}} - \Gamma k_e k_h + \Xi_3 k_e - \Xi_4 k_h\right)}{\Gamma q_{\tilde{e}} q_{\tilde{h}} + \Gamma k_e k_h + \Xi_1 k_e + \Xi_2 k_h}$$

$$t_{\tilde{e}\tilde{e}} = \frac{2u_0\left(q_{\tilde{h}} + k_h\right)\sqrt{\Gamma k_e q_{\tilde{e}}}\, e^{\frac{1}{2}i(-2xq_{\tilde{e}} + 2xk_e + \phi)}}{\Gamma q_{\tilde{e}} q_{\tilde{h}} + \Gamma k_e k_h + \Xi_1 k_e + \Xi_2 k_h} \qquad t_{\tilde{e}\tilde{h}} = -\frac{2v_0\left(k_h - q_{\tilde{e}}\right)\sqrt{\Gamma k_e q_{\tilde{h}}}\, e^{\frac{1}{2}i(2xq_{\tilde{h}} + 2xk_e + \phi)}}{\Gamma q_{\tilde{e}} q_{\tilde{h}} + \Gamma k_e k_h + \Xi_1 k_e + \Xi_2 k_h}$$

$$t_{\tilde{h}\tilde{e}} = -\frac{2v_0\left(k_e - q_{\tilde{h}}\right)\sqrt{\Gamma k_h q_{\tilde{e}}}\, e^{-\frac{1}{2}i(2xq_{\tilde{e}} + 2xk_h + \phi)}}{\Gamma q_{\tilde{e}} q_{\tilde{h}} + \Gamma k_e k_h + \Xi_1 k_e + \Xi_2 k_h} \qquad t_{\tilde{h}\tilde{h}} = \frac{2u_0\left(q_{\tilde{e}} + k_e\right)\sqrt{\Gamma k_h q_{\tilde{h}}}\, e^{-\frac{1}{2}i(-2xq_{\tilde{h}} + 2xk_h + \phi)}}{\Gamma q_{\tilde{e}} q_{\tilde{h}} + \Gamma k_e k_h + \Xi_1 k_e + \Xi_2 k_h}$$

where we defined the quantities

$$\Gamma = u_0^2 - v_0^2,$$

and

$$\begin{pmatrix} \Xi_1 & \Xi_2 \\ \Xi_3 & \Xi_4 \end{pmatrix} = \begin{pmatrix} q_{\tilde{h}} & q_{\tilde{e}} \\ q_{\tilde{h}} & q_{\tilde{e}} \end{pmatrix} u_0^2 + \begin{pmatrix} q_{\tilde{e}} & q_{\tilde{h}} \\ -q_{\tilde{e}} & -q_{\tilde{h}} \end{pmatrix} v_0^2.$$

4

Landauer Büttiker theory of transport

4.1 Landauer-Büttiker with Normal Metals

The Landauer-Büttiker [Landauer1957, Buttiker1986] (or scattering) theory of transport provides a simple and powerful theoretical framework for the description of currents flowing in normal mesoscopic conductors, when coherent and elastic scattering processes are assumed in the active region. Under these conditions, the scattering formalism has been shown [Datta1997] to be equivalent to the non-equilibrium Green's function formalism. In this respect, it represents an elegant extension of equilibrium statistical mechanics that allows to deal with non-equilibrium problems, providing a simple but accurate approach also for the description of mesoscopic superconducting structures.

The idea of the scattering approach is to relate transport properties of the system to its scattering ones, and applies to non-interacting systems in the stationary regime [Blanter2000]. In its traditional form the Landauer-Büttiker theory considers a mesoscopic sample connected to $\mathcal{R}$ macroscopic contacts (acting as particle reservoirs) via metallic leads (assumed to be perfect conductors), see Fig. 4.1. Particles which propagate along the lead from some reservoir, enter the sample, are scattered, and then leave the scattering region to go to the same or a different reservoir. To calculate the current flowing between the sample and the reservoirs it is enough to look at the incoming and outgoing particles flowing along each lead. Electrons propagating to the sample are incident, or incoming particles, while electrons propagating from the sample are scattered, or outgoing, particles. We emphasize that we consider only elastic, i.e. energy-conserving, processes. To neglect inelastic scattering we assume low temperatures when the phase coherence length is larger than the size of the sample, $\ell_\varphi(T) \gg L$. It is assumed that the reservoirs are so large that they can be considered at the thermodynamical equilibrium with temperature T_i and a chemical potential μ_i, the distribution functions of electrons in the reservoirs, defined via these parameters, are then Fermi distribution functions

$$f_i(\epsilon) = \left[e^{(\epsilon-\mu_i)/k_B T_i} + 1\right]^{-1} \tag{4.1}$$

where ϵ is the energy, k_B is the Boltzmann constant and $i = 1, ..., \mathcal{R}$ is the index for the i-th reservoir. Is important to notice that, although there are no inelastic processes in the sample,

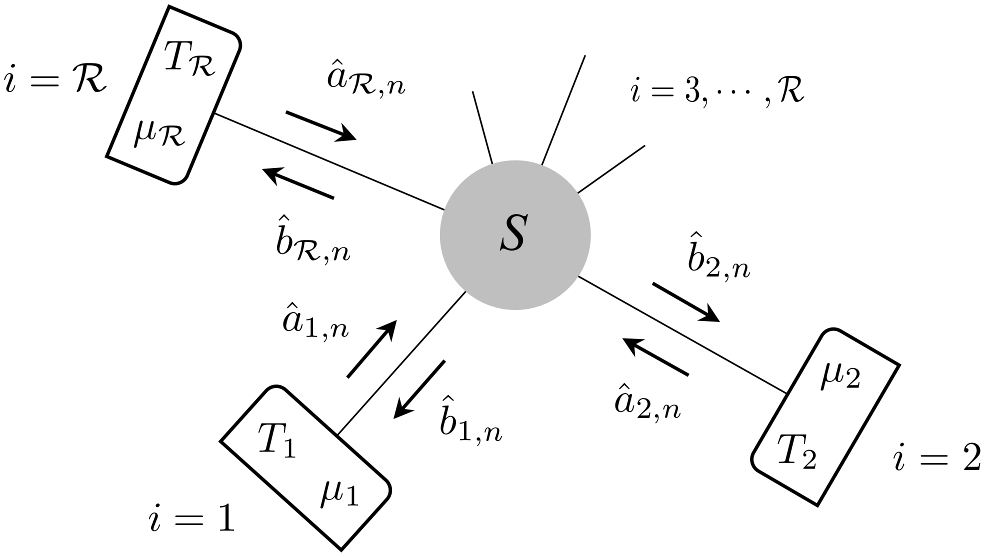

FIGURE 4.1: A mesoscopic sample described by the scattering matrix S. The index $i = 1, \cdots, \mathcal{R}$ labels electron reservoirs with temperature T_i and chemical potential μ_i. The arrows show the propagation direction for incident $\hat{a}_{i,n}$ and scattered $\hat{b}_{i,n}$ electrons per each open transverse channel $n = 1, \cdots, N_i$ of each lead i.

a strict equilibrium state in the reservoirs can be established only via inelastic processes. Notice that reservoirs act both as perfect sources and sinks of particles, irrespective of the energy of the carrier that is leaving or arriving at the conductor.

Far from the sample, and inside the leads, we can assume that transverse (across the leads) and longitudinal (along the leads) motion of electrons are separable. In the longitudinal direction the system is open, and is characterized by the continuous wave vector k. Transverse motion is quantized and described by the discrete index $n = 1, \cdots, N_i(\epsilon)$ where $N_i(\epsilon)$ in the total number of open transverse (quantum) channels at energy ϵ in the lead i (which, in general, can be different for each lead). Here n is a multicomponent index which includes all other quantum numbers associated with the lead (e. g. spin, isospin, etc).

To calculate the current flowing between the scatterer and the reservoirs we use the second quantization formalism. This formalism deals with operators creating/annihilating particles with energy ϵ, at lead i and transverse channel n. We use different operators corresponding to incident electrons, $a^{\dagger}_{i,n}(\epsilon)/a_{i,n}(\epsilon)$, and to scattered electrons, $b^{\dagger}_{i,n}(\epsilon)/b_{i,n}(\epsilon)$ respectively. The operator $a^{\dagger}_{i,n}(\epsilon)$ creates one electron in the state with wave function $\psi^{(in)}_{i,n}(\epsilon)/\sqrt{\hbar v_{i,n}(\epsilon)}$, while the operator $b^{\dagger}_{i,n}(\epsilon)$ creates one electron in the state with wave function $\psi^{(out)}_{i,n}(\epsilon)/\sqrt{\hbar v_{i,n}(\epsilon)}$ [Moskalets2011]. The incident and scattered states are normalized to $\sqrt{\hbar v_{i,n}(\epsilon)}$, where $v_{i,n}(\epsilon)$ is the group velocity of the electrons at energy ϵ, in order to carry unit flux. They obey fermionic anticommutation relations

$$\begin{aligned}
\{\hat{a}^{\dagger}_{i,n}(\epsilon), \hat{a}_{j,m}(\epsilon')\} &= \delta_{ij}\delta_{nm}\delta(\epsilon-\epsilon') \\
\{\hat{a}_{i,n}(\epsilon), \hat{a}_{j,m}(\epsilon')\} &= 0 \\
\{\hat{a}^{\dagger}_{i,n}(\epsilon), \hat{a}^{\dagger}_{j,m}(\epsilon')\} &= 0
\end{aligned} \tag{4.2}$$

with similar relations holding for the operators $b^{\dagger}_{i,n}(\epsilon)$ and $b_{i,n}(\epsilon)$.

The power of the scattering approach - in the context of electronic transport - is that any information concerning the flowing of electrons through the mesoscopic sample is compactly encoded in a single mathematical object: the scattering matrix. The scattering matrix $S(\epsilon)$ is defined as the linear operator mapping the vector of destruction operators of the incident states at energy ϵ to the vector of destruction operators of the scattered states at the same energy

$$\begin{pmatrix} \hat{b}_{1,1}(\epsilon) \\ \vdots \\ \hat{b}_{1,N_1}(\epsilon) \\ \hat{b}_{2,1}(\epsilon) \\ \vdots \\ \hat{b}_{2,N_2}(\epsilon) \\ \hat{b}_{\mathcal{R},1}(\epsilon) \\ \vdots \\ \hat{b}_{\mathcal{R},N_\mathcal{R}}(\epsilon) \end{pmatrix} = S(\epsilon) \begin{pmatrix} \hat{a}_{1,1}(\epsilon) \\ \vdots \\ \hat{a}_{1,N_1}(\epsilon) \\ \hat{a}_{2,1}(\epsilon) \\ \vdots \\ \hat{a}_{2,N_2}(\epsilon) \\ \hat{a}_{\mathcal{R},1}(\epsilon) \\ \vdots \\ \hat{a}_{\mathcal{R},N_\mathcal{R}}(\epsilon) \end{pmatrix} \qquad \Longleftrightarrow \qquad \hat{b}_{i,n}(\epsilon) = \sum_{j=1}^{\mathcal{R}} \sum_{m=1}^{N_j(\epsilon)} S_{(i,n),(j,m)}(\epsilon) \hat{a}_{j,m}, \tag{4.3}$$

where $S(\epsilon)$ has dimensions $\left[\sum_{i=1}^{\mathcal{R}} N_i(\epsilon)\right] \times \left[\sum_{i=1}^{\mathcal{R}} N_i(\epsilon)\right]$. The creation operators $\hat{a}^\dagger$ and $\hat{b}^\dagger$ for the incident and scattered states obey the same relation where $S(\epsilon)$ is replaced by its conjugate $S(\epsilon)^*$. Importantly, the flux conservation in the scattering process implies that the matrix S is unitary

$$S(\epsilon) S^\dagger(\epsilon) = \mathbb{1} \qquad \Longleftrightarrow \qquad \sum_{j=1}^{\mathcal{R}} \sum_{m=1}^{N_j(\epsilon)} \left| S_{(i,n),(j,m)}(\epsilon) \right|^2 = 1. \tag{4.4}$$

The most important application of the Landauer-Büttiker approach for the problem of quantum transport is the calculation of the mean probability (or particle) current flowing through the mesoscopic sample. As we will see later in this thesis (see Chap. 5), such probability current can be directly employed for the computation of thermodynamical relevant quantities such as electric and heat currents at different lead of the system. In the second quantization formalism the probability current operator for the i-th lead takes the following form [Blanter2000, Moskalets2011]

$$\hat{J}_i(x,t) = \frac{i\hbar}{2m} \int d\boldsymbol{r}_\perp \left\{ \frac{\partial \hat{\Psi}_i^\dagger(\boldsymbol{r},t)}{\partial x} \hat{\Psi}_i(\boldsymbol{r},t) - \hat{\Psi}_i^\dagger(\boldsymbol{r},t) \frac{\partial \hat{\Psi}_i(\boldsymbol{r},t)}{\partial x} \right\} \tag{4.5}$$

where $\boldsymbol{r} \equiv (x, \boldsymbol{r}_\perp)$ with x and $\boldsymbol{r}_\perp$ the longitudinal and transverse coordinates respectively, and where we assume that the particles have mass m. The operator $\hat{\Psi}_i(\boldsymbol{r},t)$ is the field operator for electrons in lead i

$$\begin{aligned} \hat{\Psi}_i(\boldsymbol{r},t) &= \frac{1}{\sqrt{2\pi}} \int_{-\infty}^{\infty} d\epsilon \; e^{-i\epsilon t/\hbar} \sum_{n=1}^{N_i(\epsilon)} \left\{ \frac{\psi_{i,n}^{(in)}(\epsilon,\boldsymbol{r})}{\sqrt{\hbar v_{i,n}(\epsilon)}} \hat{a}_{i,n}(\epsilon) - \frac{\psi_{i,n}^{(out)}(\epsilon,\boldsymbol{r})}{\sqrt{\hbar v_{i,n}(\epsilon)}} \hat{b}_{i,n}(\epsilon) \right\} \\ &= \frac{1}{\sqrt{2\pi}} \int_{-\infty}^{\infty} d\epsilon \; e^{-i\epsilon t/\hbar} \sum_{n=1}^{N_i(\epsilon)} \frac{\chi_{i,n}(\epsilon,\boldsymbol{r}_\perp)}{\sqrt{\hbar v_{i,n}(\epsilon)}} \left\{ \hat{a}_{i,n}(\epsilon) e^{-ik_{i,n}(\epsilon)x} - \hat{b}_{i,n}(\epsilon) e^{ik_{i,n}(\epsilon)x} \right\} \end{aligned} \tag{4.6}$$

where in the second line we used the assumption that $\psi_{i,n}^{(in)}(\epsilon, \boldsymbol{r})$ and $\psi_{i,n}^{(out)}(\epsilon, \boldsymbol{r})$ can be factorized as the products of transverse and longitudinal components

$$\psi_{i,n}^{(in)}(\epsilon, \boldsymbol{r}) = \chi_{i,n}\left(\epsilon, \boldsymbol{r}_{\perp}\right) e^{-ik_{i,n}(\epsilon)x} \tag{4.7}$$

$$\psi_{i,n}^{(out)}(\epsilon, \boldsymbol{r}) = \chi_{i,n}\left(\epsilon, \boldsymbol{r}_{\perp}\right) e^{ik_{i,n}(\epsilon)x}. \tag{4.8}$$

Usually, for all observable quantities (average current, noise, or higher moments of the current distribution), the energies ϵ and ϵ' either coincide or are close to each other [Blanter2000]. Therefore, it is reasonable to consider the above quantities within an energy interval that is much smaller than the energy itself

$$\left|\epsilon - \epsilon'\right| \ll \epsilon. \tag{4.9}$$

Within this energy interval the velocities $v_{i,n}\left(\epsilon\right) \approx v_{i,n}\left(\epsilon'\right)$ and the wave vectors $k_{i,n}\left(\epsilon\right) \approx k_{i,n}\left(\epsilon'\right)$ are assumed to vary slowly on the scale of the Fermi energy [Moskalets2011]. Substituting Eq. (4.6) into Eq. (4.5) and taking into account Eq. (4.9), together with the normalization of the transverse wavefunctions $\int d\boldsymbol{r}_{\perp} \chi_{i,n}\left(\boldsymbol{r}_{\perp}\right)^{*} \chi_{i,m}\left(\boldsymbol{r}_{\perp}\right) = \delta_{nm}$, it is possible to arrive at the following expression for the probability current operator [Buttiker1992]

$$\hat{J}_i(t) = \frac{1}{h}\int_{-\infty}^{\infty} d\epsilon\; d\epsilon' e^{-i(\epsilon-\epsilon')t/\hbar} \sum_{n=1}^{N_i(\epsilon)} \left\{\hat{a}_{i,n}^{\dagger}(\epsilon)\hat{a}_{i,n}(\epsilon') - \hat{b}_{i,n}^{\dagger}(\epsilon)\hat{b}_{i,n}(\epsilon')\right\} \tag{4.10}$$

which does not depend on the longitudinal component x. For a full derivation of Eq. (4.10) and a discussion of its limitations we refer to Refs. [Pretre1996, Blanter2000].

The expectation value of the probability current operator $J_i \equiv \left\langle \hat{J}_i(t)\right\rangle$ is obtained by taking the quantum-statistical average over the state of incoming electrons. Here we assume that the presence of a mesoscopic scatterer does not affect the equilibrium properties of reservoirs and that electrons at different reservoirs, i. e. $i \neq j$, are not correlated. Importantly, the scattering theory of transport is based on the observation that each scattering state remains in equilibrium with a particular reservoir. This is because it communicates with one and only one contact, namely the one connected to the lead from which it is incident. Therefore, the incoming particles are equilibrium particles of macroscopic reservoirs and for them we can use standard rules for calculating the quantum-statistical average of the product of creation and annihilation operators

$$\left\langle \hat{a}_{i,n}^{\dagger}\left(\epsilon\right)\hat{a}_{j,m}\left(\epsilon'\right)\right\rangle = \delta_{ij}\delta_{nm}\delta(\epsilon-\epsilon')f_i\left(\epsilon\right) \tag{4.11}$$

where $f_i\left(\epsilon\right)$ is the Fermi distribution function for electrons in the reservoir i introduced in Eq. (4.1). The operators $\hat{b}_{i,n}^{\dagger}$ and $\hat{b}_{i,n}$ concerning scattered states, however, are not coming from a reservoir at the thermodynamical equilibrium. To calculate the quantum-statistical average of their product we need to express them in terms of the operators for incoming particles for which we know how to calculate a corresponding average. Thus, by using Eqs. (4.3) and (4.11), we obtain

$$\begin{aligned}\left\langle \hat{b}_{i,n}^{\dagger}\left(\epsilon\right)\hat{b}_{j,n'}\left(\epsilon'\right)\right\rangle &= \sum_{l,l'}\sum_{m,m'} S_{(i,n),(l,m)}^{*}\left(\epsilon\right) S_{(j,n'),(l',m')}\left(\epsilon'\right)\left\langle \hat{a}_{l,m}^{\dagger}\left(\epsilon\right)\hat{a}_{l',m'}\left(\epsilon'\right)\right\rangle \\ &= \delta(\epsilon-\epsilon')\sum_{l}\sum_{m} S_{(i,n),(l,m)}^{*}\left(\epsilon\right) S_{(j,n'),(l,m)}\left(\epsilon'\right) f_l\left(\epsilon\right)\end{aligned} \tag{4.12}$$

Thanks to the expression in Eqs. (4.11) and (4.12), and by exploiting the unitarity of the scattering matrix $S(\epsilon)$, it is possible to calculate the thermodynamical average $\left\langle \hat{J}_i(t) \right\rangle$ of Eq. (4.10), which is given by

$$J_i \equiv \left\langle \hat{J}_i(t) \right\rangle = \frac{1}{h} \sum_{j=1}^{\mathcal{R}} \int_{-\infty}^{\infty} d\epsilon \left[N_i(\epsilon) \delta_{ij} - P_{i,j}(\epsilon) \right] f_j(\epsilon) \tag{4.13}$$

where we introduced the probability scattering coefficients

$$P_{i,j}(\epsilon) \equiv \sum_{n=1}^{N_i(\epsilon)} \sum_{m=1}^{N_j(\epsilon)} \left| S_{(i,n),(j,m)}(\epsilon) \right|^2 = \mathrm{Tr} \left[S_{ij}(\epsilon) S_{ij}^{\dagger}(\epsilon) \right] \tag{4.14}$$

which represent the transmission ($i \neq j$) and reflection ($i = j$) probabilities of an electron to go from lead j to lead i. The unitarity of the scattering matrix yields the following sum rules:

$$\sum_j P_{i,j}(\epsilon) = N_i(\epsilon); \qquad \sum_i P_{i,j}(\epsilon) = N_j(\epsilon) \tag{4.15}$$

which relate the scattering coefficients $P_{i,j}(\epsilon)$ to the number $N_i(\epsilon)$ of open channels at lead i, with energy ϵ. By exploiting the above relations, one can further simplify the expression of the current of Eq. (4.13), which can be written in the following more compact form

$$J_i = \frac{1}{h} \sum_{j=1}^{\mathcal{R}} \int_{-\infty}^{\infty} d\epsilon \left[f_i(\epsilon) - f_j(\epsilon) \right] P_{i,j}(\epsilon). \tag{4.16}$$

4.2 Two terminal case

It is interesting, for later convenience, to consider the case of a two terminals setup (i. e. $\mathcal{R} = 2$) where a mesoscopic sample is connected to two reservoirs, to be referred to as "left" (L) and "right" (R) respectively. In this simple scenario the scattering matrix $S(\epsilon)$ takes the following block structure

$$S(\epsilon) = \begin{pmatrix} r(\epsilon) & t(\epsilon) \\ t'(\epsilon) & r'(\epsilon) \end{pmatrix}. \tag{4.17}$$

Here the scattering matrix has dimension $[N_L(\epsilon) + N_R(\epsilon)] \times [N_L(\epsilon) + N_R(\epsilon)]$. The square diagonal blocks $r(\epsilon)$ (with size $N_L \times N_L$) and $r'(\epsilon)$ (with size $N_R \times N_R$), describe electrons reflected back to the left and right reservoirs respectively. The off-diagonal, rectangular blocks $t(\epsilon)$ (with size $N_L \times N_R$) and $t'(\epsilon)$ (with size $N_R \times N_L$), are responsible for the electron transmission through the sample. The case of two terminals simplifies the previous expression of the average probability current of Eq. (4.16)

$$J_i = \frac{1}{h} \int_{-\infty}^{\infty} d\epsilon \left[f_i(\epsilon) - f_j(\epsilon) \right] \mathcal{T}(\epsilon) \tag{4.18}$$

with $i \neq j = L, R$, and where we introduced the "transmission function" $\mathcal{T}(\epsilon)$

$$\mathcal{T}(\epsilon) \equiv \mathrm{Tr} \left[t(\epsilon) t^{\dagger}(\epsilon) \right] = \sum_{n=1}^{N_i} \sum_{m=1}^{N_j} \left| S_{(i,n),(j,m)}(\epsilon) \right|^2 = P_{i,j} \quad \text{with } i \neq j \tag{4.19}$$

which is an important basis invariant quantity which defines the transport properties of a mesoscopic two-terminal quantum system. As we will see later in this thesis, an important quantity in quantum transport theory is represented by the charge current

$$J_i^c = eJ_i = \frac{e}{h}\int_{-\infty}^{\infty} d\epsilon \left[f_i\left(\epsilon\right) - f_j\left(\epsilon\right)\right]\mathcal{T}\left(\epsilon\right), \tag{4.20}$$

in which we used the convention that positive charge currents (with e the electron charge) are directed from the reservoirs toward the sample. In the zero-temperature limit and for a small applied voltage, Eq. (4.20) gives us the conductance for the two terminals case

$$G = \frac{e^2}{h}\mathrm{Tr}\left[t\left(\epsilon_F\right)t^{\dagger}\left(\epsilon_F\right)\right]. \tag{4.21}$$

The matrix $t\left(\epsilon_F\right)t^{\dagger}\left(\epsilon_F\right)$ can be diagonalized, it has a real set of eigenvalues (also called transmission probabilities) $0 \leq T_n \leq 1$, which allows us to write the well-known Landauer formula for the conductance [Fisher1981, Imry1986]

$$G = \frac{e^2}{h}\sum_n T_n. \tag{4.22}$$

From the above equation it turns out that the conductance is finite even for ballistic conductors ($T_n = 1$). But how can a ballistic conductor have a non-zero resistance? This led to much controversy and argument in the 1980's - the common belief was that this was essentially a “weak-coupling approach” applicable only when the transmission probability is much less than one ($T_n \ll 1$) - till it was finally realized that this non-zero resistance was really an interface (or contact) resistance between the conductor and the large reservoirs [Wees1988, Wharam1988, Landauer1989, Datta1996]. In this respect, an interesting point to note is that scattering coefficients $P_{i,j}$ of Eqs. (4.14) and (4.19) are calculated from lead i to lead j and not from reservoir i to reservoir j. From a technical point of view this makes the calculation of the scattering coefficients much simpler, since we do not need to worry about the detailed nature of the connection between the lead and the reservoir. From a conceptual point of view this is somewhat surprising, since the conductance given by Eq.(4.22) already includes the interface resistance between the lead and the reservoir. The experimental observation of this interface resistance in 1988 finally made it clear that the scattering approach was applicable not just to weakly coupled tunneling systems but even to strongly coupled ballistic systems.

4.3 Landauer-Büttiker with Superconductors

So far, we have shown that the scattering theory of transport provides a rigorous theoretical framework for the description of normal mesoscopic systems. This approach is based on the observation that, as long as dissipative (inelastic) processes in the active region can be neglected, each scattering eigenstate communicates with one and only one reservoir and as such can be assumed to be in equilibrium with that reservoir. This allows us to calculate any quantity of interest under non-equilibrium conditions using a simple extension of equilibrium statistical mechanics, without the need to solve complicated kinetic equations. In this section we discuss how the same approach can be applied to mesoscopic systems including superconducting segments [Lambert1991, Datta1996].

As we have shown in Sec. 3.4, the key physical phenomenon which arises in the presence of superconductivity is the possibility that an electron can be coherently reflected into a hole and vice versa. This phenomenon, known as Andreev scattering [Andreev1964], occurs without phase breaking and can be described by using the Bogoliubov-de Gennes formalism. In this respect, the scattering theory which we presented in Section 4.1 needs to be extended to take into account the Andreev scattering processes [Buttiker1992, Lambert1993, Lambert1998, Blanter2000]. The main difference is that now we have to deal with an extra index α which discriminates between electrons $\alpha = +1$ and holes $\alpha = -1$. Hence, by proceeding in much the same way as in the previous section, we define operators in the transverse channel n at the lead i which annihilate incoming electrons $\hat{a}^{+}_{i,n}$ and holes $\hat{a}^{-}_{i,n}$, and annihilate scattered electrons $\hat{b}^{+}_{i,n}$ and holes $\hat{b}^{-}_{i,n}$ respectively. Here $n = 1, \ldots, N^{\alpha}_{i}(\epsilon)$ is a multicomponent index which includes all quantum numbers of the lead (e. g. spin, isospin, etc), and $N^{\alpha}_{i}(\epsilon)$ indicates the number of open transverse channels at lead i, with energy ϵ for particles of type α. Due to PHS, and by defning the zero of energy as being that of the chemical potential of the superconductors, we can write hole creation operators at energy ϵ, in terms of electron annihilation operators at energy $-\epsilon$ as [Lesovik2011, Jacquod2012]

$$\begin{aligned} \left[\hat{a}^{-}_{i,n}(\epsilon)\right]^{\dagger} &= \hat{a}^{+}_{i,n}(-\epsilon) \\ \left[\hat{b}^{-}_{i,n}(\epsilon)\right]^{\dagger} &= \hat{b}^{+}_{i,n}(-\epsilon). \end{aligned} \tag{4.23}$$

The electron and hole operators for the outgoing states are related to the electron and hole operators of the incoming states via the extended scattering matrix

$$\hat{b}^{\alpha}_{i,n}(\epsilon) = \sum_{\beta=\pm} \sum_{j=1}^{\mathcal{R}} \sum_{m=1}^{N^{\beta}_{j}(\epsilon)} S^{\alpha,\beta}_{(i,n),(j,m)}(\epsilon) \hat{a}^{\beta}_{j,m} \tag{4.24}$$

which, in matrix form, can be written as

$$\begin{pmatrix} \hat{b}^{+}(\epsilon) \\ \hat{b}^{-}(\epsilon) \end{pmatrix} = S(\epsilon) \begin{pmatrix} \hat{a}^{+}(\epsilon) \\ \hat{a}^{-}(\epsilon) \end{pmatrix} = \begin{pmatrix} S^{++}(\epsilon) & S^{+-}(\epsilon) \\ S^{-+}(\epsilon) & S^{--}(\epsilon) \end{pmatrix} \begin{pmatrix} \hat{a}^{+}(\epsilon) \\ \hat{a}^{-}(\epsilon) \end{pmatrix}. \tag{4.25}$$

Here the diagonal terms $S^{\alpha\alpha}$ relate the outgoing α-type particle to the same type of incoming particle, while the off diagonal terms $S^{\alpha\bar{\alpha}}$ gives the outgoing α-type particle in response to an opposite type of incoming particle. The latter terms turn out to be zero in case there are no superconducting components.

By using Eq. (4.23) inside Eq. (4.10) (obtained for normal conductors), we can write the probability current operator generalized to include superconductivity [Blanter2000]

$$\begin{aligned} \hat{J}_i(t) =& \frac{1}{h} \int_0^{\infty} d\epsilon \; d\epsilon' e^{-i(\epsilon-\epsilon')t/\hbar} \, \mathrm{Tr} \left[\hat{a}^{+\dagger}_{i}(\epsilon) \hat{a}^{+}_{i}(\epsilon') - \hat{a}^{-\dagger}_{i}(\epsilon) \hat{a}^{-}_{i}(\epsilon') \right. \\ & \left. - \hat{b}^{+\dagger}_{i}(\epsilon) \hat{b}^{+}_{i}(\epsilon') + \hat{b}^{-\dagger}_{i}(\epsilon) \hat{b}^{-}_{i}(\epsilon') \right] \end{aligned} \tag{4.26}$$

where the trace is taken over the particle and hole open transverse channels at lead i. To avoid double counting, that would have been introduced by the BdG formalism, the integral over the energies runs from 0 to $+\infty$ instead of starting from $-\infty$. Here, similarly to the case of a normal conductor we can compute the average current at lead i by exploiting the quantum-statistical average of the product of creation and annihilation operators

$$\left\langle \hat{a}^{\alpha\dagger}_{i,n}(\epsilon) \, \hat{a}^{\beta}_{j,m}(\epsilon') \right\rangle = \delta_{\alpha\beta} \delta_{ij} \delta_{nm} \delta(\epsilon - \epsilon') f^{\alpha}_{i}(\epsilon) \tag{4.27}$$

where f_i^- is the distribution function for a hole in lead i and f_i^+ is the analogous for electrons. The particle-hole symmetry implies that the occupation of a hole state is the complementary to the occupation of an electronic state with opposite energy:

$$\begin{aligned} f_i^- (\epsilon) &\equiv \left\langle \hat{a}_{i,n}^{-\dagger} (\epsilon) \, \hat{a}_{i,n}^- (\epsilon) \right\rangle \\ &= \left\langle \hat{a}_{i,n}^+ (-\epsilon) \, \hat{a}_{i,n}^{+\dagger} (-\epsilon) \right\rangle \\ &= 1 - f_i^+ (-\epsilon) \, , \end{aligned} \tag{4.28}$$

where we used the fact that a creation of a hole at energy ϵ correspond to an annihilation of an electron at energy $-\epsilon$. We can then write a generalized expression for the Fermi distribution function as follows:

$$f_i^\alpha (\epsilon) = \left\{ e^{[\epsilon - \alpha(\mu_i - \mu_S)]/k_B T_i} + 1 \right\}^{-1} , \tag{4.29}$$

where μ_i and T_i are respectively the chemical potential and the temperature of the i-th lead and μ_S is the chemical potential of the superconductors which we take as a reference for the energies. Thus, by using Eqs. (4.24)-(4.27) and acting in a similar way as in Section 4.1 for normal systems, we can finally compute the average probability current at lead i as

$$J_i \equiv \left\langle \hat{J}_i(t) \right\rangle = \frac{1}{h} \sum_{j=1}^{\mathcal{R}} \sum_{\alpha,\beta} \alpha \int_0^\infty d\epsilon \left[N_i^\alpha (\epsilon) \, \delta_{ij} \delta_{\alpha\beta} - P_{i,j}^{\alpha,\beta} (\epsilon) \right] f_j^\beta (\epsilon) \tag{4.30}$$

where we introduced the (generalized) probability scattering coefficients [Lambert1998]

$$P_{i,j}^{\alpha,\beta} (\epsilon) \equiv \sum_{n=1}^{N_i^\alpha(\epsilon)} \sum_{m=1}^{N_j^\beta(\epsilon)} \left| S_{(i,n),(j,m)}^{\alpha,\beta} (\epsilon) \right|^2 = \mathrm{Tr} \left[S_{ij}^{\alpha,\beta} (\epsilon) \, S_{ij}^{\alpha,\beta\dagger} (\epsilon) \right] \tag{4.31}$$

which represent the reflection ($i = j$) or transmission ($i \neq j$) of a quasi-particle of type β in lead j to a quasi-particle of type α in lead i. For $\alpha \neq \beta$, $P_{i,j}^{\alpha,\beta}$ represents an Andreev scattering coefficient, while for $\alpha = \beta$, it is a normal scattering coefficient. The unitarity of the scattering matrix yields the following sum rules:

$$\sum_{j,\beta} P_{i,j}^{\alpha,\beta} (\epsilon) = N_i^\alpha (\epsilon) \, ; \qquad \sum_{i,\alpha} P_{i,j}^{\alpha,\beta} (\epsilon) = N_j^\beta (\epsilon) \tag{4.32}$$

where $N_i^\alpha (\epsilon)$ is the number of open channels at lead i, with energy ϵ for particles of type α, satisfying $N_i^+(\epsilon) = N_i^-(-\epsilon)$ (due to PHS). As we did for the case of normal system, by exploiting the above relations, one can simplify the expression of the current of Eq. (4.30), which can be written in the following more compact form

$$J_i = \frac{1}{h} \sum_{j=1}^{\mathcal{R}} \sum_{\alpha,\beta} \alpha \int_0^\infty d\epsilon \left[f_i^\alpha (\epsilon) - f_j^\beta (\epsilon) \right] P_{i,j}^{\alpha,\beta} (\epsilon) \, . \tag{4.33}$$

4.4 From symmetry classes to symmetries of the Scattering matrix

The scatterer has an underlying Hamiltonian which may satisfies specific symmetries. In this respect single-particle Hamiltonian systems can be classified into ten classes, in terms of the presence or absence of time-reversal (TRS), particle-hole (PHS), and sublattice/chiral (SLS) symmetries [Schnyder2008, Jacquod2012]. Here we list such symmetries for noninteracting fermionic quantum systems and derive the fundamental relations that the scattering matrix S has to satisfy in those classes. Importantly, as we will see in Chap. 5, Onsager relations will follow from these symmetries, once they are inserted into scattering theory expressions for the computation of the linear transport coefficients [Benenti2017].

Symmetries of the Hamiltonian

According to Wigner's theorem [Wigner1931], the symmetry operations in quantum mechanics are represented by unitary or anti-unitary operators (which preserve probabilities). A unitary operator $\mathcal{U}$ preserves the inner product of two states $|\Psi\rangle$, $|\Phi\rangle$, i. e.

$$\langle \mathcal{U}\Psi | \mathcal{U}\Phi \rangle = \langle \Psi | \Phi \rangle \tag{4.34}$$

while an anti-unitary operator $\mathcal{A}$ adds an additional complex conjugation:

$$\langle \mathcal{A}\Psi | \mathcal{A}\Phi \rangle = \langle \Psi | \Phi \rangle^* = \langle \Phi | \Psi \rangle \,. \tag{4.35}$$

Each symmetry operation can commute or anti-commute with the Hamiltonian H which describes the system. Seminal works by [Altland-Zirnabauer1997] have classified all noninteracting quantum systems depending on the presence or absence of three relevant symmetries (see the Scheme 4.36 below): time reversal symmetry (TRS), particle hole (or charge conjugation) symmetry (PHS), and chiral (or sublattice) symmetry (SLS).

TRS	$\mathcal{T}$	$[\mathcal{T}, H] = 0$	$\mathcal{T}^2 = \pm 1$
PHS	$\mathcal{P}$	$\{\mathcal{P}, H\} = 0$	$\mathcal{P}^2 = \pm 1$
SLS	Γ	$\{\Gamma, H\} = 0$	$\Gamma^2 = 1$

(4.36)

The TRS is represented by the anti-unitary operator $\mathcal{T}$ that commutes with H, $\mathcal{T}H = H\mathcal{T}$. The physical operation of time-reversal ($t \to -t$) causes an inversion of both momentum $\mathcal{T}p\mathcal{T}^{-1} = -p$ and spin (angular momentum) $\mathcal{T}\sigma_i\mathcal{T}^{-1} = -\sigma_i$, and is described by the following operator

$$\mathcal{T} = \begin{cases} -iK & \text{for spinless or integer-spin particles} \\ -i\sigma_y K & \text{for half-integer-spin particles} \end{cases} \tag{4.37}$$

where σ_y acts on the spin-space and K denotes complex conjugation. The TRS operator squares to $+1$ in case of spinless or integer-spin particles, and squares to -1 for half-integer-spin particles.

The PHS is represented by the anti-unitary operator $\mathcal{P}$, which anti-commutes with H, $\mathcal{P}H = -H\mathcal{P}$. As we have already discussed in Chap. 3, the operator $\mathcal{P}$ acts on the BdG Hamiltonians of the form of Eq. (3.18), and can be written as

$$\mathcal{P} = \begin{cases} \tau_x K & \text{for triplet superconductors} \\ \tau_y K & \text{for singlet superconductors} \end{cases} \tag{4.38}$$

where τ_x and τ_y act in the particle-hole space[1]. Notice that the PHS operator squares to $+1$ in case of triplet pairing superconductors - when H breaks spin-rotation symmetry (SRS)

---

[1] In case of singlet pairing superconductors τ_y acts in a restricted particle-hole space of states of the form $\Psi = (u_\uparrow, v_\downarrow)^T$ (see discussion in Chap. 3).

- while it squares to -1 for singlet pairing (s-wave) superconductors (when H preserves SRS) [Schnyder2008].

Unitary symmetries that commute with the Hamiltonian, $\mathcal{U}H = H\mathcal{U}$ (such as SU(2) SRS), do not appear in scheme (4.36). In fact, such a symmetry can be removed by block-diagonalization, followed by a restriction to a subspace in which $\mathcal{U}$ acts as a scalar. However, this is not possible for unitary symmetries that anti-commute with the Hamiltonian. This is the case of the SLS (or chiral) symmetry operator $\Gamma = \mathcal{P}\mathcal{T}$ which is a unitary (being the product of two anti-unitary symmetries) and anticommutes with the H: $\mathcal{P}\mathcal{T}H = \mathcal{P}H\mathcal{T} = -H\mathcal{P}\mathcal{T}$. In condensed-matter systems, it is often realized as a sublattice symmetry on a bipartite lattice (i. e. the symmetry operation that changes the sign of wave functions on all sites of one of the two sublattices of the bipartite lattice), and takes the following form

$$\Gamma = \eta_z \tag{4.39}$$

with η_z acting on the sublattice space, and where $\Gamma^2 = 1$. Notice that the nomenclature is ambiguous since chiral, or chirality are also frequently used in the context of topological insulators and superconductors (this is the case of chiral edge-modes, see Sec. 2.4). However, neither of the two phases obeys an anti-commuting chiral symmetry. Moreover, similar to PHS, chiral symmetry also implies a symmetry of the energy spectrum around zero. From an eigenstate Ψ with energy ϵ, one can obtain another state $\Gamma\Psi$ with opposite energy $-\epsilon$. However, differently from PHS, the unitary chiral symmetry does not invert the momentum. It implies $\epsilon(k) = \epsilon(-k)$ rather than $-\epsilon(k) = \epsilon(-k)$.

The “tenfold way”

There is a total of ten ways to combine $\mathcal{T}$, $\mathcal{P}$ and Γ, distinguishing $\mathcal{T}^2, \mathcal{P}^2 = \pm 1$, hence the name “tenfold way” [Altland-Zirnabauer1997, Schnyder2008, Jacquod2012]. In Table 4.4, we summarize such ten classes by indicating with “0” the absence, and with “+1” or “−1” the presence of these symmetries, depending on whether the relative (antiunitary) operator squares to the identity operator or minus the identity operator respectively. The ten symmetry classes can be grouped into three categories conventionally named after the mathematical Cartan classification:

- Wigner-Dyson classes [Wigner1951, Dyson1962]: based on TRS and spin-rotational symmetry (SRS). The class “A” has both symmetries broken, the class “AI” has both symmetries present, and the class “AII” has broken SRS but unbroken TRS (there is thus no fourth class since, if TRS is broken, the presence or absence of SRS only affects the size of the Hamiltonian).

- Chiral classes: describe bipartite lattice Hamiltonians with unbroken sublattice symmetry (SLS). Examples include two-dimensional square and hexagonal lattices. Here also, there are three classes, with (apart from their chiral symmetry) the same symmetries as the Wigner-Dyson classes.

- Bogoliubov–de Gennes classes: introduced by Altland and Zirnbauer. These classes appear when normal metals are brought into contact with superconductors: with SRS (C and CI) and without SRS (D and DIII), with TRS (CI and DIII) and without TRS (C and D).

Symmetry class		TRS	PHS	SLS	Physical example
Wigner-Dyson	A	0	0	0	(no SC) mag. flux
	AI	+1	0	0	(no SC) no mag. flux, no spin orbit
	AII	−1	0	0	(no SC) spin-orbit, no mag. flux
Chiral	AIII	0	0	1	(no SC) mag. flux, bip. lattice
	BDI	+1	+1	1	(no SC) no mag. flux, no spin-orbit, bip. lattice
	CII	−1	−1	1	(no SC) no mag. flux, spin-orbit, bip. lattice
BdG	D	0	+1	0	SC, mag. flux, spin-orbit
	C	0	−1	0	SC, mag. flux, no spin-orbit
	DIII	−1	+1	1	SC, no mag. flux, spin-orbit
	CI	+1	−1	1	SC, no mag. flux, no spin-orbit

TABLE 4.1: Ten symmetry classes of single-particle Hamiltonians classified in terms of the presence or absence of time-reversal symmetry (TRS) and particle-hole symmetry (PHS), as well as sublattice (or chiral) symmetry (SLS). In the table, the absence of symmetries is denoted by "0". The presence of these symmetries is denoted by either "+1" or "−1," depending on whether the (antiunitary) operator implementing the symmetry squares to the identity operator or minus the identity operator respectively. TRS= +1 when the spin is an integer, and TRS= −1 when it is a half-integer. For the BdG symmetry classes, the Hamiltonian preserves SRS when PHS= −1 (singlet pairing superconductors), while it does not preserve SRS when PHS= +1 (triplet pairing superconductors). The rightmost column mentions microscopic realizations in each class, with SC indicating the presence of superconductivity.

Symmetries of the Scattering matrix

So far we presented the main symmetry classes in which it is possible to organize noninteracting Hamiltonians which describe the scattering region. In the remaining part of this section, we will discuss how to translate such symmetries (specifically TRS, PHS and SLS) of H into symmetries of the S matrix [Jacquod2012].

In particular, let us consider first the case in which the Hamiltonian satisfies time-reversal symmetry (TRS), i. e. $\mathcal{T} H \mathcal{T}^{-1} = H$. This means that if we reverse velocity and spin of all particles, they will follow time-reversed trajectories back to where they came from, so that incoming particles become outgoing particles and vice versa. In case the TRS is broken, the same happens, but all TRS-breaking fields (e. g. magnetic fields, fluxes, exchange fields) should be inverted too. Combining all of them into a single multicomponent field $\mathcal{B}$, one can show that the scattering matrix obeys the microreversibility relation

$$S\left(\epsilon, \mathcal{B}\right) = \sigma_y \; S^T \left(\epsilon, -\mathcal{B}\right) \sigma_y \tag{4.40}$$

where σ_y acts in spin space, and "T" indicates the matrix transpose of spin, transport channel and (with superconductivity) quasiparticle indices. Included in Eq. (4.40) is the relation $S\left(\epsilon, \mathcal{B}\right) = S^T \left(\epsilon, -\mathcal{B}\right)$ valid when the antiunitary TRS operator squares to +1 and SRS is preserved. Eq. (4.40), can be derived by constructing the scattering matrix S first with scattering states $\psi_{i,n}(\epsilon, \mathcal{B})$, then with their time-reversed $\mathcal{T}\psi_{i,n}(\epsilon, -\mathcal{B})$, and equating the two results. More important for the computation of physical currents are the symmetries of scattering coefficients $P_{i,j}^{\alpha,\beta}(\epsilon)$ defined in Eq. (4.31). In this respect, by using Eq. (4.40), it is possible to show that the microreversibility of the scattering matrix translates into the following symmetry relation for the scattering coefficients

$$P_{i,j}^{\alpha,\beta}(\epsilon, \mathcal{B}) = P_{j,i}^{\beta,\alpha}(\epsilon, -\mathcal{B}). \tag{4.41}$$

A similar result can be obtained for Hamiltonians with unbroken PHS. In this case, by using Eq. (4.38), one can show that the following relation holds for the scattering matrix

$$S\,(\epsilon, \mathcal{B}) = \tau_x \; S^*\,(-\epsilon, \mathcal{B})\,\tau_x \tag{4.42}$$

where τ_x acts in Nambu space and where the energies $\pm\epsilon$ are expressed with respect the chemical potential μ taken equal for all superconductors. Included in Eq. (4.42) is the relation $S\,(\epsilon, \mathcal{B}) = \tau_y \; S^*\,(-\epsilon, \mathcal{B})\,\tau_y$ valid when the antiunitary PHS operator squares to -1 and SRS is preserved. Similarly to the previous case, Eq. (4.42), can be derived by constructing the scattering matrix S first with scattering states $\psi_{i,n}(\epsilon, \mathcal{B})$, then with their particle-hole conjugated $\mathcal{P}\psi_{i,n}(-\epsilon, \mathcal{B})$, and equating the two results. Also in this case it is possible to translate the above-mentioned particle-hole relation for the scattering matrix to the scattering coefficients

$$P_{i,j}^{\alpha,\beta}(\epsilon, \mathcal{B}) = P_{i,j}^{-\alpha,-\beta}(-\epsilon, \mathcal{B}). \tag{4.43}$$

Importantly, by using the latter relation in the expression for the particle current of Eq. (4.33), and considering only normal processes in absence of superconducting components (such that $P_{i,j}^{\pm,\mp} = 0$), one can obtain the expression for the probability current in the case of normal systems as given by Eq. (4.16). As we will see in the next Chap. 5, relations of Eqs. (4.41) and (4.43) will be fundamental in proving Onsager reciprocal relations for mesoscopic hybrid systems.

We finally just comment on SLS. The chiral Hamiltonian symmetry reads $H = -\eta_z H \eta_z$, with η_z acting in sublattice space. For the scattering matrix, this translates into

$$S\,(\epsilon, \mathcal{B}) = \eta_z \; S^\dagger\,(-\epsilon, \mathcal{B})\,\eta_z. \tag{4.44}$$

5

Charge and Heat currents with Scattering Approach

5.1 Quantum Thermodynamics

Since the industrial revolution, the transformation of heat into work has been at the center of technology. The quest to understand the physics of this transformation led to the theory of thermodynamics. During the 19th century it became clear that heat and work were simply two different forms of energy (the first law of thermodynamics), but that heat is special because it has entropy associated with it, and no process is allowed to reduce this entropy (the second law of thermodynamics). A great revolution came with Boltzmann, who made the connection between Newton's deterministic laws of motion and thermodynamics. Boltzmann's theory of statistical mechanics completely changed the status of thermodynamics, which was no longer considered as an underlying theory of nature, but rather an effective theory that applies to macroscopic systems.

However, the advent of quantum theory completely changed the vision of statistical mechanics when applied to nanoscale devices, forcing us to consider phenomena like quantization of energy levels, the statistics of quantum particles (fermionic or bosonic), etc. Moreover, superposition, interference and correlations - while not changing the rules of thermodynamics - can give rise to numerous effects in quantum systems that are otherwise absent in the macroscopic machines typically used for heat-to-work conversion. Interference, for example, can induce thermoelectric effects in systems where they would otherwise be absent, and can modify (either reducing or increasing) them in systems which would already have a thermoelectric response. Coherence, especially in presence of superconducting components, also adds another parameter to the system: the quantum mechanical phase. When this phase can be manipulated by experimentalists, it can often be adjusted to improve the relevant properties of the system in question and make a better heat engine or refrigerator.

The perspective of investigating such phenomena and their potentials in performing useful tasks (such as creating work or cooling systems) at a microscopic level, has given rise in recent years to the field of "quantum thermodynamics". In this context, the Landauer-Büttiker's scattering theory [Landauer1957, Buttiker1986] (we introduced in Chap. 4), provides us with a simple and powerful tool capable of combining the quantum nature of a coherent system of non-interacting electrons with its relevant electrical, thermal and thermoelectric properties. In order to show that, in this chapter, we use the Landauer-Büttiker's approach (in presence of superconductors) to compute charge and heat currents at different leads of a multiterminal quantum system. We also introduced the electrical power and efficiency as performance quantifiers of such systems interpreted as thermoelectric heat engines. Then we conclude by discussing the linear response regime [Benenti2017, Mazza2014], in particular showing how the structure of the scattering theory leads to Onsager reciprocal relations.

5.2 Scattering theory for thermoelectricity

In the context of traditional thermoelectrics, one can treat the electrons inside the thermoelectric structure as being in local thermal equilibrium, with a local temperature which varies smoothly across the sample. The system can then be described by Boltzmann transport equations. In contrast, in mesoscopic or nanoscale thermoelectric devices, the thermoelectric structure is of similar size or smaller than the length scale on which electrons relax to a local equilibrium. Under such conditions and at low temperatures, particles do not behave like classical "balls" but their wave-like behavior must be taken into account. In this coherent regime, quantum-mechanical effects (like interference and correlations) become relevant, and the Boltzmann theory no longer applies. Alternatively, if the particles do not lose energy inside the conductor, quantum transport can be related to scattering events inside the sample, and the Landauer-Büttiker approach can be used to compute currents through the system.

As we have shown in Sec. 4.3, the Landauer-Büttiker approach (generalized in presence of superconducting components), can be used to compute the probability current J_i out of the i-th reservoir (which we report here for clarity)

$$J_i = \frac{1}{h} \sum_{j=1}^{\mathcal{R}} \sum_{\alpha,\beta} \alpha \int_0^{\infty} d\epsilon \left[f_i^{\alpha}(\epsilon) - f_j^{\beta}(\epsilon) \right] P_{i,j}^{\alpha,\beta}(\epsilon) , \tag{5.1}$$

in which $\mathcal{R}$ is the total number of terminals (which can be normal or superconducting), and $\alpha, \beta = \pm$ label particles and holes respectively. In a nutshell, the probability current J_i is obtained by counting each particle/hole that crosses the boundary between the scatterer and reservoir i, by assigning a sign $+$ to particles and $-$ to holes, and depends on the probability that the particles go from one reservoir to another, $P_{i,j}^{\alpha\beta}(\epsilon)$, multiplied by reservoir's occupation factor difference $(f_i^{\alpha}(\epsilon) - f_j^{\beta}(\epsilon))$. As already mentioned, the quantity

$$f_i^{\alpha}(\epsilon) = \left\{ e^{[\epsilon - \alpha(\mu_i - \mu_S)]/k_B T_i} + 1 \right\}^{-1} \tag{5.2}$$

represents the generalized occupation factors for electrons ($\alpha = +$) and holes ($\alpha = -$) respectively, and it is the only function which contains information about the chemical potential μ_i and temperature T_i of the i-th reservoir. Importantly we assume that all superconductors have the same chemical potential μ_S which we take as a reference for the energies. In cases where there are multiple superconductors with different electrochemical potentials one has to use methods beyond the scattering approach, such as the methods presented in Refs. [Klapwijk1982, Octavio1983].

In the following section we will see how the expression of the probability current of Eq. (5.1) can be naturally extended in order to compute thermodynamical relevant quantities such as electric and heat currents at different leads of the system [Lambert1993].

Charge and Heat Currents

The first simplest thermodynamical quantity which can be directly deduced from Eq. (5.1), is the charge (or electrical) current J_i^c at the i-th terminal. Such a current is given by the total flux of electrons with charge e and holes with charge $-e$, flowing from the lead i toward the scatterer and takes the following form

$$J_i^c = \frac{1}{h}\sum_{j=1}^{\mathcal{R}}\sum_{\alpha,\beta}(e\alpha)\int_0^\infty d\epsilon \left[f_i^\alpha(\epsilon) - f_j^\beta(\epsilon)\right] P_{i,j}^{\alpha,\beta}(\epsilon)\,, \tag{5.3}$$

where we use the convention that positive charge currents are directed from the reservoirs toward the sample. Notice that, Eq. (5.3) has been obtained directly from Eq. (5.1), by multiplying the probability current times the value of the electronic charge e, i. e. $J_i^c = eJ_i$.

It is important to notice that, due to Andreev reflection processes taking place at interfaces with superconducting leads, a supercurrent starts flowing inside superconductors in the form of Cooper pairs (see Sec. 3.3). This supercurrent cannot be computed with the Landauer-Büttiker approach, which only provides results for the quasiparticle current component. However, once the charge currents are determined in the normal leads, the sum of the currents in the superconducting leads can be calculated exploiting Kirchhoff's sum rule

$$J_{SC}^c = \sum_{i\in SC} J_i^c = -\sum_{i\notin SC} J_i^c \tag{5.4}$$

as a consequence of the charge conservation.

Similarly to Eq. (5.3), we can follow the same argument and define the energy current J_i^u out of reservoir i into the scatterer, except now each particle carries energy instead of the charge. More precisely, given μ_S as the reference for energies, electron-like quasiparticles carry the energy $(\epsilon + \mu_S)$ while hole-like quasiparticles transport the energy $(\epsilon - \mu_S)$, hence the energy current takes the following form

$$J_i^u = \frac{1}{h}\sum_{j=1}^{\mathcal{R}}\sum_{\alpha,\beta}\int_0^\infty d\epsilon\ (\epsilon + \alpha\mu_S)\left[f_i^\alpha(\epsilon) - f_j^\beta(\epsilon)\right] P_{i,j}^{\alpha,\beta}(\epsilon)\,. \tag{5.5}$$

It is important to notice that the energy current is conserved, namely $\sum_i J_i^u = 0$, but it is not gauge-independent. That is to say, the value of the energy current, J_i^u, depends on our choice of the zero of energy. This means that the energy current is not of physical relevance, although differences in energy currents may be. In contrast, the heat current J_i^h at the lead i is a gauge-independent quantity taking the following form [Callen1998]

$$J_i^h = J_i^u - \frac{\mu_i}{e}J_i^c \tag{5.6}$$

or, more explicitly by using Eqs. (5.3) and (5.5)

$$J_i^h = \frac{1}{h}\sum_{j=1}^{\mathcal{R}}\sum_{\alpha,\beta}\int_0^\infty d\epsilon\ \left[\epsilon - \alpha\left(\mu_i - \mu_S\right)\right]\left[f_i^\alpha(\epsilon) - f_j^\beta(\epsilon)\right] P_{i,j}^{\alpha,\beta}(\epsilon)\,. \tag{5.7}$$

Notice that, differently from the charge transport, Andreev reflection blocks energy and heat fluxes since they are propagated by quasi-particles, but not by the condensate. Moreover, even if no conservation laws hold for the heat currents, they obey to the following important relation

$$\sum_i J_i^h = -\sum_i \frac{\mu_i}{e}J_i^c, \tag{5.8}$$

obtained from Eq. (5.6) by summing over the leads and using the energy current conservation. Notice that the right hand side of Eq. (5.8) represents the electrical power generated by the system as we are about to discuss in the next section. Importantly, Eq. (5.8) corresponds to the first law of thermodynamics, since it says that the rate of work production in the junction (electrical power) equals the rate of heat absorption (total heat current) from the leads. Note that the equality between power generated and heat absorbed only holds when we sum over all reservoirs, in general it does not hold at the level of any given reservoir.

As a final remark, we point out that expressions analogous to those of Eqs. (5.3) and (5.7) for the charge and heat current respectively, can be obtained also in the case of normal systems (without superconducting components). This can be easily done by setting to zero the scattering coefficients relative to Andreev processes, i. e. $P_{i,j}^{\pm\mp}(\epsilon) = 0$, and by using PHS to write $f_i(\epsilon) \equiv f_i^{+}(\epsilon) = 1 - f_i^{-}(-\epsilon)$ and $P_{i,j} \equiv P_{i,j}^{++}(\epsilon) = P_{i,j}^{--}(-\epsilon)$.

Power and efficiency

So far we have seen how the Landauer-Büttiker approach can be used for the computation of the charge (J_i^c) and heat (J_i^h) currents at different leads of a multiterminal system. These two quantities are of fundamental importance to characterize the thermodynamic performance of a mesoscopic hybrid device thought as a thermal machine. In this context, the heat-engine's conversion of heat into work is typically described by two quantifiers: the electrical power, P, and the efficiency of the converter, η. In the case of the electrical power, it is defined as

$$P \equiv -\sum_i \frac{\mu_i}{e} J_i^c. \tag{5.9}$$

With this definition, P is positive when the current flows against the applied bias, i. e. there is a thermopower generated in the system ($P_{gen} \equiv P > 0$) that can be dissipated on an external load. In this case the scatterer is absorbing heat from the electronic reservoirs and turning it into electrical power: the device thus works as a thermoelectrical engine. In contrast, if $P < 0$, then the scatterer is absorbing electrical power and emits heat into the electronic reservoirs: one can think of this as Joule heating.

The efficiency of the thermal machine, η, is defined as the ratio between the work W extracted from the engine when it absorbs heat Q. By convention we assume positive the heat flowing into the system, hence in the steady state the definition of the efficiency is equivalent to

$$\eta = \frac{\dot{W}}{\dot{Q}} = \frac{P_{gen}}{\sum_i^{+} J_i^h} \tag{5.10}$$

where the numerator corresponds to the electrical power generated P_{gen}, while the denominator corresponds to the total heat current entering the system (the superscript $+$ in the sum means that we are summing only positive heat currents). The time derivative of the work must be positive for the machine to work as a heat to work converter, otherwise we are dealing with a refrigerator and the definition of η is no longer valid.

5.3 Linear Response

Much can be said about the scattering theory of arbitrary systems in the limit where the differences in temperature and voltage bias between reservoirs are small on the scale of the average temperature. In this respect, let us consider each lead j characterized by a temperature T_j and a voltage bias V_j (such that $eV_j = \mu_j$). Assuming a reference temperature T and a reference voltage V, each of the previous quantity can be written as to make explicit the difference from the reference values, e. g. $T_j = T + \delta T_j$ and $V_j = V + \delta V_j$, where $\delta T_j = T_j - T$ and $\delta V_j = V_j - V$. Here we assume the superconducting chemical potential $\mu_S = eV_S$ as reference. Assuming small temperature and voltage biases (i. e. $e\delta V_j, k_B \delta T_j \ll k_B T$), we can expand the generalized Fermi distribution function of Eq. (5.2) to the first order in such quantities:

$$\begin{aligned} f_j^{\alpha}(\epsilon) &\simeq f(\epsilon) + \frac{\partial f_j^{\alpha}}{\partial \delta T_j}\delta T_j + \frac{\partial f_j^{\alpha}}{\partial \delta V_j}\delta V_j \\ &= f(\epsilon) - \frac{\epsilon}{T} f'(\epsilon)\delta T_j - \alpha e f'(\epsilon)\delta V_j \end{aligned} \tag{5.11}$$

where we introduced the Fermi function $f(\epsilon) = \left[1 + e^{\epsilon/k_B T}\right]^{-1}$, and its derivative with respect the energy

$$-f'(\epsilon) = -\frac{\partial f}{\partial \epsilon} = \frac{1}{4k_B T \cosh^2(\epsilon/2k_B T)} \tag{5.12}$$

which is a bell-shaped function centered in zero and width of the order of $k_B T$. Since we consider only non-interacting systems, the scattering matrix is independent of the biases, and we can use Eq. (5.11) to linearize the currents of Eqs. (5.3) and (5.7) as follows [Groot2013]:

$$\begin{aligned} J_i^c &= \sum_j L_{ij}^{cc} \frac{\delta V_j}{T} + \sum_j L_{ij}^{ch} \frac{\delta T_j}{T^2}, \\ J_i^h &= \sum_j L_{ij}^{hc} \frac{\delta V_j}{T} + \sum_j L_{ij}^{hh} \frac{\delta T_j}{T^2}. \end{aligned} \tag{5.13}$$

Here we expressed the currents to be proportional to the thermodynamic forces $\delta V_j/T$ and $\delta T_j/T^2$ (also known as generalized forces or affinities), driving the charge and heat currents respectively. We also notice that the terms which are zeroth-order in the affinities cancel due to the difference $f_i^{\alpha}(\epsilon) - f_j^{\beta}(\epsilon)$ in Eqs. (5.3) and (5.7). These relations are referred to as phenomenological coupled transport equations or linear response equations or kinetic equations and the coefficients $L_{ij}^{\mu\nu}$ (with $\mu, \nu = c, h$) are known as Onsager coefficients, which take the following form [1]

$$L_{ij}^{cc} = \frac{e^2 T}{2} \sum_{k=1}^{\mathcal{R}} \sum_{\alpha\beta} \int_{-\infty}^{\infty} d\epsilon\ \alpha \left(-f'(\epsilon)\right) \left[\alpha \delta_{ik} - \beta \delta_{jk}\right] P_{i,k}^{\alpha,\beta}(\epsilon), \tag{5.14a}$$

$$L_{ij}^{ch} = \frac{eT}{2} \sum_{k=1}^{\mathcal{R}} \sum_{\alpha\beta} \int_{-\infty}^{\infty} d\epsilon\ \epsilon\ \alpha \left(-f'(\epsilon)\right) \left[\delta_{ik} - \delta_{jk}\right] P_{i,k}^{\alpha,\beta}(\epsilon), \tag{5.14b}$$

$$L_{ij}^{hc} = \frac{eT}{2} \sum_{k=1}^{\mathcal{R}} \sum_{\alpha\beta} \int_{-\infty}^{\infty} d\epsilon\ \epsilon \left(-f'(\epsilon)\right) \left[\alpha \delta_{ik} - \beta \delta_{jk}\right] P_{i,k}^{\alpha,\beta}(\epsilon), \tag{5.14c}$$

$$L_{ij}^{hh} = \frac{T}{2} \sum_{k=1}^{\mathcal{R}} \sum_{\alpha\beta} \int_{-\infty}^{\infty} d\epsilon\ \epsilon^2 \left(-f'(\epsilon)\right) \left[\delta_{ik} - \delta_{jk}\right] P_{i,k}^{\alpha,\beta}(\epsilon). \tag{5.14d}$$

---

[1] By using PHS, Eqs. (5.14) can be further simplified by restricting the energy integration from 0 to ∞ and dropping the 1/2 factor. This greatly simplifies the computation, since it allows to calculate the scattering coefficients only for positive energies.

All the above coefficients can be collected inside a $2\mathcal{R} \times 2\mathcal{R}$ matrix (with $\mathcal{R}$ the total number of leads)

$$\begin{pmatrix} J_1^c \\ J_1^h \\ \vdots \\ J_i^c \\ J_i^h \\ \vdots \\ J_{\mathcal{R}}^c \\ J_{\mathcal{R}}^h \end{pmatrix} = \begin{pmatrix} L_{11}^{cc} & L_{11}^{ch} & \cdots & L_{1i}^{cc} & L_{1i}^{ch} & \cdots & L_{1\mathcal{R}}^{hh} & L_{1\mathcal{R}}^{ch} \\ L_{11}^{hc} & L_{11}^{hh} & \cdots & L_{1i}^{hc} & L_{1i}^{hh} & \cdots & L_{1\mathcal{R}}^{hc} & L_{1\mathcal{R}}^{hh} \\ \vdots & \vdots & \ddots & \vdots & \vdots & \ddots & \vdots & \vdots \\ L_{i1}^{cc} & L_{i1}^{ch} & \cdots & L_{ii}^{cc} & L_{ii}^{ch} & \cdots & L_{i\mathcal{R}}^{cc} & L_{i\mathcal{R}}^{ch} \\ L_{i1}^{hc} & L_{i1}^{hh} & \cdots & L_{ii}^{hc} & L_{ii}^{hh} & \cdots & L_{i\mathcal{R}}^{hc} & L_{i\mathcal{R}}^{hh} \\ \vdots & \vdots & \ddots & \vdots & \vdots & \ddots & \vdots & \vdots \\ L_{\mathcal{R}1}^{cc} & L_{\mathcal{R}1}^{ch} & \cdots & L_{\mathcal{R}i}^{cc} & L_{\mathcal{R}i}^{ch} & \cdots & L_{\mathcal{R}\mathcal{R}}^{cc} & L_{\mathcal{R}\mathcal{R}}^{ch} \\ L_{\mathcal{R}1}^{hc} & L_{\mathcal{R}1}^{hh} & \cdots & L_{\mathcal{R}i}^{hc} & L_{\mathcal{R}i}^{hh} & \cdots & L_{\mathcal{R}\mathcal{R}}^{hc} & L_{\mathcal{R}\mathcal{R}}^{hh} \end{pmatrix} \begin{pmatrix} \delta V_1/T \\ \delta T_1/T^2 \\ \vdots \\ \delta V_i/T \\ \delta T_i/T^2 \\ \vdots \\ \delta V_{\mathcal{R}}/T \\ \delta T_{\mathcal{R}}/T^2 \end{pmatrix} \tag{5.15}$$

which takes the name of Onsager matrix, and is indicated with $\boldsymbol{L}$. By collecting all the affinities in the vector $\boldsymbol{\mathcal{F}}$, all the currents in the current vector $\boldsymbol{J}$, and by using Eq. (5.15), it is possible to write the entropy production rate in the linear response regime [Brandner2013]

$$\dot{\mathcal{S}} = \boldsymbol{\mathcal{F}}^T \boldsymbol{J} = \boldsymbol{\mathcal{F}}^T \boldsymbol{L} \boldsymbol{\mathcal{F}}. \tag{5.16}$$

Since the entropy production must be non-negative (i. e. $\dot{\mathcal{S}} \geq 0$, as required from the second law of thermodynamics), it turns out that the Onsager matrix $\boldsymbol{L}$ of phenomenological coefficients is a positive semi-definite matrix. Notice also that, from the unitarity of the scattering matrix it follows that all coefficients of type L_{ij}^{cc}, $L_{ij}^{hh} \geq 0$. From the physical point of view, this implies that the electrical ($\propto L_{ij}^{cc}$) and thermal ($\propto L_{ij}^{hh}$) conductances are always positive or zero.

Furthermore, is important to notice that, since $f'(\epsilon)$ is an even function of ϵ, it turns out that the thermoelectric (L_{ij}^{ch}) and Peltier (L_{ij}^{hc}) coefficients of Eqs. (5.14b) and (5.14c), identically vanish if the scattering coefficients are symmetric in energy with respect the chemical potential, namely

$$P_{i,k}^{\alpha,\beta}(\epsilon) = P_{i,k}^{\alpha,\beta}(-\epsilon). \tag{5.17}$$

Often in literature this latter property is referred as particle-hole symmetry [Benenti2017], in the sense that the dynamics of quasi-particles above and below the electrochemical potential is the same. However, it should be clarified that this property is distinct from the PHS property we have introduced in the context of superconducting systems, which instead requires also the inversion of the quasi-paricle index (namely $P_{i,k}^{\alpha,\beta}(\epsilon) = P_{i,k}^{-\alpha,-\beta}(-\epsilon)$, see Sec. 4.4).

Finally, by combining Eqs. (5.13), (5.14c) and (5.14d), we obtain that linear response heat current is conserved, i. e.

$$\sum_i J_i^h = 0. \tag{5.18}$$

However, this conservation of the *linear* heat current is a specificity of linear response theory, while in general we have Eq. (5.8) in place of Eq. (5.18). The latter is only accurate to first order in bias and/or temperature difference, while the electrical power (generated or absorbed by the system) is quadratic in these parameters, thus its correction to the heat is not described in the linear response.

Onsager Reciprocal Relations

Onsager's reciprocity relations (also known as Onsager-Casimir relations) are cornerstones of nonequilibrium statistical mechanics [Onsager1931, Casimir1945]. They relate linear response coefficients between flux densities and thermodynamic forces to one another. They are based on the fundamental principle of microreversibility which implies that the scattering coefficients obey the relation $P^{\alpha,\beta}_{i,j}(\epsilon, \mathcal{B}) = P^{\beta,\alpha}_{j,i}(\epsilon, -\mathcal{B})$ (as already discussed in Sec. 4.4). On a microscopic point of view, this means that, if one reverses the velocity and spin of all particles, and inverts any external TRS-breaking field $\mathcal{B}$ (such as magnetic fields, fluxes, or exchange fields), then the particles will retrace their former paths, reversing the entire succession of configurations. Hence, by using the microreversibility inside the expressions of the Onsager coefficients of Eq. (5.14), the Onsager reciprocity relations read

$$L^{\mu\nu}_{ij}(\mathcal{B}) = L^{\nu\mu}_{ji}(-\mathcal{B}) \tag{5.19}$$

with μ and ν being either charge (c) or heat (h). Such reciprocal relations - theoretically predicted by Onsager in 1931 [Onsager1931] and experimentally demostrated in quantum conductors both for the conductance symmetries [Benoit1986] and the thermoelectric response [Matthews2014] - depend only on fundamental symmetries and are equally valid in topologically trivial and nontrivial states, to the point that they are now often referred to as the fourth law of thermodynamics.

The above microscopic derivation also shows that, in the case of normal systems (thus in absence of superconducting components), one can show the following additional symmetry relation [Butcher1990]

$$L^{ch}_{ij}(\mathcal{B}) = L^{hc}_{ij}(\mathcal{B}). \tag{5.20}$$

However, it can be shown that decoherence due to inelastic scattering leads to a breaking of the equality in Eq. (5.20) [Benenti2017]. Similarly we notice that, in presence of superconductors, the fact that the Andreev reflection turns electrons into holes (and vice-versa), breaks the equality in Eq. (5.20), without affecting the reciprocity relation of Eq. (5.19).

As a final remark, it is important to comment that further symmetries in the underlying system Hamiltonian such as spin-rotation symmetry, particle–hole symmetry, or sublattice symmetry lead directly to additional relations between the above Onsager coefficients. Such relations are given in Ref. [Jacquod2012], along with similar relations for the Onsager coefficients which couple spin transport to charge and heat transport.

6

Josephson effect

The Josephson effect was first discovered by Brian Josephson in 1962 [Josephson1962] and experimentally observed by Anderson and Rowell in 1963 [Anderson1963]. It opened not only a new important chapter of physics but also new horizons for a wide variety of stimulating applications. Josephson predicted that a supercurrent could exist between two superconductors separated by a thin insulating layer and that its value would be proportional to the sine of the difference $\phi = \phi_L - \phi_R$ of the phases of the superconductor order parameters

$$J(\phi) = J_C \sin(\phi) \tag{6.1}$$

where $J_C = \max_\phi J(\phi)$ is called the critical current. This so-called dc Josephson effect extends beyond Josephson's predictions and can exist also if superconductors are connected by a "weak link" of any physical nature such as normal metal, insulators (trivial or topological), semiconductor, superconductor with smaller critical temperature, geometrical constriction, etc. The current-phase relation (CPR) is an important characteristic of a Josephson junction. In only a few cases does it reduces to the familiar sinusoidal form of Eq. (6.1), which is ordinarily used to study the dynamics and ultimate performance of analog and digital devices based on Josephson junctions [Barone1982]. The physics of the dc Josephson effect can be understood if we take into account that a quasiparticle located in the weak link cannot penetrate directly into a superconductor if its energy is smaller than the superconducting energy gap. However, another form of charge transport can occur via Andreev reflections [Andreev1964]. As already discussed in Sec. 3.3, an electron impinging on one of the interfaces is converted into a hole moving in the opposite direction, thus generating a Cooper pair in a superconductor. This hole is subsequently Andreev reflected at the second interface and is converted back into an electron, leading to the destruction of a Cooper pair in the other superconductor. As a result of this cycle, a pair of correlated electrons is transferred from one superconductor to another, creating a supercurrent flow across the junction (see Fig. 6.1(a)). Since the Andreev reflection amplitudes depend on the corresponding phases $\phi_{L,R}$, the resulting current depends on the phase difference ϕ, thus leading to the dc Josephson effect. Due to the electron-hole interference in the quantum well, standing waves with quantized energy ϵ_p appear in the weak-link region. The corresponding quantum states are referred to as Andreev bound states (ABSs). The total supercurrent J flowing through the junction is the sum of the partial currents transported via Andreev bound states.

In this chapter we briefly review some general phenomenological aspects of superconducting state and provide a qualitative interpretation of the Josephson effect on the basis of very simple models. In this framework, we derive the foundamental equations governing the behavior of a Josephson junction under the application of an external potential bias V and a magnetic field $\boldsymbol{B}$. In conclusion we describe how the Josephson current can be obtained directly from the quasi-particle excitation spectrum of the Bogoliubov-de Gennes (BdG) equation, by exploiting the scattering matrix formalism.

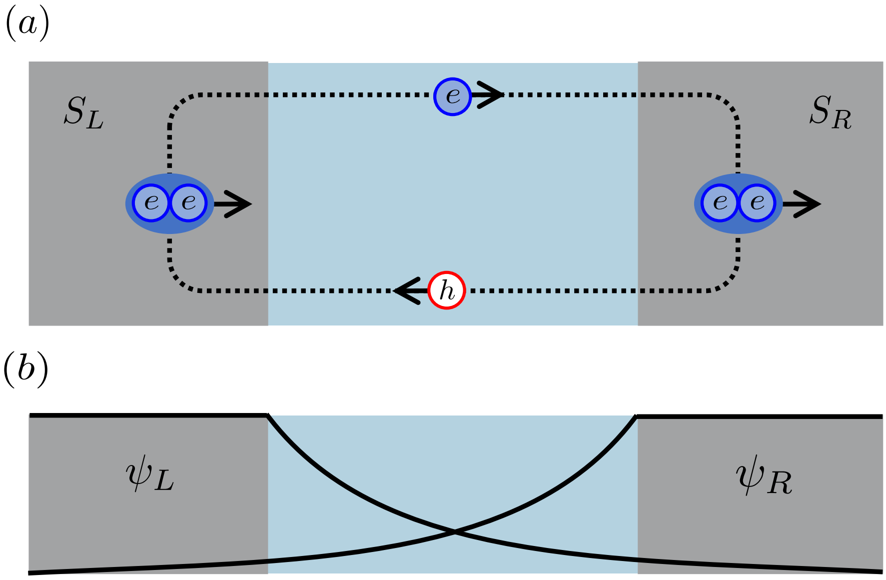

FIGURE 6.1: (a) - Formation of Andreev levels in a Josephson junction. An electron e and the Andreev-reflected hole h are shown. A Cooper pair of correlated electrons is transferred from the left superconductor S_L to the right one S_R, creating a supercurrent flow across a junction. (b) - ψ_L and ψ_R represent the left and right pair wavefunctions.

6.1 Phenomenological Aspects

After the pioneering work by London [London1935], the theory of Ginzburg and Landau [Ginzburg-Landau1950] (developed to describe second order phase transitions), provided an enormous insight into the nature of superconductivity as a quantum phenomenon on a macroscopic scale. Central to this theory was the introduction of the concept of a position dependent order parameter, $\psi(\mathbf{r})$, which gives a measure of the order in the superconducting state. Such an order parameter, which is proportional to the local value of the energy gap function $\Delta(\mathbf{r})$, is complex and can be regarded as a wave function for superconducting electrons [Barone1982].

In this framework $\psi(\mathbf{r})$ is associated with a macroscopic number of electrons which are assumed to "condense" in the same quantum state. In this sense, the superconductive state can be regarded as a "macroscopic quantum state". Therefore we are dealing with particles, having effective mass and charge m^* and e^*, respectively, which can be described as a "whole" by a macroscopic wave function of the form

$$\psi(\mathbf{r}) = |\psi(\mathbf{r})|e^{i\phi(\mathbf{r})} \tag{6.2}$$

where ϕ is the phase common to all the particles and $|\psi(\mathbf{r})|^2$ represents the density in the macrostate. The electric current density can be obtained as the functional derivative of free energy F with respect to the vector potential $\boldsymbol{A}$

$$\boldsymbol{J}(\boldsymbol{r}) = c\frac{\delta F}{\delta \boldsymbol{A}(\boldsymbol{r})} \tag{6.3}$$

where c the speed of light. In other words $\boldsymbol{J}(\boldsymbol{r})$ is the variable conjugate to $\boldsymbol{A}(\boldsymbol{r})$. By explicit calculation the current density takes the expression [Ketterson1999]

$$\boldsymbol{J}(\boldsymbol{r}) = \frac{ie^*\hbar}{2m^*}\left[\psi(\mathbf{r})\nabla\psi(\mathbf{r})^* - \psi(\mathbf{r})^*\nabla\psi(\mathbf{r})\right] - \frac{e^{*\,2}}{m^*c}|\psi(\mathbf{r})|^2\boldsymbol{A}(\boldsymbol{r}) \tag{6.4}$$

which corresponds to the standard result of the current density in quantum mechanics. As obtained within the framework of the microscopic theory of superconductivity [BCS1957], the charge e^* is twice the electronic charge e, reflecting the fact that the "particles" we are dealing with are in fact Cooper pairs of coupled electrons. Here we also assume $m^* = 2m$ with m the electronic mass. Thus with the $\psi(\mathbf{r})$ given by Eq. (6.2) the expression for $\boldsymbol{J}(\boldsymbol{r})$ becomes

$$\boldsymbol{J}(\boldsymbol{r}) = \frac{e\hbar}{m}|\psi(\mathbf{r})|^2\left[\nabla\phi - \frac{2e}{\hbar c}\boldsymbol{A}(\boldsymbol{r})\right]. \tag{6.5}$$

Gauge invariance requires that under the transformation of the vector potential $\boldsymbol{A}$

$$\boldsymbol{A} \to \boldsymbol{A} + \nabla\chi \tag{6.6}$$

and scalar potential V

$$V \to V - \frac{1}{c}\frac{\partial}{\partial t}\chi \tag{6.7}$$

the observable physical quantities remain unchanged (being $\chi(\boldsymbol{r}, t)$ an arbitrary single valued function) [Ketterson1999]. We recall that such potentials are respectively related to the magnetic field $\boldsymbol{B} = \nabla \times \boldsymbol{A}$ and the electric field $\boldsymbol{E} = -\nabla V - (1/c)(\partial\boldsymbol{A}/\partial t)$. As can be readily verified from the expression of current density $\boldsymbol{J}$, Eqs. (6.6) and (6.7) imply the following phase transformation

$$\phi \to \phi + \frac{2e}{\hbar c}\chi. \tag{6.8}$$

The choice of constant values for the scalar function χ does not affect potentials, but implies different values of the phase factor ϕ. This means that the total phase of the sample as a whole is not physical, and thus meaningless. What is meaningful to discuss, instead, is the *relative* phase that can be established between two superconducting blocks S_L and S_R which are connected by an insulating barrier. If the insulating barrier is sufficiently thin between S_L and S_R, then Cooper pairs can flow from one superconductor to the other (Josephson tunneling). The appearance of such a supercurrent flowing between two weakly couple superconductors with a given phase difference is the basis of the Josephson effect. In the following section, we set the basic equations for the Josephson effect in tunneling junctions and introduce some general peculiar features which characterize the Josephson phenomena.

6.2 Josephson equations

The two-level system approach

It is possible to follow several different approaches in order to obtain the basic Josephson relations. A very simple derivation is based on a phenomenological "two level system" picture [Feynman1965]. As mentioned in the previous section, let us consider two superconducting blocks S_L and S_R connected by an insulating barrier sufficiently thin for tunneling to occur. Each superconducting electrode can be described by a single quantum state ψ_L and ψ_R which can be regarded as the macroscopic wave functions for the left and right superconductor respectively. We indicate with the ket $|L\rangle$ ($|R\rangle$) the basis state for the left (right) superconductor so that

$$|\psi_L|^2 = \langle L|\, \psi_L^* \psi_L \,|L\rangle\,; \qquad\qquad |\psi_R|^2 = \langle R|\, \psi_R^* \psi_R \,|R\rangle \tag{6.9}$$

represent the actual Cooper pair density in the two superconducting blocks. Because of the weak coupling existing between the two superconductors, "transitions" between the two states $|L\rangle$ and $|R\rangle$ can occur. This coupling is related to the finite overlap of the two pair wave functions ψ_L and ψ_R as schematically depicted in Fig. 6.1(b). The state vector which describes the junction can be written as

$$|\psi\rangle = \psi_L \,|L\rangle + \psi_R \,|R\rangle \tag{6.10}$$

i. e. the particle can be either in a "left" or "right" state with amplitude ψ_L or ψ_R respectively. The time evolution of the system is described by the Schrödinger equation:

$$i\hbar\frac{\partial}{\partial t}\,|\psi\rangle = H\,|\psi\rangle \tag{6.11}$$

with the Hamiltonian given by

$$H = H_L + H_R + H_T \tag{6.12}$$

where $H_L = E_L\,|L\rangle\,\langle L|$ and $H_R = E_R\,|R\rangle\,\langle R|$ refer to the unperturbed superconductors with ground state energies E_L and E_R respectively. The tunneling Hamiltonian takes the following form

$$H_T = K\left(|L\rangle\,\langle R| + |R\rangle\,\langle L|\right) \tag{6.13}$$

and describes the interaction term between the states $|L\rangle$ and $|R\rangle$. Here K is the coupling amplitude of the two state system which can be assumed real in absence of a vector potential $\boldsymbol{A}$. As can be seen from the microscopic theory [Gorkov1959], in the two isolated superconductors, the energy terms $E_L = 2\mu_L$ and $E_R = 2\mu_R$ are equal to twice the electrochemical potentials μ_L and μ_R. These values represent the minimum energy required to add a Cooper pair to S_L and S_R respectively. Thus if we consider a d.c. potential difference V across the junction these chemical potentials are shifted by an amount eV and consequently it is $E_L - E_R = 2eV$. Therefore, by choosing the zero of the energy halfway between the two values on the right and on the left, and taking projections on the two base states of the Schrödinger equation (6.11), we can write

$$\begin{cases} i\hbar\dfrac{\partial}{\partial t}\psi_L = eV\psi_L + K\psi_R \\ i\hbar\dfrac{\partial}{\partial t}\psi_R = -eV\psi_L + K\psi_L \end{cases} \tag{6.14}$$

By substituting $\psi_L = |\psi_L|e^{i\phi_L}$ and $\psi_R = |\psi_R|e^{i\phi_R}$, and separating real and imaginary parts in both Eqs. (6.14) we get

$$\begin{cases} \dfrac{\partial}{\partial t}|\psi_L|^2 = \dfrac{2K}{\hbar}|\psi_L||\psi_R|\sin(\phi) \\ \dfrac{\partial}{\partial t}|\psi_R|^2 = -\dfrac{2K}{\hbar}|\psi_L||\psi_R|\sin(\phi) \end{cases} \qquad \begin{cases} \dfrac{\partial}{\partial t}\phi_L = \dfrac{K}{\hbar}\dfrac{|\psi_L|}{|\psi_R|}\cos(\phi) + \dfrac{eV}{\hbar} \\ \dfrac{\partial}{\partial t}\phi_R = \dfrac{K}{\hbar}\dfrac{|\psi_L|}{|\psi_R|}\cos(\phi) - \dfrac{eV}{\hbar} \end{cases} \tag{6.15}$$

where we introduced the phase difference

$$\phi = \phi_L - \phi_R. \tag{6.16}$$

The pair density current is simply defined as $J = e\frac{\partial}{\partial t}|\psi_L|^2 = -e\frac{\partial}{\partial t}|\psi_R|^2$, and thus from Eqs. (6.15) it follows that

$$J = \frac{2Ke}{\hbar}|\psi_L||\psi_R|\sin{(\phi)}. \tag{6.17}$$

Then, if we assume that both sides of the junction are prepared from the same kind of superconducting material, i. e. $|\psi_L| = |\psi_R| = |\psi|$, we finally obtain the current-phase relation

$$J = J_C \sin{(\phi)} \tag{6.18}$$

where $J_C = \frac{2Ke}{\hbar}|\psi|^2$ is the critical current and corresponds to the maximum current density that may be carried by the junction.

a.c. d.c. Josephson effect

It is easy to see that from Eqs. (6.15), it holds the following important voltage-phase relation

$$\frac{\partial}{\partial t}\phi = \frac{2e}{\hbar}V \tag{6.19}$$

which defines the time evolution of the phase difference ϕ under the application of the d.c. potential V. Here we notice that the same relation can be obtained also from a general gauge invariance argument by combining Eqs. (6.7) and (6.8). Notably, if $V = 0$, the phase difference ϕ results to be constant and not necessarily zero, so that a finite current density can flow through the barrier with zero voltage drop across the junction. This is the essence of the so called d.c. Josephson effect [Josephson1962, Josephson1964]. If, instead, we apply a constant (time-independent) voltage $V \neq 0$, it follows by integration of Eq. (6.19) that the phase ϕ varies in time as

$$\phi = \phi_0 + \frac{2e}{\hbar}Vt \tag{6.20}$$

which leads to the appearance of an alternating current

$$J = J_C \sin\left(\phi_0 + \frac{2e}{\hbar}Vt\right) \tag{6.21}$$

which oscillates with a frequency $\omega_J = 2eV/\hbar$. This is called the a.c. Josephson effect.

Magnetic field effects

Let us examine now the Josephson effect in the presence of a magnetic field $\boldsymbol{B}$ described by the vector potential $\boldsymbol{A}$ such that $\boldsymbol{B} = \nabla \times \boldsymbol{A}$. In this case, a similar gauge-invariant form analogous to Eq. (6.19), can be obtained for the the vector potential. Indeed, by comparing Eqs. (6.6) and (6.8), we get the following relation

$$\nabla\phi = \frac{2e}{\hbar c}\boldsymbol{A}. \tag{6.22}$$

Therefore, from Eq. (6.22), the gauge-invariant phase difference is given by

$$\phi = \phi_0 + \frac{2\pi}{\Phi_0}\int_{l}^{r} \boldsymbol{A} \cdot d\boldsymbol{\ell} \tag{6.23}$$

where $\Phi_0 = hc/2e$ is the flux quantum, and the integral is taken across the barrier between two points $\boldsymbol{l}$ on the interface with the left superconductor and $\boldsymbol{r}$ on the interface with the right one.

By combining the gauge-invariant phase relation of Eq. (6.22) together with the phase relation of Eq. (6.19) and the voltage-phase relation of Eq. (6.18), we obtain the fundamental equations governing the behavior of Josephson junctions

$$\begin{cases} J = J_C \sin\left(\phi - \dfrac{2\pi}{\Phi_0}\displaystyle\int_l^r \boldsymbol{A}\cdot d\boldsymbol{\ell}\right) \\ \dfrac{\partial}{\partial t}\left(\phi - \dfrac{2\pi}{\Phi_0}\displaystyle\int_l^r \boldsymbol{A}\cdot d\boldsymbol{\ell}\right) = \dfrac{2eV}{\hbar} \end{cases} . \tag{6.24}$$

Doppler shift effect

Another important effects which emerges in Josephson junctions under the application of an external magnetic field is the so-called Doppler shift effect [Tkachov2015]. In order to discuss this effect, we consider a 2D junction lying on the x-y plane with a constant magnetic field applied along the (negative) z direction as depicted in Fig. 6.2. The gauge invariant phase shifts may be obtained by integrating Eq. (6.22) around the closed path C (see the dotted contour in Fig. 6.2). Noting that $\nabla\phi$ is a multivalued function that can change by $2\pi n$ upon completing the path, we obtain

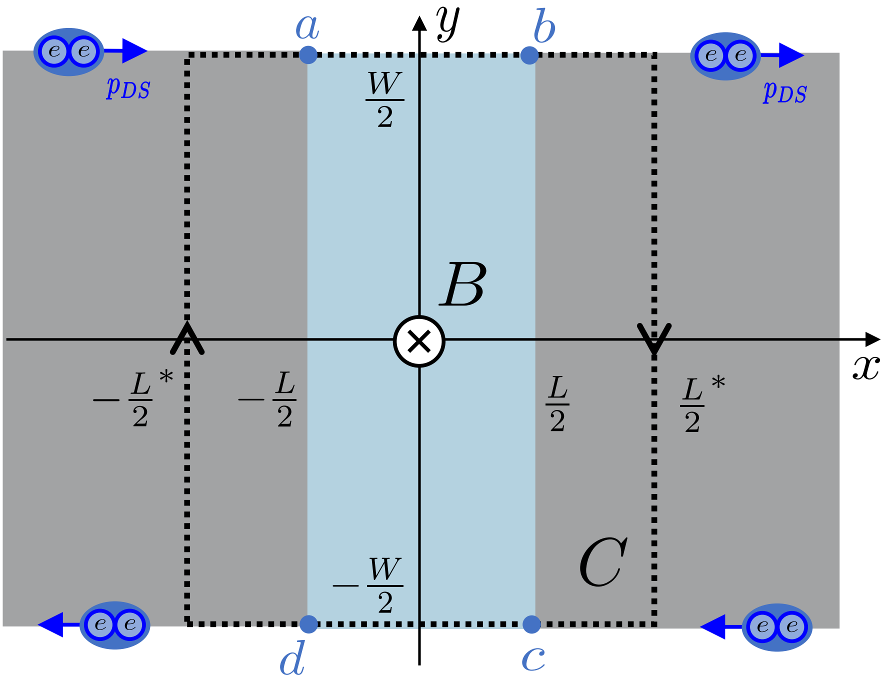

FIGURE 6.2: Schematic of a 2D Josephson junctions lying on the x-y plane with a constant magnetic field B applied along the (negative) z direction. The path of integration C is shown by the dotted line. Blue arrows indicate the Doppler shift momentum acquired by Copper pairs inside the superconductors.

$$\oint_C \nabla\phi \cdot d\boldsymbol{\ell} = (\phi_b - \phi_a) + (\phi_c - \phi_b) + (\phi_d - \phi_c) + (\phi_a - \phi_d) = 2\pi n \tag{6.25}$$

where n is the integer winding number of the order parameter phase. By using Eq. (6.23), the phase differences across the upper and lower edges of the junction are given by

$$\phi_b - \phi_a = \phi_u + \frac{2\pi}{\Phi_0} \int_a^b \boldsymbol{A} \cdot d\boldsymbol{\ell} \tag{6.26}$$

and

$$\phi_d - \phi_c = -\phi_l + \frac{2\pi}{\Phi_0} \int_c^d \boldsymbol{A} \cdot d\boldsymbol{\ell} \tag{6.27}$$

where we indicated with ϕ_u and ϕ_l the gauge-invariant phase shifts associated to the upper and lower edge of the junction. The second and fourth terms in Eq. (6.25) are phase differences inside the superconducting leads and are found by using the formula for the supercurrent of Eq. (6.5)

$$\phi_c - \phi_b = \int_b^c \nabla\phi \cdot d\boldsymbol{\ell} = \frac{2\pi}{\Phi_0} \int_b^c \left(\boldsymbol{A} + \frac{4\pi\lambda_L^2}{c} \boldsymbol{J} \right) \cdot d\boldsymbol{\ell} \tag{6.28}$$

and

$$\phi_a - \phi_d = \int_d^a \nabla\phi \cdot d\boldsymbol{\ell} = \frac{2\pi}{\Phi_0} \int_d^a \left(\boldsymbol{A} + \frac{4\pi\lambda_L^2}{c} \boldsymbol{J} \right) \cdot d\boldsymbol{\ell} \tag{6.29}$$

where we introduced the London penetration depth $\lambda_L = \sqrt{mc^2/4\pi|\psi|^2 e^2}$. Substituting the above four equations in Eq. (6.25), we obtain

$$\phi_u - \phi_l = 2\pi n + \frac{2\pi}{\Phi_0} \oint_C \boldsymbol{A} \cdot d\boldsymbol{\ell} + \frac{8\pi^2\lambda_L^2}{\Phi_0 c} \int_{C'} \boldsymbol{J} \cdot d\boldsymbol{\ell}. \tag{6.30}$$

The integration of $\boldsymbol{J}$ is taken over a path C' which excludes the insulator. By assuming the thickness d of the superconducting films along the z direction larger than the London penetration depth [Ketterson1999], the integration path can be taken deep inside the superconductors where the integral involving the supercurrent density is negligible. The integration of $\boldsymbol{A}$ is around a complete closed path C and is equal to the total flux Φ inside the area enclosed by the contour. We emphasize that the magnetic flux through the effective junction area L^*W (Fig. 6.2), depends on the screening properties of the leads. However, if the Pearl length $\lambda_P = 2\lambda_L^2/d \ll 1$ (as in the case of a thick superconducting film), we can chose $L^* = L$, which gives a flux $\Phi = LWB$. The phase difference is then simply related to the total flux by

$$\phi_u - \phi_l = 2\pi n + 2\pi \frac{\Phi}{\Phi_0}. \tag{6.31}$$

Alternatively, by taking ϕ_0 (the gauge invariant shift phase at the middle of the junction, i. e. $y = 0$) as a reference, and by neglecting the unobservable phase difference of $2\pi n$, we can recast Eq. (6.31) in the form

$$\begin{cases} \phi_u = \phi_0 + \pi \dfrac{\Phi}{\Phi_0} \\ \phi_l = \phi_0 - \pi \dfrac{\Phi}{\Phi_0} \end{cases} \tag{6.32}$$

namely, we can obtain the gauge invariant phase differences ϕ_u and ϕ_l at the opposite edges of the junction $y = \pm W/2$ by simply changing $\Phi \to -\Phi$.

Together with the appearance of a local gradient of the superconducting phase difference, the presence of the magnetic field induces a momentum-shift of the Cooper pairs inside the superconductors [Ketterson1999]

$$\boldsymbol{p} \to \boldsymbol{p} - \frac{2e}{c}\boldsymbol{A} \tag{6.33}$$

where the factor $2e$ account for the charge of the coupled electrons inside the condensate. Using the gauge $\boldsymbol{A}(y) = (-yB, 0, 0)$, and assuming W much larger than the transverse dimension L of the junction, the vector potential acting on the superconducting edge states can be approximated by its boundary value $A(\pm W/2) \approx \mp BW/2$. This results in a finite Cooper-pair momentum-shift along the edge

$$p_{DS}(\Phi) \equiv -\frac{2e}{c}A_x(\pm W/2) = \pm\frac{\pi\hbar}{L}\frac{\Phi}{\Phi_0} \tag{6.34}$$

also called Doppler shift momentum, where ± correspond to the upper and lower edge respectively (see Fig. 6.2) [Tkachov2015].

6.3 Josephson current from Scattering Formalism

In the present section we describe how the Josephson current can be obtained directly from the quasi-particle excitation spectrum of the Bogoliubov-de Gennes (BdG) equation.

As we have already seen in Chap. 3, the BdG equation consist of two Schrödinger equations for electron and hole wavefunctions $u(\boldsymbol{r})$ and $v(\boldsymbol{r})$, coupled by the pair potential $\Delta(\boldsymbol{r})$

$$\begin{pmatrix} H & \Delta \\ \Delta^* & -H^* \end{pmatrix}\begin{pmatrix} u \\ v \end{pmatrix} = \epsilon\begin{pmatrix} u \\ v \end{pmatrix}. \tag{6.35}$$

Here the excitation energy ϵ is measured relative to the chemical potential μ and $H = (\boldsymbol{p} + e\boldsymbol{A})^2/2m + V - \mu$ is the single-electron Hamiltonian in the field of a vector potential $\boldsymbol{A}(\boldsymbol{r})$ and electrostatic potential $V(\boldsymbol{r})$. In a uniform system with $\Delta(\boldsymbol{r}) = \Delta e^{i\phi}$, $\boldsymbol{A}(\boldsymbol{r}) = 0$, $V(\boldsymbol{r}) = 0$, the solution of the BdG equations correspond to the QPs and QHs plane wave eigenfuctions already introduced in Sec. 3.3. As we have seen, the excitation spectrum is continuous and characterized by an excitation gap Δ. This simple excitation spectrum, however, is modified in presence of a Josephson junction. In such a situation, the spectrum acquires a discrete part due to the non-uniformities in $\Delta(\boldsymbol{r})$ near the junction. The discrete spectrum corresponds to bound states in the gap ($0 < \epsilon < \Delta$), localized within a coherence length ξ from the junction, which take the name of Andreev bound states (ABS).

Supercurrent from Excitation Spectrum

By recalling Eqs. (6.3) and (6.22), we can express the equilibrium Josephson current as the derivative of the free energy F with respect to the phase difference ϕ [Anderson1964]

$$\boldsymbol{J} = \frac{2e}{\hbar}\frac{\partial F}{\partial \phi}. \tag{6.36}$$

Notice that the derivative is to be taken without varying the vector potential $\boldsymbol{A}$. To apply this relation we need to know how to obtain F from the BdG equations [Beenakker2006]. As follows from its definition [DeGennes1966], the free energy takes the following form

$$F = U - TS \tag{6.37}$$

where T is the temperature, and S is the entropy of the independent fermionic excitations, which can be written as

$$\begin{aligned} S &= -2k_B \sum_{\epsilon>0} \left[f \ln f + (1-f) \ln (1-f) \right] \\ &= -2k_B \sum_{\epsilon>0} \left[\ln f + (1-f)\, \epsilon / k_B T \right]. \end{aligned} \tag{6.38}$$

The energy U takes the following form

$$U = \langle H \rangle + U_{int} \tag{6.39}$$

and is the sum of the single-particle energy $\langle H \rangle$ and the interaction potential energy

$$U_{int} = -\int d\boldsymbol{r} |\Delta|^2 / g \tag{6.40}$$

which is negative, since the interaction is attractive (here g is the interaction constant of the BCS theory [BCS1957]). In order to compute the single-particle energy $\langle H \rangle$, we recall that the equilibrium average of a generic single-electron operator $\mathcal{P}$ takes the following form [Beenakker2005]

$$\langle \mathcal{P} \rangle = 2 \sum_{\epsilon>0} \int d\boldsymbol{r} f(\epsilon) u^* \mathcal{P} u + \left[1 - f(\epsilon)\right] v \mathcal{P} v^*. \tag{6.41}$$

Notice the reverse order, $u^* \mathcal{P} u$ versus $v \mathcal{P} v^*$, and the different thermal weight factors, $f(\epsilon)$ for electrons and $f(-\epsilon) = 1 - f(\epsilon)$ for holes. The prefactor of 2 accounts for spin degeneracy (assuming that $\mathcal{P}$ does not couple to the spin). Thus, by using Eqs. (3.11), (6.35) and (6.41) we obtain for the single particle energy the expression

$$\langle H \rangle = \sum_{\epsilon>0} \left[f\epsilon + \epsilon (1-f) \right] - 2U_{int} + \sum_{\epsilon>0} \epsilon \int d\boldsymbol{r} \left(|u|^2 - |v|^2 \right). \tag{6.42}$$

By making use of the completeness of the set of eigenfunctions (u, v) [Bardeen1969], the last term of the above equation can be written as follow:

$$\sum_{\epsilon>0} \epsilon \int d\boldsymbol{r} \left(|u|^2 - |v|^2 \right) = \frac{1}{2} \sum_{\epsilon} \int d\boldsymbol{r} \left(u^* H u + v^* H^* v \right) = \frac{1}{2} \operatorname{Tr} \begin{pmatrix} H & 0 \\ 0 & H^* \end{pmatrix} = \operatorname{Tr} H \tag{6.43}$$

Collecting results, the expression for the free energy becomes

$$F = -2k_B \sum_{\epsilon>0} \ln \left[2 \cosh \left(\epsilon / 2k_B T \right) \right] + \int d\boldsymbol{r} |\Delta|^2 / g + \operatorname{Tr} H. \tag{6.44}$$

The first term (the sum over ϵ) can be formally interpreted as the free energy of non-interacting electrons, all of one single spin, in a "semiconductor" with Fermi level halfway between the "conduction band" (positive ϵ) and the "valence band" (negative ϵ) [Beenakker2005]. The second term (corresponding to $-U_{int}$) corrects for a double-counting of the interaction energy in the semiconductor model. The third term ($\operatorname{Tr} H$) cancels a divergence at large ϵ of the series in the first term.

In conclusion, by substituting F into Eq. (6.36), we obtain the required expression for the Josephson current:

$$\boldsymbol{J} = -\frac{2e}{\hbar}\sum_p \tanh\left(\epsilon_p/2k_BT\right)\frac{d\epsilon_p}{d\phi} - \frac{2e}{\hbar}2k_BT\int_{\Delta_0}^{\infty} d\epsilon \ln\left[2\cosh\left(\epsilon/2k_BT\right)\right]\frac{d\rho}{d\phi} + \frac{2e}{\hbar}\frac{\partial}{\partial\phi}\int d\boldsymbol{r}|\Delta|^2/g \tag{6.45}$$

where the sum is over discrete positive eigenvalues ϵ_p, and an integration over the continuous spectrum with density of states $\rho(\epsilon)$. Notice that, the term $\operatorname{Tr} H$ in Eq. (6.44) does not depend on ϕ, and therefore does not contribute to the current. The spatial integral of $|\Delta|^2/g$ does contribute in general. However, if rigid boundary condition holds for the gap order parameter (see the discussion below), Δ can be considered independent of ϕ so that this contribution can be disregarded. A calculation of the Josephson current from Eq. (6.45) then requires only knowledge of the eigenvalues. In the following we show how to relate the excitation spectrum of Bogoliubov quasiparticles to the scattering matrix of normal electrons.

6.4 Excitation spectrum from scattering matrix

So far we have seen that, from Eq. (6.45), the Josephson current can be fully obtained from the excitation spectrum of the BdG Hamiltonian. In the following section we will show how to compute the excitation spectrum of a Josephson junction by exploiting the scattering matrix formalism [Beenakker1991]. In order to do that, let us now consider an SNS junction as depicted in Fig. 6.3. It consists of a disordered normal region sandwiched between two superconducting leads S_L and S_R with interfaces located at $x = \pm L/2$. To obtain a well-defined scattering problem (see Chap. 4) we insert ideal (impurity-free) normal leads L and R to the left and right of the disordered region. The leads should be long compared to the Fermi wavelength λ_F, but short compared to the coherence length ξ [Beenakker2006].

Moreover, we let $\Delta(\boldsymbol{r}) \to \Delta e^{\mp i\phi/2}$ deep inside the superconducting bulk (for $x \to \pm\infty$), and $\Delta(\boldsymbol{r}) = 0$ for $|x| < L/2$ inside the normal region. As discussed in Chap. 3, in general, to determine $\Delta(\boldsymbol{r})$ near the junction one has to solve the self-consistency equation (see Eq. (3.11)). However, if the width W of the junction is small compared to the coherence length, the non-uniformities in $\Delta(\boldsymbol{r})$ extend only over a distance of order W from the junction. Since non-uniformities on length scales $\ll \xi$ do not affect the dynamics of the quasiparticles, these can be neglected [Likharev1979]. Under this assumption one can safely use the "rigid boundary-condition" (also referred as "step-function model") for the gap order parameter

$$\Delta(\boldsymbol{r}) = \begin{cases} \Delta e^{i\phi/2} & \text{for} \quad x < -L/2, \\ 0 & \text{for} \quad |x| < L/2, \\ \Delta e^{-i\phi/2} & \text{for} \quad x > L/2. \end{cases} \tag{6.46}$$

Such an approximation is justified if the resistivity of the junction region is much bigger than the resistivity of the bulk superconductor [Kupriyanov1982].

We first construct a basis for the scattering matrix in the normal region s_N. A wave incident on the disordered normal region is described by a vector of coefficients (in the basis of Eq. (3.32))

$$c_N^{in} \equiv \left(c_L^+, c_R^-, b_L^+, b_R^-\right)^T \tag{6.47}$$

as schematically shown in Fig.(6.3). We indicate with $c^{\pm}_{L/R}/b^{\pm}_{L/R}$ the incoming electrons/holes in the N region, with L/R labeling the left/right lead and $\pm$ indicating the direction of

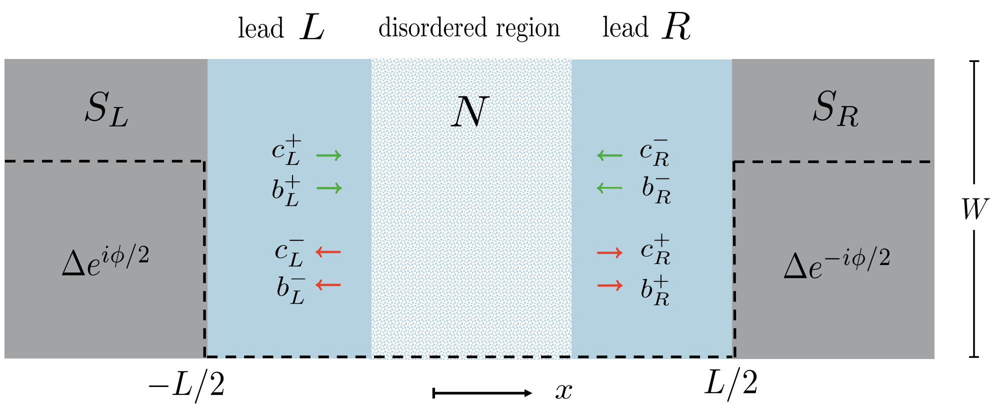

FIGURE 6.3: Josephson junction containing a disordered normal region N. Scattering states in the normal leads L and R are indicated schematically. Rigid boundary conditions are assumed for the gap order parameter.

propagation of particles along the x axis ($+$ for right movers and $-$ for left movers). The scattered wave has vector of coefficients

$$c_N^{out} \equiv \left(c_L^-, c_R^+, b_L^-, b_R^+\right)^T. \tag{6.48}$$

The scattering matrix s_N of the disordered normal region relates these two vectors, namely

$$c_N^{out} = s_N c_N^{in}. \tag{6.49}$$

Because the normal region does not couple electrons and holes, this matrix has a block-diagonal form

$$s_N(\epsilon) = \begin{pmatrix} s_0(\epsilon) & \emptyset \\ \emptyset & s_0(-\epsilon)^* \end{pmatrix}, \quad s_0 \equiv \begin{pmatrix} r & t \\ t' & r' \end{pmatrix}. \tag{6.50}$$

Here s_0 is the unitary scattering matrix associated with the single electron Hamiltonian H of Eq. (6.35). By assuming for simplicity that the number of modes in leads L and R is the same, the reflection and transmission matrices $r(\epsilon)$, $r'(\epsilon)$ and $t(\epsilon)$, $t'(\epsilon)$ are $N \times N$ matrices, with $N(\epsilon)$ being the number of propagating modes at energy ϵ (see also Sec. 4.2).

For energies $0 < \epsilon < \Delta$ there are no propagating modes in the superconducting leads S_L and S_R. We assume also that the only scattering at the interfaces with superconductors consists of perfect Andreev reflections, i.e. we consider the case that the disorder is contained entirely within the normal region. We can then define an scattering matrix s_A for Andreev reflection at the SN interfaces by

$$c_N^{in} = s_A c_N^{out}. \tag{6.51}$$

The elements of s_A can be obtained by matching the wavefunctions at $x = \pm L/2$ as we already discussed in Sec. 3.4. In the case of ideal interface and within the Andreev approximation, i. e. $\epsilon, \Delta \ll \mu$, we can write

$$s_A(\epsilon) \equiv \alpha(\epsilon)\tilde{s_A} = \alpha(\epsilon)\begin{pmatrix} \emptyset & r_A \\ r_A^* & \emptyset \end{pmatrix}; \quad r_A \equiv \begin{pmatrix} e^{-i\phi/2}\mathbb{1} & \emptyset \\ \emptyset & e^{i\phi/2}\mathbb{1} \end{pmatrix} \tag{6.52}$$

where $\alpha(\epsilon) = \exp\left[-i \arccos\left(\epsilon/\Delta\right)\right]$. Here we explicitly divided s_A in two contributions: a phase shift $-\arccos\left(\epsilon/\Delta\right)$ due to the penetration of the wavefunction into the superconductor, and a phase shift (included in $\tilde{s_A}$) equal to $\pm$ the phase of the pair potential in the superconductor ($+$ for reflection from hole to electron, $-$ for the reverse process).

For supra-gap energies $\epsilon > \Delta$ we can define the scattering matrix s_{SNS} of the whole junction, by $c_S^{out} = s_{SNS} c_S^{in}$, where we introduced the vector of coefficients

$$c_S^{in} \equiv \left(\tilde{c}_L^{+}, \tilde{c}_R^{-}, \tilde{b}_L^{+}, \tilde{b}_R^{-}\right)^T \tag{6.53}$$

$$c_S^{out} \equiv \left(\tilde{c}_L^{-}, \tilde{c}_R^{+}, \tilde{b}_L^{-}, \tilde{b}_R^{+}\right)^T \tag{6.54}$$

where, similarly to Eqs. (6.47) and (6.48), we indicate with $\tilde{c}^{\pm}_{L/R}/\tilde{b}^{\pm}_{L/R}$ the incoming and outgoing QPs/QHs inside the superconducting reservoirs S_L and S_R. Also in this case, by matching the wavefunctions at $x = \pm L/2$, and using again the Andreev approximation, we can write

$$s_{SNS} = U^{-1} \left(\mathbb{1} - M\right)^{-1} \left(\mathbb{1} - M^{\dagger}\right) s_N U \tag{6.55}$$

$$U = \begin{pmatrix} \emptyset & r_A \\ r_A^* & \emptyset \end{pmatrix}^{\frac{1}{2}}, \quad M = s_A s_N . \tag{6.56}$$

The three matrices $s_N(\epsilon)$, $s_A(\epsilon)$ and $s_{SNS}(\epsilon)$ defined above are all unitary ($s^{\dagger}s = ss^{\dagger} = \mathbb{1}$) and satisfy the symmetry relation $s_{ij}(\epsilon, \phi) = s_{ji}(\epsilon, -\phi)$, as required by quasiparticle-current conservation and by time-reversal invariance, respectively.

We are now ready to relate the excitation spectrum of the Josephson junction to the scattering matrix of the normal region. Regarding the discrete spectrum, by combining Eqs. (6.49) and (6.52), we obtain the condition

$$c_N^{in} = s_A s_N c_N^{in} \tag{6.57}$$

which, for a bound state, implies the following secular equation

$$\mathrm{Det}(\mathbb{1} - s_A(\epsilon_p) s_N(\epsilon_p)) = 0. \tag{6.58}$$

Analogously the density of states of the continuous spectrum is related to s_{SNS} by the general relation [Akkermans1991]

$$\frac{\partial \rho}{\partial \phi} = -\frac{1}{\pi} \frac{\partial^2}{\partial \phi \partial \epsilon} \mathrm{Im} \ln \mathrm{Det}(\mathbb{1} - s_A(\epsilon_p) s_N(\epsilon_p)). \tag{6.59}$$

Short-Junction Limit

In the short-junction limit $L \ll \xi$ when $\Delta \ll \epsilon_c$ (here $\epsilon_c \equiv \hbar/\tau_{dwell}$ is the correlation energy in terms of the dwell time τ_{dwell} in the junction) we may approximate $s_0(\epsilon) \approx s_0(-\epsilon) \equiv s_0$. In this regime, for $\epsilon > \Delta$, α is real (see Sec. 3.4) and so is the determinant $\mathrm{Det}(\mathbb{1} - s_A(\epsilon_p) s_N(\epsilon_p))$ of Eq. (6.58). In this case Eq. (6.59) reduces to $\partial\rho/\partial\phi = 0$, from which we conclude that the continuous spectrum does not contribute to the Josephson current. Therefore the expression of the Josephson current of Eq. (6.45), in the regime of short-junction and with rigid boundary conditions simply reduces to

$$J = -\frac{2e}{\hbar} \sum_p \tanh\left(\frac{\beta}{2}\epsilon_p\right) \frac{d\epsilon_p}{d\phi} \tag{6.60}$$

(where $\beta = 1/k_B T$) for those ϵ_p which satisfy Eq. (6.58) . In particular it can be shown that Eq. (6.58) can be solved for ϵ_p, in the short-junction limit, in terms of the eigenvalues $0 \leq T_p \leq 1$ (with $p = 1, 2, \ldots N$) of the hermitian $N \times N$ matrix $tt^{\dagger}$ (or $t't'^{\dagger}$)

$$\epsilon_p = \Delta \sqrt{1 - T_p \sin\left(\phi/2\right)^2} \tag{6.61}$$

Substitution of Eq. (6.61) into Eq. (6.60) yields the Josephson current

$$J(\phi) = \frac{e\Delta}{2k_B} \sum_{p=1}^{N} \frac{T_p \sin(\phi)}{\sqrt{1 - T_p \sin^2(\phi/2)}} \tanh\left(\frac{\Delta\beta}{2}\sqrt{1 - T_p \sin^2(\phi/2)}\right). \tag{6.62}$$

Notice that, the above equation holds for an arbitrary transmission matrix $tt^\dagger$, i.e. for arbitrary disorder potential. A formula of similar generality for the conductance is the multi-channel Landauer formula already introduced in Eq. (4.22). It is important to notice that, in contrast to the Landauer formula, Eq. (6.62), is a non-linear function of the transmission eigenvalues T_p. It follows that knowledge of the conductance (i.e. of the sum of the eigenvalues) is not sufficient to determine the supercurrent.

Part II

Original Results

7

Nonlocal Thermoelectricity in a S-TI-S Junction with a Metal Probe: Evidence for Helical Edge States

This chapter is based on the results published in the paper:
G. Blasi, F. Taddei, L. Arrachea, M. Carrega, and A. Braggio. *Nonlocal Thermoelectricity in a Superconductor–Topological-Insulator–Superconductor Junction in Contact with a Normal-Metal Probe: Evidence for Helical Edge States.* Phys. Rev. Lett., **124**(22) 227701 (2020).

Quantum spin Hall systems in 2DTIs are receiving a lot of attention [Moore2009, Hasan2010, Qi2011, Ando2013] due to their non-trivial topological properties. As we discussed in Chap. 2, the clearest signature of the quantum spin Hall phase is the existence of Kramers pairs of helical edge states, which propagate in opposite directions with opposite spin orientations (spin-momentum locking) [Tkachov2015a]. After the pioneering theoretical ideas [Kane2005, Kane2005a, BHZ2006] and experimental realizations in HgTe quantum wells [Konig2007, Roth2009, Brune2012], other platforms to realize this topological phase, preserving time-reversal symmetry, have been proposed in different materials [Tang2017, Jia2017, Reis2017, Li2018, Wu2018, Shi2019, Liu2020]. In HgTe the helical nature of the edge states is commonly probed by means of nonlocal transport measurements in a Hall bar geometry with four or more terminals [Konig2007, Roth2009, Brune2012] and quantum point contacts [Citro2011, Ronetti2016, Ronetti2017]. This can be very hard to implement in some other systems, where evidence is shown on the existence of edge states but not yet on their helical nature [Tang2017, Jia2017, Reis2017, Wu2018, Li2018, Shi2019, Liu2020].

When the Kramers pairs of helical edge states are embedded in a superconducting junction, the Andreev states inherit non-trivial properties. Topological Josephson junctions formed by 2DTIs have been studied recently [Fu2009, Kopnin2011, Tkachov2013, Lee2014, Dolcini2015, Tkachov2015, Sothmann2016, Tkachov2017, Shapiro2017, Bours2018, Blasi2019, Bours2019] and experimentally realized [Hart2014, Wiedenmann2016, Deacon2017]. In particular, as we have seen in Sec. 6.2, a small magnetic flux in topological junctions can lead to very interesting features due to the effective orbital *Doppler shift* (DS) acquired by the electrons in the edge states [Tkachov2015].

In the present chapter we argue that the DS leads to a nonlocal thermoelectric effect as a unique consequence of the helical nature of the edge states. The setup under investigation is shown in Fig. 7.1, where a pair of edge states are contacted to superconductors, while a normal-metal probe – such as STM tip [Das2011, Liu2015, Hus2017, Voigtlander2018] – is directly contacted to the edge states. A similar geometry has been considered in Refs. [Sothmann2017, Bours2018], where however, only the voltage-driven charge transport in the tunneling regime or the heat transport with no probe have been analyzed. In the absence of DS, particle-hole symmetry, inherently present in superconducting systems, prevents the development of any thermoelectric effect. Remarkably, the DS has an effect akin to a Zeeman splitting in the two spin-polarized members of the Kramers pair. Although the whole system is particle-hole symmetric by construction (see Sec. 3.2), the local density of states for each spin species at the contact with the probe lack of symmetry between positive and negative energies due to the DS. Therefore, when a temperature difference is applied between the two superconductors a thermoelectric current flows between the TI and the probe. The key for this response is the fact that the proximity to superconductors gives rise to a simultaneous flow of helical electrons and holes. Since they move in opposite directions, they thermalize with different reservoirs, see Fig. 7.2(b).

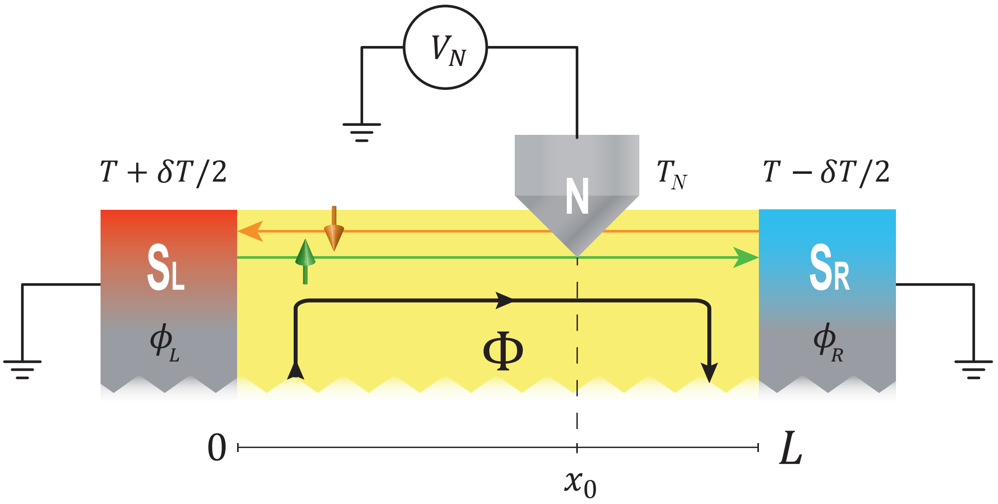

FIGURE 7.1: Sketch of the setup. A helical Kramers pair of edge states of a quantum spin Hall bar is put in contact with two superconductors at different temperatures $T_L = T + \delta T/2$ and $T_R = T - \delta T/2$. A bias voltage V_N is applied to the normal-metal probe coupled to the edge at the point x_0 and kept at temperature $T_N = T$. L is the length of the junction. The structure is threaded by a magnetic flux Φ which induces a Doppler shift in the edge states. A Josephson phase difference $\phi \equiv \phi_L - \phi_R$ may be applied between the two superconductors. The green arrow depicts spin-↑ right-moving quasi-particles, the orange arrow indicates spin-↓ left-moving quasi-particles.

The intrinsic particle-hole symmetry of a normal metal-superconducting junction can be broken, in order to generate thermoelectric current, by using a Zeeman field and spin-polarized barriers or nonlinearities [Ozaeta2014, Bergeret2018, Keidel2020, Marchegiani2020]. Our proposal, on the contrary, relies on a completely different mechanisms which makes use of the helicity of the edge states under the effect of the DS. In the following we quantitatively discuss this peculiar effect in the linear response regime, using the scattering matrix approach developed in Chap. 5. We analyze different figures of merit, and show that it is possible to achieve very high values of the nonlocal Seebeck coefficient.

7.1 Model

We consider the topological Josephson junction depicted in Fig. 7.1 with the upper edge of length L tunnel coupled with a normal (N) probe. The width of the TI is assumed large such that upper and lower edges are decoupled, and thus we focus only on the former one. The two electrodes induce superconducting correlations on the edge states via proximity effect [Tkachov2015, Sothmann2016]. The associated Bogoliubov-de Gennes (BdG) Hamiltonian reads

$$H_{BdG} = \begin{pmatrix} H(x) & i\sigma_y \Delta(x) \\ -i\sigma_y \Delta(x)^* & -H(x)^* \end{pmatrix}, \tag{7.1}$$

expressed in the four-component Nambu basis $(\psi_\uparrow, \psi_\downarrow, \psi_\uparrow^*, \psi_\downarrow^*)^T$ with spin $\uparrow$ and $\downarrow$ collinear with natural spin quantization axis of the TI edge pointing along z-direction, and where $H(x) = v_F \left(-i\hbar\partial_x + p_{DS}/2\right)\sigma_z - \mu\sigma_0 + \Lambda(x)$ with $-H(x)^*$ its time-reversal partner. We include also a contact potential $\Lambda(x) = \Lambda_L \delta(x) + \Lambda_R \delta(x-L)$ at the junction boundaries; v_F indicates Fermi velocity, μ is the chemical potential and σ_i are the Pauli matrices. The momentum $p_{DS} = (\pi\hbar/L)(\Phi/\Phi_0)$, already introduced in Sec. 6.2, represents the so-called Doppler shift (DS) contribution describing the gauge invariant shift of momentum induced by a small magnetic flux Φ through the TI junction [Tkachov2015], while $\Phi_0 = h/2e$ is the magnetic flux quantum. We consider rigid boundary conditions for the order parameter $\Delta(x) = \Delta\left[\Theta(-x)e^{i\phi_L} + \Theta(x-L)e^{i\phi_R}\right]$, with $\Theta(x)$ the step function, Δ is the proximity induced gap, and $\phi \equiv \phi_L - \phi_R$ is the gauge invariant Josephson phase difference between the two superconductors. In this chapter we mainly focus on the Doppler shift effect induced by the external flux Φ. The case of the application of a finite phase bias ϕ, involving Andreev interference effects, deserves to be investigated separately as we will do in Chap. 8. In this respect, is important to notice that the flux Φ and the phase bias ϕ represent two independent degrees of freedom needed to fully characterize the state of the topological junction as we will better discuss in Chap. 9.

The eigenspectrum of the BdG Hamiltonian relative to the homogeneous proximized TI edge, is reported in Fig. 7.2(a) and is given by $E_\pm^\chi(k) = \left(\epsilon_{DS}(\Phi) + \chi\sqrt{(\hbar v_F k \mp \mu)^2 + \Delta^2}\right)$, with $\chi = \pm$ indicating branches with positive/negative concavity and $\epsilon_{DS}(\Phi) = v_F p_{DS}/2 = (v_F h/4L)(\Phi/\Phi_0)$ being the Doppler-shift energy. The effect of the DS on the dispersion curve is to shift the various branches vertically by an amount $\epsilon_{DS}(\Phi)$, upwards or downwards, as shown in Fig. 7.2(a). A finite value of the magnetic flux Φ reduces the gap, which closes when $\epsilon_{DS}(\Phi) = \Delta$. The quasiparticle (QP) eigenfunctions in Nambu notation of both left/right superconductors ($i = L, R$) are given by

$$\begin{aligned} \Psi_{e_+}^{i,\chi} &= \frac{1}{\sqrt{2\pi\hbar w_{e_+}^j}}(ju_- e^{i\frac{\phi_i}{2}}, 0, 0, v_- e^{-i\frac{\phi_i}{2}})^T e^{ik_{e_+}^j x} \\ \Psi_{e_-}^{i,\chi} &= \frac{1}{\sqrt{2\pi\hbar w_{e_-}^\chi}}(0, -ju_+ e^{i\frac{\phi_i}{2}}, v_+ e^{-i\frac{\phi_i}{2}}, 0)^T e^{ik_{e_-}^\chi x}, \end{aligned} \tag{7.2}$$

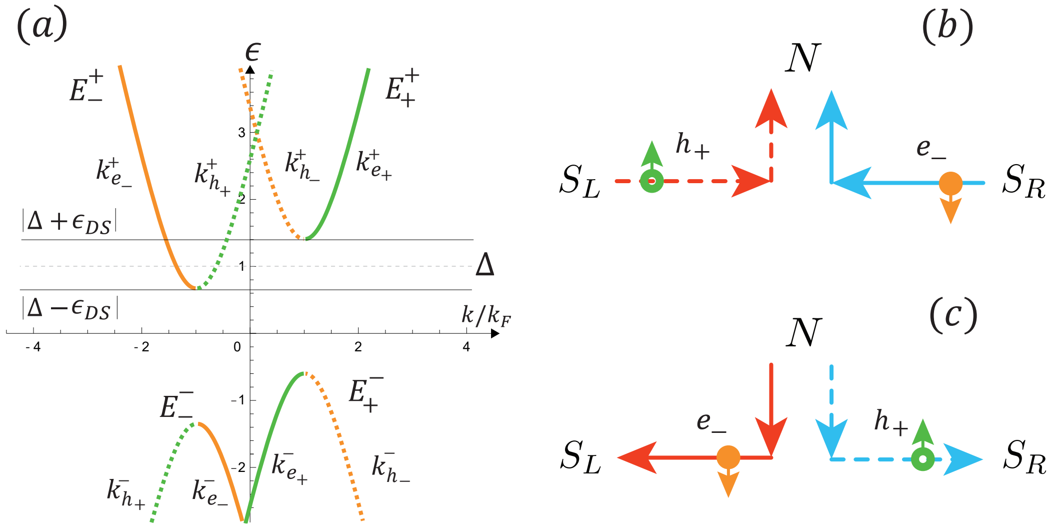

FIGURE 7.2: (a) Dispersion curves for quasiparticles $e_\pm$ (solid lines) and quasiholes $h_\pm$ (dashed lines) in the proximized superconductor S_L/S_R for $0<\epsilon_{DS}(\Phi)<\Delta$. Transport processes are depicted in panel (b) for $V_N=0, \delta T\neq 0$ and in panel (c) for $V_N\neq 0, \delta T=0$, when the spectrum for e_+, h_- is assumed fully gapped.

where

$$u_\pm=\sqrt{\frac{\Delta}{2\epsilon_\pm}}e^{\frac{1}{2}h(\epsilon_\pm)};\quad v_\pm=\sqrt{\frac{\Delta}{2\epsilon_\pm}}e^{-\frac{1}{2}h(\epsilon_\pm)}$$

with $\epsilon_\pm=\epsilon\pm\epsilon_{DS}(\Phi)$ and $h(\epsilon_\pm)=\mathrm{arcCosh}\,(\epsilon_\pm/\Delta)$ for $\epsilon_\pm>\Delta$ and $h(\epsilon_\pm)=i\arccos{(\epsilon_\pm/\Delta)}$ for $\epsilon_\pm<\Delta$. Here, the quasiparticle momentum is $k_{e_\pm}^\chi=\pm k_F(\chi\sqrt{(\epsilon_\mp^2-\Delta^2)/\mu^2}+1)$ and $w_{e_\pm}^\chi=\hbar^{-1}|\partial_k E_\pm^\chi|=v_F(u_\mp^2-v_\mp^2)$ is the associated group velocity. The quasihole (QH) eigenfunctions $\Psi_{h_\pm}^{i,\chi}$ can be obtained by replacing $(u_\pm,v_\pm)\to(v_\pm,u_\pm)$, $k_{e_\pm}^\chi\to k_{h_\mp}^\chi=k_{e_\pm}^{-\chi}$ and $w_{e_\pm}^\chi\to w_{h_\mp}^\chi=w_{e_\pm}^\chi$ in the expressions $\Psi_{e_\mp}^{i,\chi}$ of Eq. (9.2).

Finally, the normal-metal probe N – which would model for instance a STM tip – is assumed to be directly contacted to the upper edge at the point x_0 (see Fig. 7.1) and modelled by an energy- and spin-independent transmission amplitude t (see Appendix A for more details). Due to the helical nature of the TI, electrons injected through the probe with spin component collinear with the natural spin quantization axis of the TI edge propagate in one direction, while electrons with opposite spin component propagate in the other one .

7.2 Relevant Currents

In the setup depicted in Fig. 7.1, a voltage bias V_N is applied between the probe N at the temperature T_N and the superconducting electrodes which are both grounded in order to avoid any time-dependent dynamics (as a consequence of the Josephson relation - see Sec. 6.2). In this configuration the only thermal bias that gives rise to a nonlocal thermoelectric response in the probe is $\delta T=T_L-T_R$ imposed between the superconductors. In the following we will investigate only the dissipative currents flowing through the structure which can be obtained by using the Landauer-Büttiker scattering [Blanter2000] formalism generalized in order to include superconductivity [Lambert1998]. More precisely, we are not interested in the dissipationless (Josephson) contribution to the charge current flowing in the superconducting electrodes, which has been already discussed elsewhere [Tkachov2013, Snelder2013, Sochnikov2015, Dolcini2015, Kurter2015, Marra2016, Stehno2016, Scharf2020]. By using the scattering approach already introduced in Sec. 4.3 [Datta1997, Lambert1998], one can write the charge current J_N^c flowing in the probe as follows:

$$J_N^c = \frac{1}{h}\sum_j \sum_{\alpha,\beta} (\alpha e) \int_0^\infty d\epsilon \, \left(f_N^\alpha(\epsilon) - f_j^\beta(\epsilon) \right) P_{i,j}^{\alpha,\beta}(\epsilon), \tag{7.3}$$

where $\alpha, \beta = \pm$ stand for QPs and QHs respectively. The Fermi functions of the leads $j = L, R, N$ are $f_j^\alpha(\epsilon) = \{\exp[(\epsilon - \alpha\mu_j)/k_B T_j)] + 1\}^{-1}$, where $\mu_N = eV_N$, $\mu_L = \mu_R = 0$, i.e. superconductors are grounded. The charge current flowing in the two superconductors is dominated by the dissipationless Josephson current which, in the linear response regime (i. e. $\delta T, V_N \to 0$), is unaffected by the temperature difference between the electrodes. As already discussed in Sec. 5, such a non-dissipative contribution cannot be caught by the Landauer-Büttiker approach, though it can be obtained by using the method presented in Sec. 6.3. Moreover, in the linear response regime, the temperature of the probe can be chosen as the average temperature of the superconducting leads, i.e., $T_N = (T_L + T_R)/2 = T$ (see Fig. 7.1). With this choice, due to the left/right symmetry of the system, there is no heat current flowing inside the probe, i. e. $J_N^h = 0$ (see Appendix A.3), hence the heat current flowing in the left superconducting lead is exactly opposite to the current flowing in the right lead, i. e. $J_L^h = -J_R^h$. Thus, the only relevant heat current in our system is that flowing in one (say the left) superconductor, which takes the following form

$$J_L^h = \frac{1}{h}\sum_j \sum_{\alpha,\beta} \int_0^\infty d\epsilon \; \epsilon \left[f_L^\alpha(\epsilon) - f_j^\beta(\epsilon) \right] P_{i,j}^{\alpha,\beta}(\epsilon) \, . \tag{7.4}$$

As discussed in Sec. 4.3, the scattering coefficients $P_{i,j}^{\alpha,\beta}$ in Eqs. (7.3) and (7.4), represent the reflection ($i = j$) or transmission ($i \neq j$) probabilities of a quasi-particle of type β in lead j to a quasi-particle of type α in lead i [Lambert1998]. As a consequence of the helical nature of the edge states, the fact that the probe is not spin-polarized and for superconductors with equal gap, it is found that the scattering coefficients $P_{i,j}^{\alpha,\beta}$ do not depend on the probe position (see Appendix A.2). This is because each path taken by particles comes in pair with its symmetric one (obtained by exchanging left and right). Hence, all the results discussed in this chapter do not depend on x_0. This is no longer valid in case the gaps of the superconducting leads are different, as we will discuss in Chap. 9.

As a final remark, it is worth to notice that from their explicit expressions there is no dependence of the scattering coefficients on the contact potential parameter $\Lambda_{L/R}$. This is a direct consequence of the helicity of the edge channels which do not admit ordinary reflections at the interfaces (i. e. Klein tunnelling [Lee2019]). Notice that the independence of $\Lambda_{L/R}$ is a generic result valid also with other form (not delta like) of the interface potential at least in the absence of interaction.

7.3 Nonlocal thermoelectric response: the mechanism

We now demonstrate and quantify the appearance of a nonlocal thermoelectric response due to the presence of a DS and the helical nature of the topological Josephson junction. We focus on linear response with $V_N, \delta T \to 0$. A simple physical picture of the thermoelectric mechanism can be grasped analyzing the dispersion-curves in Fig. 7.2(a). When $\epsilon_{DS} > 0$, left-moving (right-moving) QPs e_- (QHs h_+) shift down with respect to the right-moving (left-moving) QPs e_+ (QHs h_-). For simplicity, we assume $0 < (\Delta - \epsilon_{DS}(\Phi)) \sim k_B T \ll (\Delta + \epsilon_{DS}(\Phi))$ so that only left-moving QPs (right-moving QHs), thermalizing with the T_R (T_L), contribute to the current. This unbalance between the fluxes of cold QPs and hot QHs - see Fig. 7.2(b) - leads to a thermoelectric current flowing in the N probe. Moreover, it is worth to notice that, as we will see in the next Chap. 8, also in the non-linear regime, the thermoelectric current does not depend explicitly on the probe's temperature as long as $T_N \lesssim T$. In this respect, the fact that T_N is assumed to be exactly in between the temperatures of the two superconductors (see Fig. 7.1) it is not a necessary requirement. For an in-depth analysis of this fact, we refer to Appendix A.3.

In addition to the thermoelectric current, a Φ-controlled nonlocal Peltier cooling may be also induced due to the application of a voltage V_N. In this case, as shown in Fig. 7.2(c), a charge current from the probe induces mainly left-moving QPs e_- and right-moving QHs h_+ which determine a net energy transport from right to left between the two superconductors even if they are kept at the same temperature. Notably, both the sign of the net thermoelectric current and the direction of the cooling can be varied by changing $\Phi \to -\Phi$. These conclusions are not affected by the ABS, since they do not contribute neither to the thermal nor to the thermoelectrical transport processes.

7.4 Onsager coefficients

As we discussed in Sec. 5.3, for small values of V_N and δT, the currents of Eqs. (7.3) and (7.4), can be expanded up to the linear order in these quantities. Quantitatively, the linear response regime is thus characterized by the following relations [Benenti2017, Mazza2014, Roura-Bas2018, Hussein2019, Sanchez2018, Kirsanov2019]

$$\begin{aligned} J_N^c &= L_{11}(V_N/T) + L_{12}(\delta T/T^2) \\ J_L^h &= L_{21}(V_N/T) + L_{22}(\delta T/T^2), \end{aligned} \tag{7.5}$$

where V_N/T and $\delta T/T^2$ are the two relevant thermodynamic forces (affinities) for the configuration of interest. Notice that, although the configuration contains three terminals, the driving affinities are two. Hence, the Onsager matrix is effectively 2×2 [Mazza2014, Benenti2017, Sanchez2015, Roura-Bas2018, Mani2018], where we defined (using the notation of Sec. 5.3)

$$\begin{aligned} L_{11} &= L_{NN}^{cc}, & L_{12} &= (L_{NL}^{ch} - L_{NR}^{ch})/2, \\ L_{21} &= L_{LN}^{hc} = (L_{LN}^{hc} - L_{RN}^{hc})/2, & L_{22} &= (L_{LL}^{hh} - L_{LR}^{hh})/2. \end{aligned} \tag{7.6}$$

Remarkably, in the present setup, the off-diagonal coefficients are nonlocal and satisfy the relation $L_{12} = -L_{21}$, as a consequence of the Onsager reciprocal relations (see Sec. 5.3). The behavior of the Onsager coefficients L_{ij} $(i, j = 1, 2)$ are shown in Fig. 7.3 as functions of $\epsilon_{DS}(\Phi)/\Delta$. The diagonal and local coefficients L_{11} and L_{22} are plotted in units of $G_0 T$ and $G_T T^2$, while the nonlocal thermoelectrical coefficient L_{12} is plotted in units of $\sqrt{G_0 G_T T^3}$; with $G_0 = 2e^2/h$ and $G_T = (\pi^2/3h)k_B^2 T$ being respectively the electrical conductance quantum and the thermal conductance quantum. In these plots, the length of the junction L is set equal to the superconducting coherence length $\xi = \hbar v_F/\Delta$. Similar results can be obtained in the case of short $L \ll \xi$ or long $L \gg \xi$ junctions, as discussed below in Sec. 7.5.

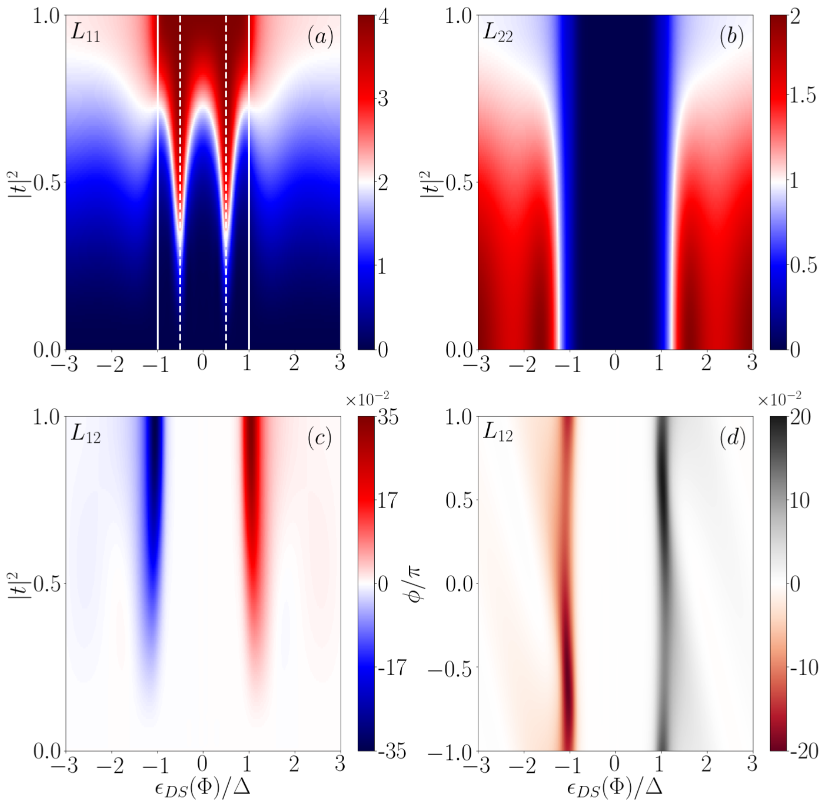

Figure 7.3: Onsager coefficients L_{11} (a), L_{22} (b) and $L_{12} = -L_{21}$ (c) as functions of $\epsilon_{DS}(\Phi)/\Delta$ and the coupling parameter $|t|^2$ for phase bias $\phi = \phi_L - \phi_R = 0$, $T/T_C = 0.1$ and $L/\xi = 1$. (d) L_{12} as a function of $\epsilon_{DS}(\Phi)/\Delta$ and the phase difference ϕ for $|t|^2 = 0.5$. Such quantities are normalized as follows: $L_{11}/(G_0 T)$, $L_{22}/(G_T T^2)$ and $L_{12}/(\sqrt{G_0 G_T T^3})$.

In Figs. 7.3(a) and (b) we plot L_{11} and L_{22}, respectively, as functions of $\epsilon_{DS}(\Phi)/\Delta$ and $|t|^2$, setting $\phi = \phi_L - \phi_R = 0$. When the gap is open ($|\epsilon_{DS}(\Phi)|/\Delta < 1$), and for low coupling $|t|^2 \ll 1$, the electrical conductance $L_{11}/(G_0 T)$ is almost zero apart from two sharp resonances located at $\epsilon_{DS}(\Phi)/\Delta = \pm 1/2$, where the ABSs cross zero-energy (indicated by white dashed lines in Figs. 7.3(a)) as expected in the tunneling limit [Bours2018]. By increasing the coupling $|t|^2$ the resonances are broadened as a consequence of the enhancement of the effective linewidth of the ABSs. When $|t|^2$ increases towards unity, the ABSs are spread and give rise to a finite electrical conductance in the whole range of values of $\epsilon_{DS}(\Phi)$, something that cannot be caught with a tunneling approach (see Appendix A.4). For all values of $|t|^2$ the thermal conductance L_{22} takes the largest values when the gap is closed $|\epsilon_{DS}(\Phi)|/\Delta > 1$, as one can see in Fig. 7.3(b). This is consistent with the fact that in the linear response regime the heat transport in a superconductor is mediated by quasiparticles [Sothmann2016, Sothmann2017]. On the other hand, L_{22} vanishes within the gap when $|\epsilon_{DS}(\Phi)|/\Delta < 1$. This is due to the fact that ABSs cannot allow any thermal transport, while mediating the transport of charge through the Andreev reflection mechanism. When the gap is closed, the thermal conductance L_{22} presents small fluctuations as a consequence of interference effects and decreases at increasing coupling strength with the probe. In Fig. 7.3(c) we plot L_{12} as a function of $\epsilon_{DS}(\Phi)/\Delta$ and $|t|^2$, with $\phi = 0$. We distinguish two peaks at $|\epsilon_{DS}(\Phi)| \sim \Delta$. This is because in this condition the orange band (for $\epsilon_{DS}(\Phi) \sim \Delta$) and the green band (for $\epsilon_{DS}(\Phi) \sim -\Delta$) shown in Fig. 7.2($a$) nearly touch zero energy, thus allowing a small temperature bias to drive a charge current even for a temperature $k_B T \ll \Delta$. The absolute value of L_{12} increases as a function of $|t|^2$ and its sign changes when changing the sign of DS (or Φ). Fig. 7.3(d) visualizes the impact of the Josephson phase ϕ (vertical axes) in the behavior of the nonlocal thermoelectric coefficient L_{12} for $|t|^2 = 0.5$. Here, we can notice that due to symmetry reasons $L_{12}(\Phi, \phi) \to -L_{12}(-\Phi, -\phi)$. As a final remark, when $|t|^2 \approx 1$ (i. e. perfect coupling with the probe) L_{12} does not depend neither on the phase bias ϕ nor on the junction length L.

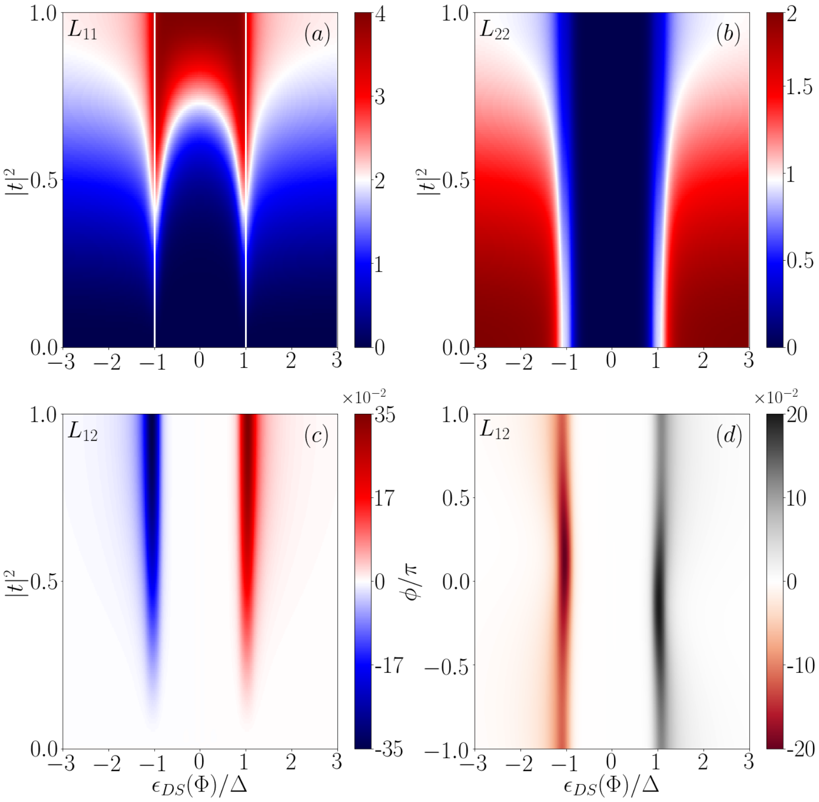

FIGURE 7.4: Onsager coefficients L_{11} (a), L_{22} (b) and $L_{12} = -L_{21}$ (c) in the case of short $L/\xi = 0.1$ junction, as functions of $\epsilon_{DS}(\Phi)/\Delta$ and the coupling parameter $|t|^2$ for phase bias $\phi = \phi_L - \phi_R = 0$, $T/T_C = 0.1$ and $L/\xi = 1$. (d) L_{12} as a function of $\epsilon_{DS}(\Phi)/\Delta$ and the phase difference ϕ for $|t|^2 = 0.5$. Such quantities are normalized as follows: $L_{11}/(G_0 T)$, $L_{22}/(G_T T^2)$ and $L_{12}/(\sqrt{G_0 G_T T^3})$.

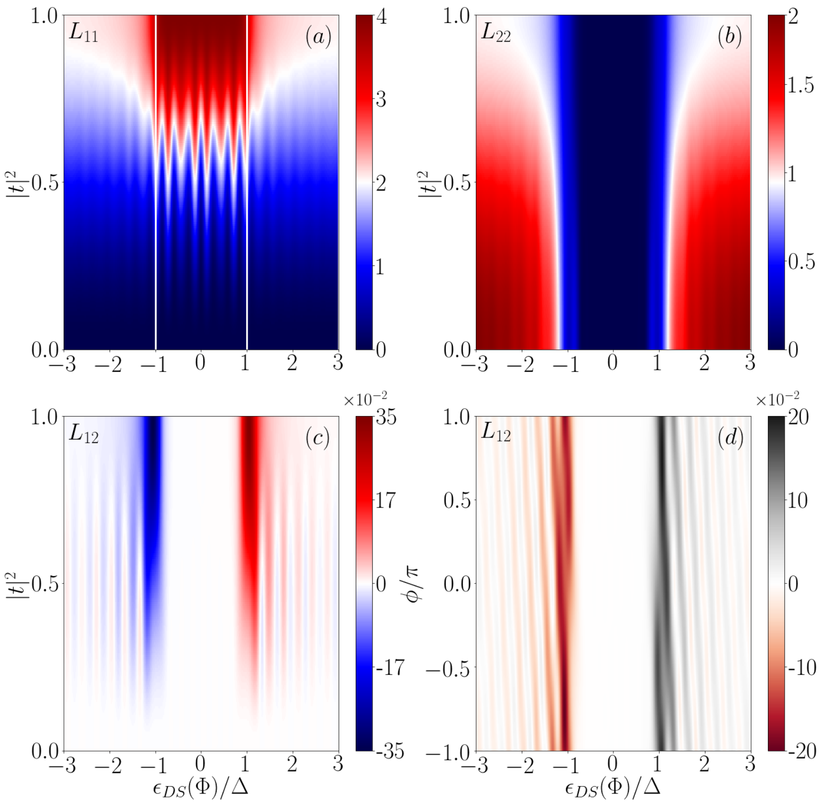

FIGURE 7.5: Onsager coefficients L_{11} (a), L_{22} (b) and $L_{12} = -L_{21}$ (c) in the case of long junction $L/\xi = 5$, as functions of $\epsilon_{DS}(\Phi)/\Delta$ and the coupling parameter $|t|^2$ for phase bias $\phi = \phi_L - \phi_R = 0$, $T/T_C = 0.1$ and $L/\xi = 1$. (d) L_{12} as a function of $\epsilon_{DS}(\Phi)/\Delta$ and the phase difference ϕ for $|t|^2 = 0.5$. Such quantities are normalized as follows: $L_{11}/(G_0 T)$, $L_{22}/(G_T T^2)$ and $L_{12}/(\sqrt{G_0 G_T T^3})$.

7.5 Dependence on the junction length L

In the previous section we discussed the case in which the length of the junction is equal to the coherence length of the system, i. e. $L = \xi$. For our setup, this situation is reasonable assuming a STM tip with state-of-the-art size of 100 nm and a coherence length ξ in the proximized TI of the order of 600 nm [Hart2014, Bocquillon2017]. Further a length $L \sim \xi$ assures that the transport along the edge state is ballistic [Groenendijk2018] at the operating temperatures for our the setup, typically of a few K. Here we complete the analysis by investigating the behavior of the Onsager coefficients L_{ij} as functions of $\epsilon_{DS}(\Phi)/\Delta$ and the coupling parameter $|t|^2$ for short ($L/\xi = 0.1$, Fig. 7.4) and long ($L/\xi = 5$, Fig. 7.5) junctions. By comparing Figs. 7.4 and 7.5 with Fig. 7.3, it is easy to see that the main result (namely, the occurrence of a purely non-local thermoelectric current due to the helical nature of the edge states) is not modified. In particular, when the gap closes due to the flux bias Φ, i.e. when $|\epsilon_{DS}(\Phi)/\Delta| \approx 1$, the non-local thermoelectric current is maximized *for any length*. For long junctions the only additional feature is the presence of oscillations in the linear-response coefficients, due to the proliferation of resonant states in the junction - see Fig. 7.5. No oscillations occur, though, at any lengths when $|t|^2 \approx 1$.

7.6 Nonlocal Seebeck coefficient

To characterize the nonlocal effect induced by the DS we analyze the nonlocal Seebeck coefficient. In particular, by setting $J_N^c = 0$ in Eq. (7.5) and solving for V_N one finds the Seebeck thermovoltage V_N^S, through which we can compute the *nonlocal* Seebeck coefficient

$$S \equiv -\frac{V_N^S}{\delta T} = \frac{1}{T}\frac{L_{12}}{L_{11}}, \tag{7.7}$$

similarly to the derivation of the local case. The latter is shown in Fig. 7.6, in units of $\mu V/K$, in the case of a weak coupling $|t|^2 = 10^{-2}$, where the Seebeck coefficient takes the highest values. In order to make realistic predictions in a wide temperature range, we have also included the self-consistent temperature behavior $\Delta(T) = \Delta_0 \tanh\left(1.74\sqrt{T_C/T - 1}\right)$, accurate better than 2% with respect to the self-consistent BCS result [Tinkham1966, Kamp2019]. In Fig. 7.6(a) the Seebeck coefficient is reported at $\phi = \pi/2$ for different values of temperatures: its peak value is quite high ($\sim 65\mu V/K$), reaching the same order of magnitude of the values predicted for hybrid ferromagnetic-superconducting junctions [Giazotto2015, Bergeret2018]. The maximum value of the Seebeck coefficient decreases by increasing the temperature T and it is reached at $|\epsilon_{DS}(\Phi)| \sim \Delta(T)$. The shape of S also depends on the phase bias ϕ (see Fig. 7.6(b)); namely for $\phi \neq 0$ it is not antisymmetric $S(\phi, \Phi) \neq -S(\phi, -\Phi)$ with respect to Φ while it becomes exactly antisymmetric for $\phi = 0$.

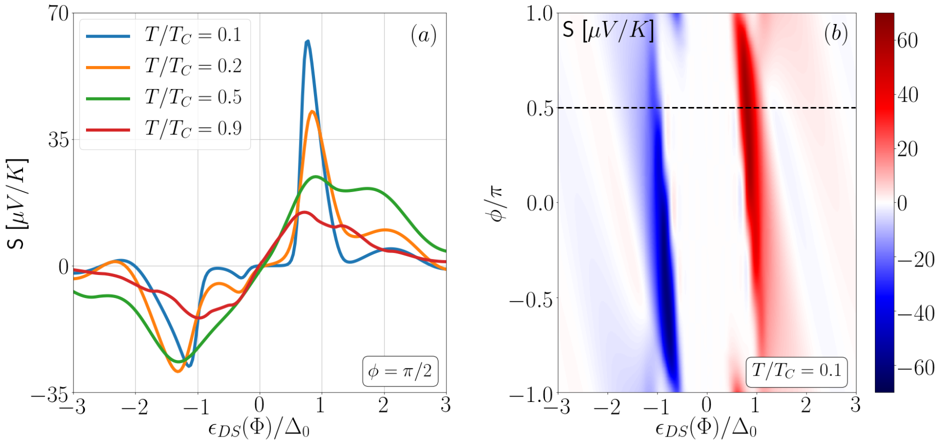

FIGURE 7.6: Seebeck coefficient as function of $\epsilon_{DS}(\Phi)/\Delta_0$ for different temperatures at $\phi = \pi/2$ (a) and as function of $\epsilon_{DS}(\Phi)/\Delta_0$ and ϕ for $T/T_C = 0.1$ (b). The blue curve in panel (a) correspond to the cut at $\phi = \pi/2$ of the Seebeck coefficient depicted in panel (b) (dashed line) obtained for the same set of parameters: $L/\xi = 1$ and $|t|^2 = 10^{-2}$.

7.7 Thermoelectric figure of merit ZT

Here we show the figure of merit ZT [Benenti2017] which parametrizes the maximum achievable efficiency $\eta^{max} = \eta_C \frac{\sqrt{ZT+1}-1}{\sqrt{ZT+1}+1}$ (which approaches to the Carnot efficiency $\eta_C = \delta T/T$

for $ZT \to \infty$) in the linear regime when the device is regarded as a thermoelectric heat-engine/refrigerator. In our case this is defined as

$$ZT = -\frac{L_{12}L_{21}}{L_{11}L_{22}}, \tag{7.8}$$

since $L_{12} = -L_{21}$. We plot ZT in Fig. 7.7 as a function of ϵ_{DS} and $|t|^2$ for the parameters specified in the caption. Notice that the value of ZT achieves its highest value at $\epsilon_{DS} \sim \pm\Delta$ (where the Seebeck is maximal). Interestingly, ZT is maximal for $|t|^2 = 1$, i.e. in the regime of maximum coupling with the probe, but reaching quite small values ~ 0.1. As a final remark, we notice that the ZT and the Seebeck coefficient S present opposite behaviors as functions of coupling parameter $|t|^2$. More specifically the Seebeck coefficient takes higher values in the weak coupling limit ($|t|^2$ small), while ZT is largest in the strong coupling limit ($|t|^2$ close to 1). First we notice that, in general the Seebeck coefficient S and the figure of merit ZT are not expected to have the same behavior. Being more specific, in our system (similarly to the standard case of ordinary two-terminal systems), this can be understood by rewriting Eq. (7.8) as $ZT = S^2T^2\frac{L_{11}}{L_{22}}$, where we explicitly see that ZT does not only depend on S but also on the quotient between the electrical ($\propto L_{11}$) and thermal ($\propto L_{22}$) conductances. For clarity, let us consider $\epsilon_{DS}/\Delta \simeq \pm 1$ where the Seebeck coefficient is maximal. We can see that S increases as $|t|^2$ decreases, while $\frac{L_{11}}{L_{22}}$ gets suppressed for $|t|^2 \to 0$, since L_{22} in the denominator tends to a constant (see Fig.7.3 (b)), while L_{11} in the numerator goes to zero (due to the decoupling with the probe). As a consequence, ZT tends to zero in the weak coupling limit. In the strong coupling limit ($|t|^2 \to 1$), S goes to a constant, while L_{11} increases and L_{22} decreases (see Figs. 7.3(b) and (c)), resulting in an overall increase of the ZT.

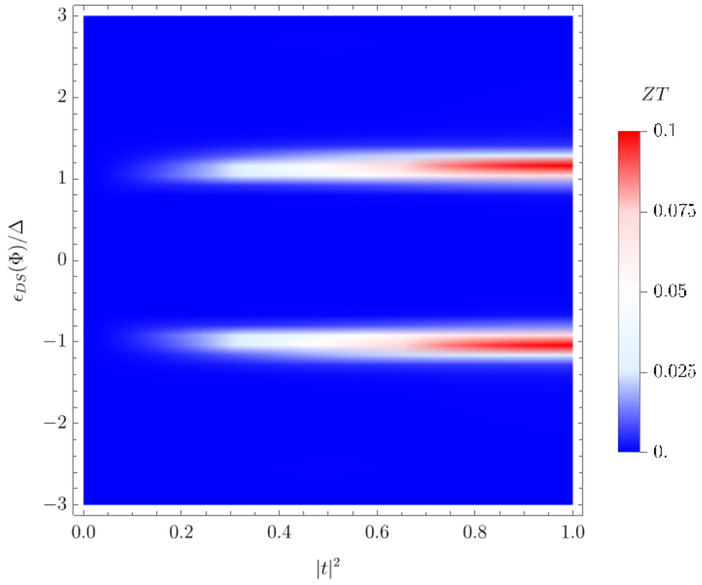

FIGURE 7.7: Density plot of the figure of merit ZT plotted as a function of $\epsilon_{DS}(\Phi)/\Delta$ and $|t|^2$. The parameters used are: $L/\xi = 1$, $T/T_C = 1/10$ and $\phi = 0$.

7.8 Thermoelectric current for a proximized 2DTI

In this section we apply our results to the case of a 2DTI made of HgTe/HgCdTe quantum wells, proximized with Aluminum with an induced gap $\Delta \approx 40\mu eV$ (see Ref. [Bocquillon2018]). More precisely, we compute the non-local thermoelectric current $J^c_{12} = J^c_N|_{V_N=0}$, defined as the charge current at the probe when $V_N = 0$. We assume a bad (ohmic) contact with the probe (namely $|t|^2 \approx 0.1$) and a thermal gradient of the order of 80-120 mK, a realistic value for these type of experimental setups [Giazotto2006]. In Fig. 7.8 we depict the thermoelectric current J^c_{12} as a function of the flux bias Φ and the temperature gradient $\delta T \lesssim 120mK$, such that the induced gap of the right and left proximized regions are constant and equal to Δ. Fig. 7.8 (main panel and inset (b)) shows that when the gap closes by tuning the flux bias Φ such that $|\epsilon_{DS}(\Phi)/\Delta| \approx 1$, the nonlocal thermoelectric current is maximal, reaching values of the order $\approx 30\ pA$ (a reasonable value for these kind of experiments [Hart2014]). Moreover, we notice that, as shown in the inset (a) of Fig. 7.8, the current has a linear behavior in δT up to 80 mK. As a final remark, we notice that the specific choice of paramenters we have just discussed is not optimal. Indeed, we stress that much higher values of the current and larger operation temperatures can be obtained with different materials [Bernevig2013, Franz2013, Tkachov2015a] or fully proximized structures, i. e. when the induced gap in the 2DTI is equal to the Δ of the superconductor.

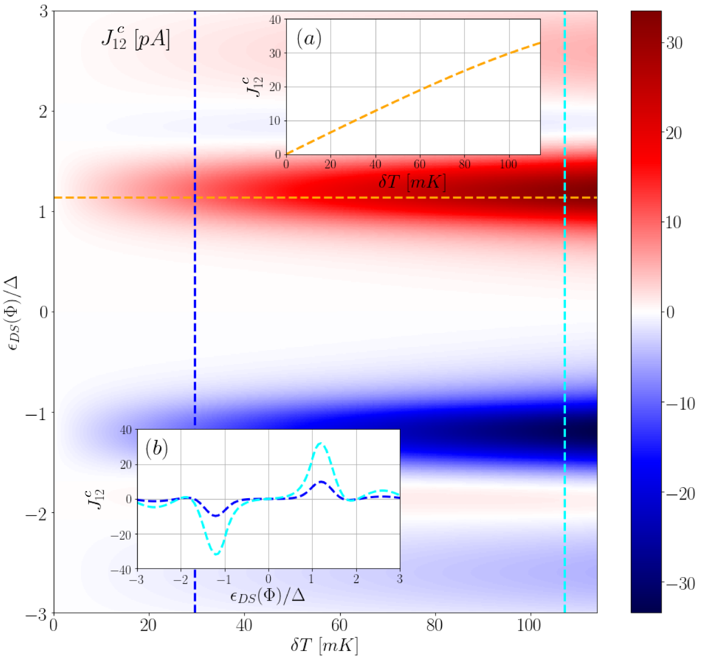

FIGURE 7.8: Density plot of the thermoelectric current J^c_{12} expressed in pA, as function of $\epsilon_{DS}(\Phi)/\Delta$ and the thermal gradient δT expressed in units of mK, for phase bias $\phi = \phi_L - \phi_R = 0$, $L/\xi = 1$ and $|t|^2 = 0.1$. In the inset (a) is depicted the behavior of J^c_{12} as a function of δT corresponding to an horizontal cut at $\epsilon_{DS}(\Phi)/\Delta \approx 1$ (orange dashed line). In the inset (b) is depicted the behavior of J^c_{12} as a function of $\epsilon_{DS}(\Phi)/\Delta$ corresponding to vertical cuts at $\delta T = 30\ mK, 110\ mK$ (dark and light blue dashed lines).

7.9 Conclusions

We have discussed a striking consequence of the helical properties of the edge states in a topological Josephson junction in the presence of a normal metal probe coupled to one edge of a quantum spin Hall system. We showed that a thermal gradient between the superconductors in the presence of the Doppler shift generates a nonlocal thermoelectrical transport in the probe even in absence of any spin polarization. By using scattering matrix approach, we have quantitatively evaluated both local and nonlocal Onsager transport coefficients as a function of Doppler shift and phase difference. The nonlocal Seebeck coefficients can achieve high values, comparable with the best hybrid devices based on ferromagnetic elements, in the weak coupling limit (tunneling regime). These nonlocal features are a consequence of the spin-momentum locking of helical states and the induced Doppler shift which can be tuned by means of small external magnetic fields. This additional knob can be used to tune the sign of the off-diagonal Onsager coefficient, and therefore to control heat and thermoelectric response in a topological Josephson junction based device. Such effects are not limited to the tunneling regime, but occur also for an ohmic contact with the probe, provided that the Josephson coupling is not spoiled. The present device is a very promising tool for probing the helical nature of the edge states in systems where the Hall bar configuration of edge states is difficult to realize.

As a final remark, we notice that our analysis is not limited to the case of full proximization due to a perfect contact, which can be realized with superconducting pads laying on the TI edges over a few μm (being much bigger than the superconducting coherence length in the proximized TI $\xi \approx 600$ nm) [Hart2014, Wiedenmann2016, Deacon2017]. A bad contact, though, can be taken into account in our calculations by considering a reduced gap, without changing our results [Bocquillon2018]. Furthermore, a length of the junction $L \sim \xi$ is sufficient to host the contact with a metallic probe (such as an STM tip with a width of 100 nm), and preserves, at the same time, the ballistic nature of the transport along the edges [Lunczer2019]. Moreover, studies on the impact of electron-phonon interaction [Budich2012] and spin-phonon interaction [Groenendijk2018] in helical edge states support the idea that the transport is ballistic at the operating temperatures for our the setup, typically of a few kelvin.

8

Nonlocal thermoelectricity in a topological Andreev interferometer

This chapter is based on the results published in the paper:
G. Blasi, F. Taddei, L. Arrachea, M. Carrega, and A. Braggio. *Nonlocal thermoelectricity in a topological Andreev interferometer*. Phys. Rev. B, **102**(24) 241302(R) (2020).

Prominent topics in hybrid superconducting quantum technologies concern the thermal management [Partanen2016, Fornieri2017, Senior2020] and the thermoelectricity [Claughton1996, Mazza2015, Sanchez2018, Kamp2019, Hussein2019, Kirsanov2019, Marchegiani2020]. These represent novel functionalities for quantum sensing [Giazotto2015, Heikkila2018], entanglement manipulation [Blasi2019] and thermal engines [Mazza2014, Yamamoto2015, Vischi2019, Scharf2020, Marchegiani2020a].

Usually, finite thermoelectric response appears in hybrid superconducting systems only when the particle-hole symmetry, encoded in the Bogoliubov-de Gennes (BdG) Hamiltonian, is broken, e.g. by means of ferromagnetic correlations [Machon2013, Ozaeta2014, Kolenda2017, Shapiro2017, Keidel2020] or by exploiting nonlinearities [Sanchez2016]. Recently, mechanisms able to generate *nonlocal* thermoelectricity have been predicted in Cooper pair splitters [Hussein2019] and Andreev interferometers [Jacquod2010, Kalenkov2020], and experimentally investigated [Eom1998, Jiang2005, Tan2021].

In Chap. 7 we have demonstrated [Blasi2020] that a Josephson junction based on a two-dimensional (2D) topological insulator (TI) [BHZ2006, Konig2007, Qi2011, Ando2013, Ronetti2017] threaded by a magnetic flux with one edge attached to a normal metallic probe [Bours2018] presents nonlocal thermoelectricity when a temperature difference is applied between the two superconducting leads. The responsible mechanism is the so-called Doppler shift induced by the magnetic flux in the junction, which has an effect akin to a Zeeman splitting in the two spin-polarized members of the Kramer pair of the 2DTI [Tkachov2015]. In this chapter, we show that a phase bias *alone* in a topological Josephson junction is sufficient to establish finite nonlocal thermoelectricity. This is very appealing since, differently from the mechanism of Chap. 7 [Blasi2020], the present one takes place without the necessity of a magnetic field, and solely relies on the superconducting Andreev interferometric effect. We argue that, with state-of-the-art technologies the corresponding nonlocal Seebek coefficient results of the order of few $\mu V/K$ at temperatures of few kelvins. Even if the analysis of this chapter focuses on the 2DTI case, we show that a similar physics occurs also in 3D topological surfaces - see the Appendix B.

8.1 Model

Differently from Chap. 7, here we consider the topological Josephson junction (TJJ) depicted in Fig. 8.1, which consists of two superconducting electrodes placed on top of a 2DTI at a distance L, without the application of any external magnetic flux, i. e. $\Phi = 0$. The two electrodes induce superconducting correlations on the edge states via proximity effect [Tkachov2015, Sothmann2016]. The width of the TI strip is assumed to be large enough such that upper and lower edges are decoupled, and we focus only on the upper edge. The system is described by the following BdG Hamiltonian

$$H_{BdG} = \begin{pmatrix} H(x) & i\sigma_y \Delta(x) \\ -i\sigma_y \Delta(x)^* & -H(x)^* \end{pmatrix}, \tag{8.1}$$

expressed in the Nambu basis $(\psi_\uparrow, \psi_\downarrow, \psi_\uparrow^*, \psi_\downarrow^*)^T$ with spin $\uparrow$ and $\downarrow$ collinear with natural spin-quantization axis of the TI edge along z-direction, where $H(x) = v_F\,(-i\hbar\partial_x)\,\sigma_z - \mu\sigma_0$ with $-H(x)^*$ being its time-reversal partner. The Fermi velocity is v_F, μ is the chemical potential and σ_i are the Pauli matrices. We consider rigid boundary conditions with order parameter $\Delta(x) = \Delta\left[\Theta(-x)e^{i\phi_L} + \Theta(x-L)e^{i\phi_R}\right]$, where $\Theta(x)$ is the step function, Δ is the proximity induced gap and $\phi \equiv \phi_L - \phi_R$ is the gauge invariant Josephson phase difference between the two superconductors. A normal-metal probe N – such as a STM tip [Das2011, Liu2015, Hus2017, Voigtlander2018] – is directly contacted to the upper edge on the point x_0 (see Fig. 8.1) and modeled by an energy- and spin- independent transmission amplitude t (see Appendix A for more details).

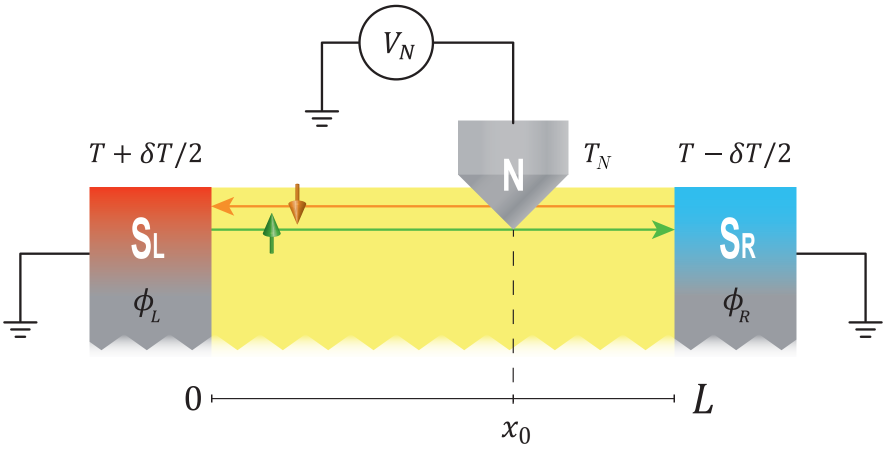

FIGURE 8.1: A helical Kramers pair of edge states of the quantum spin Hall effect is contacted by two superconductors at different temperatures $T_L = T + \delta T/2$ and $T_R = T - \delta T/2$, and a phase difference $\phi \equiv \phi_L - \phi_R$. A bias voltage V_N is applied to the normal-metal probe at temperature T_N and coupled to the edge at the point $0 \le x_0 \le L$, with L the length of the junction.

8.2 Charge Current at the probe

In the setup depicted in Fig. 8.1, a voltage bias V_N is applied between the probe N at the temperature T_N and the superconducting electrodes which are assumed equipotential and grounded (this is important in order to not induce time dependent Josephson effects). In this configuration the only thermal bias that gives rise to a nonlocal electric response in the probe is $\delta T = T_L - T_R$ imposed between the superconductors. Similarly to Chap. 7, by using the scattering approach [Lambert1998, Blanter2000] one can write the charge current J_N^c flowing in the probe as follows:

$$J_N^c = \frac{1}{h} \sum_j \sum_{\alpha,\beta} (e\alpha) \int_0^\infty d\epsilon \, \left(f_N^\alpha(\epsilon) - f_j^\beta(\epsilon) \right) P_{N,j}^{\alpha,\beta}(\epsilon, \phi) \tag{8.2}$$

where $\alpha, \beta = +$ stand for quasiparticle (QP), $\alpha, \beta = -$ for quasihole (QH), and with j running over leads indices (L, R and N). In Eq. (8.2) we consider the chemical potentials of the grounded superconductors as reference for the energies. The current depends on the generalized Fermi distributions $f_j^\alpha(\epsilon) = \{e^{(\epsilon - \alpha e V_j)/k_B T_j} + 1\}^{-1}$, where T_j and V_j are respectively the temperature and the voltage at the lead j. Notice that when $V_j = 0$ (for the grounded superconductors $V_L = V_R = 0$), $f_j^-(\epsilon) = f_j^+(\epsilon)$. The scattering coefficients $P_{i,j}^{\alpha,\beta}(\epsilon, \phi)$, with $i, j = N, L, R$, represent the reflection ($i = j$) or transmission ($i \neq j$) probabilities of a quasiparticle of type β in lead j to a quasiparticle of type α in lead i (see Sec. 4.3).

8.3 Symmetries

As a consequence of the helical nature of the edge states, the fact that the probe is not spin-polarized and for superconductors with equal gap, it is found that the scattering coefficients $P_{i,j}^{\alpha,\beta}(\epsilon, \phi)$ do not depend on the probe position. This is because each path taken by particles comes in pair with its symmetric one (obtained by exchanging left and right). Hence, all the results discussed hereafter in this chapter do not depend on x_0. This is no longer valid in case the gaps of the superconducting leads are different, as we will discuss in Chap. 9. Furthermore, it can be shown that peculiar *nonlocal* symmetries hold for the scattering coefficients of Eq. (8.2) between the probe and the left/right superconductors, namely $P_{N,L/R}^{\alpha\beta}(\epsilon, \phi) = P_{N,R/L}^{-\alpha-\beta}(\epsilon, \phi)$ and $P_{N,L/R}^{\alpha\beta}(\epsilon, \phi) = P_{N,L/R}^{-\alpha-\beta}(\epsilon, -\phi)$, while the reflection coefficients at the probe N satisfy the relation $P_{N,N}^{\alpha\beta}(\epsilon, \phi) = P_{N,N}^{-\alpha-\beta}(\epsilon, \phi)$ between QP and QH states. A generalized version of these symmetries of the scattering coefficients, obtained in the general case in which both the Doppler shift and the phase bias are present, is discussed in Appendix A.2.

8.4 Nonlocal thermoelectric response

By exploiting the aforementioned symmetry relations, one can write the charge current at the probe J_N^c in the following form:

$$J_N^c = \frac{1}{h} \int_0^\infty d\epsilon \, \left\{ F_N^-(\epsilon) A(\epsilon, \phi) - F_S^-(\epsilon) \left[Q(\epsilon, \phi) - Q(\epsilon, -\phi) \right] \right\} \tag{8.3}$$

where in the first term we recognize the Fermi function differences for normal probe $F_N^- \equiv f_N^+ - f_N^-$ weighted with a scattering coefficient

$$A(\epsilon,\phi) = e\left(N_N^+ - P_{NN}^{++} + P_{NN}^{+-}\right) = e\left(N_N^- - P_{NN}^{--} + P_{NN}^{-+}\right) \tag{8.4}$$

that represents the electronic charge transferred from the probe N into the edge, being $P_{NN}^{\pm\pm}$ normal reflections, $P_{NN}^{\pm\mp}$ the Andreev ones and $N_N^{+(-)}$ the number of open channels for electrons (holes) at the probe. The second term instead contains the Fermi function differences between the two superconductors $F_S^- \equiv f_L^{\pm} - f_R^{\mp}$ which are non-zero when a thermal bias $\delta T \neq 0$ is applied between the superconductors. The function F_S^- is weighted with the odd parity component, with respect to ϕ, of the function

$$Q(\epsilon,\phi) = e\left(P_{N,L}^{++} - P_{N,L}^{-+}\right) = -e\left(P_{N,R}^{+-} - P_{N,R}^{--}\right). \tag{8.5}$$

A visualization of the meaning of the quantity Q is given in Fig. 8.2 where we sketch the resonant processes where a QP or QH is injected from right or left superconductors and is transferred after multiple resonant Andreev processes to the probe as an electron (solid) or a hole (dashed). In particular Q represents the net electronic charge transferred into the probe N when a QP is injected from S_L (see Fig. 8.2 (a)). The symmetries show that a QH injected from the right superconductor S_R brings exactly the same amount of charge, with opposite sign [second identity of Eq. (8.5)] as represented in Fig. 8.2 (b). Alongside these processes (represented in Figs. 8.2 (a)-(b)), there are also dual processes, depicted in Fig. 8.2 (c)-(d), which correspond to the same amount of transferred charge given in Eq. (8.5) obtained by exchanging the side of injection (i. e. $S_L \rightleftarrows S_R$) and inverting the sign of $\phi \to -\phi$.

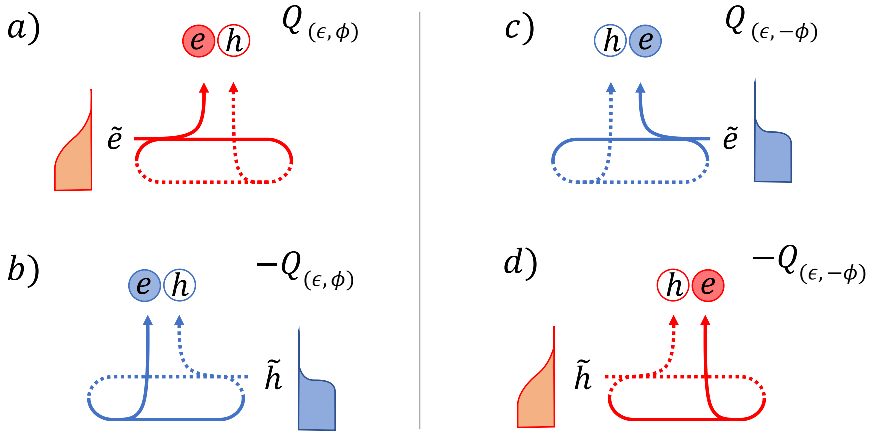

FIGURE 8.2: Resonant processes describing the transfer of the charge Q from the superconducting leads S_L, S_R into the probe N. $\tilde{e}$,$\tilde{h}$ label respectively QP and QH at the superconducting leads. Solid and dashed lines correspond to the trajectories traveled by electrons and holes respectively. Red (blue) correspond to processes originated at the hot (cold) lead S_L (S_R) whose Fermi distribution $f_L = f_L^{\pm}$ ($f_R = f_R^{\pm}$) is sketched on the side. In (a)-(b) are depicted the processes of QP and QH injected from S_L and S_R respectively, and corresponding to a transfer of the opposite amount of charge $Q(\epsilon,\phi)$ (a) and $-Q(\epsilon,\phi)$ (b). In (c)-(d) are depicted the dual processes obtained by inverting the lead of injection ($S_L \rightleftarrows S_R$) and the sign of $\phi \to -\phi$.

We now discuss the physical consequence of the result reported in Eq. (8.3). When $V_N = 0$ there is no contribution from the Fermi functions of the normal probe (i. e. $F_N^- = 0$) because

$f_N^+(\epsilon) = f_N^-(\epsilon)$. Since T_N does not enter these expressions, the possibility of inducing *local* thermoelectricity by means of a thermal bias between the TI and the probe is ruled out. This is particularly important at experimental level since the temperature of the probe does not need to be controlled during the measurement of nonlocal thermoelectricity. The only thermoelectric response in the probe is the *nonlocal* one when a thermal bias between the two superconductors δT is applied, i.e. $F_S^- = f_L^\pm(\epsilon) - f_R^\mp(\epsilon) \neq 0$. This nonlocal thermoelectric response (see Eq. (8.3)) is determined by the integral over the energies of the odd parity component in ϕ of the function $Q(\epsilon, \phi)$, i.e. $Q(\epsilon, \phi) - Q(\epsilon, -\phi)$. If $\phi = 0$, one cannot have nonlocal thermoelectricity. The physical reason of this result comes from the exact cancellation of the contributions of the processes represented in Fig. 8.2: in particular (a) cancels with (d) and (b) with (c).

8.5 Phase dependent thermoelectricity

Here we concentrate on the action of the Josephson phase bias ϕ showing that it is responsible for the generation of nonlocal thermoeletricity in the probe due to a peculiar Andreev interferometric effect associated to the helical nature of the edge, as pictorially sketched in Fig. 8.2. This can be rationalized looking at the analytical expressions of the quantities A and Q of Eqs. (8.4) and (8.5):

$$\begin{aligned} A(\epsilon, \phi) = &\sum_{\sigma=\pm} \frac{2e|t|^4 \cdot \Theta(\Delta - \epsilon)}{1 + |r|^4 + 2|r|^2 \cos\left(2\pi \frac{L\epsilon}{\xi\Delta} + \sigma\phi + 2 \arcsin\left(\frac{\epsilon}{\Delta}\right)\right)}, \\ &+ \sum_{\sigma=\pm} \frac{e(g(\epsilon)+1)(g(\epsilon) - |r|^2)|t|^2 \cdot \Theta(\epsilon - \Delta)}{g(\epsilon)^2 + |r|^4 - 2g(\epsilon)|r|^2 \cos\left(2\pi \frac{L\epsilon}{\xi\Delta} + \sigma\phi\right)} \end{aligned} \tag{8.6}$$

$$Q(\epsilon, \phi) = \frac{e(g(\epsilon)-1)(g(\epsilon) - |r|^2)|t|^2 \cdot \Theta(\epsilon - \Delta)}{g(\epsilon)^2 + |r|^4 - 2g(\epsilon)|r|^2 \cos\left(2\pi \frac{L\epsilon}{\xi\Delta} - \phi\right)}, \tag{8.7}$$

where $g(\epsilon) = \left(\epsilon/\Delta + \sqrt{\epsilon^2/\Delta^2 - 1}\right)^2$, $|r|^2 = 1 - |t|^2$ and $\xi = \hbar v_F/\pi\Delta$ is the superconducting coherence length. Notice that Eq. (8.6) consists of two parts each related to the sub-gap (first line) and supra-gap (second line) processes, while Eq. (8.7) contains only the supra-gap contribution. In particular, from Eq. (8.7), it emerges that $Q(\epsilon, \phi)$ has no definite symmetry in ϕ for $L \neq 0$ so that one would expect a finite nonlocal thermoelectric response. The interferential nature of the phenomena can be better enlightened by investigating the behavior of the Onsager coefficients in the linear response regime as we discuss next.

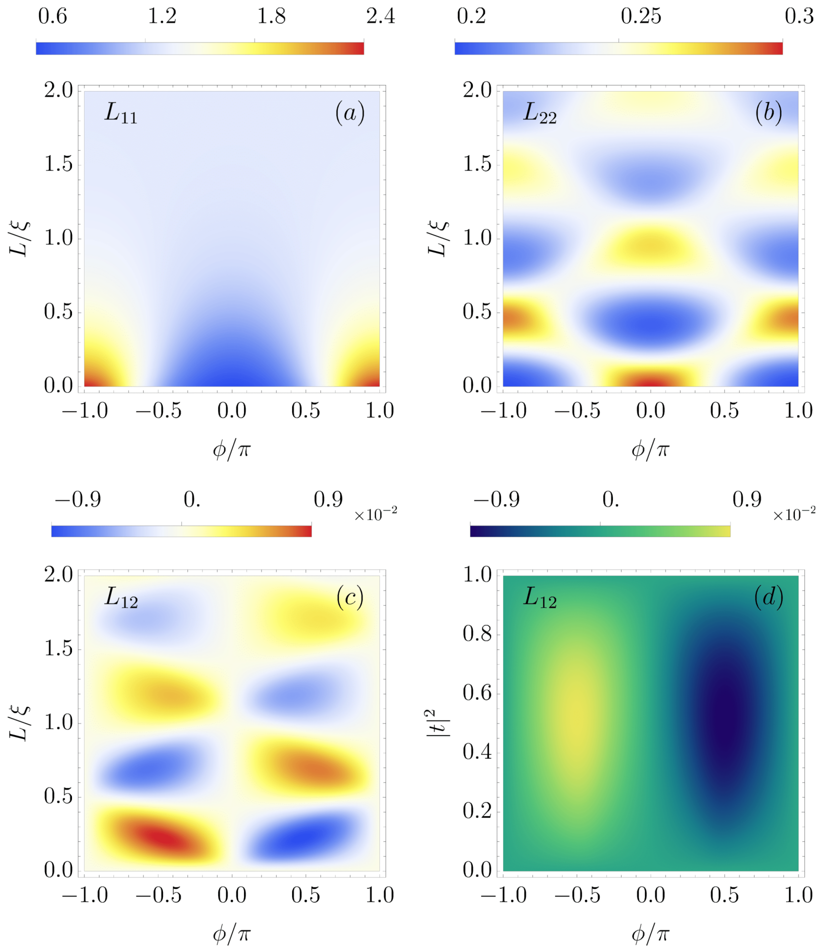

FIGURE 8.3: Phase dependence of the Onsager coefficients. L_{11} (a), L_{22} (b) and $L_{12} = -L_{21}$ (c) as functions of ϕ/π and the junction length L/ξ for $|t|^2 = 0.5$. (d) L_{12} as a function of ϕ/π and coupling parameter $|t|^2$ with the junction length $L/\xi = 0.25$ (for which is maximal) . Such quantities are taken at $T/T_C = 0.4$ and normalized as follows: $L_{11}/(G_0 T)$, $L_{22}/(G_T T^2)$ and $L_{12}/(\sqrt{G_0 G_T T^3})$, with $G_0 = 2e^2/h$ and $G_T = (\pi^2/3h)k_B^2 T$ being respectively the electrical conductance quantum and the thermal conductance quantum.

8.6 Linear response regime

As already mentioned in Chap. 7, in the linear response regime, for $\delta T, V_N \to 0$, the temperature of the probe can be chosen as the average temperature of the superconducting leads, i. e. $T_N = (T_L + T_R)/2 = T$. With this choice the heat current in the probe is zero while it flows only between the two superconductors (see Appendix A.3 for more details). So the relevant responses are the charge current flowing in the probe J_N^c and the heat current flowing in one (say the left) superconductor [Lambert1998, Blanter2000]

$$J_L^h = \frac{1}{h}\sum_j \sum_{\alpha,\beta} \int_0^\infty d\epsilon\ \epsilon \left(f_L^\alpha(\epsilon) - f_j^\beta(\epsilon)\right) P_{L,j}^{\alpha,\beta}(\epsilon,\phi). \tag{8.8}$$

The electric current flowing between the superconducting leads is mainly dominated by the Josephson (equilibrium) current determined by the superconducting phase difference, unless it overcomes the value of the critical current of the junction. Hence, no linear thermovoltage response can take place between the two superconductors. Quantitatively, the linear response regime is thus characterized by the following relations [Benenti2017, Mazza2014, Roura-Bas2018, Hussein2019, Sanchez2018, Kirsanov2019]

$$
\begin{aligned}
J_N^c &= L_{11}(V_N/T) + L_{12}(\delta T/T^2)\\
J_L^h &= L_{21}(V_N/T) + L_{22}(\delta T/T^2).
\end{aligned}
\tag{8.9}
$$

where the Onsager coefficients L_{ij} have been already defined in Eq. (7.6). As already mentiond in Chap. 7, although the configuration contains three terminals, the relevant driving affinities for nonlocal thermoelectric response of this setup are only two namely V_N/T and $\delta T/T^2$. Hence, the Onsager matrix, with entries L_{ij}, is effectively 2×2 [Mazza2014, Benenti2017, Sanchez2015, Roura-Bas2018, Mani2018]. In this effective formulation one should remind that L_{12} and L_{21} are *nonlocal* thermoelectrical coefficients. In Fig. 8.3 the Onsager coefficients are plotted as functions of ϕ/π and the length measured as L/ξ. In Figs. 8.3(a),(b) and (c) we plot respectively, the local Onsager coefficients L_{11}, L_{22} and the nonlocal thermoelectrical coefficient L_{12} setting the strength of the coupling with the probe at an intermediate value $|t|^2 = 0.5$ [1] and the temperature fixed at $T/T_C = 0.4$ (the highest temperature at which the induced gap of the right and left superconductors remain approximately constant and equal to Δ). Notice that, by exploiting the aforementioned symmetries of the scattering coefficients, it can be shown that the off-diagonal nonlocal coefficients satisfy a generalized nonlocal Onsager symmetry relation $L_{12}(\phi) = L_{21}(-\phi) = -L_{21}(\phi)$, similarly to the case discussed in Chap. 7 [Blasi2020].

We observe that L_{11} (which is proportional to the conductance at the probe), is an even function [Jacquod2012] of ϕ and, for small length $L \ll \xi$, presents a minimum for $\phi \approx 0$ and a maximum at $\phi \approx \pm\pi$. Increasing the length L, the conductance become featureless and flat due to an effective averaging between the (increasing) number of available states involved in the transport. More interesting, instead, is the behavior of L_{22} and L_{12} which present a periodicity of one coherence length ξ as functions of the length of the junction [Sothmann2016]. This periodicity is determined by the oscillatory change of available states at energies $\epsilon \gtrsim \Delta$, which dominate the spectral contribution to the transport window, oscillating between a maximum to a minimum when the junction length changes by one ξ length. This effect is not present in L_{11} since it is mostly determined by subgap states given by the Andreev contributions. Remarkably, this oscillatory behavior affects also the thermal conductance ($\propto L_{22}$) which crucially differs from the nonlocal thermoelectric coefficient ($\propto L_{12}$) since the first is even with the phase bias ϕ while the latter is odd [Jacquod2012, Engl2011] (see Eq. (8.3)). The different symmetry in ϕ is due to the fact that QPs and QHs contribute with the same sign to the heat transport but with opposite sign to the thermoelectric current.

In Fig. 8.3 (d) we show how L_{12} changes with the coupling parameter $|t|^2$, keeping the length of the junction fixed to $L/\xi = 0.25$ (for which it is maximal, see Fig. 8.3 (c)). It emerges that the absolute value of the nonlocal Onsager coefficient L_{12} reaches its maximum for an intermediate value of the coupling parameter (i. e. $|t|^2 \approx 0.5$), while is zero either when $|t|^2 \to 0$ (when the probe is decoupled) or $|t|^2 \to 1$ (when the two superconductors are mutually decoupled). Notably, similar results for the nonlocal thermoelectrical coefficient L_{12} can be obtained in the case of 3DTI based Josephson junctions as shown in the Appendix B.

---

[1] The Onsager coefficients behave similarly to Figs. 8.3(a)–(c) for any value of $|t|^2 \neq 0, 1$.

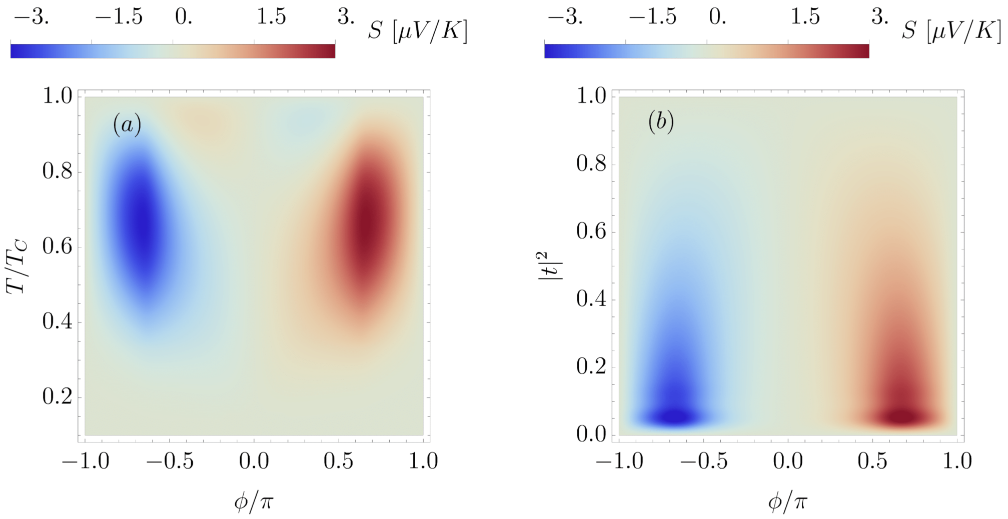

Figure 8.4: (a) Nonlocal Seebeck coefficient as function of ϕ/π versus T/T_C for $|t|^2 = 10^{-2}$. (b) Nonlocal Seebeck coefficient as function of ϕ/π versus the probe coupling $|t|^2$ for $T/T_C = 0.7$. Both (a)-(b) have been obtained for the same length $L/\xi = 0.25$.

8.7 Nonlocal Seebeck coefficient

As a final remark, it is important to give a realistic estimation of the strength of the thermoelectrical effect we are discussing. In this regard, we compute the nonlocal Seebeck coefficient (already defined in Eq. (7.7)) $S = (1/T)L_{12}/L_{11}$ [Benenti2017] as a function of ϕ (see Fig. 8.4). As a consequence of the latter relation, we notice that S, being proportional to L_{12}, stems from Andreev interference effetcs. In order to make realistic predictions in a wide temperature range, here we also include the temperature dependence of the gap order parameter [2]. Fig. 8.4 (a) shows that the nonlocal Seebeck coefficient grows with the operating temperature and reaches a maximum of 3 $\mu V/K$ roughly at $T/T_C \approx 0.7$ for $\phi/\pi \approx \pm 0.6$. At higher temperatures the gap closes reducing the nonlocal thermoelectricity, hence confirming the fundamental role of the superconducting state. It is important to notice that higher values of the nonlocal Seebeck coefficient can be obtained in the case of Josephson junctions based on 3DTIs, in which case it reaches a maximum of 20 $\mu V/K$ - see Appendix B.

Fig. 8.4 (b) (obtained for $T/T_C = 0.7$) shows how the nonlocal Seebeck effect scales with the probe coupling $|t|^2$ as a result of the scaling of the ratio L_{12}/L_{11}. At small coupling $|t|^2 \approx 10^{-2}$ it returns highest values. Notably these values of the phase-dependent nonlocal Seebeck coefficient are roughly 6% of the values determined by the Doppler shift mechanism discussed in Chap. 7 [Blasi2020] (see Fig. 7.6). The advantage in the present case, is that there is no need of any magnetic field since it is enough to impose a dissipationless current between the two superconductors to induce the phase bias ϕ. This experimental protocol seems quite attractive due to its simplicity and the absence of any spurious Nernst

---

[2] We took $\Delta(T) = \Delta_0 \tanh\left(1.74\sqrt{T_C/T - 1}\right)$, an approximation good at 2% with respect to the self-consistent BCS result (here we indicate with Δ_0 the zero-temperature value of the superconducting gaps) [Tinkham1966, Kamp2019]

effect [Ettingshausen1886, Behnia2016, Zuev2009, Zhu2010].

In Figs. 8.4 we considered the length of the junction $L/\xi = 0.25$. This situation is reasonable assuming a STM tip with state-of-the-art size of 100 nm and a coherence length ξ in the proximized TI of the order of 600 nm [Hart2014, Bocquillon2018]. Further, this choice of the length assures that the transport along the edge state is ballistic [Groenendijk2018] at the operating temperatures for our setup, typically of a few kelvins.

8.8 Conclusions

We have investigated a phase-dependent nonlocal thermoelectricity in a 2D topological Josephson junction coupled to a probe. We have shown that an Andreev interferometric mechanism affects QPs and QHs differently resulting in a nonlocal thermoelectric response. We have discussed the dependence of this mechanism over the junction length L and the coupling with the probe $|t|^2$. We have estimated, with realistic parameters, a nonlocal Seebeck coefficient of few $\mu V/K$ at temperatures of few kelvins. We underline that the provided estimations are quite conservative since the critical temperature T_C of the induced proximized gap is given by the critical temperature of the parent superconductors which is usually much higher further increasing the nonlocal Seebeck coefficient which is proportional to the operating temperature. Notice also that a nonlocal Seebeck coefficient of $\approx 20\ \mu V/K$ can be obtained in 3DTI based Josephson junction (see Appendix B).

Some of the experimental conditions for nonlocal Seebeck effect measurement are similar to the proposed measurements of heat conductance in topological Josephson junctions [Sothmann2016, Sothmann2017] but here we have discussed a mechanism which takes place in absence of any magnetic field. The investigation of the nonlocal character in thermoelectrical coherent devices may open novel possibilities in thermal management and quantum sensing.

9

Nonlocal thermoelectric engines in hybrid topological Josephson junctions

This chapter is based on the results published in the paper:
G. Blasi, F. Taddei, L. Arrachea, M. Carrega, and A. Braggio. *Nonlocal thermoelectric engines in hybrid topological Josephson junctions.* Phys. Rev. B, **103**, 235434 (2021).

Hybrid topological Josephson junctions have been actively investigated in the recent years [Sacepe2011, Veldhorst2012, Hart2014, Sochnikov2015]. In particular, their potential to localize Majorana fermions [Fu2008, Fu2009, Schrade2015, Stehno2016] could represent a novel platform for topological quantum computation [Virtanen2018, Hegde2020]. Topological Josephson junctions are also a unique resource in the field of low-temperature thermal management [Giazotto2006, Partanen2016, Fornieri2017, Bohling2018, Hwang2020], which could play an important role for quantum technologies in general. New applications based on the proximized helical edge states have been envisioned [Tkachov2015, Sothmann2016, Sothmann2017, Bours2018, Blasi2019, Vischi2019, Scharf2020]. For such cases a fundamental step is the capability to identify the helical nature of the edge states as result of the spin-momentum locking, determined by the topological protection [Moore2009, Hasan2010, Qi2011, Ando2013]. After the theoretical prediction [Kane2005, BHZ2006], experimental evidence [Konig2007, Roth2009, Brune2012] have been shown on the existence of edge states in several systems but not yet on their helical nature [Pribiag2015, Jia2017, Reis2017, Li2018, Wu2018, Shi2019, Liu2020]. For this purpose different strategies have been identified [Das2011, Mani2017]. In previous Chaps. 7 and 8, we have shown that the helical nature determines an unique signature in the thermoelectrical properties of topological Josephson junctions [Blasi2020, Blasi2020a].

Thermoelectricity is in itself an important trend in material science [Goldsmid2010], which found a renaissance in low-dimensional [Dresselhaus2007, Dubi2011] and quantum-based [Whitney2014, Sothmann2014, Kheradsoud2019] devices. The thermoelectric response in superconducting systems is expected to be negligible due to the particle-hole symmetry which is enforced by superconducting correlations as clearly shown in the BdG Hamiltonian [DeGennes1966]. Still, thermoelectric response of superconductors has a long history since Ginzburg's seminal work [Ginzburg1944] and following literature [Galperin1974, Shelly2016]. There are various strategies aimed at inducing thermoelectricity in superconducting or proximized systems by explicitly breaking the particle-hole symmetry by means of ferromagnetic correlations [Machon2013, Ozaeta2014, Kolenda2017, Shapiro2017, Keidel2020] and nonlocal geometries [Machon2013, Mazza2015, Heidrich2019] or by using nonlinearities [Sanchez2016, Pershoguba2019, Marchegiani2020a, Germanese2021]. Recently, several authors have discussed Andreev interferometers [Virtanen2004, Titov2008, Jacquod2010, Kalenkov2017, Kalenkov2020] and nonlocal thermoelectric effects in Cooper pair splitters [Hussein2019, Kirsanov2019], which found experimental confirmations [Eom1998, Parsons2003, Jiang2005, Tan2021]. The application of thermal gradients to Josephson junctions has also suggested novel technologies [Giazotto2015, Heikkila2018, Guarcello2018a, Hajiloo2019, Guarcello2019, Guarcello2019a, Marchegiani2020b, Marchegiani2020c], showing that the peculiar properties of topological Josephson junctions could also play an important role in this perspective [Bours2018, Bours2019, Kamp2019, Guarcello2020, Scharf2020, Scharf2021, Gresta-Blasi2021].

In this chapter we discuss how, in realistic situations, the nonlocal thermoelectric response is intimately connected to the helical nature of edge states in a topological Josephson junction (TJJ). In previous Chaps. 7 and 8 [Blasi2020, Blasi2020a], we analyzed a three terminal structure where the TJJ, obtained by proximizing the two ends of a 2DTI bar through superconducting electrodes, is contacted on one edge with a normal metal probe [Das2011, Liu2015, Hus2017, Voigtlander2018, Bours2018, Bours2019]. In this configuration there is a nonlocal thermoelectric response when a temperature bias is applied between the two superconductors, which consists in the occurrence of a current flowing in the probe. We note that in order to observe such nonlocal thermoelectric effect it is necessary to break the particle-hole symmetry at nonlocal level [Benenti2017]. This can be done by introducing a magnetic field orthogonal to the plane of the TI, which induces the so called Doppler shift (DS) of the TI bands [Blasi2020], or simply by applying [Blasi2020a] a Josephson phase difference ϕ, which may be generated by imposing a dissipationless current throughout the junction. In Chaps. 7 and 8 we assumed equal proximized gaps in the two superconducting right/left ends and we concentrated only on the linear regime. In this chapter we generalize to the case where we have different gaps, which better describes a realistic experimental situation [Guarcello2019, Guarcello2019a, Marchegiani2020, Marchegiani2020a], showing how the unique nonlocal signature survives in the asymmetric case. At the same time we take the opportunity to analyze in detail the nonlinear regime, discussing the thermodynamic performance of the nonlocal thermoelectric engine obtained in such configuration. Even if the analysis of this chapter focuses on the 2DTI case, we expect a similar physics to occur also in 3D topological surfaces, where Doppler shift effects can be induced [Yuan2018, Zhu2020] (see also Appendix B).

More specifically, in Sec. 9.1, we present the three terminal setup and introduce the model Hamiltonian. Notice that, it consists of the same system used in Chap. 7, except this time we consider the possibility of having superconductors with different gaps. By using the scattering approach, we discuss how the dissipative currents can be computed. In Sec. 9.2 we investigate the nonlocal Onsager coefficients in the linear-response regime and discuss how the junction asymmetry affects the nonlocal thermoelectricity. In Sec. 9.3 we study the performance quantifiers (electrical power, efficiency and nonlocal Seebeck coefficient) in the non-linear regime and in the presence of finite voltage bias and/or finite temperature difference between the two superconducting electrodes. In Sec. 9.4 we present the relevant conclusions concerning the nonlocal effects of the topological Josephson junctions and possible perspectives.

9.1 System and Model

We consider a TJJ which consists of two superconducting electrodes placed on top of a 2DTI at a distance L (see Fig. 9.1). The two electrodes induce superconducting correlations on the edge states via proximity effect [Tkachov2015, Sothmann2016]. A normal-metal probe is contacted to one side of the junction as depicted in Fig. 9.1, thus putting it in electrical contact with only one edge. In the setup, a voltage bias V_N may be applied between the probe N and the superconducting electrodes, which are equipotential and grounded. [1] The two superconductors are kept at different temperatures in order to maintain a thermal bias $\delta T = T_L - T_R$. A superconducting phase difference $\phi = \phi_L - \phi_R$ is also applied between the two. We fix the temperature of the probe at the average temperature $T_N = (T_L + T_R)/2 = T$. As we will see below, this choice is the most convenient experimental one in order to extract the nonlocal signal. The width of the TI strip is assumed to be large enough such that we can neglect the lower edge, i.e. we focus only on the upper one.

The proximized system in the upper-edge can be described by the following Bogoliubov-de Gennes (BdG) Hamiltonian

$$H_{BdG} = \begin{pmatrix} H(x) & i\sigma_y \Delta(x) \\ -i\sigma_y \Delta(x)^* & -H(x)^* \end{pmatrix}, \tag{9.1}$$

expressed in the four-component Nambu basis $(\psi_\uparrow, \psi_\downarrow, \psi_\uparrow^*, \psi_\downarrow^*)^T$ with spin $\uparrow$ and $\downarrow$ collinear with the natural spin quantization axis of the TI edge pointing along the z-direction. In Eq. (9.1) $H(x) = v_F\,(-i\hbar\partial_x + p_{DS}/2)\,\sigma_z - \mu\sigma_0 + \Lambda(x)$ is the low-energy effective Hamiltonian of a 2DTI, with $-H(x)^*$ being its time-reversal partner. Here v_F indicates the Fermi velocity, μ is the chemical potential and σ_i are the Pauli matrices. The momentum $p_{DS} = (\pi\hbar/L)(\Phi/\Phi_0)$ represents the so-called DS contribution describing the gauge invariant shift of momentum induced by a small magnetic flux Φ threading the weak link, while $\Phi_0 = h/2e$ is the magnetic flux quantum [Tkachov2015]. A contact potential $\Lambda(x) = \Lambda_L\delta(x) + \Lambda_R\delta(x-L)$ is also included at the junction boundaries. $\Delta(x)$ is the superconducting order parameter which is assumed to obey rigid boundary conditions: $\Delta(x) = \Delta_L\Theta(-x)e^{i\phi_L} + \Delta_R\Theta(x-L)e^{i\phi_R}$, where $\Theta(x)$ is the step function and Δ_i (with $i = L/R$) is the proximity induced gap for the left and right superconducting regions. The two gaps can indeed be different for many reasons. For example, the two superconductors may be made of different materials [Tinkham1966], or the two superconducting films might have different thicknesses [Chubov1969, Meservey1971, Ilin2004], or the two S-TI interfaces might be made of different quality [McMillan1968, Maier2012]. Moreover, in realistic experimental conditions, the finite temperature difference in the non-linear regime may induce the superconducting gaps to take different values on the two sides [Tinkham1966]. In the latter case, in order to make realistic predictions in a wide temperature range, we need to include the self-consistent temperature dependence of the gaps. Despite these facts, a careful study of topological Josephson junctions with asymmetric gaps

---

[1] Keeping the two superconductor equipotentials is important in order to *not* induce time dependent Josephson effect.

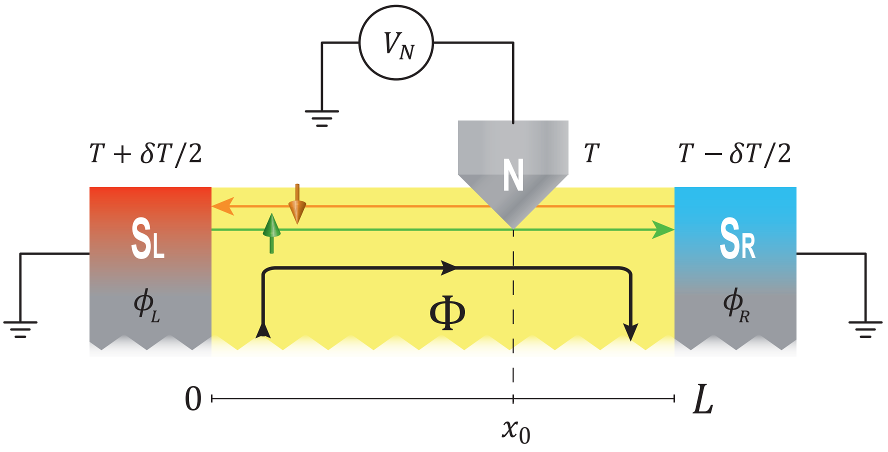

FIGURE 9.1: Sketch of the setup. It consists of the same system used in Chap. 7 (see Fig. 7.1), except this time we consider the possibility of having superconductors with different gaps. A helical Kramers pair of edge states of a quantum spin Hall bar is put in contact with two superconductors at different temperatures $T_L = T + \delta T/2$ and $T_R = T - \delta T/2$. A bias voltage V_N is applied to the normal-metal probe coupled to the edge at the point x_0 and kept at temperature $T_N = T$. L is the length of the junction. The structure is threaded by a magnetic flux Φ which induces a Doppler shift in the edge states in addition to a Josephson phase difference $\phi \equiv \phi_L - \phi_R$ applied between the two superconductors. The green arrow depicts spin-↑ right-moving quasi-particles, the orange arrow indicates spin-↓ left-moving quasi-particles.

is something not frequently done in literature, even if non-identical gaps may introduce many unexpected not trivial effects especially when Doppler shift effects are involved.

The eigenspectrum of the BdG Hamiltonian relative to a homogeneously proximized 2DTI upper edge is given by $E^{i\chi}_{\pm}(k) = \left(\epsilon_{DS}(\Phi) + \chi\sqrt{(\hbar v_F k \mp \mu)^2 + \Delta_i^2}\right)$. Here the lower index $\pm$ labels the right/left parabola, $\chi = \pm$ indicates branches with positive/negative concavity, $i = L, R$ for the left and right superconducting regions and $\epsilon_{DS}(\Phi) = v_F p_{DS}/2 = (v_F h/4L)(\Phi/\Phi_0)$ is the DS energy. The effect of the DS on the dispersion curve is to shift the various branches vertically by an amount $\epsilon_{DS}(\Phi)$, upwards or downwards, as shown in the example of Fig. 9.2, where we plot the dispersion curves for the three regions composing the TJJ. As a consequence, a finite value of the magnetic flux Φ reduces the gap in the eigenspectrum, which eventually closes when $|\epsilon_{DS}(\Phi)| = \Delta_{L/R}$ in the left/right superconducting regions of the 2DTI, respectively. Clearly, when the values of Δ_L and Δ_R are different, such a gap closing in the left and right regions occurs at different values of the flux Φ.

The eigenfunctions of the electron-like Bogoliubov quasiparticles (QPs) of the BdG Hamiltonian for both left/right ($i = L/R$) superconducting regions can be written, in Nambu notation, as

$$\begin{aligned}\Psi^{i,\chi}_{e+} &= (\chi u_{i-} e^{i\frac{\phi_i}{2}}, 0, 0, v_{i-} e^{-i\frac{\phi_i}{2}})^T e^{ik^{i\chi}_{e+} x} \\ \Psi^{i,\chi}_{e-} &= (0, -\chi u_{i+} e^{i\frac{\phi_i}{2}}, v_{i+} e^{-i\frac{\phi_i}{2}}, 0)^T e^{ik^{i\chi}_{e-} x},\end{aligned} \tag{9.2}$$

where the energy-dependent coherence factors (spinor components) are

$$u_{i\pm} = \sqrt{\frac{\Delta_i}{2\epsilon_\pm}} e^{\frac{1}{2} h_i(\epsilon_\pm)}; \quad v_{i\pm} = \sqrt{\frac{\Delta_i}{2\epsilon_\pm}} e^{-\frac{1}{2} h_i(\epsilon_\pm)}, \tag{9.3}$$

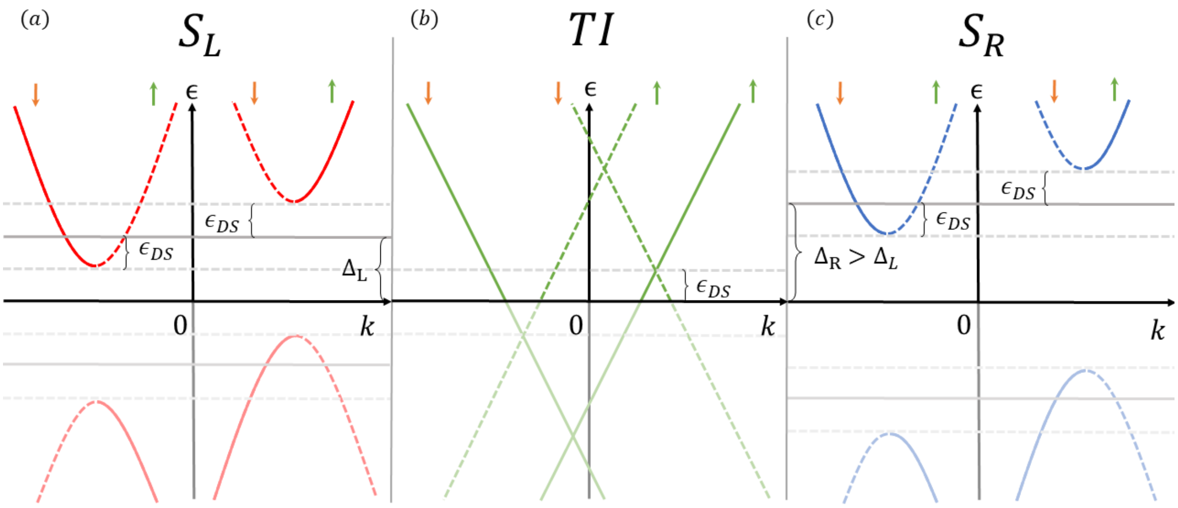

FIGURE 9.2: Dispersion curves for QPs (solid lines) and QHs (dashed lines) in the left [panel (*a*)] and right [panel (*c*)] proximized regions, and in the weak link TI region [panel (*b*)], for $0 < \epsilon_{DS}(\Phi) < \Delta_L$ (with $\Delta_R > \Delta_L$). Green arrows represent spin-↑ right-moving QPs, while orange arrows spin-↓ left-moving QPs.

with $\epsilon_\pm = \epsilon \pm \epsilon_{DS}(\Phi)$ and $h_i(\epsilon_\pm) = \text{arcCosh}\,(\epsilon_\pm/\Delta_i)$ for $\epsilon_\pm > \Delta_i$ and $h_i(\epsilon_\pm) = i \arccos\,(\epsilon_\pm/\Delta_i)$ for $\epsilon_\pm < \Delta_i$. The QP's momentum is $k^{i\chi}_{e\pm} = \pm k_F(\chi\sqrt{(\epsilon^2_\mp - \Delta^2_i)/\mu^2 + 1})$, while the related group velocity is $w^{i\chi}_{e\pm} = \hbar^{-1}|\partial_k E^{i\chi}_\pm| = v_F(u^2_{i\mp} - v^2_{i\mp})$. The eigenfunctions $\Psi^{i,\chi}_{h\pm}$ relative to QHs can be obtained by replacing $(u_{i\pm}, v_{i\pm}) \to (v_{i\pm}, u_{i\pm})$, $k^{i\chi}_{e\pm} \to k^{i\chi}_{h\mp} = k^{i,\bar{\chi}}_{e\pm}$ (with $\bar{\chi} = -\chi$) and $w^{i\chi}_{e\pm} \to w^{i\chi}_{h\mp} = w^{i\chi}_{e\pm}$ in the expressions of Eq. (9.2). Clearly, the limit $\Delta_i \to 0$ returns the standard 1D Dirac spectrum [shown in Fig. 9.2(*b*)] which characterizes the 2DTI (non-proximized) edge.

The normal-metal probe N – which would model for instance a STM tip [Das2011, Liu2015, Hus2017, Voigtlander2018] – is assumed to be directly contacted to the upper edge at the point x_0 (see Fig. 9.1) and modelled by an energy- and spin-independent transmission amplitude t (see Appendix A).

9.1.1 Charge and Heat Currents

In the following we will investigate only the dissipative currents flowing through the structure which can be obtained by using the Landauer-Büttiker scattering [Blanter2000] formalism generalized in order to include superconductivity [Lambert1998]. More precisely, we are not interested in the dissipationless (Josephson) contribution to the charge current flowing in the superconducting electrodes, which has been already discussed elsewhere [Tkachov2013, Snelder2013, Sochnikov2015, Dolcini2015, Kurter2015, Marra2016, Stehno2016, Scharf2020]. The dissipative charge current J^c_N at lead N and heat currents J^h_i exiting from leads $i = L, R, N$ can be written in the following compact form

$$\begin{bmatrix} J^c_N \\ J^h_i \end{bmatrix} = \frac{1}{h}\sum_j \sum_{\alpha,\beta} \int_0^\infty d\epsilon \begin{bmatrix} \alpha e \\ (\epsilon - \alpha\mu_i) \end{bmatrix} F^{\alpha\beta}_{ij}(\epsilon) P^{\alpha,\beta}_{i,j}(\epsilon, \vec{\theta}), \tag{9.4}$$

with $\alpha, \beta = +/-$ for QPs and QHs respectively, and where we set $\mu_N = eV_N$ and $\mu_L = \mu_R = 0$. The function

$$F_{ij}^{\alpha\beta} = f_i^{\alpha}(\epsilon) - f_j^{\beta}(\epsilon) \tag{9.5}$$

is a compact way to write differences of the generalized Fermi functions $f_i^{\alpha}(\epsilon) = \{e^{(\epsilon-\alpha\mu_i)/k_B T_i}+1\}^{-1}$, where T_i represents the temperature of lead i. In Eq. (9.4) the most important physical quantities are the scattering coefficients $P_{i,j}^{\alpha,\beta}(\epsilon, \vec{\theta})$ which are calculated from the scattering matrix $S_{(i,\sigma),(j,\sigma')}^{\alpha,\beta}$ as follows (see Sec. 4.3)

$$P_{i,j}^{\alpha,\beta}(\epsilon, \vec{\theta}) = \sum_{\sigma,\sigma'} \left| S_{(i,\sigma),(j,\sigma')}^{\alpha,\beta}(\epsilon, \vec{\theta}) \right|^2 \tag{9.6}$$

[see Appendix A.1 for the details of the computation and Appendix A.2 for the discussion of the special symmetries of the scattering coefficients in the symmetric case (i. e. when $\Delta_L = \Delta_R$)]. The scattering coefficients $P_{i,j}^{\alpha,\beta}(\epsilon, \vec{\theta})$ represents the reflection ($i = j$) or transmission ($i \neq j$) probability of a QP of type β injected from lead j to end up as a QP of type α in lead i. We introduced the vector parameter $\vec{\theta} \equiv (\Phi, \phi)$ which includes both the magnetic flux Φ and the gauge invariant Josephson phase difference $\phi \equiv \phi_L - \phi_R$. The two quantities should be treated independently, since Φ depends directly on the magnetic-field flux in the junction, while the phase bias ϕ depends also on the dissipationless current imposed through the junction. They represent two different degrees of freedom needed to fully characterize the state of the TJJ. Their difference is reflected in the fact that the observables relative to the Josephson junction are 2π-periodic with respect to phase bias ϕ (as required by the gauge invariance), but are not periodic in the flux bias Φ (once the gap is closed it does not open again). Moreover, there is another important difference between the two quantities: the flux bias operates differently on the two opposite helical edges states of the TI, while the phase bias affects the two edges in the same way.

Finally, it is worth to notice that there is no dependence of the scattering coefficients on the contact potential [BTK1982] parameters Λ_i. [2]. This is a direct consequence of the helicity of the edge channels which do not admit ordinary reflections at barriers (akin to the Klein paradox) [Lee2019].

9.2 Linear response regime

The occurrence of a nonlocal thermoelectric response in the presence of a DS [Blasi2020] or of a phase difference [Blasi2020a] was discussed in the previous Chaps. 7 and 8, where - for simplicity - only the symmetric case of equal gaps $\Delta_L = \Delta_R$ was considered. We refer to the Appendix A.3 for a thorough discussion of such symmetric case, which complete the analysis done in Chap. 8 by presenting the analytical expressions of the heat and charge currents flowing through the probe obtained in the general case in which both the DS and the phase bias are present.

In this section we explore the asymmetric case (where $\Delta_L \neq \Delta_R$). This is not a mere generalization of previous results, since it provides important information relevant for realistic (experimental) realizations. Indeed, when one of the two temperatures T_i is bigger than $0.4T_{C,i}$ (with $T_{C,i}$ being the critical temperature of the i-th superconductor) the self-consistent

---

[2] This can be checked directly from the analytic expressions of the scattering coefficients, not reported here for brevity. The independence of Λ_i is a generic result valid also with other form – not delta like – of the interface potential at least in the absence of interaction.

gap $\Delta_i(T_i)$ gets reduced from the zero-temperature value $\Delta_{i,0}$ and the right-left symmetric gap condition is hardly valid [Tinkham1966].

Let us first clarify which is the relevant thermoelectrical response for the three terminal setup depicted in Fig. 9.1. We use the approach developed in Ref. [Mazza2014] to investigate thermoelectrical properties for multiterminal systems [Benenti2017]. The first step is to identify the independent currents. Since charge and energy must be conserved, we are only left with 4 independent currents, out of 6 (3 charge currents and 3 heat currents). In our three-terminal Josephson junction setup we consider the case of a stationary superconducting phase bias ($\dot{\phi} = 0$), which indeed necessarily requires $V_L = V_R$.[3] In such configuration the charge current flowing in the two superconductors is dominated by the dissipationless Josephson current which, in the linear response regime, is unaffected by the temperature difference between the electrodes. In the following, in analogy to Chaps. 7 and 8, we mainly discuss the only relevant currents which allow us to characterize the nonlocal thermoelectric response of our setup. These are the charge current (J_N^c) flowing in the normal probe and the heat current associated to the superconductors (see below for the proper definition). Moreover, interesting features emerge also from the analysis of the linear heat current (J_N^h) flowing in the normal probe, which will be presented for completeness in Sec. 9.2.5.

9.2.1 Nonlocal thermoelectric and Peltier coefficients

For small values of V_N and δT, the charge current J_N^c can be expanded up to the linear order in these quantities [Benenti2017, Mazza2014, Roura-Bas2018, Hussein2019, Sanchez2018, Kirsanov2019]. The charge current for the probe reads

$$J_N^c = L_{11}^N \frac{V_N}{T} + L_{12}^N \frac{\delta T}{T^2}, \tag{9.7}$$

with V_N/T and $\delta T/T^2$ taking the role of the relevant affinities of the problem, while L_{11}^N and L_{12}^N are linear transport coefficients defined as (using the notation of Sec. 5.3)

$$L_{11}^N = L_{NN}^{cc}, \qquad L_{12}^N = (L_{NL}^{ch} - L_{NR}^{ch})/2. \tag{9.8}$$

We note that the electrical response to the bias V_N is given by the conductance $G = L_{11}^N/T$, while the linear response to δT (temperature difference between the superconductors) corresponds to a *nonlocal* thermoelectric current, represented by the coefficient L_{12}^N. It is important to stress now that in the linear-response regime the system is close to equilibrium. As a result, the temperature of the probe needs to be set to its equilibrium value, namely $T_N = T$. By setting $J_N^c = 0$ in Eq. (9.7) and solving for V_N one finds the linear Seebeck thermovoltage V_N^S, through which we can compute the *nonlocal* Seebeck coefficient $S = -V_N^S/\delta T = (1/T)L_{12}^N/L_{11}^N$, similarly to the derivation of the local case.

Let us now consider the heat currents. In the symmetric case ($\Delta_L = \Delta_R$) and for $T_N = T$, the heat current flowing in left superconducting lead J_L^h is exactly opposite to the current flowing in the right lead J_R^h, namely $J_L^h = -J_R^h$, while $J_N^h = 0$ (i.e. there is no heat current at the probe), due to the symmetries of the configuration, see Appendix A.3 for details. When the left-right symmetry is broken ($\Delta_L \neq \Delta_R$), the two superconducting terminals are no more equivalent and the heat currents in the two superconducting terminals are different. In such a case it is convenient to describe the heat current associated to the two superconductors by the average

$$J_S^h \equiv \frac{J_L^h - J_R^h}{2}. \tag{9.9}$$

---

[3] This is an implicit consequence of the Josephson relation which states $\dot{\phi} = 2e(V_L - V_R)/\hbar$.

In the linear-response regime it is expressed as

$$J_S^h = L_{21}^S \frac{V_N}{T} + L_{22}^S \frac{\delta T}{T^2}, \tag{9.10}$$

where we defined

$$L_{21}^S = (L_{LN}^{hc} - L_{RN}^{hc})/2, \qquad L_{22}^S = \left[(L_{LL}^{hh} - L_{LR}^{hh})/2 + (L_{RR}^{hh} - L_{RL}^{hh})/2\right]/2. \tag{9.11}$$

Notice that, Eq. (9.11) reduces to Eq. (7.6) for symmetric gaps (i e. $\Delta_L = \Delta_R$), in which case it turns out that $L_{RN}^{hc} = -L_{LN}^{hc}$, $L_{RR}^{hh} = L_{LL}^{hh}$ and $L_{RL}^{hh} = L_{LR}^{hh}$. The last term in Eq. (9.10) is the *local* heat conductance $\kappa = L_{22}^S/T^2$ between the two terminals, while the first term represents the *nonlocal* Peltier-like contribution. We notice that, in general, for a multi-terminal system [Mazza2014] one does not expect any specific symmetry relation between the nonlocal linear coefficients. However, with the definition of Eq. (9.9), the Onsager-Casimir relations [Onsager1931, Casimir1945, Jacquod2012, Benenti2017] (see Sec. 5.3) for the linear coefficients defined by Eqs. (9.7) and (9.10) can be expressed in the following form: $L_{12}^N(\vec{\theta}) = -L_{21}^S(\vec{\theta})$. In the next section we will numerically verify that such a relation holds independently of the ratio between the gaps.

We will divide the analysis in two limiting situations. In the first case we will discuss the Onsager coefficients as functions of the DS in absence of any phase-bias, i.e. $\phi = 0$. In the second case, instead, we analyze how in an extremely asymmetric case the thermoelectrical effect depends on the phase bias in absence of the DS ($\Phi = 0$). In real experiments the discussed effects, which are different aspects of the nonlocal thermoelectricity, are probably mixed but it is interesting to discuss them separately in order to clearly recognize their contributions to the nonlocal thermoelectrical signal.

9.2.2 Asymmetric case for $\phi = 0$

In this section we investigate the linear transport coefficients in the case where the right/left symmetry is broken by different zero-temperature superconducting gaps ($\Delta_{0,R} \neq \Delta_{0,L}$), and we define the ratio $\delta \equiv \Delta_{0,R}/\Delta_{0,L} = \xi_L/\xi_R$ where the second identity is expressed in terms of the coherence lengths $\xi_i = \hbar v_F/\pi\Delta_{0,i}$, with $i = R, L$. We notice that, when $\delta \neq 1$, the scattering coefficients $P_{i,j}^{\alpha,\beta}$ of Eq. (9.6) depend on the position of the probe. This is different from the left/right symmetric case (when $\delta = 1$) in which the scattering coefficients do not depend on the position x_0 of the probe, but simply on the total length L of the junction (see Appendix A.2 for more details). For the sake of convenience, hereafter we consider the probe positioned exactly in between the two superconductors (i. e. $x_0 = L/2$) and we fix $\delta \geq 1$. [4]

The behavior of the linear coefficients $L_{ij}^{N/S}$ of Eqs. (9.7) and (9.10) is shown in Fig. 9.3 as a function of the DS $\epsilon_{DS}(\Phi)/\Delta_{0,L}$ and of the asymmetry parameter δ, for fixed phase bias $\phi = 0$. The local coefficients L_{11}^N and L_{22}^S are plotted in units of $G_0 T$ and $G_T T^2$, respectively, where G_0 denotes the electrical conductance quantum and $G_T = (\pi^2/3h)k_B^2 T$ the thermal one. The nonlocal thermoelectrical coefficients L_{12}^N and L_{21}^S are plotted in units of $\sqrt{G_0 G_T T^3}$. In these plots, we consider an intermediate coupling parameter to the probe ($|t|^2 = 0.5$) and set the length of the junction three times longer than the superconducting coherence length, i.e. $L/\xi_L = 3$. Such a value of L corresponds to the case of a long junction (given a coherence length ξ_L in the proximized TI of the order of 600 nm), which allows the emergence of oscillations in the linear-response coefficients due to the proliferation of

---

[4] The same results are obtained for $\delta \leq 1$ by inverting the temperature bias and the sign of $\vec{\theta}$.

resonant states in the junction. The choice of the value $|t|^2 = 0.5$ comes from the fact that, by increasing the coupling $|t|^2$, the resonances get broadened, eventually disappearing when the coupling approaches unity, irrespective of the length L (not shown).

Assuming $\Delta_{0,L} < \Delta_{0,R}$ (namely $\delta > 1$), it turns out that the DS energy $\epsilon_{DS}(\Phi)$, modulated by the flux Φ, modifies the dispersion curves of Fig. 9.2 in a different way for the right and left superconductor. In particular, for $|\epsilon_{DS}(\Phi)| < \Delta_{0,L}$ the spectrum is gapped for energies $\epsilon < \Delta_{0,L} - |\epsilon_{DS}(\Phi)|$ in both superconducting leads. For $\Delta_{0,L} < |\epsilon_{DS}(\Phi)| < \Delta_{0,R}$ we are in a situation where the gap is closed for the left superconductor, but open for the right one. Finally when $|\epsilon_{DS}(\Phi)| > \Delta_{0,R}$ the gaps are closed for both sides of the junction.

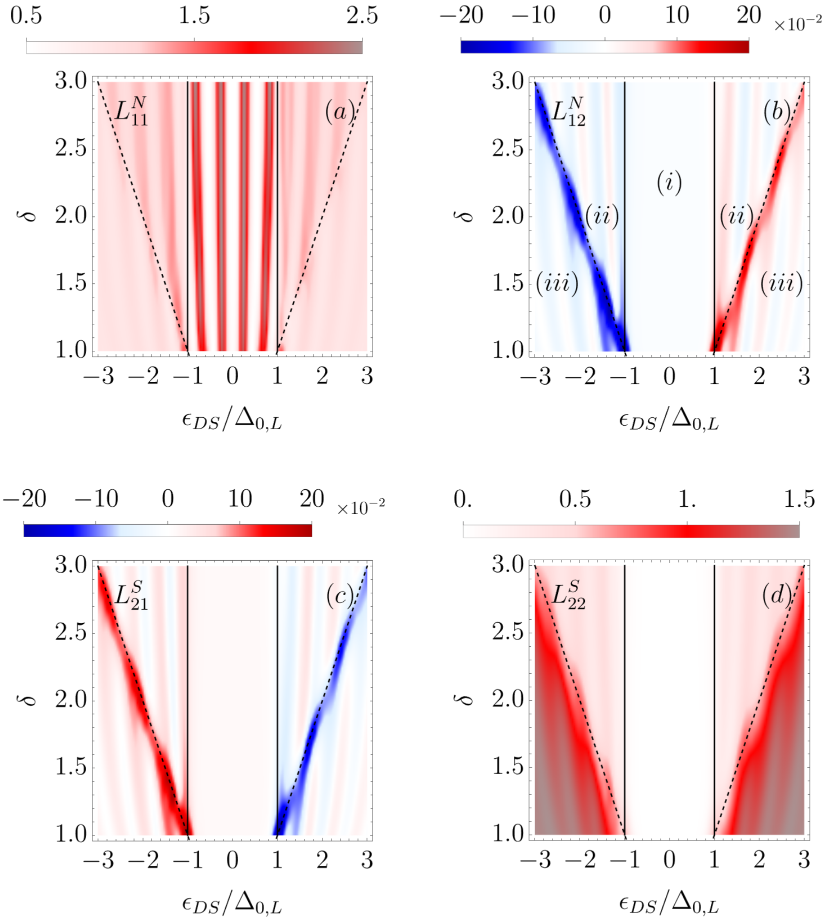

FIGURE 9.3: Onsager coefficients L_{11}^N (a), L_{12}^N (b), L_{21}^S (c) and L_{22}^S (d) as functions of $\epsilon_{DS}(\Phi)/\Delta_{0,L}$ and $\delta = \Delta_{0,R}/\Delta_{0,L}$ for $\phi = \phi_L - \phi_R = 0$, $T/T_{C,L} = 0.1$, $L/\xi_L = 3$ and $|t|^2 = 0.5$. Such quantities are normalized as follows: $L_{11}^N/(G_0 T)$, $L_{22}^S/(G_T T^2)$ and $(L_{12}^N, L_{21}^S)/(\sqrt{G_0 G_T T^3})$.

These different regimes can be recognized in the behavior of the Onsager coefficients, depicted in Fig. 9.3, computed at low temperature $T/T_{C,L} = 0.1$ (with $T_{C,L}$ the critical temperature of the left superconductor). In particular we recognize a subgap region (i) (between vertical solid lines) for $|\epsilon_{DS}(\Phi)/\Delta_L| < 1$, a partially gapped region (ii) (between the dashed and solid lines) and the supragap region (iii) (below diagonal dashed lines). Notice that the clear distinction of the different regions emerging in the behavior of all the Onsager coefficients of Fig. 9.3 can be used, in principle, as an experimental observation of the different zero temperature gaps of the superconductors forming the junction.

For the electrical coefficient L^N_{11}/G_0T, depicted in Fig. 9.3(a), we can recognize a similarity with SINIS (superconductor-insulator-normal metal-insulator-supercondutor) junctions where transport is typically suppressed in the subgap regime (i), though resonances are present (vertical red stripes) that correspond to Andreev bound states (ABSs) crossing zero energy. We checked that the linewidth of ABS resonances depends on the coupling parameter (by increasing the coupling $|t|^2$ the resonances broaden). Furthermore, the number of resonances inside the region (i) grows with the ratio L/ξ_L due to the proliferation of ABSs in the junction (not shown). Similarly, in the partially gapped (ii) and the supragap (iii) regions we see a weak oscillating behavior (vertical stripes) reminiscent of Andreev interferometric effects. On the other hand, we observe that the thermal coefficient L^S_{22}/G_TT^2 [Fig. 9.3(d)] is completely suppressed in region (i) since, in this case, the ABS resonances cannot contribute to thermal transport due to the Andreev mirror effect. Indeed, Andreev reflection does not allow the flow of energy through the S interface, since energy is carried by QPs, but not by the condensate. However, the thermal conductance becomes finite and large in the supragap region (iii) where energy can be carried by QPs. In the region (ii) the thermal transport between the two superconductors is not completely suppressed and it is influenced by an Andreev interferometric mechanism which determines an oscillating behavior.

Concerning the nonlocal coefficients L^N_{12} and L^S_{21}, depicted in Fig. 9.3(b) and (c) respectively, we confirm the validity of the discussed generalized Onsager symmetry which becomes $L^N_{12}(\Phi) = -L^S_{21}(\Phi)$ (being here $\phi = 0$). The nonlocal coefficients clearly resemble some aspects of those discussed in Chap. 7 for identical gaps. In particular, L^N_{12} is suppressed in the subgap region (i) and two main peaks at $|\epsilon_{DS}(\Phi)| = \Delta_{0,R}$ appear at the boundaries of regions (ii) and (iii) (dashed lines). In this condition, for $\epsilon_{DS} > 0$ ($\epsilon_{DS} < 0$), the top left (top right) band of the right proximized region in Fig. 9.2(c) nearly touch zero energy opening the possibility for thermoelectrical effects. In particular, the helicity of the edge states allows (for example, for $\epsilon_{DS} > 0$) a flow of QHs [whose dispersion is represented by the dashed red curve in Fig. 9.2(a)] to move to the right from the proximized region S$_L$ and a flow of QPs [whose dispersion is represented by the solid blue curve in Fig. 9.2(c)] to move to the left from the proximized region S$_R$. Under the application of a small temperature bias between the superconductors, the unbalance between the flow of cold QPs from the right and hot QHs from the left leads to a net thermoelectric current flowing through the probe [Blasi2020].

9.2.3 Interference character of Doppler shift in region (ii)

The true novel feature of the asymmetric case is represented by the appearance of a finite thermoelectric contribution ($L^N_{12} \neq 0$) in region (ii) [see Fig. 9.3(b)], where the right superconductor is still gapped. In such a case the situation resembles the Andreev interferometric mechanism of Chap. 8, even if in this case $\phi = 0$. In this respect, the presence of a finite thermoelectric effect in region (ii) allows us to single out the Andreev interferential character of the Doppler shift effect (which contributes as an effective finite phase bias) from that of band-shifting. Notice that this effect, in principle, is also present in the subgap region (i) even if it is exponentially suppressed as $\sim e^{-(|\epsilon_{DS}(\Phi)|-\Delta_L)/k_BT}$. Indeed, only the supragap states contribute to thermoelectricity as long as they are thermally activated. This behavior is clarified by investigating the evolution of L^N_{12} for different temperatures. Figure 9.4 represents a horizontal cut of Fig. 9.3(b) at $\delta = 2$ for four different values of the temperature T [the blue curve corresponds to the data plotted in Fig. 9.3(b)]. When the temperature increases,

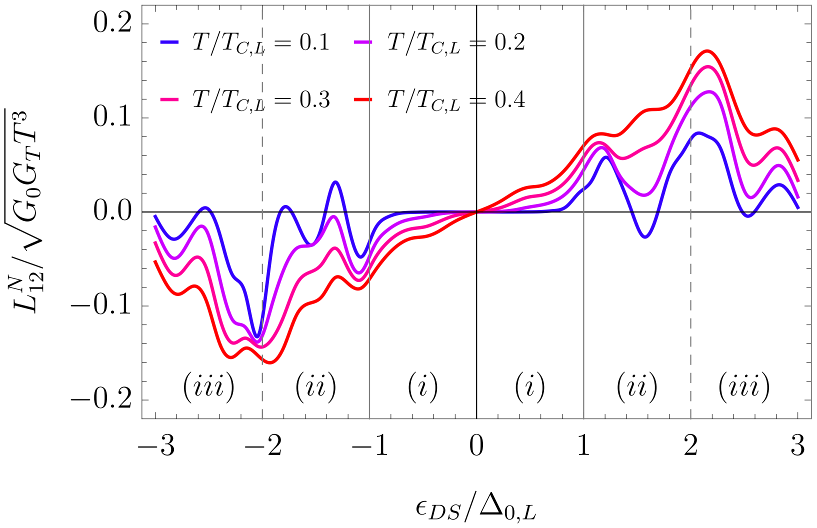

Figure 9.4: Nonlocal thermoelectrical coefficient L_{12}^N, expressed in units of $\sqrt{G_0 G_T T^3}$, as a function of $\epsilon_{DS}(\Phi)/\Delta_{0,L}$ for $\delta = 2$ and different temperatures. We see that also in the subgap region $L_{12}^N \neq 0$ when temperature increase. Parameters are as in Fig. 9.3.

L_{12}^N also increases even in the subgap region (i). Furthermore, for higher temperatures all the resonances are smoothened due to the averaging between different energies.

At the lowest temperature L_{12}^N presents changes of sign which disappear for higher values of T. This can be understood by noting that the sign of L_{12}^N directly reflects the nature of the dominant carriers in the junction. For $k_B T \ll \Delta_{0,L}$ and for $|\epsilon_{DS}| \lesssim \Delta_{0,R}$, only one type of carries, coming from the superconductor with the smaller gap, are allowed for the transport within the energy window $0 \leq \epsilon \lesssim k_B T$ (see Fig. 9.2): namely QHs (QPs) for $\epsilon_{DS} > 0$ ($\epsilon_{DS} < 0$). This flux of QHs (QPs) is contrasted by an opposite flux of QPs (QHs) originated due to Andreev reflections occurring at the interface with the other superconductor which is still gapped in that energy window. The (nontrivial) unbalance between these positive and negative charged carries determines the sign of the charge current flowing inside the probe and thus the sign of L_{12}^N.

As a final remark, it is important to notice that, differently from the results discussed in Chap. 7 for identical gaps where L_{12}^N was an odd function of Φ (namely $L_{12}^N(\Phi) = -L_{12}^N(-\Phi)$), in the asymmetric case (i. e. $\Delta_L \neq \Delta_R$) $L_{12}^N(\Phi)$ does not manifest any particular symmetry under the inversion $\Phi \to -\Phi$ (as clearly emerges from Fig. 9.4). This is due to the fact that in the symmetric case there are extra symmetries in the scattering coefficients, as discussed in Appendix A.2.

9.2.4 Asymmetric case for $\Phi = 0$: interference effects on local thermoelectricity

Let us first recall that in Chap. 8 we have shown that a finite ϕ alone, i.e. even in the absence of the DS, is sufficient to establish a nonlocal thermoelectric response due to an Andreev interferometric effect. Here we demonstrate that Andreev interferometry generates another peculiar effect that contributes to L_{12}^N, which emerges only by increasing the left/right asymmetry. We consider the extreme situation in which $\Delta_{0,R} \to \infty$ (i. e. $\delta \to \infty$), so that we can neglect all the contributions from the QPs on the right side, allowing us to obtain a simple analytical result for the charge current at probe J_N^c. In other words we are focusing on the regime where $k_B T_L, \Delta_L \ll \Delta_R$. As a consequence of that choice, the temperature T_R will not even enter in the discussion. Therefore, the only thermal bias capable to drive a thermoelectric current through the probe is the local one present between the left superconductor S_L and the probe N itself. Interestingly, the right superconductor S_R, even if it does not directly contribute to the energy transport (being fully gapped), still influences the exchange of charge between the N and S_L through the Andreev reflection processes occurring at the interface with S_R. The resulting dependence of the current J_N^c on the phase difference ϕ, see below, is due to the Josephson coupling established between the two superconducting leads. Notice that this interference (coherent) effect on the local thermoelectricity between N and S_L can be controlled by the application of a dissipationless current between the two superconductors, which changes the phase difference ϕ. The charge current at the probe takes the form

$$J_N^c = \frac{e}{h}\int_0^{\Delta_L} d\epsilon\; F_{NN}^{+-}(\epsilon)\,[\mathcal{A}(\epsilon,\phi)+\mathcal{A}(\epsilon,-\phi)] + \frac{e}{h}\sum_{\sigma,\sigma'=\pm}\int_{\Delta_L}^{\infty} d\epsilon\;\sigma\;|r|^{|\sigma-\sigma'|}\;F_{NL}^{\sigma,\sigma'}(\epsilon)\;\mathcal{Q}(\epsilon,-\sigma'\phi) \tag{9.12}$$

where the first term is the subgap energy contribution and the function

$$\mathcal{A}(\epsilon,\phi) = \frac{2|t|^4\,\cdot\,\Theta(\Delta_L-\epsilon)}{1+|r|^4+2|r|^2\cos\left(2\pi\frac{L\epsilon}{\hbar v_F}+\phi+\arcsin\left(\frac{\epsilon}{\Delta_L}\right)\right)},$$

with $|r|^2 = 1-|t|^2$. Such first term vanishes when $V_N = 0$, since $F_{NN}^{+-} = 0$ in that case (see Eq. (9.5)). The second term, instead, collects all the contribution for energies above the left gap and the function

$$\mathcal{Q}(\epsilon,\phi) = \frac{\left(g(\epsilon)^2-1\right)\;\cdot\,\Theta(\epsilon-\Delta_L)}{g(\epsilon)^2+|r|^4-2g(\epsilon)|r|^2\sin\left(2\pi\frac{L\epsilon}{\hbar v_F}+\phi\right)}, \tag{9.13}$$

with $g(\epsilon) = e^{\mathrm{arcCosh}(\epsilon/\Delta)}$. Note that in Eq. (9.12) the function $F_{NL}^{\alpha\beta} = f_N^{\alpha}(\epsilon) - f_L^{\beta}(\epsilon)$ involves only the electrodes N and S_L. From Eq. (9.12) it is possible to derive the analytical expressions of the Onsager coefficients L_{11}^N and L_{12}^N of Eq. (9.7) in the case $V_N, \delta T \to 0$:

$$L_{11}^N = -\frac{e^2}{h}\int_0^{\Delta_L} d\epsilon\; 2Tf_0'(\epsilon)\,[\mathcal{A}(\epsilon,\phi)+\mathcal{A}(\epsilon,-\phi)] - \frac{e^2}{h}\int_{\Delta_L}^{\infty} d\epsilon\; Tf_0'(\epsilon)(1+|r|^2)\,[\mathcal{Q}(\epsilon,\phi)+\mathcal{Q}(\epsilon,-\phi)]\,, \tag{9.14}$$

$$L_{12}^N = -\frac{2e}{h}\int_{\Delta_L}^{\infty} d\epsilon\;\epsilon\;Tf_0'(\epsilon)|t|^2\,[\mathcal{Q}(\epsilon,\phi)-\mathcal{Q}(\epsilon,-\phi)]\,, \tag{9.15}$$

where $f_0'(\epsilon) = \left[4k_BT\cosh\left(\epsilon/2k_BT\right)^2\right]^{-1}$, is the derivative of the Fermi function $f_0(\epsilon) = \left[1+e^{\epsilon/k_BT}\right]^{-1}$. From Eqs. (9.14) and (9.15) clearly emerges the even and odd parity in ϕ of L_{11}^N and L_{12}^N, respectively. In Fig. 9.5 we plot those two quantities with respect to the phase bias ϕ and the junction length L. The main difference with respect to the purely nonlocal thermoelectric coefficient of Chap. 8 is that the thermoelectric coefficient L_{12}^N of Eq. (9.15) depends on $\sin\left(2\pi\frac{L\epsilon}{\hbar v_F}+\phi\right)$ (see Eq. (9.13)) instead of $\cos\left(2\pi\frac{L\epsilon}{\hbar v_F}+\phi\right)$ (see Eq. 8.7). For long junctions (i. e. $L\to\infty$) the contributions for different energies average to zero

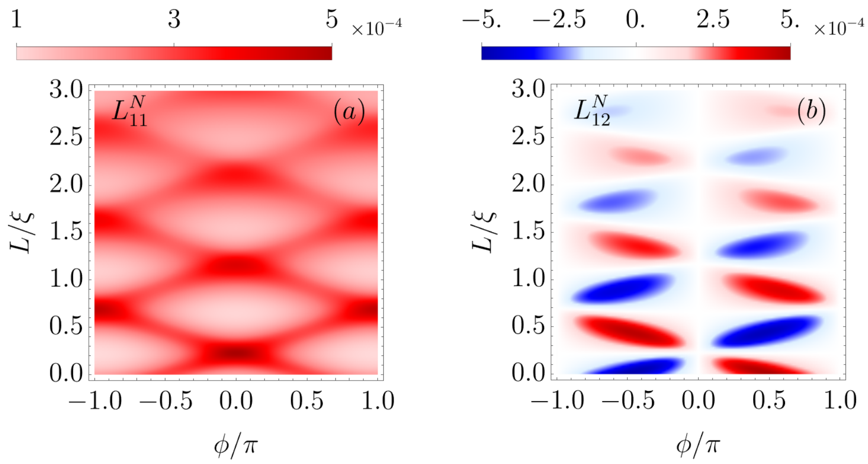

FIGURE 9.5: Charge current J_N^c linear coefficients L_{11}^N and L_{12}^N in the extreme asymmetric limit $\delta \to \infty$ as a function of the phase bias ϕ and junction length L. Other parameters are $T/T_{C,L} = 0.2$, $|t|^2 = 0.5$

recovering the expected result of a standard NS junction. This clearly shows that when the superconducting leads are far from each other, the Andreev interferometric mechanism on the local thermoelectrical transport is suppressed.

We conclude this section by observing that the *local* thermoelectric effect in the probe, which emerges with gap asymmetry, represents one of the main source of disturbance to the measurement of the *nonlocal* thermoelectric effect discussed in the sections above. This implies that, in order to clearly see the nonlocal thermoelectrical effect, it is convenient to be in a situation with weak asymmetry. However, we estimated that this local thermoelectric effect is of the order of few μV/K, to be compared with the nonlocal thermoelectric effect determined by DS, discussed before, which could reach values of the order of many tenths μV/K (see below). So we do not expect that spurious local thermoelectrical effects would substantially affect the nonlocal measurements at least for moderate gap asymmetry.

9.2.5 Linear-response heat current at the probe

In the asymmetric case ($\Delta_R \neq \Delta_L$) it is interesting to discuss the behavior of the heat current flowing in the probe J_N^h. Similarly to Eq. (9.7), in the linear-response regime we can write

$$J_N^h = L_{21}^N \frac{V_N}{T} + L_{22}^N \frac{\delta T}{T^2}, \tag{9.16}$$

where we defined

$$L_{21}^N = L_{NN}^{hc}, \qquad L_{22}^N = (L_{NL}^{hh} - L_{NR}^{hh})/2. \tag{9.17}$$

The coefficient L_{21}^N accounts for the local Peltier effect at the probe (describing how the heat current at the probe is influenced by the voltage bias V_N). While L_{22}^N represents the transverse heat response at the probe, i.e. the heat current induced in the probe as determined by a trasversal temperature gradient *between* the superconductors. In contrast to the symmetric case in which $J_N^h = 0$ in the linear response regime (see Appendix A.3), in the asymmetric configuration J_N^h can be finite even in linear response. This can be interpreted as the consequence of the contributions of the different heat currents flowing from the two superconducting leads kept at different temperatures. In Fig. 9.6 we plot L^N_{21}, panel (a), and L^N_{22}, panel (b), as functions of ϵ_{DS} and δ; both quantities are significantly different from zero only in region (ii). Indeed in region (i), J^h_N vanishes since the system is not able to activate enough supragap states. [5] On the other hand, in region (iii) the two gaps are both closed and there is almost no difference in the thermal coupling between right and left leads. Since the probe is at the average temperature $T = (T_R + T_L)/2$, the system behaves very similarly to the symmetric case ($\delta = 1$ bottom border of the figures) where the thermal flux from hotter lead is compensated with the thermal losses in the colder lead giving a null net thermal current in the probe.

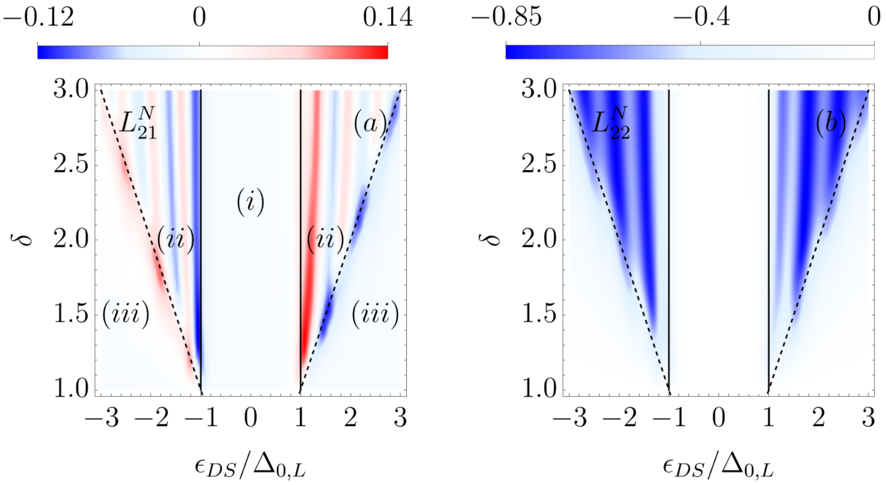

FIGURE 9.6: Heat current J^h_N Onsager coefficients L^N_{21} (a), L^N_{22} (b) as functions of $\epsilon_{DS}(\Phi)/\Delta_{0,L}$ and $\delta = \Delta_{0,R}/\Delta_{0,L}$, for $\phi = \phi_L - \phi_R = 0$, $T/T_{C,L} = 0.1$, $L/\xi_L = 3$ and $|t|^2 = 0.5$. Such quantities are normalized as follows: $L^N_{21}/(\sqrt{G_0 G_T T^3})$, $L^S_{22}/(G_T T^2)$.

Furthermore, we notice the behavior of the transverse thermal coefficient L^N_{22} of the system can be described in terms of a thermal divider, i.e. a device that controls the sign of the heat current in an intermediate third terminal (the probe) assuming that there is a main heat flow generated from the thermal gradient δT (between the superconductors). [6] In particular the three terminal setup can be described as a series of two thermal conductances with the probe in the middle. In such a case, the heat flux in the probe would depend essentially on the ratio of thermal resistances. Indeed, in region (ii) for $\delta > 1$ the thermal coupling of the probe with right lead is very opaque with respect to the left lead. Since the probe temperature is fixed at $T = (T_R + T_L)/2$ there is more heat flowing from the left lead than into the right one, determining the negative sign of L^N_{22} (since positive thermal current of the probe is defined exiting from the probe).[7] We verified that the sign of L^N_{22} changes globally for the opposite

---

[5] Note that the Joule component can be neglected in the linear regime since it scales at least as V_N^2.

[6] The name is inspired by an evident analogy with voltage dividers.

[7] The negative sign of this quantity is simply determined by the adopted convention for probe currents but clearly the spontaneous thermal flux always flows from the hotter to the colder lead, in agreement with the laws of thermodynamics.

case $\delta < 1$ (not shown). This behavior qualitatively resembles the concept of the thermal router [Timossi2018] in superconducting hybrid systems.

In region (ii), we notice that both linear coefficients are also oscillating (see the vertical stripes). In particular, the sign changing of L_{21}^N with Φ reflects the change of the main carrier as determined by Andreev interference discussed in Sec. 9.2.2. It is indeed important to remind that, being L_{21}^N a local Peltier-like coefficient, its sign will directly depend on the sign of the dominant carrier. Instead L_{22}^N has not similar sign changes being associated to a transversal thermal response that cannot distinguish on the main carrier charge sign.

9.3 Non-linear response regime

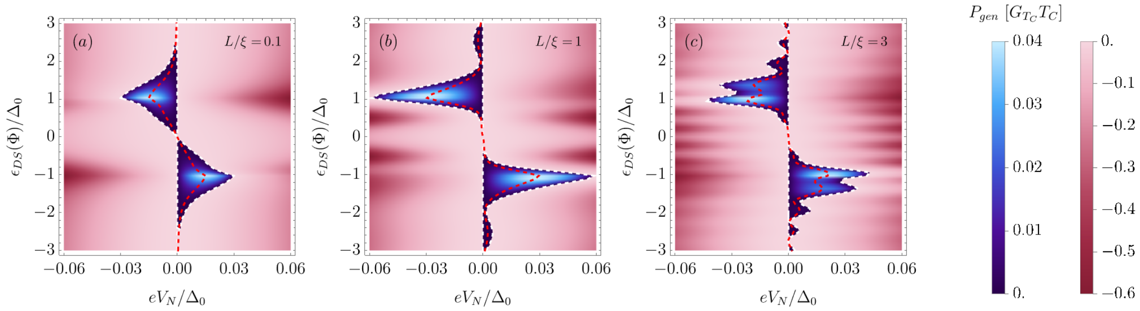

FIGURE 9.7: Electrical power P in units of $G_{T_C}T_C$ as a function of eV_N/Δ_0 versus $\epsilon_{DS}(\Phi)/\Delta_0$ in the case of short (a) $L/\xi = 0.1$, medium (b) $L/\xi = 1$ and long (c) $L/\xi = 3$ junction. In blue is depicted the generated power $P_{gen} = P > 0$. The white dashed line corresponds to the stopping voltage curve, while the red dashed line indicates the maximum generated power P_{max}. Here we chosen $|t|^2 = 0.5$ (an intermediate coupling parameter representing a not fully Ohmic contact with the probe), $\delta T/T_C \approx 0.4$ (large enough to guarantee the highest possible electrical power by keeping constant and equal the gaps of the superconductors) with $T/T_C = 0.2$ and $\phi = 0$.

In this section we investigate the behavior of the nonlocal thermoelectricity from the perspective of a thermodynamic engine within the nonlinear regime. The laws of thermodynamics set very general constraints on the currents of Eq. (9.4). As discussed in Sec. 5.2, the first law of thermodynamics, which guarantees energy conservation, can be written as

$$\sum_i J_i^h = P, \tag{9.18}$$

where P is the electrical power

$$P = -\sum_i J_i^c V_i. \tag{9.19}$$

With this definition, P is positive when the current flows against the applied bias, i. e. there is a thermopower generated in the system that can be dissipated on an external load ($P \equiv P_{gen}$). The device thus works as a thermoelectrical engine [Whitney2013, Whitney2014, Sothmann2014, Mazza2014, Benenti2017]. Notice that, since we set $V_L = V_R = 0$, Eq. (9.19) reduces only to $P = -J_N^c V_N$, which means that the power is dissipated in the probe circuit only. As already mentioned in Sec. 5.2, another important performance quantifier is the efficiency defined as

$$\eta = \frac{P_{gen}}{\sum_i^+ J_i^h}, \tag{9.20}$$

where the numerator corresponds to the electrical power generated P_{gen}, while the denominator corresponds to the total heat current entering the system (the superscript $+$ in the sum means that we are summing only positive heat currents). In the remaining part of this chapter we discuss the symmetric case ($\delta = 1$), with $\Delta_0 \equiv \Delta_{0,L} = \Delta_{0,R}$ and $T_C \equiv T_{C,L} = T_{C,R}$. However, when the temperature difference between the two superconductors becomes comparable with the critical temperatures, the superconducting gaps on the two sides of the junction will take different values. In what follows we take into account this fact by including self-consistent temperature dependence of the two gaps.

9.3.1 Electrical Power and maximum Power

The electrical power P of Eq. (9.19) is presented in Fig. 9.7 and expressed in units of $G_{T_C}T_C$ (with $G_{T_C} = (\pi^2/3h)k_B^2 T_C$ the thermal conductance quantum at T_C), as a function of eV_N/Δ_0 and $\epsilon_{DS}(\Phi)/\Delta_0$ in the case of short $L/\xi = 0.1$ (Fig. 9.7 (a)), medium $L/\xi = 1$ (Fig. 9.7 (b)) and long $L/\xi = 3$ (Fig. 9.7 (c)) junctions, with $\xi = \hbar v_F/\pi\Delta_0$. Here we set $|t|^2 = 0.5$, representing a intermediate Ohmic contact with the probe, and a phase difference $\phi = 0$. It is important to notice that here we set $T = 0.2T_C$ and $\delta T/T_C \approx 0.4$, which is the largest thermal bias for which $T_L, T_R \lesssim 0.4T_C$, such that the superconducting gaps can be safely considered still constant $[\Delta_L(T_L) \approx \Delta_R(T_R) \approx \Delta_0]$.

In Fig. 9.7 the white dashed lines represent the stopping voltage V_{stop} defined through the equality $P_{gen}(V_{stop}) = J_N^c(V_{stop}) = 0$, while the red dashed lines locate the maximum generated power $P_{max} = \max_{V_N}[P_{gen}]$. By comparing Figs. 9.7 (a), (b) and (c), we can see that the behavior of the electrical power for different lengths of the junction remains roughly the same. In particular, when the gap closes due to the flux bias Φ, i.e. when $|\epsilon_{DS}(\Phi)/\Delta_0| \approx 1$, the electrical generated power P_{gen} is maximized irrespective of the length L. For long junctions, the only additional feature is the presence of ripples in the generated power due to the proliferation of resonant states inside the junction [see Fig. 9.7 (c)] which in turn affects also the supragap states. No oscillations occur at any lengths when $|t|^2 \approx 1$ (not shown). Furthermore, another important feature which emerges from Fig. 9.7, is that the sign of the stopping voltage V_{stop} changes when $\Phi \to -\Phi$ as a consequence of the antisymmetry of the thermoelectricity under the magnetic field inversion.

A study of the dependence of the maximum generated power on the phase difference ϕ is presented in Fig. 9.8. Here, P_{max} is plotted in units of $G_{T_C}T_C$, as a function of the two external tuneable knobs, i. e. $\epsilon_{DS}(\Phi)/\Delta_0$ and ϕ/π, setting $L = \xi$. This length is realistic assuming a scanning tunneling microscopy (STM) tip with a state-of-the-art width of 100 nm and a coherence length ξ in the proximized TI of the order of 600 nm [Deacon2017]. Furthermore, over a length $L \sim \xi$ no backscattering events are expected to occur at the operating temperatures for our setup, typically of a few kelvin. Also in this case we consider an intermediate coupling parameter $|t|^2 = 0.5$ with the probe and a thermal gradient $\delta T/T_C \approx 0.4$ with $T/T_C = 0.2$. Importantly, Fig. 9.8 shows that the following symmetry holds: $P_{max}(\vec{\theta}) = P_{max}(-\vec{\theta})$. The same holds, in general for the electrical power, i. e. $P(\vec{\theta}, V_N) = P(-\vec{\theta}, -V_N)$.

In Fig. 9.9 we present the results of the maximum generated power P_{max} as a function of $\delta T/T_C$ for different values of the coupling parameter $|t|^2$. In this case, we explicitly consider the temperature dependence of the superconducting gaps by using the approximated formula $\Delta_i = \Delta_0 \tanh\left(1.74\sqrt{T_C/T_i - 1}\right)$ (with $i = L, R$) which is accurate better than 2% with respect to the self-consistent BCS result [Tinkham1966, Kamp2019]. We compare

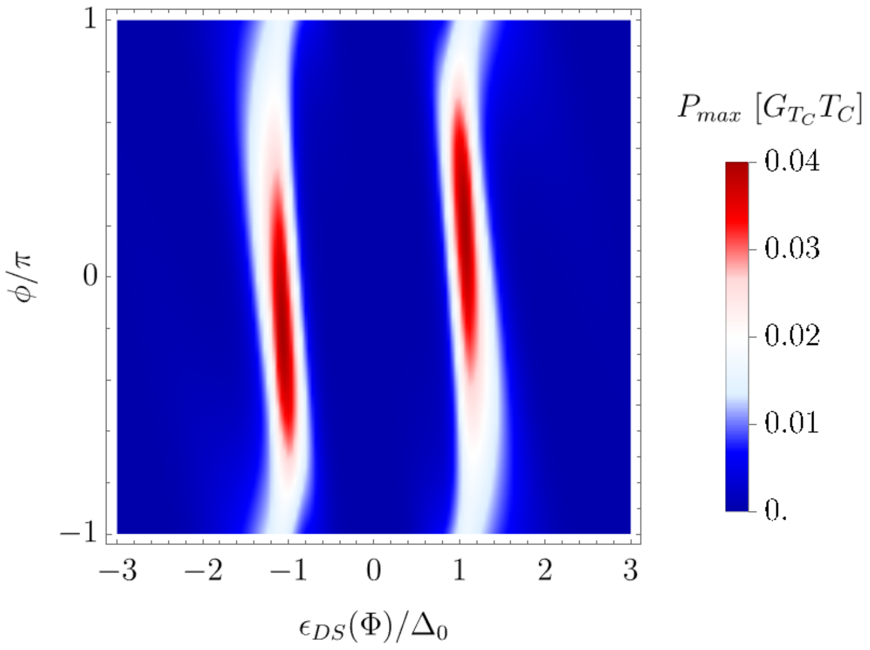

FIGURE 9.8: Maximum generated power P_{max} in units of $G_{T_C} T_C$ as a function of $\epsilon_{DS}(\Phi)/\Delta_0$ versus ϕ/π. Here we considered $L/\xi = 1$, $|t|^2 = 0.5$ and $\delta T/T_C \approx 0.4$ (large enough to guarantee the highest possible electrical power by keeping constant and equal the gaps of the superconductors) with $T/T_C = 0.2$.

it with the maximum power in the linear response regime given by the relation $P_{max} = \frac{GS^2}{4}\delta T^2 = \frac{L_{12}^2}{L_{11}}\frac{\delta T^2}{4T^3}$(dashed lines) [Benenti2017]. In the figure we consider $T/T_C = 0.5$ in order to maximize the excursion of the thermal gradient $\delta T/T_C \in [0, 1]$ by preserving the superconducting state of the leads (namely, such that the gap of the hotter superconductor does not close, i. e. $T_L/T_C \lesssim 1$). Here we set $L/\xi = 1$, $\phi = 0$ and $\epsilon_{DS}(\Phi)/\Delta_0 = 1$. From an analysis of the result of Fig. 9.9 emerges that all the curves match the trend of the linear regime for small δT as expected. Nonlinearities emerge only for $\delta T/T_C \gtrsim 0.4$ due to the closure of the gap of the hotter superconductor.

It is important to notice that the red curves of Fig. 9.9, corresponding to the case of perfect coupling with the probe ($|t|^2 = 1$), do not depend on neither the phase difference ϕ nor the length of the junction L. This curve clearly maximizes the performance with respect to all the other cases $|t|^2 < 1$.

9.3.2 Efficiency and Lasso diagram

We now present in Fig. 9.10, the results for the efficiency, defined in Eq. (9.20), by assuming perfect coupling with the probe $|t|^2 = 1$ and $\epsilon_{DS}(\Phi)/\Delta_0 = 1$, for which we have maximum power (according to the discussion of the previous section). In this situation, both the efficiency η and P_{max} do not depend on the phase difference ϕ and the junction length L. Here, we consider different values of the temperature of the probe, namely $T = 0.25\ T_C$, $0.5\ T_C$ and $0.75\ T_C$, corresponding to different colors in Fig. 9.10. For each value of T, we take three different values of the thermal bias $\delta T = 0.1\ \delta T_{max}, 0.5\ \delta T_{max}, \delta T_{max}$ (corresponding to the

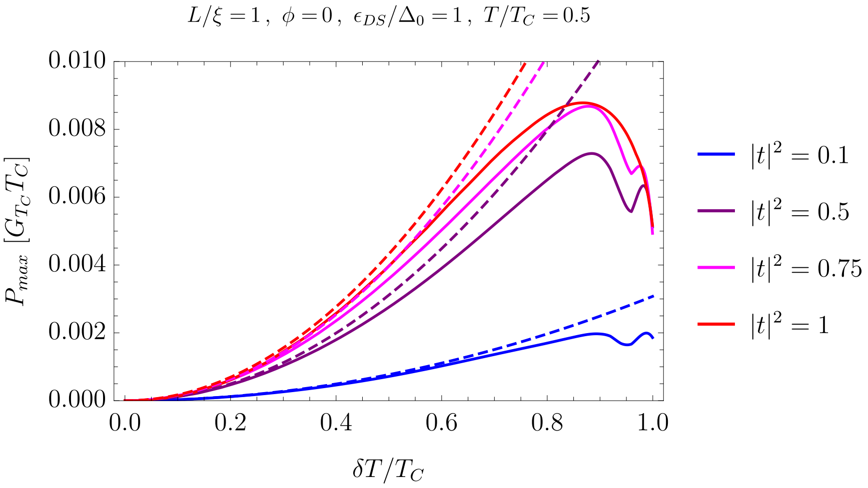

FIGURE 9.9: Maximum generated power P_{max} in units of $G_{T_C}T_C$ as a function of $\delta T/T_C$ for different values of the coupling parameter $|t|^2$ (solid lines) in comparison with the maximum power in the linear regime (dashed lines). Other parameters in the heading. Here we chosen $T/T_C = 0.5$ in order to maximize the range of the thermal gradient $\delta T/T_C$ so that the gap of the hotter superconductor does not close (i. e. $T_L/T_C \lesssim 1$).

different style of the lines: solid, dashed, dotdashed). δT_{max} take the following value

$$\delta T_{max} = \min\{2T, 2(T_C - T)\} \tag{9.21}$$

in order to always fulfill the condition $0 < T_L, T_R < T_C$ for any operating temperature of the superconductors. All the curves in Fig. 9.10(a) present the same "reversed-parabola" behavior, passing through $V_N = 0$ when the themocurrent becomes null again, similarly to what is expected for a linear thermoelectrical engine [Benenti2017]. The nonlocal thermoelectrical engine has a quite small maximum value for the efficiency, i. e. $\eta/\eta_C \lesssim 3.5\%$. This low efficiency can be attributed to the large flux of heat entering the system [thus increasing the denominator of Eq. (9.20)] which occurs when gaps close as a consequence of the DS.

A convenient way to present the efficiency at a given power output, and vice versa, is in the form of lasso diagrams as depicted in Fig. 9.10(b). The parameter that is changed along the lasso-line is the applied voltage V_N. As we can notice, the lasso-curves in Fig. 9.10(b) are long and narrow loops for all values of the controlling parameters (T and δT). This implies that maximum efficiency and maximum output power occur at the same value of parameters. This is advantageous for the operation of a thermoelectric device, where one typically must decide whether to optimize the engine operation with respect to efficiency or power output and constitute a major difference between this nonlocal thermoelectrical engine and standard linear thermoelectrical engines [Benenti2017].

9.3.3 Nonlinear Seebeck coefficient

In this section we present the result of the nonlinear Seebeck coefficient as a function of $\delta T/T_C$ for different values of the coupling parameter $|t|^2$. In Fig. 9.11 we plot the nonlinear nonlocal Seebeck coefficient defined as

$$S = -\frac{V_{stop}}{\delta T} \tag{9.22}$$

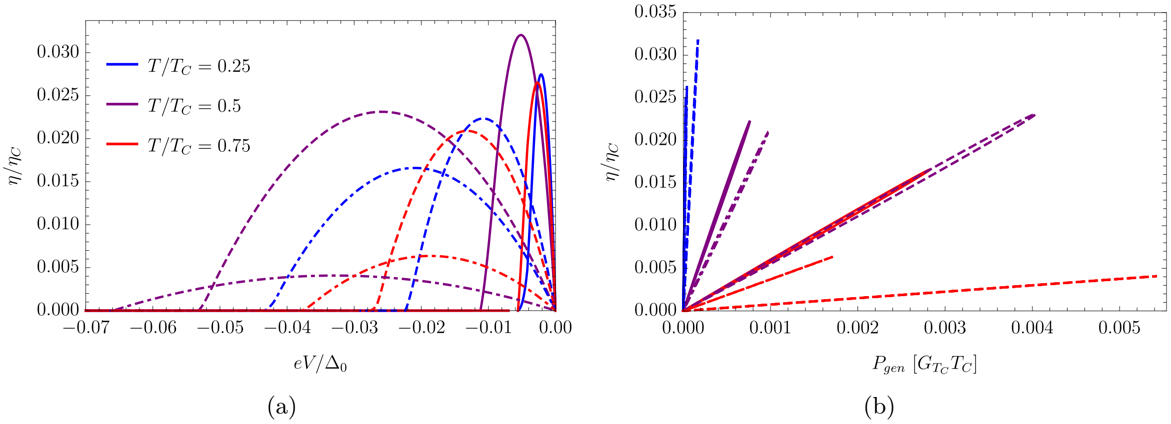

(a) (b)

FIGURE 9.10: (a) - Efficiency η normalized with respect the Carnot efficiency $\eta_C = \delta T/T$ as a function of eV_N/Δ_0. (b) - So-called lasso diagrams showing the normalized efficiency η/η_C at every power output expressed in units of $G_{T_C}T_C$. Different colors correspond to different probe's temperature $T/T_C = 0.25$ (blue line), $T/T_C = 0.5$ (yellow line), $T/T_C = 0.75$ (red line). Different style of lines correspond to different values of the thermal gradient (normalized with respect to δT_{max} of Eq. (9.21): $\delta T/\delta T_{max} = 0.1$ (solid line), $\delta T/\delta T_{max} = 0.5$ (dashed line), $\delta T/\delta T_{max} = 1$ (dot-dashed line).

expressed in units of $\mu V/K$, where V_{stop} is the stopping voltage for which $J_N^c(V_{stop}) = P_{gen}(V_{stop}) = 0$ (see white dashed lines of Fig. 9.7). We observe that the nonlinear Seebeck coefficient is quite big, considering that the operating temperature for these devices is of the order of few kelvin. Moreover, we see that S weakly depends on the temperature difference as long as the gap remains unaffected. Furthermore, we see that S increases going toward the tunnelling limit $|t|^2 \to 0$. We can conclude that nonlocal thermoelectricity is a strong effect.

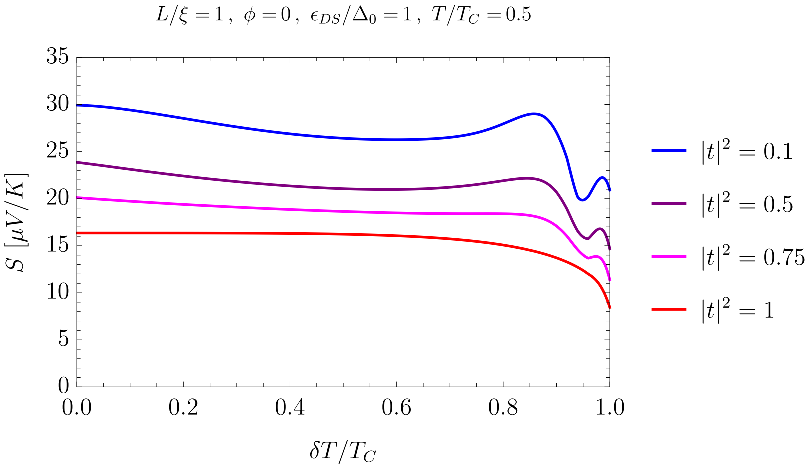

FIGURE 9.11: Seebeck coefficient in units of $\mu V/K$ as a function of $\delta T/T_C$ for different values of the coupling parameter $|t|^2$. The other parameters are the same of Fig. 9.9 (see the heading).

9.4 Conclusions

We have discussed the nonlocal thermoelectricity generated in a three terminal topological Josephson engine where one edge of a 2DTI is coupled to a normal metal probe. The nonlocal thermoelectricity is associated to the helical nature of the edge states and it is triggered by the application of the Doppler shift $\epsilon_{DS}(\Phi)$ (flux bias Φ) and/or by the phase difference ϕ between the superconductors. We have discussed in detail the case of asymmetric gaps which generalize previous studies (see Chaps. 7 and 8) of the same device to a more realistic situation where the right and left leads are not exactly identical. This is also necessary in order to investigate strong nonlinear conditions which typically occur in experiments. We have found that nonlocal thermoelectricity is present also in the asymmetric case. The nonlocal Onsager coefficients satisfy the standard symmetry between Seebeck and Peltier coefficients if the heat current between the two superconductors is properly defined to take into account the nonlocality. We have found that, in the asymmetric gap case, the Doppler shift develops a strong nonlocal thermoelectric effect when the two gaps close. We have discussed how the gap asymmetry gives rise to a new intermediate regime (for $\Delta_L < |\epsilon_{DS}(\Phi)| < \Delta_R$) where Andreev interference determines a weak nonlocal thermoelectrical effect without applying a phase bias. We have investigated how this Andreev mechanism influences also the local thermoelectric effect. We have estimated that such a local thermoelectric effect is of the order of a few μV/K, to be compared with the nonlocal thermoelectric effect determined by the Doppler shift discussed before, which could reach values of the order of many tenths μV/K. We can conclude that the thermoelectricity generated in the probe by the Doppler shift can be used as a clear evidence of the helical nature of the edge modes of the 2DTI. Similarly, we expect that the Doppler shift will potentially generate a nonlocal thermoelectrical response also in 3D topological structures [Yuan2018, Zhu2020]. Furthermore, we have also analyzed the heat current in the probe finding that it can be finite and the system can be viewed as a flux controlled thermal router depending on the difference between the superconducting gaps.

Finally, we have discussed the nonlinear performance of the nonlocal thermoelectric machine. In particular, we have studied the symmetry of the Seebeck coefficient, the power generated and the efficiency. The latter turns out to be quite low (with a maximum value $\eta/\eta_c \approx 3.5\%$). Notably, efficiency and power are maximized simultaneously for a wide range of parameters. We have finally estimated that the nonlocal Seebeck coefficient for large nonlinear temperature differences reaches a few tenths of μV/K, which is an impressive value given the operating temperature of few kelvin required by the BCS superconductors. We hope that this research will trigger further experimental investigations for similar setups both for 2D and 3D topological insulators. We also expect that the stability against the possible gap asymmetries and the intensity of the effect would be detectable with nowadays low-temperature technologies.

10

Signatures of Jackiw-Rebbi resonance in the thermal conductance of topological Josephson junctions with magnetic islands

This chapter is based on the results published in the paper:
D. Gresta, G. Blasi, F. Taddei, M. Carrega, A. Braggio, and L. Arrachea. *Signatures of Jackiw-Rebbi resonance in the thermal conductance of topological Josephson junctions with magnetic islands*. Phys. Rev. B, **103**(7) 075439 (2021)

The edge states defining the 1D helical conducting channels of a 2DTI offer a large variety of quantum phenomena in combination with magnets [Barash2002, Arrachea2015, Duan2015, Ghosh2017] and superconductors [Stanescu2010, Ronetti2017, Zhang2019, Michelsen2020, Ronetti2020, Sedlmayr2021]. A prominent example is the platform for topological superconductivity proposed by Fu and Kane [Fu2009], which consists in a Josephson junction made of a Kramers pair of helical edge states in close proximity to a s-wave superconductor and a magnet embedded in the junction. For a magnetic moment having a component perpendicular to the natural quantization axis of the 2DTI, Majorana bound states are formed. The concomitant signatures in the behavior of the Josephson current have been investigated in several works [Fu2009, Meng2012, Jiang2013, Houzet2013, Barbarino2013, Tkachov2013, Lee2014, Crepin2014, Hart2014, Marra2016, Bocquillon2017, Blasi2019, Ren2019, Keidel2020].

The key role played by a magnetic island placed inside the 2DTI is to introduce a boundary with a backscattering process in the Dirac system constituted by the helical edge states. Without the superconducting ingredient, this phenomenon leads to interesting effects in the electron transport [Qi2008, Meng2014, Arrachea2015, Locane2017, Silvestrov2016, Madsen2021] and in thermoelectric [Roura-Bas2018, Gresta2019, Hajiloo2020] properties. The fact that the magnetic island may have multiple domains further extends the scenario to interesting topological structures. The simplest of such situations corresponds to two domains with opposite orientations of the magnetic moments, which is a realization of the so-called Jackiw-Rebbi (JR) model - see Chap. 2 - of a 1D Dirac system with a space-dependent soliton mass [Jackiw-Rebbi1976, Shen2012]. Similarly to the discrete Hamiltonian by Su-Schrieffer-Heeger

[SSH1980] (SSH), this model is known to host topologically protected modes within the spectral gap. The high thermoelectric response generated as a consequence of these modes was recently pointed out in Ref. [Gresta2019]. JR physics on junctions with embedded superconductors was recently addressed also in Refs. [Malciu2019, Ziani2020], while the emergence of other states with fractional charges in helical edge states with many-body interactions has been also studied[Maciejko2009, Zhang2014, Ziani2015].

Thermal and thermoelectric effects in 2DTI in contact with superconductors have recently attracted a significant interest [Sothmann2016, Sothmann2017, Shapiro2017, Zhang2017, Bours2018, Keidel2020, Blasi2020, Blasi2020a, Hwang2020, Scharf2020]. It is remarkable that topological properties, which typically have associated spectral features close to zero energy may also have an impact on the thermal response. In this sense, interference patterns in topological Josephson junctions were studied in Refs. [Sothmann2016, Blasi2020a].

The aim of this chapter is to analyze the thermal conductance of a topological Josephson junction with an embedded magnetic island. A sketch of the device is shown in Fig. 10.1, which consists of a Josephson junction constructed by proximity effect to a 2DTI with a magnetic island contacting the two states of the Kramers pair in one of the edges. The junction is biased with a small temperature difference, δT and with a phase difference, ϕ, between the two superconducting pairing potentials. Here, we will focus on a magnetic island with one or two magnetic domains. Our goal is to identify features in the thermal transport that could indicate the topological nature of the junction. We show that the thermal conductance is very sensitive to the characteristics of the junction, in particular, to the domain structure of the magnetic island. Interestingly, systems hosting JR resonant states lead to a peculiar behavior of the thermal conductance, such that it decreases for increasing temperature just above the superconducting critical temperature.

The chapter is organized as follows. In Section 10.1 we present the model for the Kramers pair of 2DTI edge states in contact to s-wave superconductors with a phase bias and magnetic domains with different orientations of the magnetic moments. In Section 10.2 we discuss the scattering matrix approach used to analyze the topological junction. In Section 10.3 we present our main results concerning the Andreev spectrum and the thermal conductance obtained in different configurations. Section 10.4 is devoted to summary and conclusions.

10.1 Model

The system under investigation is depicted in Fig. 10.1. It consists of a 2DTI strip attached to two superconducting electrodes with a phase difference ϕ are placed on top and kept at slightly different temperatures, T, $T + \delta T$ (see light blue and red blocks in the sketch). Due to the proximity effect, the two superconductors induce a pairing potential in the portion of the 2DTI beneath it. In addition, a magnetic island with one or two domains (yellow blocks) with the magnetization directions forming an angle θ, are put in contact with one of the pairs of edge states of the strip. The lengths of the two magnetic domains along the edge are L_1 and L_2, respectively, and they are placed at distance l_S from each superconducting electrode. The width of the TI strip is assumed to be large enough such that the helical states (represented by solid lines) on the two edges are uncoupled one another and therefore we can restrict our analysis to a single Kramers pair. The Hamiltonian describing the system taking into account the proximity-induced pairing potential and the coupling to the magnetic island, expressed in the basis of Nambu spinors $\Psi(x) = \left(\psi_\uparrow(x), \psi_\downarrow(x), \psi_\downarrow^\dagger(x), -\psi_\uparrow^\dagger(x)\right)^T$, reads

$$H = \int_{-\infty}^{+\infty} dx \Psi^\dagger(x) \left[\mathcal{H}_0(x) + \mathcal{H}_M(x) + \mathcal{H}_S(x)\right] \Psi(x). \tag{10.1}$$

The term

$$\mathcal{H}_0(x) = (-i\hbar v_F \partial_x)\, \sigma_z \tau_z - \mu \sigma_0 \tau_z, \tag{10.2}$$

describes the free Kramers pair, with z as the natural quantization axis of the topological insulator. The terms

$$\mathcal{H}_M(x) = J\vec{m}(x) \cdot \vec{\sigma}, \qquad \mathcal{H}_S = \vec{\Delta}(x) \cdot \vec{\tau}, \tag{10.3}$$

describe, respectively, the effect of the coupling to the magnetic island and the BCS superconducting potential. The matrices $\sigma_0, \vec{\sigma} = (\sigma_x, \sigma_y, \sigma_z)$ and $\tau_0, \vec{\tau} = (\tau_x, \tau_y, \tau_z)$ operate, on the spin and particle-hole degrees of freedom, respectively. The pairing potential induced by superconducting proximity is described as follows,

$$\vec{\Delta}(x) = \left[\vec{\Delta}(\phi/2)\Theta(-x) + \vec{\Delta}(-\phi/2)\Theta(x - x_S)\right], \tag{10.4}$$

with $\vec{\Delta}(\pm\phi/2) = \Delta_0 (\cos\phi/2, \pm\sin\phi/2, 0)$ where ϕ is the phase bias and x_S is the distance between the two superconductors, which are considered to be semi-infinite. The magnetization of the island is accounted for by

$$\begin{aligned} \vec{m}(x) &= \vec{m}_1 \left[\Theta(x - l_S) - \Theta(x - x_1)\right] \\ &+ \vec{m}_2 \left[\Theta(x - x_1) - \Theta(x - x_2)\right], \end{aligned} \tag{10.5}$$

where $\vec{m}_j = m_j (\cos\theta_j, \sin\theta_j, 0)$, for $j = 1, 2$ and $x_1 = L_1 + l_S$ and $x_2 = L_2 + x_1$. The total length of the magnetic island is $L_m = L_1 + L_2$. The case with $\theta_1 = \theta_2$ and $m_1 = m_2 \equiv m$ effectively reduces to a single magnetic domain of length L_m. For sake of simplicity, we assume a fully anisotropic magnetic moment with a vanishing $\hat{z}$-component of the magnetization (direction parallel to the natural quantization axis of the topological insulator). Notice that the component of the magnetization perpendicular to $\hat{z}$ is the only mechanism introducing a backscattering processes in the present problem, and it is precisely this ingredient the one generating non-trivial effects in the two-terminal transport properties. For simplicity we discuss results corresponding to the configuration where the magnetic island occupies all the space of the junction, in which case $l_S = 0$ and $x_S = L_m$. However, for $l_S \neq 0$, we find qualitatively similar features.

In the absence of superconducting contacts ($\Delta = 0$), the component of the magnetization perpendicular to the natural spin quantization axis of the helical edge states is analogous to a mass term in the Dirac system and opens a gap in the spectrum. There are several consequences when this mass is not uniform in space. The magnetic island indeed plays the role of a barrier for the propagating helical states and it must be long enough in order to completely suppress the tunneling [Gresta2019]. Hence, in order to have a well defined gap in the spectrum, for which the tunneling probability is exponentially suppressed, the magnetic island must be larger than the characteristic length

$$\xi_M = \frac{\hbar v_F}{Jm}, \tag{10.6}$$

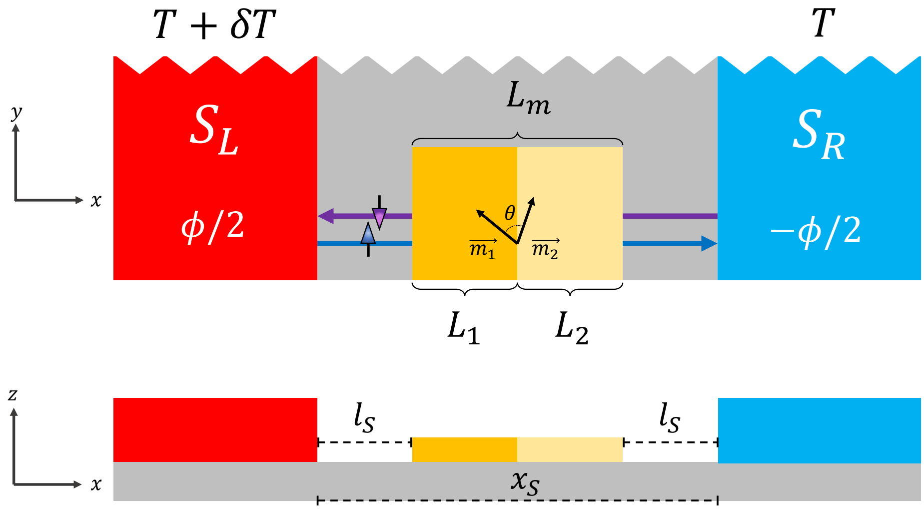

Figure 10.1: Top and lateral view of the device. Two semi infinite superconductors at slightly different temperatures, T and $T+\delta T$ and with a phase bias ϕ, proximized to a 2DTI in the quantum spin Hall regime. A magnetic island, of total length L_m composed with two magnetic domains of length L_1 and L_2 respectively, is placed at distance l_S from both superconductors, and contacted to the Kramers pair of helical states localized at one of the edges. The magnetic moments of the two domains are oriented with a relative tilt θ.

being Jm the magnetic energy gap in the limit of uniform magnetization along infinite-length helical modes. In summary, the inequality $L_m > \xi_M$ must be satisfied in order to show a clear suppression of the transmission probability due to the opening of the magnetic gap. Another interesting effect introduced by a non-uniform magnetization takes place in the case of two magnetic domains with exactly opposite orientations, i.e. $\theta = \pi$, which realizes the JR model [Jackiw-Rebbi1976], where two consecutive masses with different sign define a soliton domain wall in a 1D Dirac system. This model, along with its SSH discrete version [SSH1980] hosts a topological zero mode at the interface. As analyzed in Ref. [Gresta2019], this mode survives as a resonant state in the magnetic gap, shifted away from zero energy for a wide range of relative tilting angle θ in the orientations of the magnetic moments, and the width of this resonance scales with the inverse of the length of the magnetic domains. The reason for its stability is due to the fact that the system realizes a Goldstone-Wilczek soliton, as discussed in Refs. [Goldstone1981, Qi2008, Fleckenstein2016].

In combination with superconductivity, for a finite magnetization embedded in the junction between the two superconductors, a topological state develops, with Majorana zero modes localized in the boundaries between the superconductors and the magnetic island [Fu2009, Jiang2013, Crepin2014]. Notably, a magneto-Josephson duality exists [Jiang2013], such that the role of the magnetization can be interchanged with the superconducting potential. This can be understood by noticing that in the Hamiltonian for the device, Eq. (10.3), the terms with the Pauli matrices acting on the spin degrees of freedom, $\vec{\sigma}$, have the same structure as those with Pauli matrices $\vec{\tau}$, which act on the particle-hole degrees of freedom. Due to the s-wave nature of the superconducting order parameter, the relevant physical parameter characterizing the orientation of the magnetic moments is the relative tilt θ. Furthermore, this angle is related through the above mentioned duality to the phase difference ϕ between the two superconductors.

Importantly, in the presence of the superconducting contacts, the other characteristic length in the problem is the superconducting coherence length $\xi_S = \hbar v_F/\Delta$. As we will see, most of the interesting effects in the behavior of the thermal conductance arise from the interplay between the magnetic and superconducting spectral gaps. The conditions under which they are most remarkable correspond to comparable values for the two characteristic lengths ξ_M and ξ_S.

10.2 Scattering matrix approach

We rely on the scattering matrix approach to evaluate the subgap Andreev spectrum (see Sec. 6.4), as well as the transmission function ruling the behavior of the thermal conductance (see Sec. 5.3). In the absence of inelastic processes, dc transport is determined by the quantum mechanical matrix S, which yields scattering properties at energy ϵ, of a phase-coherent, non-interacting system described by the Hamiltonian H of Eq. (10.1). The scattering problem in terms of the S-matrix can be formulated as

$$\Psi^{\alpha}_{(i,\sigma)}\Big|_{\text{out}} = S^{\alpha,\beta}_{(i,\sigma)(j,\sigma')}\ \Psi^{\beta}_{(j,\sigma')}\Big|_{\text{in}}, \tag{10.7}$$

where summation is implicit on repeated indices. This equation relates incoming/outgoing states $(j,\sigma')/(i,\sigma)$ with $\{\sigma,\sigma'\} = \{\uparrow,\downarrow\}$ labeling the spin-channel at the respective superconducting lead $i,j = L,R$. In Eq.(10.7), $\alpha,\beta = \pm$ label the QPs $(+)$ and QHs $(-)$ in the superconductors. Following the standard procedure presented in Ref. [Datta1997], we computed the full scattering matrix of the system

$$S = S_L \circ S_M \circ S_R. \tag{10.8}$$

The matrices $S_{L,R}$ describe the left and right interfaces of the 2DTI with the superconductors. These matrices are combined with the matrix S_M describing the 2DTI edges in contact with the magnetic domain. In Appendix C we present in more detail the calculation of the different matrices $S_{L,R}$ (Sec. C.1) and S_M (Sec. C.2). By taking the trace over spin channels of the scattering matrix of Eq. (10.8) we can compute the probability scattering coefficients (see Sec. 4.3) [Lambert1998]

$$P^{\alpha,\beta}_{i,j} = \sum_{\sigma,\sigma'} \left| S^{\alpha,\beta}_{(i,\sigma),(j,\sigma')} \right|^2, \tag{10.9}$$

which represents the reflection $(i = j)$ or transmission $(i \neq j)$ probabilities of a quasiparticle of type β in the lead j to a quasiparticle of type α in lead i.

10.2.1 Andreev bound states and thermal conductance

As discussed in Sec. 6.4, under suitable conditions [Beenakker1991, Martin-Rodero2011], Andreev bound states develop with energies below the superconducting gap Δ. These states are crucial in the behavior of the Josephson current (see Sec. 6.3). To calculate the Andreev spectrum for $|\epsilon| < \Delta$, we proceed as in Refs. [Crepin2014, Beenakker1991]. Recall that for the non-superconducting region we have $\Psi_{\text{out}} = S_M \Psi_{\text{in}}$, with $\Psi_{\text{in,out}}$ defined as in Eq. (10.7) (see also Eq. (C.11)). For the subgap regime only perfect Andreev reflection is allowed, which leads to $\Psi_{\text{in}} = S_A \Psi_{\text{out}}$, being

$$\begin{aligned} S_A = &\exp\left[2i\frac{\epsilon}{\Delta}\frac{l_S}{\xi_S} - i\arccos(\frac{\epsilon}{\Delta})\right] \times \\ &\begin{pmatrix} 0 & \text{Diag}[e^{i\phi/2}, e^{-i\phi/2}] \\ \text{Diag}[e^{-i\phi/2}, e^{i\phi/2}] & 0 \end{pmatrix}. \end{aligned} \tag{10.10}$$

By combining these two expressions we obtain the secular equation [Beenakker1991]

$$\mathrm{Det}\left[1 - S_A S_M\right] = 0, \tag{10.11}$$

which we solve numerically to investigate the Andreev bound state spectrum.

Given the scattering matrix, we can also calculate the heat current generated as a response to the temperature bias δT. This quantity provides a complementary information to the Andreev spectrum, since it depends only on the quasiparticle spectrum above the gap. We focus on small δT, such that linear response applies (see Sec. 5.3). Indeed the corresponding heat current in this regime is proportional to δT and the thermal conductance is the natural transport coefficient. We find it convenient to characterize the response to the thermal bias in terms of the *relative thermal conductance*

$$\kappa_{\mathrm{th}}(T) \equiv \frac{L_{LL}^{hh}}{G_T T}, \tag{10.12}$$

where L_{LL}^{hh} is the local Onsager coefficient defined in Eq. (5.14d), and $G_T = \pi^2 k_B^2 T/3h$ is the quantum of thermal conductance. Explicitly it reads [Butcher1990, Benenti2017, Lambert1998]

$$\kappa_{\mathrm{th}}(T) = -\frac{1}{G_T}\int_{\Delta}^{\infty} \epsilon^2 \frac{\partial f(\epsilon)}{\partial \epsilon}\mathcal{T}(\epsilon) d\epsilon; \tag{10.13}$$

where $f(\epsilon) = \left[\exp\left(\frac{\epsilon}{k_B T}\right) - 1\right]^{-1}$ is the Fermi-Dirac distribution. Note that, according to this definition, the relative thermal conductance is dimensionless and express clearly the ratio between the actual conductance and the maximum achievable thermal conductance for a quantum channel which is G_T. The transmission function, $\mathcal{T}(\epsilon)$, can be written in terms of the probability scattering coefficients as

$$\mathcal{T}(\epsilon) = \sum_{\alpha,\beta=\pm} P_{R,L}^{\alpha,\beta}, \tag{10.14}$$

with $P_{R,L}^{\alpha,\beta}$ given by Eq. (10.9). We recall that in the next section, for sake of simplicity, we will focus on $l_S = 0$. Similar results are obtained when $l_S \neq 0$.

10.3 Results

We now turn to discuss results for the Andreev spectrum obtained by solving Eq. (10.11) for two configurations: the single-domain magnetic island (Sec. 10.3.1) and the two-domain island (Sec. 10.3.2) in the Josephson junction. The properties of the Andreev states strongly affect the behavior of the dc Josephson current. Although the quasiparticle states above the gap also contribute to the Josephson current, the signatures of the topological phase, like the jumps in the current-phase relation in the dc case and the periodicity in the ac case, fully depend on the behavior of the Andreev states [Fu2009, Houzet2013, Jiang2013, Marra2016, Bocquillon2017]. Instead, the latter do not play any direct role in the response to the difference of temperature δT between the two superconductors. The latter manifests itself in the thermal conductance, which we analyze for both configurations in Sec. 10.3.3 and Sec. 10.3.4. As already mentioned, we focus on configurations with $l_S = 0$, since this parameter does not affect the main results we aim to discuss. In addition, we find sometimes convenient to characterize the strength of the magnetic coupling with respect the proximized superconducting gap Δ_0 through the dimensionless parameter

$$\Gamma = \frac{Jm}{\Delta_0} = \frac{\xi_S}{\xi_M}. \tag{10.15}$$

Importantly, as highlighted in the last equality, this parameter also defines the ratio between the magnetic and superconducting lengths.

10.3.1 Andreev spectrum of a junction with a single-domain magnetic island

The Andreev bound states for the configuration corresponding to a magnetic island with a single magnetic domain have been already analyzed in Refs. [Fu2009, Houzet2013, Crepin2014]. Here, we review those results in order to have them as a reference.

Figure 10.2 presents the Andreev spectra calculated for several lengths L_m of the magnetic island. The left panel of Fig. 10.2 shows the spectrum for $\Gamma = 0$, which corresponds to a junction hosting bare helical edge states between the superconducting contacts. We can identify two degenerate states corresponding to a Kramers pair at the time-reversal symmetric case $\phi = 0, \mathrm{mod}(2\pi)$. The degeneracy is broken as ϕ advances with one of the states evolving to a higher energy and hybridizing with the quasiparticle continuum for $|\epsilon| > \Delta$. A crossing point at zero energy takes place at $\phi = \pi$. For $\Gamma \neq 0$ time reversal symmetry is broken even for $\phi = 0$, and the degeneracy is consequently lifted. According to calculations [Fu2009, Crepin2014], Majorana modes are stabilized at the boundaries of the magnetic domain in the present case. Hence, the Andreev states with lowest absolute value of the energy result from the hybridization of these Majorana modes. These two states have different parity and cross at $\phi = \pi$. Since they are completely decoupled from the quasiparticle continuum, the spectrum is effectively 4π-periodic and so does the ac Josephson current if parity is conserved, in contrast to the $\Gamma = 0$ case, which is 2π-periodic due to the hybridization of the subgap states with the continuum. An interesting feature to highlight is the fact that the Andreev spectra are qualitatively different in the case $\Gamma < 1$ (panel (b) of Fig 10.2) and $\Gamma \geq 1$ (panel (c) of Fig. 10.2). For $\Gamma < 1$, several Andreev bound states may exist in the gap for large enough junctions, in addition to the ones with lowest absolute energy. Instead, for $\Gamma \geq 1$ the spectrum has only two Andreev states, which result from the hybridization of the two Majorana zero modes.

10.3.2 Andreev spectrum of a junction with a magnetic island with two domains

The spectrum for two domains of lengths $L_{1,2} = L_m/2$, equal magnetizations $\Gamma_{1,2} = \Gamma = Jm/\Delta$ and relative tilt $\theta = \pi$ in the orientation of the magnetization of the domains is presented in the left panel of Fig 10.3.

For $\phi = 0$, this system is invariant under spatial inversion symmetry with respect to the center of the junction, i. e. $x = x_S/2$ and the simultaneous inversion of the magnetic moments and spin. For this reason, in this configuration, the Andreev bound states are degenerate for $\phi = 0, \mathrm{mod}(2\pi)$ (see the level crossing in the left panel of Fig. 10.3). In general this degeneracy is broken and a gap appears in the spectrum. A representative example is illustrated in the right panel of Fig 10.3. This panel shows a zoom at $\phi = 0, \mathrm{mod}(2\pi)$ for configurations which

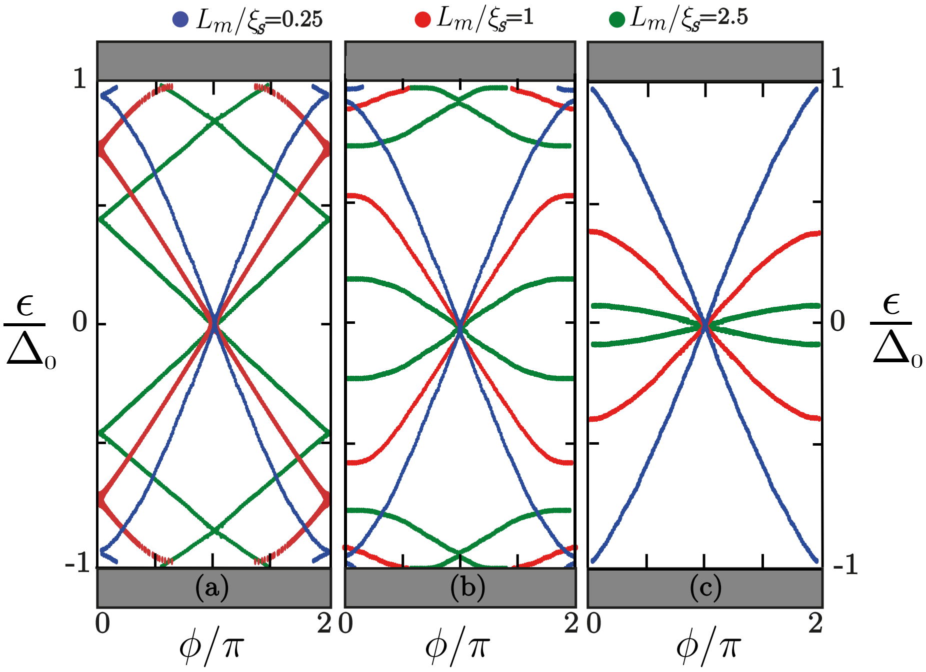

FIGURE 10.2: Andreev spectrum of the junction with a single magnetic domain of different lengths. Panel (a), (b) and (c) correspond to $\Gamma = 0,\ 0.5,\ 1$, respectively. Grey bands indicate the continuum spectrum. Different colors correspond to different lengths $L_m/\xi_S = 0.25, 1, 2.5$ of the magnetic island.

slightly depart from the symmetric case with $L_m/\xi_S = 1$ (red curve in both panels of Fig. 10.3). Namely, for the light blue curve we set $L_2 = 0.45\xi_S$, for the yellow curve $\theta = 0.99\pi$ and for the violet we set $\Gamma_2 = 0.9$ while all the other parameters are equal to the symmetric case. The plot in red lines is a reference equal to the red one in the left panel. For all the configurations examined, the crossing at $\phi = \pi$ is topologically protected, as in the case of a single magnetic domain. The behavior as a function of the coupling Γ is also similar to the case of a single magnetic domain analyzed in Fig. 10.2. Namely, for $\Gamma > 1$ the spectrum is composed of only two Andreev states crossing at $\phi = \pi$, which can be identified as hybridized Majorana states.

10.3.3 Thermal conductance of a junction with a single-domain magnetic island

The relative thermal conductance, defined in Eq. (10.13) is completely determined by the behavior of the transmission function given in Eq. (10.14). The analytical expression of the transmission function for a system with a magnet and without superconductors has been presented in Refs. [Bustos-Marun2013, Sternativo2014, Gresta2019]. Here, instead, we discuss the numerical results of the transmission function introduced in Eq. (10.14) for the hybrid system with the superconducting contacts. In this configuration, in addition to the magnetic gap, the transmission function depends on the effect of the superconducting gap which has a strong temperature dependence. We approximated the usual self-consistence dependence of the BCS theory for the superconducting gap as a function of the temperature, with $\Delta(T) = \Delta_0 \tanh\left(1.74\sqrt{\frac{T_C}{T} - 1}\right)$ being Δ_0 the corresponding value at $T = 0$. Since in

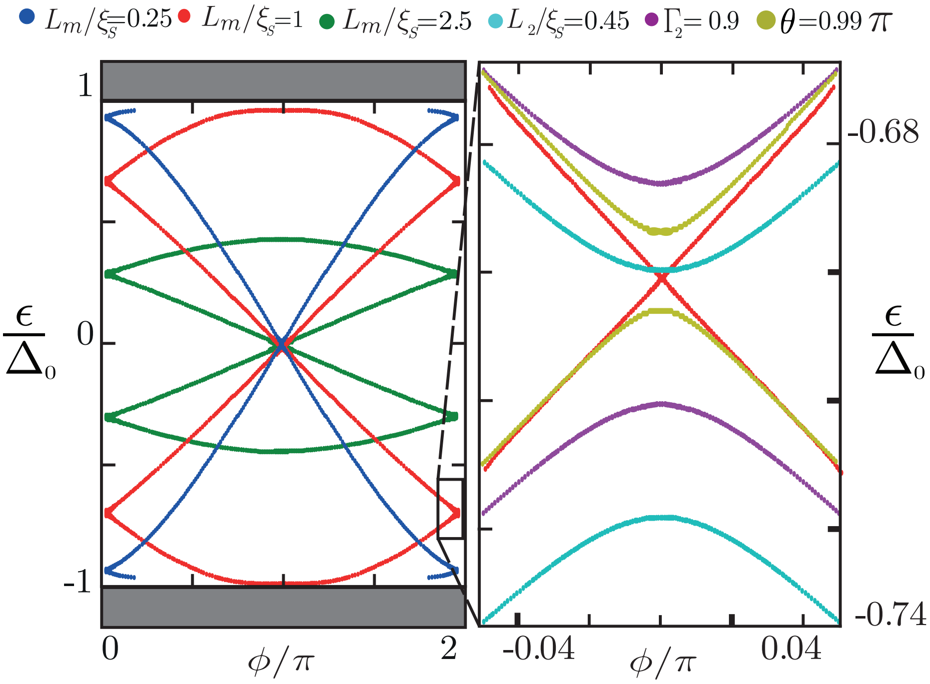

FIGURE 10.3: Andreev spectrum of the junction with two magnetic domains. Left panel correspond to $\Gamma = 1$ and $\theta = \pi$ and each domain of length $L_1 = L_2 = L_m/2$. Different colors correspond to different lengths, $L_m/\xi_S = 0.25, 1, 2.5$ of the full magnetic island. Grey band indicates the continuum spectrum. Black box indicates zoom on spectrum around $\phi = 0, \mathrm{mod}(2\pi)$ for two domains. Right panel: Andreev spectra for two domains, in the range covered by the box of the left panel. Different lines correspond to a single parameter variation: $L_2 = 0.45\xi_S$ (light blue), $\theta = 0.99\pi$ (yellow) and $\Gamma_2 = 0.9$ (violet). Red line is the same in both panels.

the present problem Δ_0 is the gap induced by proximity effect on the 2DTI, it is expected to be smaller than the corresponding value in the bulk of the superconducting contact. On the other hand, the magnetic gap does not change in magnitude within the temperature range we will consider hereafter. Therefore, the transmission function depends on the temperature T, as well as on the amplitude of the magnetic coupling, governed by the dimensionless parameter, Γ, and the length of the magnet L_m. This is illustrated in Fig. 10.4, where results for the transmission function are presented for the dimensionless magnetic coupling $\Gamma = 2$ and several lengths of the magnetic island at temperatures $T < T_C$ (solid lines) and $T > T_C$ (dashed lines). Notice that for $T > T_C$ the superconducting gap is closed. Hence, in this case, the transmission function coincides with the one for a magnetic island contacting the helical edge states without superconductivity analyzed in Ref. [Gresta2019].

Focusing on the plots of Fig. 10.4 we see that the quasiparticle transmission is strongly suppressed for the case $L_m = 2\xi_S$ (corresponding to $L_m = 4\xi_M$) up to energies $\epsilon \simeq 2\Delta_0$, for both temperatures. This is a clear manifestation of the fact that a gap opens in the spectrum of the edge states when the length of the island is $L_m \gg \xi_M$, while for $T > T_C$ the gap is not fully developed for islands of length $L_m \simeq \xi_M$ or shorter. When the magnetic gap is not fully formed the superconductivity can suppress the transmission. Indeed, within the low temperature regime shown in solid lines, superconductivity dominates, and the superconducting gap erases all the spectral features with energies $\epsilon < \Delta(T)$. This implies that for the short

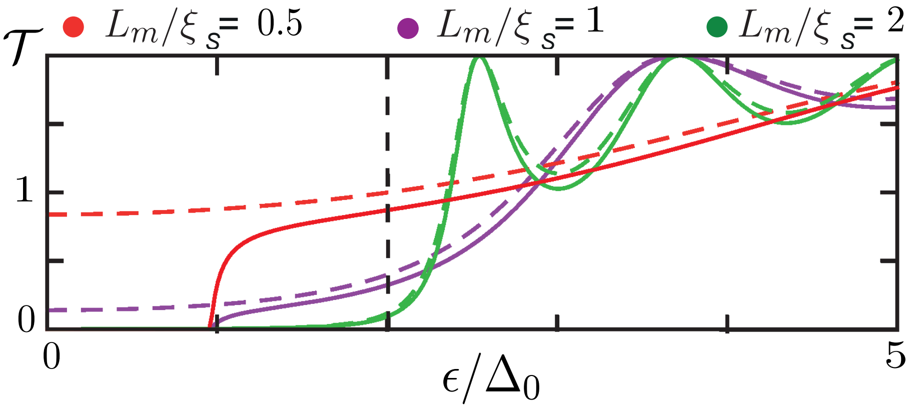

FIGURE 10.4: Transmission function for a single magnetic domain of length L_m embedded in the Josephson junction with $\Gamma = 2$ ($\xi_M = \xi_S/2$) and $\phi = 0$. Solid lines correspond to $T = 0.44T_C$ while dashed lines correspond to $T = 1.1T_C$. Vertical line indicates the magnetic gap. Other details are in the figure.

magnets considered in the figure, (with length $L_m < \xi_M$) the spectrum is still gapped, while there is a finite spectral weight at higher temperatures when the superconductivity is suppressed. On the other hand at energies $\epsilon > \Delta(T)$, the transmission function has a structure of peaks and minima that depends on L_m. For low temperatures, the features above $\Delta(T)$ also depend on the superconducting phase difference ϕ (that was set to zero in the Fig. 10.4). In conclusion, for the long islands, like the one shown in the figure with $L_m = 2\xi_S = 4\xi_M$, we can clearly see the dominance of the magnetic gap over the superconducting one. In fact, there is a gap of $\Gamma\Delta_0$ (see vertical dashed line) in the transmission function in both regimes of temperatures, in strong contrast with the cases of the shorter magnets, with $L_m = \xi_M,\ 2\xi_M$. This will be reflected in the behavior of the thermal conductance, to be discussed shortly.

After the analysis of the transmission function we discuss the relative thermal conductance, κ_{th}. Indeed, the competition between the magnetic and the superconducting gaps is particularly evident in the behavior of this response function as a function of temperature. This is shown in Fig. 10.5. The upper panel corresponds to $\Gamma = 1$ (where $\xi_M = \xi_S$) and the lower one to $\Gamma = 2$ (where $\xi_M = \xi_S/2$). In all the plots we can clearly identify the exponentially small value of the thermal conductance at low temperatures as well as the high temperature saturation to the quantum bound $\kappa_{\text{th}} = 1$ [Bekenstein1981, Pendry1983, Bekenstein1984] for $L_m \to 0$. The limit where $L_m = 0$ corresponds to the junction without magnetic island, in which case, the transport channel is fully open only when the superconducting gap closes, for $T > T_C$.

At finite L_m, the magnetic gap remains open even when the superconducting gap is closed, and the thermal conductance is smaller than the quantum bound. This feature is enhanced with increasing Γ (compare both panels of the figure). The changes in κ_{th} as the superconducting gap closes are more visible in the behavior of its derivative $\kappa'_{\text{th}} = d\kappa_{\text{th}}/dT$, which is shown in each panel with dashed lines. At $T = T_C$ the derivative has a discontinuity, as expected when the phase transition happens between a superconducting regime and a non-superconducting one. For $T > T_C$ the derivative of the thermal conductance monotonically increases with both Γ and L_m, while the opposite behavior takes place for $T < T_C$.

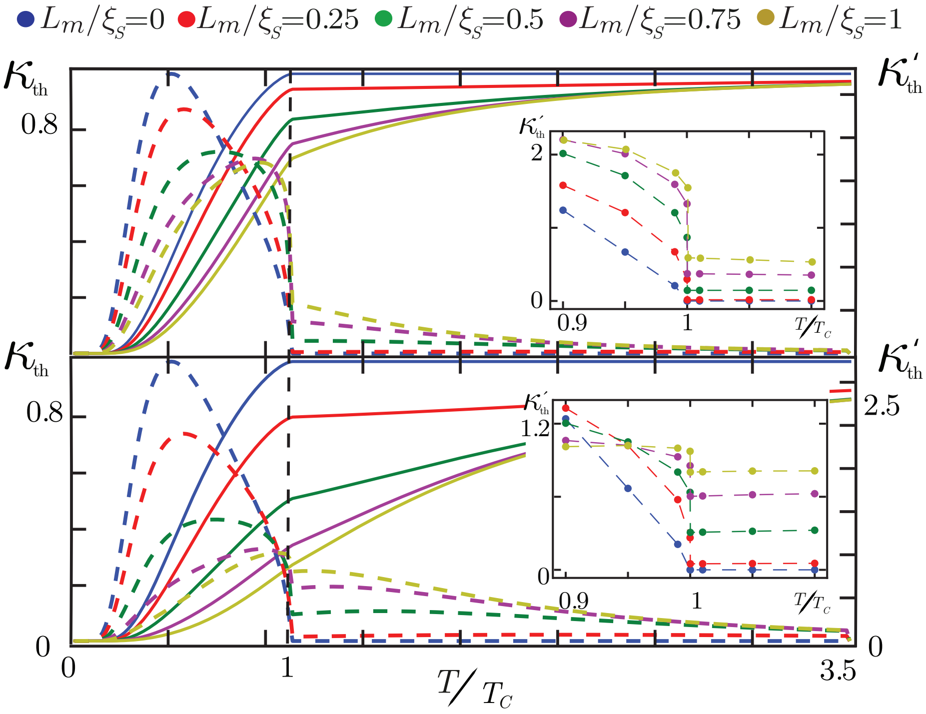

FIGURE 10.5: Relative thermal conductance $\kappa_{\text{th}}(T)$ (left axis, solid line) and its temperature derivative $\frac{d\kappa_{\text{th}}}{dT} = \kappa'_{\text{th}}$(right axis, dashed line) for a magnet with a single magnetic domain embedded in the Josephson junction with $\phi = 0$. Top panel corresponds to $\Gamma = 1$ and bottom panel corresponds to $\Gamma = 2$. Black dashed vertical line indicates $T = T_C$. Inset: zoom of κ' near $T = T_C$. Other details are on the figure.

When $T > T_C$ there is no superconductivity, hence it cannot be defined a fixed phase bias ϕ in the setup. On the other hand, when $T < T_C$ there exists a phase difference ϕ in the Josephson junction which introduces quantum interference in the behavior of the thermal conductance. We better analyze the features related to this effect in Fig. 10.6, which shows the behavior of κ_{th} as function of ϕ and L_m for a fixed temperature $T < T_C$ and different values of Γ in the different panels. The limit $\Gamma = 0$, corresponding to the junction without magnetic island, has been previously analyzed in Refs. [Sothmann2017, Blasi2020a] and is shown in panel (a). The main feature to highlight is the oscillatory response which is even and $2\pi-$ periodic in ϕ and oscillatory but decreasing on L_m/ξ_S, as shown in panel (b) for $\Gamma = 0.5$. Further details on the oscillatory behavior as a function of the length are presented in the inset of the panel (c), where results for κ_{th} as function of L_m are shown only for $\phi = 0,\ \pi$ and $\Gamma = 0, 0.5, 1$ up to length $L_m = 20\xi_S$. We see that, for finite $\Gamma < 1$, the pattern of damped oscillations is very similar to the one without magnet (corresponding to $\Gamma = 0$). Notice, in particular that, besides a shift and a smaller amplitude, the period of the oscillations is basically the same in the cases with $\Gamma = 0,\ 0.5$. Albeit, as the strength of the magnetic coupling is increased and overcomes $\Gamma = 1$, this response is much less sensitive to ϕ and decreases very fast with the length. This is consistent with a behavior dominated by the magnetic gap, even for temperatures below T_C, where the superconducting gap is finite. In the inset of panel (c) it can be appreciated how the thermal conductance tends to some limit when $L_m \gg \xi_S$ that depends on Γ but does not depend on ϕ. This saturation value is achieved as a limit of the damped oscillations for $\Gamma < 1$, while it is approached fast and

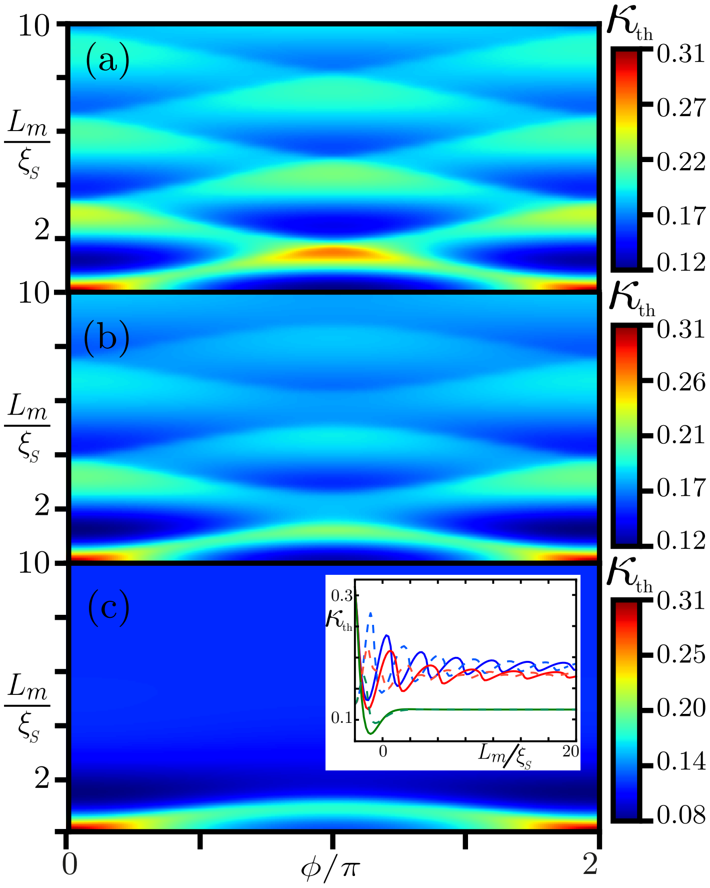

FIGURE 10.6: Relative thermal conductance of the junction with a single magnetic domain with temperature $T = 0.44T_C$. Different panels correspond to different ratios $\Gamma = Jm/\Delta_0$. Panel (a) corresponds to $\Gamma = 0$, panel (b) to $\Gamma = 0.5$ and panel (c) to $\Gamma = 1$. Inset in panel (c) is κ_{th} as function of L_m/ξ_S, blue line corresponds to $\Gamma = 0$, red line corresponds to $\Gamma = 0.5$ and green line corresponds to $\Gamma = 1$. Solid lines are for $\phi = 0$ and dashed lines are for $\phi = \pi$.

without oscillations for $\Gamma \geq 1$.

10.3.4 Thermal conductance for a magnetic island with two magnetic domains

The transmission function for the magnet with two domains is shown in Fig. 10.7 for $T < T_C$ (solid lines) and $T > T_C$ (dashed lines), for $\theta = \pi$ and $\Gamma = 2$ with $L_{1,2} = L_m/2$. In the absence of superconducting contacts, or equivalently, for $T > T_C$, the main feature is the presence of resonant peaks inside the gap, as it was discussed in Ref [Gresta2019]. In this case we can clearly distinguish the resonance that develops at $\epsilon = 0$. This peak has a width that decreases with the length of the island L_m and for these parameters it corresponds to a JR zero mode. For other relative orientations $\theta \neq \pi$ the resonance is shifted from $\epsilon = 0$, albeit remains being a robust feature within the gap for a wide range of parameters [Goldstone1981, Qi2008, Fleckenstein2016, Gresta2019]. The value of the expected magnetic gap, $\Gamma\Delta_0$, corresponding to the island with uniform magnetization is indicated as a reference

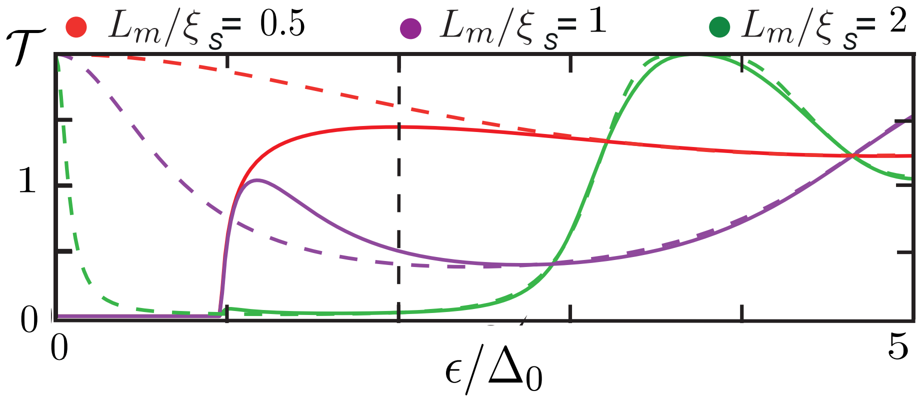

FIGURE 10.7: Transmission function for two magnetic domains of length $L_1 = L_2 = L_m/2$ with opposite orientation, $\theta = \pi$, and equal magnetization m, embedded in the Josephson junction for $\Gamma = 2$ and $\phi = 0$. Solid lines correspond to $T = 0.44T_C$ while dashed lines correspond to $T = 1.1T_C$. Vertical dashed line indicates the magnetic gap. Other details are on the figure.

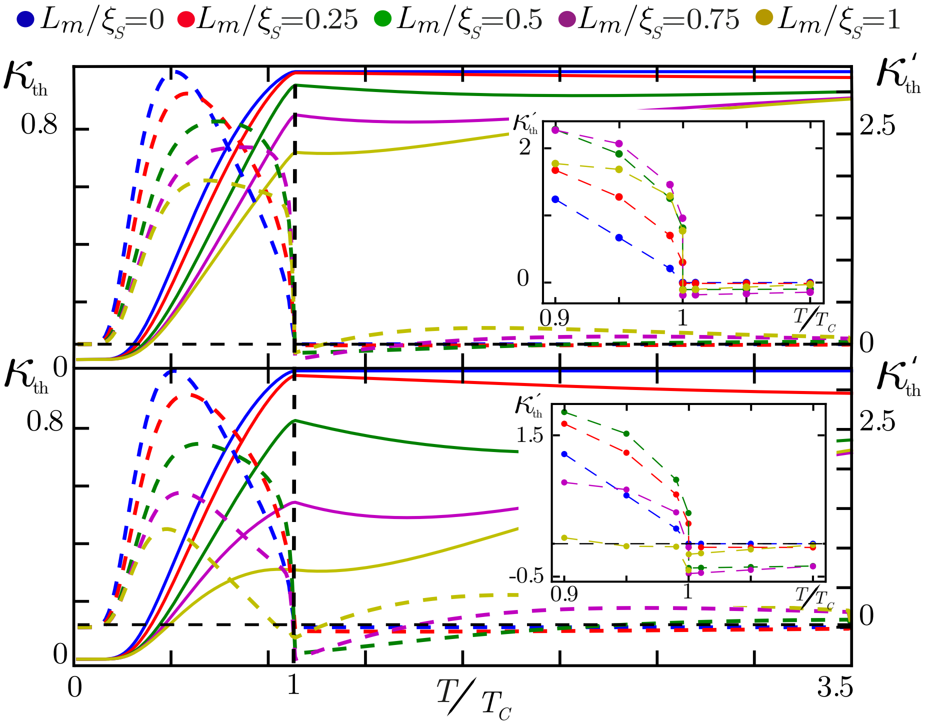

FIGURE 10.8: Relative Thermal conductance $\kappa_{\rm th}(T)$ (left axis, solid lines) and its derivative $\kappa'_{\rm th}$ (right axis, dashed line) for two magnetic domains with opposite orientations, equal length $L_m/2$ and equal magnetizations $m_1 = m_2 = m$ for $\phi = 0$. Top panel corresponds to $\Gamma = 1$ and bottom panel corresponds to $\Gamma = 2$. Black dashed horizontal line on both panels indicates $\kappa'_{\rm th} = 0$ while vertical line indicates $T = T_C$. Inset shows a zoom of κ' near $T = T_C$. Other details are on the figure.

with a vertical line in the figure.

In the plots corresponding to $T < T_C$ we can clearly see the effect of the superconducting gap, i. e. the transmission function is vanishing for $\epsilon < \Delta(T)$. Anyway the JR resonance in the gap leads to a remarkable behavior of the thermal conductance as a function of the temperature, which is presented in Fig. 10.8 for a configuration with two domains with equal length, $L_{1,2} = L_m/2$, equal magnetization and opposite orientation, i. e. $\theta = \pi$. As in the case of the island with a single domain, when $L_m \to 0$, κ_{th} tends to saturate at the quantum bound for $T > T_C$ and is exponentially small at low temperatures. However, we now see that the derivative κ'_{th} is negative right above T_C. We can trace back this peculiar feature to the development of the resonant peak in the gap as the temperature overcomes the critical temperature. From the mathematical point of view, this can be understood by calculating the derivative with respect to the temperature on Eq. (10.13), which leads to

$$\kappa'_{\text{th}} = \frac{2\kappa_{\text{th}}}{T} - \frac{1}{G_T T}\int_0^\infty \epsilon^3 \frac{\partial f}{\partial \epsilon}\frac{\partial \mathcal{T}}{\partial \epsilon} d\epsilon, \qquad T \geq T_C. \tag{10.16}$$

The first term on RHS is due to the contribution of G_T – recall that this quantity is linear with T – and is always positive. Instead, the sign of the second term depends on the sign of the derivative of the transmission function. Therefore, since $\partial f/\partial\epsilon < 0$, if $\partial\mathcal{T}/\partial\epsilon$ is negative and the contribution of the second term is large enough, the derivative of the relative thermal conductance may be negative. This is precisely the case of the configuration with two magnetic domains due to the resonance where, within the window defined by the function $-\partial f/\partial\epsilon$, the transmission function $\mathcal{T}(\epsilon)$ has a negative slope, which leads to a large contribution to the integral when multiplied by ϵ^3. This contribution becomes small as the length of the island increases and the resonance becomes narrow enough. In conclusion, the result of having κ'_{th} negative just above T_C can be regarded as an indication of the presence of a JR peak in a Josephson junction.

This effect is analyzed in more detail in Fig. 10.9, where κ'_{th} is shown as function of the relative orientation of the islands and the length for fixed Γ in each panel at a temperature just above T_C. We can see that there is a wide range of lengths and orientations close to $\theta = \pi$ where κ'_{th} is negative. These cases coincide with configurations leading to resonant peaks of the transmission function inside the magnetic gap. Importantly, the width of the resonant peak scales with the inverse of the length of the magnetic island (see plots in dashed lines in Fig. 10.7). Hence, the impact of this feature in generating a negative derivative of the relative thermal conductance just above T_C becomes negligible as the length of the magnetic island increases. This shows that the JR peak can be identified by the negativity of κ'_{th} only if $L_m \leq \xi_S$, i. e. for sufficiently short magnetic islands.

As in the case of a single-domain configuration, we expect some dependence of the thermal conductance on ϕ in the low-temperature regime with $T < T_C$. This is analyzed in Fig. 10.10 for the case of two magnetic domains with opposite orientations of the magnetic moments ($\theta = \pi$). The interference pattern is still even and $2\pi-$ periodic in ϕ but different from the one observed in Fig. 10.6 for a single domain. However, like in that case, as the length of the magnetic island increases and becomes significantly larger than ξ_M, the magnetic gaps becomes dominant, and the features introduced by ϕ become suppressed. This is highlighted in the inset shown in the bottom panel of the figure and we can pose similar observations as in the case of the single magnetic domain. Namely, for $\Gamma \geq 1$, where the magnetic gap dominates, the conductance is practically non-sensitive to the superconducting phase

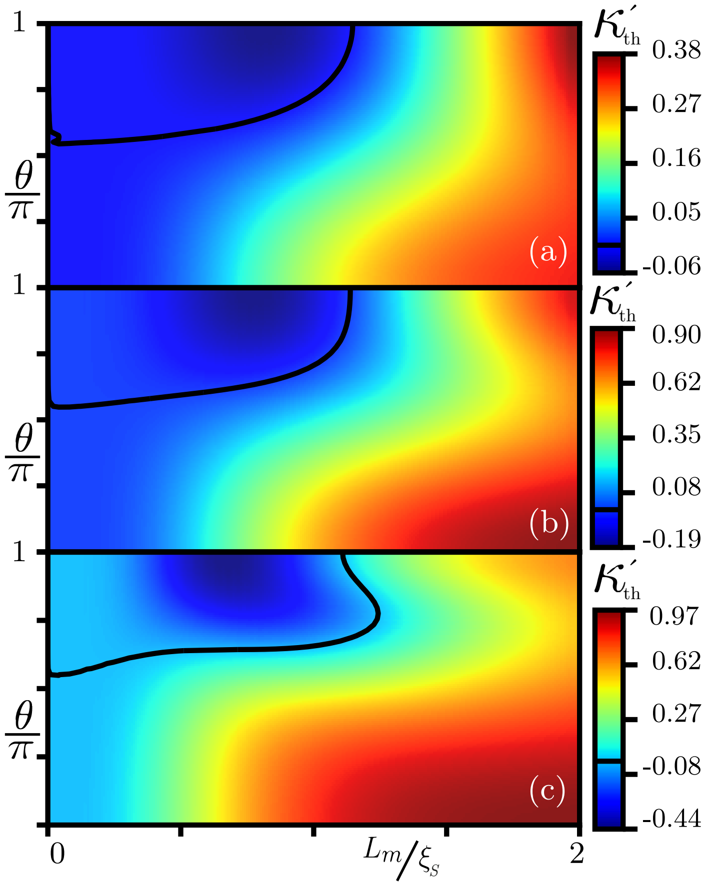

Figure 10.9: Derivative of the relative thermal conductance, κ'_{th} at $T = 1.01T_C$ as function of the relative tilt θ in the orientation of the magnetic moments with $L_m/2 = L_1 = L_2$ and $\phi = 0$. Panels (a), (b) and (c) correspond to $\Gamma = 0.5, 1, 2$, (with $\xi_M = 2\xi_S, \xi_S, \xi_S/2$) respectively. The black line in each panel indicates the boundary for the region with $\kappa'_{\text{th}} < 0$.

ϕ and it decreases rapidly with L_m. Instead, for $\Gamma < 1$, thermal conductance depends on ϕ and displays oscillations as a function of L_m. The pattern of such oscillations is very different and much less regular than the one observed in the junction without magnetic island (corresponding to $\Gamma = 0$). Hence, in the regime of $\Gamma < 1$, the interference pattern of the thermal conductance provides clear signatures of the domain structure of the magnetic island. Instead, for $\Gamma \geq 1$, the rapid suppression of the thermal conductance is an indication of the effect of the magnetic island, but no information on the domain structure can be extracted from that behavior.

Finally in Fig. 10.11, we analyze the combined effect of θ and ϕ on the behavior of the thermal conductance for different lengths of the magnetic island, a magnetic coupling corresponding to $\xi_M = \xi_S$ where we expect the maximal interplay between superconductivity and magnetic scales, and setting $T < T_C$. The figure highlights the fact that, not only the superconducting phase bias ϕ generates interference patterns but also the tilting angle θ. Furthermore, we notice that the specific features as function of ϕ are similar to those as function of θ. This is not surprising in the view of the duality relation between these two parameters [Jiang2013]. Notice that such duality implies that similar physical properties should be observed if the magnetic islands are interchanged with the superconductors, with

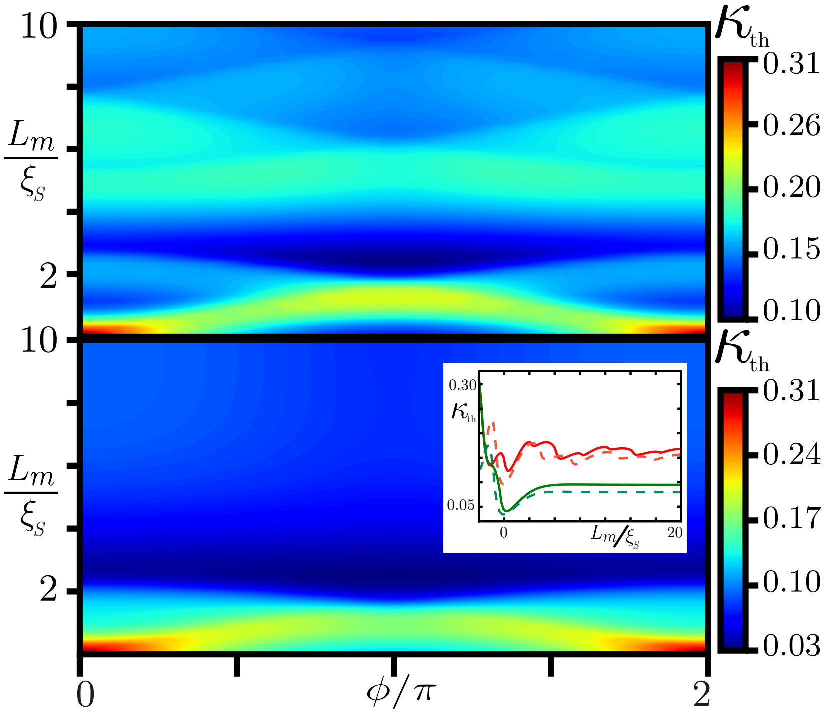

FIGURE 10.10: Relative thermal conductance of the junction with two magnetic domain with opposite magnetic moments and $L_1 = L_2 = L_m/2$ at temperature $T = 0.44T_C$. Upper and lower panels correspond to $\Gamma = J_m/\Delta_0 = 0.5,\ 1$ ($\xi_M = 2\xi_S,\ \xi_S$). The inset in the lower panel shows $\kappa_{\rm th}$ as function of L_m/ξ_S. Red line is for $\Gamma = 0.5$ and green line is $\Gamma = 1$ for $\phi = 0,\ (\pi)$ for solid (dashed) lines.

θ playing the role of ϕ and viceversa, due the similar structure of the massive terms, as is explicit in Eq. (10.3). In the Josephson-junction configuration studied here, we can observe signatures of the aforementioned duality, in a context where the superconductors have infinite length, while the magnetic islands are finite. In fact, we see that panel (a), which corresponds to a purely superconducting junction has a pattern of straight vertical features, reflecting the sensitivity of the thermal conductance only with the phase bias ϕ. In the opposite limit of a long enough magnetic island shown in panel (d), the magnetic effect becomes dominant and the pattern tends to follow horizontal straight lines, indicating a sensitivity on the tilt θ but loosing the dependence on ϕ. Configurations between these two cases can be observed in panels (b) and (c). These results show that the interplay of the tilting angle and phase difference may be an interesting phenomenology in the studied system.

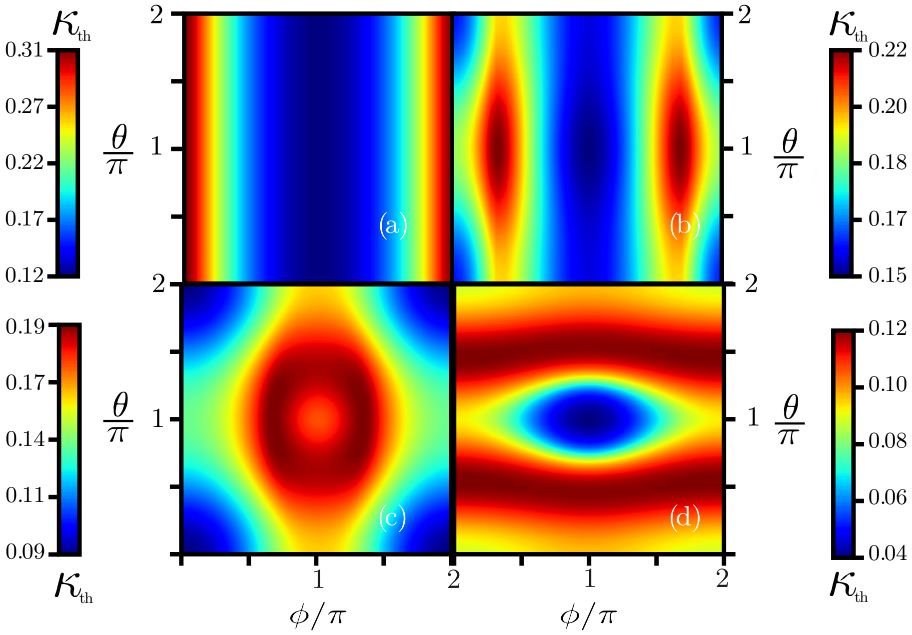

FIGURE 10.11: Relative thermal conductance $\kappa_{\mathrm{th}}(T = 0.44T_C)$ as function of the tilting angle in the orientation of the magnetic domains θ and the phase difference of the superconducting potentials ϕ for $\Gamma = 1$ ($\xi_M = \xi_S$) and $L_1 = L_2 = L_m/2$. Panel (a) corresponds to $L_m/\xi_S = 0$, panel (b) to $L_m/\xi_S = 0.5$, panel (c) to $L_m/\xi_S = 1$ and panel (d) to $L_m/\xi_S = 2$.

10.4 Conclusions

In this chapter we have analyzed the Andreev spectrum and the thermal conductance of a one edge Josephson junction of a 2D topological insulator hosting a magnetic island with one and two magnetic domains. We have shown that the Andreev spectrum, which defines the behavior of the Josephson current, is qualitative similar for these two configurations of islands. Instead, the behavior of the thermal conductance shows several features as a function of ϕ and the temperature T that characterize the nature of the junction. We have analyzed in detail all these properties. Most of them can be understood as a consequence of a competition between the temperature-dependent superconducting gap $\Delta(T)$ below the superconducting critical temperature T_C and the magnetic gap, which typically remains constant within this temperature range.

A remarkable result is the fact that for configurations with two magnetic domains with different orientations, which host JR resonant modes, the thermal conductance decreases with the temperature, just above the superconducting critical temperature. This is a peculiar behavior that could be useful to identify the existence of these intriguing modes. So far, no experimental signatures of JR resonances have been reported and this signature in the thermal conductance can be useful to identify them. Notice that the Josephson current is not sensitive to the existence of this resonant state. The Josephson current is defined by the derivative of all the negative energies of the spectrum of the superconducting junction with respect to the phase bias, including the quasiparticle continuum and the subgap Andreev states. We have shown that the spectra for systems where the magnets have different orientations are similar. Furthermore, they are also similar to those without any magnet. These results rule out the Josephson current as an appropriate witness of the existence of a JR mode.

More importantly, the peak in the transmission probability associated to the JR resonance develops when the superconducting gap closes, in which case there is no Josephson effect at all. Instead, the thermal conductance, being a non-equilibrium quantity, depends not only on the spectrum but also on the transmission properties of the system, irrespectively of the fact that the system is superconducting or not. The development of the JR resonance above T_C generates a large transmission probability at low energies, which significantly affects the behavior of the thermal conductance.

In the low-temperature regime, for $T < T_C$, the thermal conductance in the two-domain configuration shows interference patterns as a function of both the phase bias of the superconductors and the angle between the magnetic moments. This feature is particularly clear for islands where the magnetic and superconducting lengths are similar, $\xi_M \sim \xi_S$.

According to estimates presented in Ref. [Gresta2019], reasonable configurations of the magnetic island, compatible with the present state of the art experiments, should have magnetic lengths below $\xi_M \sim 10 - 20\mu m$, which is of the same order of magnitude of the superconducting coherence length ξ_S and energy gaps of $Jm \sim 1.2 - 2.4K$. These correspond to a regime with $\Gamma \sim 1, 2$, similar to the one analyzed in the present chapter, where the different features of κ_{th} as a function of ϕ below T_C, as well as the corresponding behavior as a function of temperature close to T_C, clearly distinguish the different type junctions.

11

Manipulation of Cooper pair entanglement in hybrid topological Josephson junctions

This chapter is based on the results published in the paper:
G. Blasi, F. Taddei, V. Giovannetti, and A. Braggio. *Manipulation of Cooper pair entanglement in hybrid topological Josephson junctions*. Phys. Rev. B, **99**(6) 064514 (2019)

Quantum mechanics may revolutionize the way we encode, transmit and elaborate the information. A crucial element is the capability to generate and manipulate entangled states [Einstein1935, Bell1966, Clauser1969]. First successful steps has been performed on photons [Aspect1981, Ekert1991, Tittel1998, Gisin2002]. To deal with quantum technology and the development of a quantum computer, though, one needs to bring those capabilities in the solid state platform to afford the embeddability and scalability issues [Loss1998, Burkard2000, Recher2001, Bena2002, Kim2004, DiLorenzo2005, Hussein2016, Hussein2017]. In Refs. [Sato2010, Chen2012, Virtanen2012, Choi2014, Veldhorst2014, Sato2014, Crepin2014, Zhang2015, Strom2015, Wang2015, Hou2016, Islam2017], 2DTIs has been put forward for the production and detection of spin-entangled singlet Cooper pairs originating in s-wave superconductors. The reason lies in the property the edge states of 2DTIs which are topologically protected ensuring robustness against perturbations with very long ($\gtrsim 1\mu m$) decoherence lengths [Chen2012, Konig2007, Roth2009, Wiedenmann2016]. These properties make TIs promising platforms for the manipulation of spin-entangled electrons in solid state systems.

In this chapter we demonstrate that combining s-wave superconductivity with the helical properties of 2DTIs [Jacquet2019], the non-local manipulation of spin-entangled states by means of local gating can be done. The proposed setup - see Fig. 11.2 - is composed of two parallel 2DTIs properly connected to two superconducting electrodes, and comprises electrical gates for the manipulation. We calculate analytically the current-phase relationship (CPR) of the Josephson current making use of the scattering matrix approach and we identify the various local and non-local scattering mechanisms. In particular, we show how the different external potentials selectively operate over the local and non-local components. We demonstrate that the application of gates affects the symmetry of the non-local entangled states (from singlet to triplet) which arise from crossed Andreev reflection between the two edges. This entanglement symmetry manipulation does not affect the purity of the entangled state but directly impact the Josephson coupling due to the intrinsic singlet nature of s-wave superconducting leads. We find that the Josephson critical current, remarkably, allows a direct quantification of the entanglement manipulation in the structure. We fully interpret the described phenomenology in terms of the multiple Andreev processes which mediate the Josephson coupling in the structure.

The chapter is organized as follows. In Sec. 11.1 we discuss the setup of the Josephson nanojunction done with topological insulators, we clarify why non-local entanglement may be realised and how the external potentials may be used to manipulate over the system. In Sec. 11.2 we briefly discuss how the computation in the scattering matrix formalism is done introducing the concept of electron losses at the TI-superconductor interfaces (all the details are reported in the Appendix D). In Sec. 11.3 we discuss euristically how external potentials affect the entanglement symmetry of the Cooper pairs in the junction, showing a simple way to interpret the complex behavior of the Josephson current. In Sec. 11.4 we present our analytical and numerical results for the CPR and for the critical current, discussing with care the interpretation in terms of multiple Andreev reflection processes in some notable limits. Finally we discuss the experimental feasibility of the proposal in the conclusions.

11.1 The Setup

As we discussed in Sec. 6.3, in a Josephson system with ideal interfaces and rigid boundary conditions the phase difference $\phi = \phi_R - \phi_L$ between the two superconductors induces a stationary Josephson current. Microscopically it originates from Andreev reflection processes that describe the transfer of Cooper pairs (CPs) at the interfaces between the superconductors and the weak link (see Sec. 3.3). In a single 2DTI sandwiched between two conventional s-wave superconductors, as the S-TI-S junction depicted in Fig. 11.1, CPs can only be injected or absorbed locally on a specific edge. Indeed, while the helical nature of the TI edge modes allows for local Andreev reflections (LARs) at the boundaries with the superconductors [Choi2014], i. e. an electron (hole) propagating through a helical mode and impinging onto a superconductor is reflected as a hole (electron) with opposite spin in the other helical mode on the *same* edge (see right side of Fig. 11.1), it prohibits crossed Andreev reflections (CARs) [Crepin2015, Fleckenstein2018], i. e. an electron (hole) propagating through a helical mode impinging onto a superconductor cannot be reflected as a hole (electron) with opposite spin in the other helical mode on the *other* edge (see left side of Fig. 11.1). In order to overcome this limitation one needs to consider a double TI junction [Sato2010]. Specifically we focus on the architecture depicted in Fig. 11.2 where a Josephson junction is obtained by sandwiching two planes of 2DTIs in between two s-wave superconductors. This system allows for CAR processes if the distance W between the two TI-planes is comparable with the coherence length ξ, e. g. choosing Al as a superconducting material $\xi \approx 100$ nm. Moreover, the properties of the edge modes can be tuned through external voltage gate and magnetic flux controls which mimics the presence of “local” (i.e. which acts differently on the upper and lower edge modes) time reversal and time reversal breaking fields respectively (see Fig. 11.2).

Specifically the first consists in gate electrodes placed in the vicinity of the edges modes (see Fig. 11.2) so to electrostatically affect the dynamical phase of the carriers [Xiao2016] by assigning to particles moving (say) along the lower edge the same phase factor $\theta_V = 2eVL/\hbar v_F$ independently of their propagation direction and spin (with v_F the Fermi velocity). The second instead, consists in the application of a moderate, uniform magnetic field B

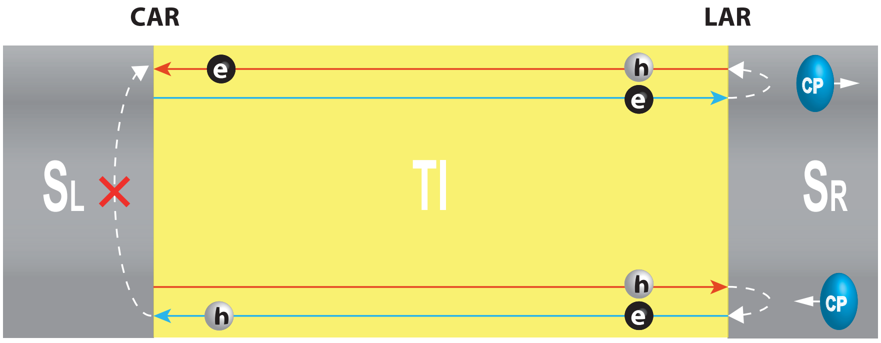

FIGURE 11.1: Standard S-TI-S junction: $S_{L/R}$ superconductors (gray) and the TI (yellow). The arrowed blue (red) solid lines represent the 1D helical edge states with spin ↑ (↓). At interface with S_R, two example of emission/absorption of CPs due to LARs. The impossibility of a CAR process where a ↑-h in the lower-edge is Andreev reflected in a ↓-e is represented at at S_L interface with a cross.

which, by Doppler shift effect [Tkachov2015, Sothmann2017] (see also Sec. 6.2), acts on (say) the upper edge by assigning a phase factor $\theta_\Phi = 4\pi\Phi/\Phi_0$ to spin-up (right-moving) electrons and $-\theta_\Phi$ to spin-down (left-moving) electrons (with Φ_0 the magnetic flux quantum and $\Phi = B_y W L$ the magnetic flux in the junction).

The way we implement both the fields ensures their differential action among the upper and lower edges of the TIs such that they can be effectively described, in the spin space, in terms of local unitary operators:

$$\mathcal{U}_V^\ell(\theta_V) = e^{i\;\theta_V \mathbb{1}/2}, \tag{11.1}$$

$$\mathcal{U}_\Phi^u(\theta_\Phi) = e^{i\;\theta_\Phi \boldsymbol{\sigma}\,\cdot\,\hat{\mathbf{n}}/2}, \tag{11.2}$$

with $\hat{\mathbf{n}}$ the natural spin-quantization axis of both the TIs [Qi2008, Maciejko2010] and with $\boldsymbol{\sigma}$ the Pauli matrix vector. In Eqs. (11.1) and (11.2) the labels u and ℓ indicate the action of the fields on the upper and lower edge respectively; other configurations, though, are fully equivalent as discussed in Appendix D.4.

11.2 Model

Following the scattering approach [Buttiker1986, Buttiker1992, Datta1997, Lambert1998], the scattering matrix of the Andreev processes occurring on the left L (right R) TI-S interface, in the u-ℓ space, can be written as [Beenakker1991, Beenakker1992]

$$\begin{pmatrix} \left|\Lambda_{L(R)}\right| & i\left|X_{L(R)}\right| \\ i\left|X_{L(R)}\right| & \left|\Lambda_{L(R)}\right| \end{pmatrix} e^{i\phi_{L(R)}}, \tag{11.3}$$

with $\Lambda_{L(R)}$ and $X_{L(R)}$ representing respectively the amplitude for the LAR and CAR events (these terms being related by the unitarity conditions $|\Lambda_{L(R)}|^2+|X_{L(R)}|^2 = 1$). In other words the Andreev reflection is given by the superposition of LAR and CAR processes. Notice that we neglected the presence of the edge modes running in the backside edges (i. e. along the

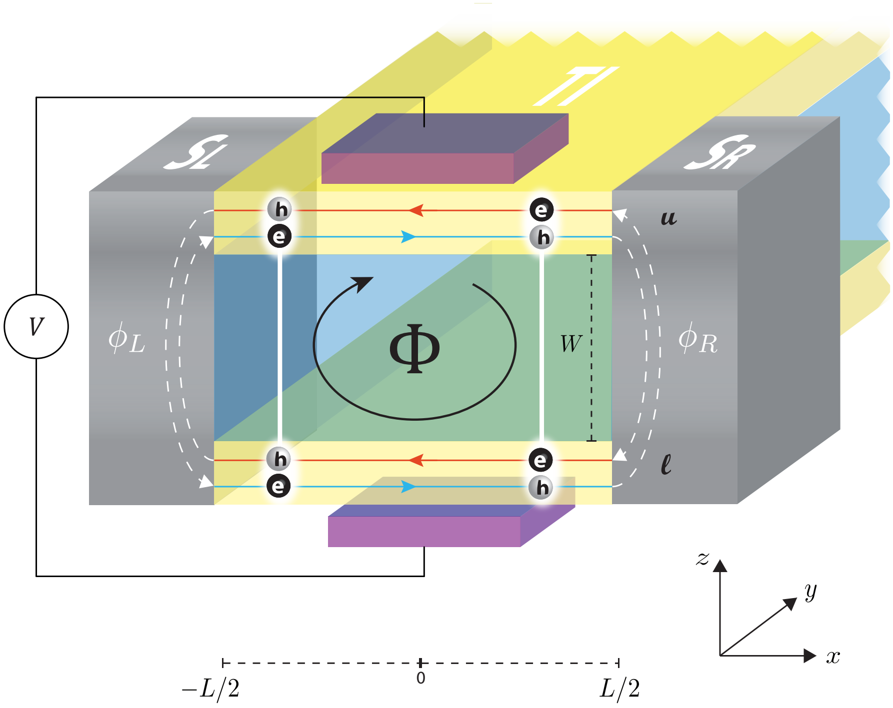

FIGURE 11.2: Proposed double TI junction - 3D scheme. It consists of an heterostructure (say CdTe-HgTe) grown along the z-axis resulting in two layers of TIs. The arrowed blue (red) solid lines represent the 1D helical edge states with spin ↑ (↓). Edge modes running in the backside part of the device here are not represented. On the frontal side, in the x-z-plane of the scheme, are depicted two CAR processes where CP are non-locally splitted. The application of the V- and Φ-field due to the presence of side gates and the induced magnetic flux. Such a fields act in terms of the unitary operators $\mathcal{U}^{u}_{\Phi}(\theta_{\Phi})$ and $\mathcal{U}^{\ell}_{V}(\theta_V)$ (see text) on the upper and lower edges respectively. Other configurations of local fields can be considered and in Appendix D.4 it is indeed shown they are fully equivalent.

y-direction) of the device of Fig. 11.2, which in turn represent an alternative coherent path between the two superconducting leads. Anyway one can nullify their contribution to the Josephson current by simply suppressing their transport coherence. This can be obtained assuming that the size of the TI in the y-direction is much larger than the coherence length ℓ_ϕ or having intentionally broken superconducting coherence introducing a dephasing source along those edges [1]. In such case they no longer contribute coherently to the transport even if they still represent available channels for ordinary reflected particles at interfaces. Such ordinary reflections, involving the backside modes, contribute by decreasing the supercurrent. This can be described by introducing an effective loss parameter $\eta \in [0, 1]$ where $\eta = 0$ represents lossless regime. When this loss mechanism is present, in order to describe the dephasing along the backside modes, we calculate the current by averaging with respect the dephasing angles – see Appendix D.3 for details.

---

[1] This can be done by adding a floating metal pad over those edge modes which will induce electron decoherence.

11.3 Local fields selective action

The V-field and Φ-field defined before and respectively associated to the angles θ_V and θ_Φ, operate independently and selectively on the local and non-local components of the Josephson current [2]. Before calculating explicitly the Josephson current in the model, a preliminary evidence of this fact is obtained via an heuristic argument applied to the simplified scenario where LARs are absent (i. e. $\Lambda_{L(R)} = 0$). Under this circumstance the non-local emission of a CP from a superconducting electrode, say S_L, results in the formation of a spin-entangled CP state, which arises from two superimposed CAR processes. In the first one, a spin-$\downarrow$ hole propagating in the lower edge gets reflected into an spin-$\uparrow$ electron in the upper edge, while in the second one, a spin-$\downarrow$ hole propagating in the upper edge gets reflected into an spin-$\uparrow$ electron in the lower edge (see Fig. 11.2). Such spin-entangled state could be represented as $|C\rangle = \left(\left|e_u^\uparrow h_\ell^\downarrow\right\rangle - \left|h_u^\downarrow e_\ell^\uparrow\right\rangle\right)/\sqrt{2}$, where the minus sign recall the fact that the CP is in a spin-singlet state as required by the s-wave nature of the superconducting leads. The action of $\mathcal{U}_V(\theta_V)$ and $\mathcal{U}_\Phi(\theta_\Phi)$ on $|C\rangle$ results in the state: $e^{i\frac{\theta_\Phi}{2}}\left(e^{-i\theta_V/2}\left|e_u^\uparrow h_\ell^\downarrow\right\rangle - e^{+i\theta_V/2}\left|h_u^\downarrow e_\ell^\uparrow\right\rangle\right)/\sqrt{2}$. This expression shows that while the Φ-field introduces only a global phase, that can be reabsorbed with a gauge transformation, the V-field modifies the entanglement symmetry of the non-local CP state $|C\rangle$ by introducing a relative phase factor $\exp(i\ \theta_V)$, without altering its entanglement content. In particular, if $\theta_V = \pi$ the non-local spin-singlet CP changes into a spin-triplet one, thus giving rise to a mismatch with respect to the intrinsic CPs singlet symmetry of the electrodes, thus hindering the Josephson coupling. In view of this fact, in the absence of LAR processes, one hence expects the Josephson current to depend upon the quantity $\mathcal{C} = |\langle C|\,\mathcal{U}_V(\theta_V)\,|C\rangle\,| = |\cos(\theta_V/2)|$, which measures the degree of change of the symmetry of the entangled CP. This emerges clearly from the study of the critical current, especially in the scenario where multiple Andreev reflections can be neglected (single-shot limit) – see Eq. (11.11) below. The interplay between CAR and LAR and the possibility of multiple reflections, on the contrary, tend to reduce the visibility of the effect: still, as we shall show in the following, also in this case the Josephson current keeps record of the phenomenon in a way that ultimately allows us to discriminating between CAR and LAR processes.

---

[2] The angular notation for the action of the local fields imply a 2π-periodicity of their actions.

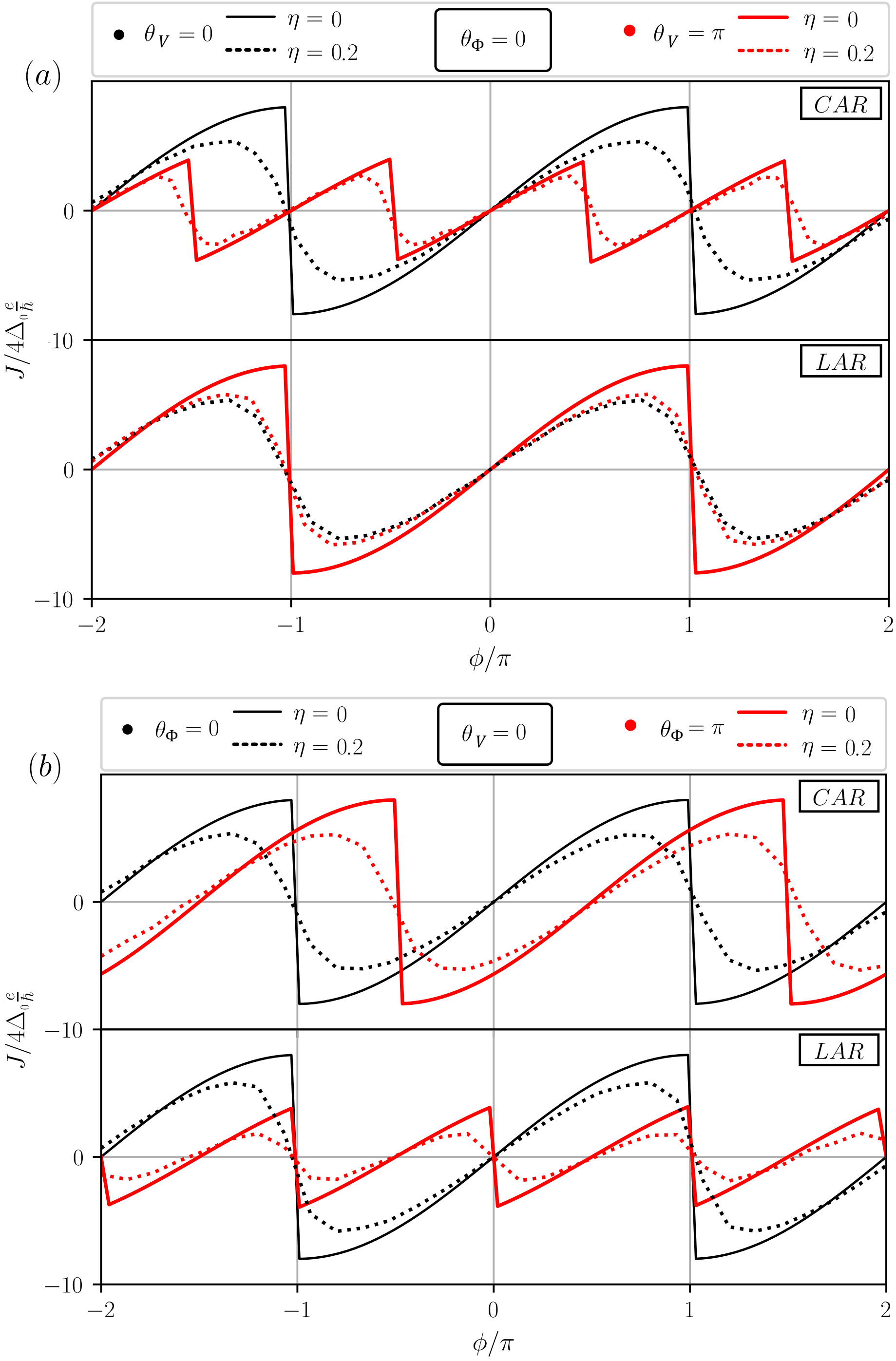

FIGURE 11.3: CPR. The Josephson current versus the phase difference ϕ expressed in units of $4\Delta_0\frac{e}{\hbar}$ at fixed temperature $k_BT/\Delta_0 = 10^{-3}$. The curves in panel (a) have been obtained fixing the value of the magnetic field ($\theta_\Phi = 0$), for different values of the V-field ($\theta_V = 0$ for the solid black line and $\theta_V = \pi$ for the solid red line). Panel (b) shows the opposite situation in which the V-field is fixed ($\theta_V = 0$) and θ_Φ is varied ($\theta_\Phi = 0$ for the solid black line and $\theta_\Phi = \pi$ for the solid red line). The respective black/red dashed curves, depicting the case with $\eta = 0.2$, have been obtained numerically. For both the realizations we have considered the two extremal cases, i. e. only CAR $|X_{L(R)}|^2 = 1$ (upper panels) and only LAR $|X_{L(R)}|^2 = 0$ (lower panels).

11.4 Josephson current

To set the above observations on firm ground in the remaining of this chapter we calculate the Josephson current flowing through the system using the scattering formalism [Beenakker1991, Beenakker1992, Beenakker2003] in the short junction limit (i. e. when $L \ll \xi$), with ideal interfaces and rigid boundary conditions, i. e. with the order parameter

$$\Delta(x) = \Delta_0 \left[\Theta(-x - L/2)e^{i\phi_L} + \Theta(x - L/2)e^{i\phi_R}\right], \tag{11.4}$$

where $\Theta(x)$ is the Heaviside function. As already discussed in Sec. 6.4, the Josephson current can be calculated as

$$J = -\frac{2e}{\hbar}\sum_p \tanh\left(\frac{\epsilon_p}{2k_BT}\right)\frac{d\epsilon_p}{d\phi}, \tag{11.5}$$

where ϵ_p are Andreev bound state energies obtained solving the self-consistent secular problem of Eq. 6.58 [Beenakker2003]. In case of no losses ($\eta = 0$) we find the following analytical expression of the CPR at finite temperature T

$$\begin{aligned}J(\phi) =& 4\frac{e\Delta_0}{\hbar}\sum_{\sigma=\pm}\left\{\sin\left(\frac{\theta_\Phi}{4} + \frac{\phi}{2} + \sigma\tan^{-1}\left(\sqrt{\frac{1-\Gamma}{1+\Gamma}}\right)\right)\times\right.\\ &\left.\tanh\left[\frac{\Delta_0}{2k_BT}\cos\left(\frac{\theta_\Phi}{4} + \frac{\phi}{2} + \sigma\tan^{-1}\left(\sqrt{\frac{1-\Gamma}{1+\Gamma}}\right)\right)\right]\right\},\end{aligned} \tag{11.6}$$

with

$$\Gamma = \cos(\theta_V/2)|X_L||X_R| + \cos(\theta_\Phi/2)|\Lambda_L||\Lambda_R|. \tag{11.7}$$

Firstly we note that $\theta_\Phi/4$ in Eq. (11.7) acts as a global phase which shifts the CPR, and manifests itself as an anomalous current at $\phi = 0$ when TRS is broken [Campagnano2015, Minutillo2018]. For simplicity, in what follows we will limit ourselves to consider the fully symmetric case $|X_L| = |X_R| = |X|$ and $|\Lambda_L| = |\Lambda_R| = |\Lambda| = \sqrt{1 - |X|^2}$.

In Fig. 11.3(a) and (b) we plot separately the contributions to the CPR arising from only CAR ($|X|^2 = 1$ for top panels) and only LAR processes ($|X|^2 = 0$ for bottom panels), for various choices of parameters. Solid curves refer to the CPR of Eq. (11.6), while dashed curves are numerical results obtained in the presence of backside edges losses ($\eta = 0.2$) [3]. Firstly we note that the curves resembles the CPR of a weak-link in the presence of spin-orbit and magnetic fields, as we may indeed naively expect [Yokoyama2013, Eto2014, Dolcini2015, Marra2016, Nava2016, Mellars2016, Nesterov2016]. In Fig. 11.3(a) we fix $\theta_\Phi = 0$ and consider two values of the V-field, namely $\theta_V = 0$ (black curves) and $\theta_V = \pi$ (red curves), while in Fig. 11.3(b) we fix $\theta_V = 0$ and consider two values of Φ-field, namely $\theta_\Phi = 0$ (black curves) and $\theta_\Phi = \pi$ (red curves).

Figs. 11.3(a) and (b) allows us to appreciate the selective action of the Φ- and V- fields on the CAR and LAR contributions to the supercurrent by their effect on the shape of the CPR. In particular, in the case of CAR processes, the shape of the CPR depends on the value of θ_V (Fig. 11.3(a), top panel), independently of the value of θ_Φ, which only induces a global phase-shift (Fig. 11.3(b), top panel). Indeed in Fig. 11.3(a), where we fix for simplicity $\theta_\Phi = 0$, black ($\theta_V = 0$) and red ($\theta_V = \pi$) curves have different shapes in the top panel ($|X|^2 = 1$ only CAR) differently to the bottom panel ($|X|^2 = 0$ only LAR) where the black and red

---

[3] We numerically tested that for $\eta \to 0$ one obtain again the analytical result.

curves are superposed having exactly the same shape. Conversely, as shown in Fig. 11.3(b), the CPR shape is affected by the value of θ_Φ (black lines $\theta_\Phi = 0$ and red ones $\theta_\Phi = \pi$) when only LAR processes are present (bottom panel) but not affected, forgetting an unessential global phase shifting, in case of only CAR processes. For other values of θ_V the CPR shape is changed, in comparison to the figure $\theta_V = 0$, but the shape changes with θ_Φ only when LAR contribution are indeed present.

We can conclude that, although in general the Josephson current contains both CAR and LAR contributions, any variation of the shape of the CPR due to the action of the V-field is a direct indication of the presence of CAR processes, (i. e. of non-local injection of spin-singlet CPs). The presence of losses ($\eta \neq 0$) simply leads to a smoothing of the CPR shape, similarly to the effect of a finite temperature (see Sec. 11.4.3), but not affect the previous discussion.

11.4.1 Single-shot limit

At this point is interesting to investigate the behaviour of the Josephson current in the limit of high losses where $\eta \approx 1$, i. e. looking at the lowest order in $(1-\eta)$. In that regime few CPs tunnel into the junction (the Josephson current is dramatically reduced). Different orders in the power $(1-\eta)$ corresponds to bounces of Cooper pairs at the interfaces with the superconductors, i. e. multiple Andreev processes. In particular one expects that the lowest order of the Josephson current corresponds to a term proportional to $(1-\eta)^4$ which describes a process where a Cooper pair is emitted on one side and absorbed on the other side and viceversa [4]. This corresponds to the propagation of the single Cooper pair along the junction (single shot limit). Higher orders $(1-\eta)^\alpha$ with $\alpha > 4$ corresponds to multiple Andreev processes where the emitted Cooper pair is at least reflected back one time.

We present below the analytical results of the Josephson current in the single shot limit following the scheme presented in the previous section. More specifically, we considered two scenarios (the same as those represented in Fig. 11.3 (a)-(b)): in the first case we just account for the local application of the V-field along one of the edge states of the TI (hence setting $\theta_\Phi = 0$); while in the second case the Φ-field is applied by fixing $\theta_V = 0$. Again, per each scenario, we consider the extremal situations in which only CAR ($|X_L| = |X_R| = |X| = 1$) or only LAR ($|X| = 0$) processes are involved at both the interfaces, in order to have only non-local or local CP-splitted states inside the junction.

- Case-(a): application of V-field ($\theta_\Phi = 0$)

$\boxed{\text{CAR}}$:

$$\bar{J}(\phi) = \frac{e}{\hbar}\Delta_0 \tanh\left(\frac{\Delta_0}{2T}\right)\cos\left(\frac{\theta_V}{2}\right)\sin(\phi)(1-\eta)^4 + \mathcal{O}((1-\eta)^6), \tag{11.8a}$$

$\boxed{\text{LAR}}$:

$$\bar{J}(\phi) = \frac{e}{\hbar}\Delta_0 \tanh\left(\frac{\Delta_0}{2T}\right)\sin(\phi)(1-\eta)^4 + \mathcal{O}((1-\eta)^6). \tag{11.8b}$$

---

[4] The lowest order $(1-\eta)^4$ accounts for the single shot CP process, where the CP is splitted at one barrier, taking an $(1-\eta)^2$ factor, and another factor when it recombines on the other barrier.

- Case-(b): application of Φ-field ($\theta_V = 0$)

$\boxed{\text{CAR}}$:

$$\bar{J}(\phi) = \frac{e}{\hbar}\Delta_0 \tanh\left(\frac{\Delta_0}{2T}\right) \sin\left(\phi + \frac{\theta_\Phi}{2}\right)(1-\eta)^4 + \mathcal{O}((1-\eta)^6), \tag{11.9a}$$

$\boxed{\text{LAR}}$:

$$\bar{J}(\phi) = \frac{e}{\hbar}\Delta_0 \tanh\left(\frac{\Delta_0}{2T}\right) \left[\sin(\phi) + \sin\left(\phi - \frac{\theta_\Phi}{2}\right)\right](1-\eta)^4 + \mathcal{O}((1-\eta)^6). \tag{11.9b}$$

Here $\bar{J}(\phi)$ represents the CPR averaged with respect the dephasing angles acquired along the backside edges of the model – see Appendix D.3. It is important to note that Eqs. (11.8) and (11.9) are fully in agreement with the behaviours of the Josephson current as described by the results reported in Fig. 11.3. In particular, in Case-(a), the V-field just affects the CAR component of the CPR Eq. (11.8a) while plays no role when only LAR processes are involved Eq. (11.8b). In Case-(b), the action of the Φ-field just operates as a global shifting on the CAR component of the CPR Eq. (11.9a), while it affects the shape of the supercurrent in case only LAR processes occur at both the interfaces Eq. (11.9b). It is worth noting that the modification of the shape of the CPR in the cases related to Eqs. (11.8a) and (11.9b) respectively, have two different origins. More specifically, in the case of Eq. (11.9b), as a consequence of the presence of only LAR processes the two CPs are separately injected in the two different TI-planes. The resulting Josephson current takes the form of a sum of two independent currents: one concerning the edge of the TI interested by the application of the Φ-field (which is shifted by an amount of $\theta_\Phi/2$), and the other, that instead refers to the free edge, which takes the usual form of $\sin(\phi)$. On the contrary, for only CAR the modification of the profile of the CPR of Eq. (11.8a), which is ruled by the factor $\cos(\theta_V/2)$, exactly reflects the action the V-field which operates on the non-local states affecting their entanglement symmetry as discussed in Sec. 11.3. For the only CAR case this is even clearer by looking at the critical current of the system as we will see in the next section.

11.4.2 Critical current

Let us now consider the behavior of the critical current, defined as $J_C = \max_\phi\{|J(\phi)|\}$, which is plotted in the main panel of Fig. 11.4 as a function of θ_V for different sets of parameters. Remarkably, we find that the critical current can be written in the following compact form

$$J_C = \alpha(\eta, T)\,|\Gamma| + \beta(\eta, T), \tag{11.10}$$

where Γ, defined in Eq. (11.7), depends only on the Andreev reflection amplitudes X_L and X_R, and on the fields strengths θ_Φ and θ_V, while the prefactor α and the off-set β depend only on the temperature T and on the losses η.

The main panel of Fig. 11.4 shows how the formula of Eq. (11.10) (white dotted lines) exactly fits the numerical results of the critical current (black and red lines) for an arbitrary choice of the CAR/LAR amplitudes and of the manipulation parameters. We first consider the ideal case of no losses $\eta = 0$ and $T = 0$ for which $\alpha = \beta = 1$. The different lines corresponds to different cases: only CAR $|X|^2 = 1$ (black lines) and the intermediate case with CARs and LARs both present $|X|^2 = 0.6$ (red lines). We show with solid lines the cases $\theta_\Phi = 0$ and with dashed lines $\theta_\Phi = \pi/4$.

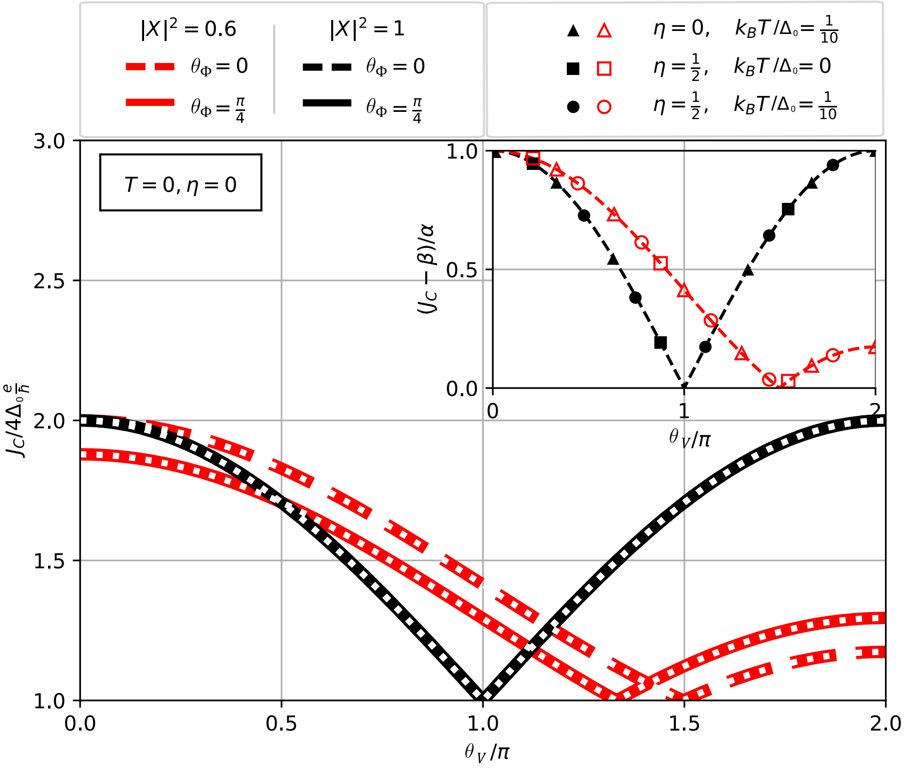

FIGURE 11.4: Critical current in units of $4\Delta_0\frac{e}{\hbar}$ as a function of θ_V. In the main box, different set of black ($|X|^2 = 1$) and red ($|X|^2 = 0.6$) curves have been obtained numerically for fixed $T = 0$ and $\eta = 0$. For each $|X|^2$, plots are shown in case of $\theta_\Phi = 0$ (dashed lines) and $\theta_\Phi = \frac{\pi}{4}$ (solid lines) respectively. We superimposed (white dotted line) the analytical behaviour as predicted by Eq. (11.10). The inset in the upper-right corner depicts the rescaled critical current (namely $(J_C - \beta)/\alpha$), obtained numerically for fixed $\theta_\Phi = 0$ in three different conditions of η and T (different point shape) for $|X|^2 = 1$ (black color) and $|X|^2 = 0.6$ (red color). All the data, independently of temperature and losses, perfectly match the curve $|\Gamma|$ (dashed lines), confirming the universality character of the shape of the critical current upon different external parameters.

We see, for only CAR, that the minimum of J_C occurs at $\theta_V = \pi$ and θ_Φ does not affect J_C (solid and dashed curves coincides), in full agreement with the discussion done before on the CPR. Red lines shows that for the case where both CAR and LAR contributions are present the J_C is still described by the general formula for any value of θ_Φ.

Furthermore we can show the general validity of this formula for finite values of η and T. In the inset of Fig. 11.4 we plot the quantity $(J_C - \beta)/\alpha$ for different values of the temperatures and losses (see label). All the points perfectly match the corresponding $|\Gamma|$ curve (thin dashed lines) as predicted by Eq. (11.10).

Hereafter we claim that the dependence on θ_V of J_C such as the one shown by Eq. (11.10) reflects the entanglement symmetry manipulation due to the action of the V-field. We first notice that the critical current, resulting from Andreev bound states within the junction, can be seen as consisting of the sum of contributions arising from multiple Andreev reflection processes. In the only-CAR regime one can identify, for any values of η, two classes of processes: the ones corresponding to Cooper pairs which traverse the junction back and forth an even number of times and the processes which traverse the junction an odd number of times. For the even class, the singlet symmetry is not modified by the effect of the V-field, since the backward time-reversed propagation cancels the V-field induced phase taken during the forward propagation. The spin entanglement symmetry is instead changed only for the odd class processes. This suggests that, at zero temperature and without losses ($\eta = 0$), the odd class processes contribute to the critical current with the term, introduced before, $\mathcal{C} = |\langle C|\mathcal{U}_V(\theta_V)|C\rangle| = |\cos(\theta_V/2)|$ in units of $J_0 = 4\Delta_0\frac{e}{\hbar}$. At the same time the even class is independent of θ_V and contributes to the current with the constant value J_0 (this give rise to the off-set β in Eq. (11.10)). As a result, the critical current can be written as $J_C = J_0(1+\mathcal{C})$. In particular, at $\theta_V = \pi$ the entanglement symmetry of the non-local electronic state is changed into triplet in half of the processes (the odd ones) and is left singlet in the other half (the even ones). As a result, the non-local electronic state is an equal weighted mixture of singlet and triplet states. This interpretation is actually corroborated by the fact that when only the lowest order processes contribute, i. e. in the single-shot limit occurring when $\eta \simeq 1$, the critical current in the leading term of $(1-\eta)$ takes the form

$$J_C = \frac{e\Delta_0}{\hbar}|\cos(\theta_V/2)|(1-\eta)^4 + \mathcal{O}((1-\eta)^6) \,, \tag{11.11}$$

that is equal to zero in when $\theta_V = \pi$. Such a result shows that in the single shot regime the action of the local V-field returns exactly the expected entanglement manipulation signature $\mathcal{C}$. Furthermore, Eq. (11.10) clarifies that the critical current allows one to access experimentally the product $|X_R||X_L|$ which determines the relative weight between the LAR and CAR processes. Ultimately this can be seen as a consequence of the selective action of the fields on the local and non-local components of the current (second and first term in Γ).

11.4.3 Effect of the temperature T and η

In this section we investigate in more detail the effect of the temperature T and losses η on the critical current. As pointed out in Sec. 11.4.2, the general expression of the critical current of the system takes the compact form of Eq. (11.10) where the amplitude α and the off-set β just depend on the temperature T and on the losses η. In Sec. 11.4.1 we calculate the Josephson current at the lowest order in $(1-\eta)$ for any temperature, see Eqs. (11.8) and (11.9). J_C can be also calculated analytically in the regime of no losses ($\eta = 0$) in the limit cases of low ($k_BT \ll \Delta_0$) and high ($k_BT \gg \Delta_0$) temperature. Indeed, we find

$$\begin{cases} J_C \simeq J_0(1+|\Gamma(\theta_V,\theta_\Phi)|) \text{ for } k_BT \ll \Delta_0 & \text{(11.12a)} \\ J_C \simeq J_0\dfrac{\Delta_0}{2k_BT}|\Gamma(\theta_V,\theta_\Phi)| \text{ for } k_BT \gg \Delta_0 & \text{(11.12b)} \end{cases}$$

which clearly shows the fundamental dependence of the critical current on the Γ function of Eq. (11.7). In particular, in the limit of low temperature, Eq. (11.12a), we have $\alpha = \beta = 1$, while for high temperatures, Eq. (11.12b), we have $\alpha/J_0 = \frac{\Delta_0}{2k_BT}$ and $\beta = 0$. The numerical plot of α (red line) and β (blue line) as functions of k_BT, in the case $\eta = 0$, is shown in Fig. 11.5.

We note that by increasing the temperature, the critical current is depressed being both α and β decreasing (β gets suppressed much faster than α). The behavior of the off-set β as a function of temperature is consistent with the interpretation, given in Sec. 11.4.2, that it corresponds to the contribution to the critical current of processes where CPs bounce back and forth along the junction, i. e. multiple Andreev reflections. Indeed increasing the temperature

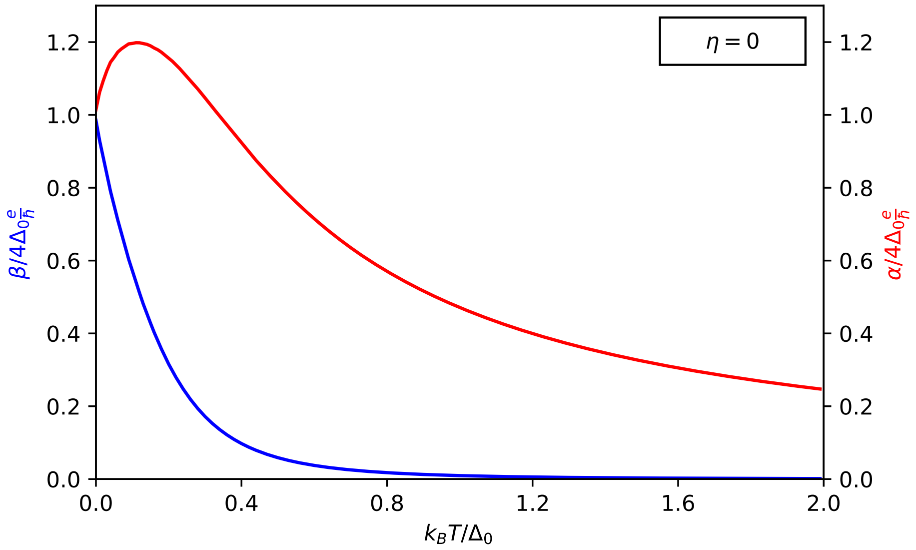

FIGURE 11.5: Numerical plots of the amplitude α (red line) and the off-set β (blue line) of the critical current of Eq. (11.10) in case of no losses ($\eta = 0$), expressed in units of $4\Delta_0\frac{e}{\hbar}$ as functions of the thermal energy k_BT (in units of Δ_0). Note in the limits of $k_BT \ll \Delta_0$ and $k_BT \gg \Delta_0$ we recover the analytical results of Eq. (11.12).

we expect that multiple Andreev processes are strongly suppressed in comparison to the single transmission of a Cooper pair which will dominate the Josephson current contribution in the high temperature regime. This is why, in the high-temperature limit, the critical current is directly proportional to the Γ function which effectively describes the manipulation induced by the local fields over a single CP transfer.

We discussed at the beginning of Sec. 11.4 that the presence of losses η only smoothens the shape of the CPR. In Fig. 11.6 we compare the CPR in the case of finite η (dashed lines) with the case of no-losses (solid lines) for two different temperatures $T = 0$ and $k_BT/\Delta_0 = 0.1$. One can easily see how the smoothening induced by the losses described by η are similar to the smoothening induced by the temperature effects.

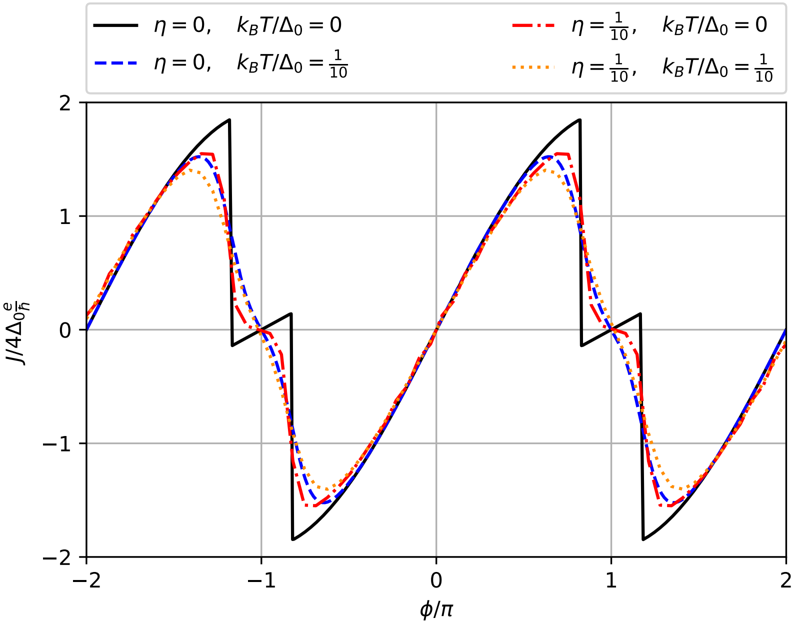

FIGURE 11.6: Josephson CPR expressed in units of $4\Delta_0\frac{e}{\hbar}$. For the sake of simplicity, symmetric conditions have been considered at left/right boundaries for the splitting amplitudes: $|X_L| = |X_R| = |X|$. All the curves have been obtained for the following choice of parameters: $|X|^2 = 1/2$, $\theta_\Phi = 0$, $\theta_V = \pi/2$. Solid lines correspond to the ideal case of no losses, i. e. $\eta = 0$, with $k_BT = 0$ (dark-blue solid line) and $k_BT/\Delta_0 = 1/10$ (light-blue solid line). Dashed lines depict the case of finite losses, namely $\eta = 1/10$, for the same values of temperature as before, i. e. $k_BT = 0$ (red dashed line) and $k_BT = 1/10$ (magenta dashed line). The result of finite losses η is to smooth out the shape of the Josephson current similarly to the effect of a finite temperature.

11.5 Conclusions

In this chapter we have proposed a system which makes use of helical edge states of a 2D topological insulator (TI), in a specific configuration, to spatially separate the two electrons composing a Cooper pair of an s-wave superconductor. Such spatial separation can described, in the scattering approach, as a crossed Andreev reflection (CAR) process. The application of an external gate potential, which do not break time-reversal symmetry, enables the manipulation of the entanglement symmetry of the CAR state preserving its purity. We have also shown that a time-reversal breaking field can be used to tune the strength of the local Andreev reflection (LAR) processes without affecting the previously discussed entanglement manipulation. In particular we have shown, both analytically and numerically, that a measurable signature of the manipulation is provided by the Josephson current. We have derived the analytical formula for the current-phase-relationship in the structure as a function of the external fields, for any temperature in the absence of losses $\eta = 0$. In this configuration, the critical current can be directly connected to the relative weights between LAR and CAR processes, thus representing a simple way to identify the existence of non-local processes. Finally we have demonstrated, by carefully discussing the multiple Andreev reflections process occurring in the structure, the origin and the universality (independently of temperature or losses) of the obtained results. In essence, the Josephson current phenomenology is naturally associated to the entanglement symmetry evolution in the junction. We think that the proposed structure, can be realized with present technology of the hybrid topological nano-junctions, thus opening a new route toward entanglement manipulation in electronic solid state systems.

We conclude by estimating the strength of the potential voltage necessary to manipulate the entanglement symmetry from singlet to triplet. In this case, in order to have $\theta_V \approx \pi$ - with a junction length of $L \approx 600\ nm$ [Wiedenmann2016] and a TI Fermi velocity of $v_F = 10^5$ m/s - the gate voltage can be estimated as $V = 1.7\ mV$. A similar estimation shows that, using the Doppler shift, the magnetic field strength necessary to perform a manipulation of the angle $\theta_\Phi \approx \pi$ - able to suppress the LAR component - is $8\ mT$, which is not too prohibitive in order to not break the topological protection of the TI.

12

Conclusions and Future Perspectives

In this thesis we studied the transport properties of hybrid topological Josephson junctions based on two dimensional topological insulators (2DTIs). In Chaps. 2 and 3 we provided the basic concepts that underlie the two main constituent materials necessary for the realization of a hybrid topological Josephson junction, namely: topological insulators and superconductors. In Chap. 4 we introduced the Landauer-Büttiker theory generalized to include superconducting components, in Chap. 5 we applied the scattering approach to the case of the linear response regime to compute the Onsager coefficients, and in Chap. 6 we reviewed the main aspects of the Josephson effect and discussed the constitutive equations governing the behavior of Josephson junctions. In Chaps. 7, 8 and 9 we consider a system consisting of a topological Josephson junction hosting a Kramers pair of helical edge states of a quantum spin Hall bar in contact with a normal-metal probe. In Chap. 7, we showed that a thermal gradient between the superconductors in the presence of the Doppler shift generates a nonlocal thermoelectrical transport inside the probe. This purely nonlocal thermoelectric effect is a unique signature of the helical nature of the edge states and it can constitute a useful tool for probing helicity in systems where the Hall bar configuration is difficult to achieve. In Chap. 8 we showed that a phase-dependent nonlocal thermoelectricity can be generated by a purely Andreev interferometric mechanism through the application of a dissipationless current between the two superconductors, even without the need of applying an external magnetic field. We discussed the dependence of this mechanism over the junction length L and the coupling with the probe $|t|^2$, and provided also a realistic estimation of the nonlocal Seebeck coefficient. In Chap 9 we generalized the analysis done in Chaps. 7 and 8 to the case where we have different gaps in order to better describe a realistic experimental situation. In this configuration we also analyzed the heat current in the probe, finding that it can be finite and the system can be viewed as a flux controlled thermal router, depending on the difference between the superconducting gaps. Finally, we discussed the nonlinear performance of the nonlocal thermoelectric machine finding that it reaches maximum power at maximal efficiency for a well coupled normal probe. In Chap. 10, we analyzed the Andreev spectrum and the thermal conductance of a 2DTI Josephson junction hosting a magnetic island with one and two magnetic domains. We showed that, features related to the interplay between superconductivity and magnetism in these systems cannot be easily discerned looking at behavior of the Andreev spectrum. Instead, we verified that the thermal conductance is very sensitive to the nature of the junction and the domain structure of the magnetic island. A remarkable result is the fact that for configurations with two magnetic domains with different orientations, which host Jackiw-Rebbi resonant modes, the thermal conductance decreases with the temperature. Finally, in Chap. 11, we investigated the supercurrent in a hybrid topological Josephson junction consisting of two planes of topological insulator. We described the effects of gate voltage and magnetic flux controls applied to the edge states of each TI. In particular, we demonstrated that the voltage gating allows the manipulation of the entaglement symmetry of non-local Cooper pairs associated to the crossed Andreev reflection process. Remarkably, we showed that the behavior of the critical current reflects the change in the symmetry occurred to the entangled state and allows to determine the microscopic parameters of the junction.

As future direction, it would be interesting to further assess the impact of multiple Andreev reflections (MARs) on the manipulation of the entaglement symmetry of nonlocal Cooper pairs in a system similar to that presented in Chap. 11, when a voltage is applied between the two superconducting leads. Furthermore, as another possible direction, we are already working on a generalization of our results on nonlocal thermoelectricity - obtained for 2DTI Josephson junctions - to the case of a 3DTI Josephson junction. In this regard, by following the calculations already presented in the Appendix B, we expect that Doppler shift effects will also potentially generate a nonlocal thermoelectrical response on the surface states of a 3D topological insulator. Finally, another possibility could be to use thermoelectric effects as a tool of detection for Majorana zero modes in 2DTI based Josephson junction systems with a magnetic island and in contact with a metallic probe.

A

Appendix: S-TI-S Josephson junction with an N-metal probe

In this appendix we report details of the calculations about the S-TI-S Josephson junction system in contact with an N-metal probe discussed in Chaps. 7, 8 and 9.

A.1 Scattering matrix

Here we consider the general case of superconducting leads with different gap order parameters Δ_L and Δ_R (as discussed in Chap. 9), the left/right symmetric case discussed in Chaps. 7 and 8 can then be easily recovered by imposing $\Delta_L = \Delta_R = \Delta$. We analyze the setup of Fig. 9.1, assuming the absence of inelastic scattering since it may only appear for junctions longer than coherence length $L \gg \xi$ and/or high temperatures where standard low temperature BCS superconductivity cannot survive. In such case dc transport is determined by the quantum mechanical scattering matrix S [Lambert1998], which yields scattering properties at energy ϵ, of a phase-coherent, non-interacting system described by a Hamiltonian H_{BdG} such as Eq. (9.1) . The scattering problem, in terms of scattering matrix, can be formulated as

$$\Psi^{\alpha}_{(i,\sigma)}|_{out} = S^{\alpha\beta}_{(i,\sigma)(j,\sigma')}\Psi^{\beta}_{(j,\sigma')}|_{in}. \tag{A.1}$$

It relates incoming/outgoing states $(j,\sigma')/(i,\sigma)$ with $\{\sigma,\sigma'\} = \{\uparrow,\downarrow\}$ labeling the spin-channel at the respective lead $i, j = N, L, R$. In Eq. (A.1), $\{\alpha,\beta\} = \{e,h\}$ may indicate electrons and holes in the normal probe N, or eventually $\{\alpha,\beta\} = \{\tilde{e},\tilde{h}\}$ label QPs and QHs in the superconductors. In order to compute the full scattering matrix S of the system, we proceed by writing first the scattering matrix S_N describing the coupling of the metallic probe with the TI upper edge

$$\begin{pmatrix} c_N^{\downarrow} \\ b_N^{\downarrow} \\ c_N^{\uparrow} \\ b_N^{\uparrow} \\ c_L^{\downarrow} \\ b_L^{\downarrow} \\ c_R^{\uparrow} \\ b_R^{\uparrow} \end{pmatrix} = \begin{pmatrix} 0 & 0 & r & 0 & 0 & 0 & t & 0 \\ 0 & 0 & 0 & r^* & 0 & 0 & 0 & t^* \\ r & 0 & 0 & 0 & t & 0 & 0 & 0 \\ 0 & r^* & 0 & 0 & 0 & t^* & 0 & 0 \\ 0 & 0 & t & 0 & 0 & 0 & r & 0 \\ 0 & 0 & 0 & t^* & 0 & 0 & 0 & r^* \\ t & 0 & 0 & 0 & r & 0 & 0 & 0 \\ 0 & t^* & 0 & 0 & 0 & r^* & 0 & 0 \end{pmatrix}_{S_N} \begin{pmatrix} c_N^{\uparrow} \\ b_N^{\uparrow} \\ c_N^{\downarrow} \\ b_N^{\downarrow} \\ c_L^{\uparrow} \\ b_L^{\uparrow} \\ c_R^{\downarrow} \\ b_R^{\downarrow} \end{pmatrix} \tag{A.2}$$

where we indicated with $c_N^{\sigma}/b_N^{\sigma}$ the incoming and outgoing electrons/holes in the probe N, and with $c_{L/R}^{\sigma}/b_{L/R}^{\sigma}$ the incoming and outgoing electrons/holes in the TI region. The index $i = L/R$ labels the interface with the left/right superconductor and $\sigma = \uparrow, \downarrow$ indicate the spin. Notice that spin and direction of propagation of particles moving along the x axis inside the TI region are locked due to the helicity of the edge states: hence spin-up particles are right movers and spin-down particles are left movers. In particular, for the previous formula S_N, we assumed a symmetric beam splitter which effectively describes the contact interface between the normal lead N and the TI edge. The beam splitter is characterized by spin and energy independent reflection and transmission amplitudes

$$r = \cos(\eta) \quad \text{and} \quad t = i\ \sin(\eta), \tag{A.3}$$

which depend on only one parameter $\eta \in \left[0, \frac{\pi}{2}\right]$ such that unitarity is satisfied, i. e. $|r|^2 + |t|^2 = 1$. In order to keep the presentation simple, here we preferred not to specifically discuss any energy dependency of the coupling amplitude t. In fact, if this was the case, the actual value of the nonlocal thermoelectric current discussed in Chaps. 7, 8 and 9 would depend on the details of the function $t(\epsilon)$ which has non universal nature.

Notice that, in the S_N matrix of Eq. (A.2), the complex conjugate coefficients r^* and t^* represent the scattering amplitudes for the holes. Indeed, as discussed in Sec. 4.4, if $S^{ee}_{N\ (i,\sigma)(j,\sigma')}(\epsilon)$ acts in the particle sector, the scattering (sub-)matrix for the holes satisfies the relation: $S^{hh}_{N\ (i,\sigma)(j,\sigma')}(\epsilon) = \left[S^{ee}_{N\ (i,\sigma)(j,\sigma')}(-\epsilon)\right]^*$ as requested by the particle-hole symmetry of the system [Pershoguba2019]. Obviously the elements $S^{\alpha\bar{\alpha}}_{N\ (i,\sigma)(j,\sigma')}(\epsilon)$ (with $\alpha = e, h$), coupling incoming electrons(holes) with outgoing holes(electrons) are necessarily zero since only ordinary scattering processes are involved, i. e. no Andreev reflections occur for normal metal probe. Moreover, by using Eq. (A.3), the scattering matrix S_N describing the contact between the normal-metal probe and the TI edge, can be also recasted in the more compact fashion $S_N(\eta) = i \sin(\eta)\zeta_1 \otimes \sigma_1 \otimes \tau_3 + \cos(\eta)\zeta_0 \otimes \sigma_1 \otimes \tau_0$, expressed in terms of the Pauli matrices ζ, σ and τ respectively acting in the N-TI channels space, spin space and particle-hole space.

At this point we are ready to compute the scattering matrices S_i with $i = L/R$ describing respectively left/right interfaces of the TI with the superconductors. In order to find the solutions for the scattering amplitudes we have to solve the wave function matching problem at both interfaces by imposing the following boundary condition obtained by integrating the

BdG Hamiltonian of Eq. (9.1):

$$\begin{cases} -\lambda_i^* u_\uparrow(x_{\text{int}}^-) = -\lambda_i u_\uparrow(x_{\text{int}}^+) \\ \lambda_i u_\downarrow(x_{\text{int}}^-) = \lambda_i^* u_\downarrow(x_{\text{int}}^+) \\ -\lambda_i v_\uparrow(x_{\text{int}}^-) = -\lambda_i^* v_\uparrow(x_{\text{int}}^+) \\ \lambda_i^* v_\downarrow(x_{\text{int}}^-) = \lambda_i v_\downarrow(x_{\text{int}}^+) \end{cases} \tag{A.4}$$

where $\lambda_i = 1 + i\frac{\Lambda_i}{2\hbar v_F}$ accounts for the contact potential Λ_i at left ($i = L$) and right ($i = R$) interface located at $x_{\text{int}} = 0, L$. Following this prescription we find (for example) the scattering matrix S_L for the left interface

$$\begin{pmatrix} \tilde{c}_L^\downarrow \\ \tilde{b}_L^\downarrow \\ c_L^\uparrow \\ b_L^\uparrow \end{pmatrix} = \begin{pmatrix} 0 & r_{\tilde{e}\tilde{h}}^L & t_{\tilde{e}e}^L & 0 \\ r_{\tilde{h}\tilde{e}}^L & 0 & 0 & t_{\tilde{h}h}^L \\ t_{e\tilde{e}}^L & 0 & 0 & r_{eh}^L \\ 0 & t_{h\tilde{h}}^L & r_{he}^L & 0 \end{pmatrix}_{S_L} \begin{pmatrix} \tilde{c}_L^\uparrow \\ \tilde{b}_L^\uparrow \\ c_L^\downarrow \\ b_L^\downarrow \end{pmatrix} \tag{A.5}$$

where we indicated with $\tilde{c}_L^{\uparrow\downarrow}$ and $\tilde{b}_L^{\uparrow\downarrow}$ the incoming and outgoing QPs and QHs respectively inside the left superconductor. The obtained coefficients $r_{\alpha\beta}^L$ and $t_{\alpha\beta}^L$ represent respectively the reflection and transmission amplitudes of an incoming particle of type β to a particle of type α at the interface. Those coefficients can be compactly written as

$$\begin{aligned} r_{\gamma\bar{\gamma}}^L &= \gamma\frac{v_{L\bar{\gamma}}}{u_{L\bar{\gamma}}} e^{i\alpha_{\bar{\gamma}}} e^{i\gamma\phi_L}, \\ r_{\tilde{\gamma}\tilde{\bar{\gamma}}}^L &= -\frac{v_{L\gamma}}{u_{L\gamma}} e^{-i\beta_\gamma^L} \cdot \Xi_\gamma^L(\epsilon), \\ t_{\gamma\tilde{\gamma}}^L &= \frac{\sqrt{u_{L\bar{\gamma}}^2 - v_{L\bar{\gamma}}^2}}{u_{L\bar{\gamma}}} e^{\frac{i}{2}\left(\alpha_{\bar{\gamma}} - \beta_{\bar{\gamma}}^L\right)} e^{-i\gamma\frac{\phi_L}{2}} e^{i\bar{\gamma}2\arg(\lambda_L)} \cdot \Xi_{\bar{\gamma}}^L(\epsilon), \\ t_{\tilde{\gamma}\gamma}^L &= \bar{\gamma}\frac{\sqrt{u_{L\gamma}^2 - v_{L\gamma}^2}}{u_{L\gamma}} e^{\frac{i}{2}\left(\alpha_\gamma - \beta_\gamma^L\right)} e^{i\bar{\gamma}\frac{\phi_L}{2}} e^{i\bar{\gamma}2\arg(\lambda_L)} \cdot \Xi_\gamma^L(\epsilon), \end{aligned} \tag{A.6}$$

where the electron/hole index ($\gamma = e/h$) in the *l.h.s.* is converted in a simple sign ($\gamma = +/-$) in the *r.h.s.* to match with the notation used in Eq. (9.3). We also introduced the symbol

$$\Xi_\pm^L(\epsilon) \equiv \begin{cases} 1 & |\epsilon_{DS}| > \Delta_L \ \wedge \ 0 < \epsilon < |\Delta_L - |\epsilon_{DS}|| \\ \Theta(|\epsilon_\pm| - \Delta_L) & \text{otherwise} \end{cases} \tag{A.7}$$

with $\epsilon_\pm = \epsilon \pm \epsilon_{DS}(\Phi)$. The phases take the form

$$\alpha_\pm = \epsilon_\pm/\epsilon_c \quad \text{and} \quad \beta_\pm^L = \sqrt{\epsilon_\pm^2 - \Delta_L^2}/\epsilon_c, \tag{A.8}$$

with $\epsilon_c = \hbar v_F/L$ the Thouless energy of the junction. A similar result for the scattering matrix at the right interface S_R can be computed. The scattering coefficients can be obtained from Eq. (A.6) by replacing $(r_{\alpha\beta}^L, t_{\alpha\beta}^L) \to (r_{\beta\alpha}^R, t_{\beta\alpha}^R)$ in the *l.h.s.* and, in the *r.h.s.*, making the substitution $L \to R$ and $\phi_L \to -\phi_R$.

In conclusion, following the standard procedure presented in Ref. [Datta1997] (see also Appendix C), the full scattering matrix of the system is obtained by combining together the three scattering matrices such as

$$S = S_L \circ S_N \circ S_R, \tag{A.9}$$

which determines the scattering between the three terminals. More precisely, by taking into account the scattering amplitudes obtained above and using Eq. (A.9), we can write the full scattering matrix of the system in its explicit form:

$$\begin{pmatrix} c_N^{\downarrow} \\ c_N^{\uparrow} \\ \tilde{c}_L^{\downarrow} \\ \tilde{c}_R^{\uparrow} \\ b_N^{\downarrow} \\ b_N^{\uparrow} \\ \tilde{b}_L^{\downarrow} \\ \tilde{b}_R^{\uparrow} \end{pmatrix}_{out} = \begin{pmatrix} 0 & a_2 & 0 & a_4 & C_1 & 0 & C_3 & 0 \\ a_1 & 0 & a_3 & 0 & 0 & C_2 & 0 & C_4 \\ 0 & b_2 & 0 & b_4 & D_1 & 0 & D_3 & 0 \\ b_1 & 0 & b_3 & 0 & 0 & D_2 & 0 & D_4 \\ A_1 & 0 & A_3 & 0 & 0 & c_2 & 0 & c_4 \\ 0 & A_2 & 0 & A_4 & c_1 & 0 & c_3 & 0 \\ B_1 & 0 & B_3 & 0 & 0 & d_2 & 0 & d_4 \\ 0 & B_2 & 0 & B_4 & d_1 & 0 & d_3 & 0 \end{pmatrix}_S \begin{pmatrix} c_N^{\uparrow} \\ c_N^{\downarrow} \\ \tilde{c}_L^{\uparrow} \\ \tilde{c}_R^{\downarrow} \\ b_N^{\uparrow} \\ b_N^{\downarrow} \\ \tilde{b}_L^{\uparrow} \\ \tilde{b}_R^{\downarrow} \end{pmatrix}_{in} \tag{A.10}$$

where

$$a_1 = r + \frac{r_{eh}^L r_{he}^R t^2 r^*}{1 - r_{eh}^L r_{he}^R |r|^2}; \quad a_2 = \frac{r_{eh}^R r_{he}^L t^2 r^*}{1 - r_{eh}^R r_{he}^L |r|^2} + r; \quad a_3 = \frac{t t_{e\tilde{e}}^L}{1 - r_{eh}^L r_{he}^R |r|^2}; \quad a_4 = \frac{t t_{e\tilde{e}}^R}{1 - r_{eh}^R r_{he}^L |r|^2};$$

$$b_1 = \frac{t t_{\tilde{e}e}^R}{1 - r_{eh}^L r_{he}^R |r|^2}; \quad b_2 = \frac{t t_{\tilde{e}e}^L}{1 - r_{eh}^R r_{he}^L |r|^2}; \quad b_3 = \frac{r t_{e\tilde{e}}^L t_{\tilde{e}e}^R}{1 - r_{eh}^L r_{he}^R |r|^2}; \quad b_4 = \frac{r t_{\tilde{e}e}^L t_{e\tilde{e}}^R}{1 - r_{eh}^R r_{he}^L |r|^2};$$

$$c_1 = r^* + \frac{r r_{eh}^R r_{he}^L \left(t^2\right)^*}{1 - r_{eh}^R r_{he}^L |r|^2}; \quad c_2 = r^* + \frac{r r_{eh}^L r_{he}^R \left(t^2\right)^*}{1 - r_{eh}^L r_{he}^R |r|^2}; \quad c_3 = \frac{t_{h\tilde{h}}^L t^*}{1 - r_{eh}^R r_{he}^L |r|^2}; \quad c_4 = \frac{t_{h\tilde{h}}^R t^*}{1 - r_{eh}^L r_{he}^R |r|^2};$$

$$d_1 = \frac{t_{\tilde{h}h}^R t^*}{1 - r_{eh}^R r_{he}^L |r|^2}; \quad d_2 = \frac{t_{\tilde{h}h}^L t^*}{1 - r_{eh}^L r_{he}^R |r|^2}; \quad d_3 = \frac{t_{h\tilde{h}}^L t_{\tilde{h}h}^R r^*}{1 - r_{eh}^L r_{he}^R |r|^2}; \quad d_4 = \frac{t_{Hh}^L t_{hH}^R r^*}{1 - r_{eh}^L r_{he}^R |r|^2};$$

$$A_1 = \frac{r_{he}^R |t|^2}{1 - r_{eh}^L r_{he}^R |r|^2}; \quad A_2 = \frac{r_{he}^L |t|^2}{1 - r_{eh}^L r_{he}^R |r|^2}; \quad A_3 = \frac{r r_{he}^R t_{e\tilde{e}}^L t^*}{1 - r_{eh}^L r_{he}^R |r|^2}; \quad A_4 = \frac{r r_{he}^L t_{e\tilde{e}}^R t^*}{1 - r_{eh}^L r_{he}^R |r|^2};$$

$$B_1 = \frac{r_{he}^R t t_{\tilde{h}h}^L r^*}{1 - r_{eh}^L r_{he}^R |r|^2}; \quad B_2 = \frac{r_{he}^L t t_{\tilde{h}h}^R r^*}{1 - r_{eh}^L r_{he}^R |r|^2}; \quad B_3 = r_{\tilde{h}\tilde{e}}^L + \frac{r_{he}^R t_{e\tilde{e}}^L t_{\tilde{h}h}^L |r|^2}{1 - r_{eh}^L r_{he}^R |r|^2}; \quad B_4 = r_{\tilde{h}\tilde{e}}^R + \frac{r_{he}^L t_{e\tilde{e}}^R t_{\tilde{h}h}^R |r|^2}{1 - r_{eh}^L r_{he}^R |r|^2};$$

$$C_1 = \frac{r_{eh}^R |t|^2}{1 - r_{eh}^L r_{he}^R |r|^2}; \quad C_2 = \frac{r_{eh}^L |t|^2}{1 - r_{eh}^L r_{he}^R |r|^2}; \quad C_3 = \frac{r_{eh}^R t t_{h\tilde{h}}^L r^*}{1 - r_{eh}^L r_{he}^R |r|^2}; \quad C_4 = \frac{r_{eh}^L t t_{h\tilde{h}}^R r^*}{1 - r_{eh}^L r_{he}^R |r|^2};$$

$$D_1 = \frac{r r_{eh}^R t_{\tilde{e}e}^L t^*}{1 - r_{eh}^L r_{he}^R |r|^2}; \quad D_2 = \frac{r r_{eh}^L t_{\tilde{e}e}^R t^*}{1 - r_{eh}^L r_{he}^R |r|^2}; \quad D_3 = r_{\tilde{e}\tilde{h}}^L + \frac{r_{eh}^R t_{\tilde{e}e}^L t_{h\tilde{h}}^L |r|^2}{1 - r_{eh}^L r_{he}^R |r|^2}; \quad D_4 = r_{\tilde{e}\tilde{h}}^R + \frac{r_{eh}^L t_{\tilde{e}e}^R t_{h\tilde{h}}^R |r|^2}{1 - r_{eh}^L r_{he}^R |r|^2}.$$

As an example of the derivation of the non-zero entries of the scattering matrix, let us explicit the calculation of the term a_1, which relates an incoming spin-up electron with an outgoing spin-up electron at the same N metallic lead

$$\begin{aligned} c_N^{\uparrow} \to c_N^{\uparrow} : & \\ a_1 &= r + t r_{he}^R r^* r_{eh}^L t + t r_{he}^R r^* r_{eh}^L r r_{he}^R r^* r_{eh}^L t + \dots \\ &= r + t^2 r_{he}^R r^* r_{eh}^L \sum_{n=0}^{\infty} \left(r_{eh}^L r_{he}^R \, |r|^2 \right)^n \\ &= r + \frac{r_{eh}^L r_{he}^R t^2 r^*}{1 - r_{eh}^L r_{he}^R \, |r|^2}. \end{aligned} \tag{A.11}$$

Notice that, multiple reflections occurring inside the junction have been taken into account, as results from the geometrical series in Eq. (A.11).

A.2 Symmetries of the scattering coefficients

As we discussed in Secs. 4.3 and 4.4 [Lambert1998, Jacquod2012, Blasi2020a], the scattering coefficients satisfy relations due to microreversibility $P_{i,j}^{\alpha,\beta}(\epsilon,\vec{\theta}) = P_{j,i}^{\beta,\alpha}(\epsilon,-\vec{\theta})$, particle-hole symmetry $P_{i,j}^{\alpha,\beta}(\epsilon,\vec{\theta}) = P_{i,j}^{-\alpha,-\beta}(-\epsilon,\vec{\theta})$ and unitarity

$$\begin{aligned}\sum_{\alpha i} P_{i,j}^{\alpha,\beta}(\epsilon,\vec{\theta}) &= N_j^{\beta}(\epsilon,\vec{\theta}))\\ \sum_{\beta j} P_{i,j}^{\alpha,\beta}(\epsilon,\vec{\theta}) &= N_i^{\alpha}(\epsilon,\vec{\theta}),\end{aligned}$$

where $N_i^{\alpha}(\epsilon,\vec{\theta})$ is the number of open channels for α-like QPs at energy ϵ in lead i and where we introduced the vector parameter $\vec{\theta} \equiv (\Phi,\phi)$ which includes both the magnetic flux Φ and the gauge invariant Josephson phase difference $\phi = \phi_L - \phi_R$ (according to the notation used in Chap. 9). Moreover, when $\Delta_L = \Delta_R$ (namely, the system is left/right symmetric), the scattering coefficients show also the following additional symmetries

$$\begin{aligned}P_{N,N}^{\alpha,\beta}(\epsilon,\vec{\theta}) &= P_{N,N}^{-\alpha,-\beta}(\epsilon,\vec{\theta}),\\ P_{N,L}^{\alpha,\beta}(\epsilon,\vec{\theta}) &= P_{N,R}^{-\alpha,-\beta}(\epsilon,\vec{\theta}),\\ P_{N,L/R}^{\alpha,\beta}(\epsilon,\vec{\theta}) &= P_{N,L/R}^{-\alpha,-\beta}(\epsilon,-\vec{\theta}).\end{aligned} \tag{A.12}$$

Interestingly, again in the left/right symmetric case, one finds that the scattering coefficients $P_{i,j}^{\alpha,\beta}$ do not depend on the position x_0 of the probe (see Fig. 9.1), but simply on the total length L of the junction. The reason for this relies on the symmetry exhibited by the different paths that take a QP of type β from lead j to a QP of type α in lead i. More specifically, due to the helicity of the edge state and the spin-independence of the transmission amplitude t, each of these paths comes in pair with its symmetric one (obtained by exchanging left and right), in such a way that their contribution to $P_{i,j}^{\alpha,\beta}$ only depends on L. On the contrary, in the asymmetric case, i. e. when $\Delta_L \neq \Delta_R$, the position of the probe x_0 along the edge does matter. Notice that, in Chap. 9, when we discuss the asymmetric case we assume to fix the probe tip just in the middle of the junction, i.e. $x_0 = L/2$.

A.3 Analytical results of the probe's currents in the symmetric case $\Delta_L = \Delta_R$

Here we discuss some analytical results for the symmetric case (i. e. $\Delta_L = \Delta_R = \Delta$) exploiting the symmetry expressed in the relations of Eqs. (A.12). We concentrate mainly on the quasi-particle charge (J_N^c) and heat (J_N^h) current at the probe N that can be written as

$$J_N^c = \frac{e}{h}\int_0^{\infty} d\epsilon \left\{F_N^-(\epsilon)\left[A^-(\epsilon,\vec{\theta}) + A^-(\epsilon,-\vec{\theta})\right] - F_{LR}^-(\epsilon)\left[Q^-(\epsilon,\vec{\theta}) - Q^-(\epsilon,-\vec{\theta})\right]\right\}, \tag{A.13}$$

$$J_N^h = \frac{1}{h}\int_0^{\infty} d\epsilon \; (\epsilon - eV_N)\left\{F_N^+(\epsilon)\left[A^+(\epsilon,\vec{\theta}) + A^+(\epsilon,-\vec{\theta})\right] - F_{LR}^+(\epsilon)\left[Q^+(\epsilon,\vec{\theta}) + Q^+(\epsilon,-\vec{\theta})\right]\right\}, \tag{A.14}$$

in which we defined the Fermi function sums/differences at the probe $F_N^{\pm} = f_N^{+} \pm f_N^{-}$ or among the two superconductors $F_{LR}^{\pm} = f_L^{\pm} \pm f_R^{\mp}$. The quantity

$$\begin{aligned} A^{\gamma}(\epsilon, \vec{\theta}) &= \left(N_N^{+} - P_{NN}^{++} + \gamma P_{NN}^{-+}\right)/2 \\ &= \left(N_N^{-} - P_{NN}^{--} + \gamma P_{NN}^{+-}\right)/2 \end{aligned} \tag{A.15}$$

represents the strength of the charge (with $\gamma = -$) or the heat flux (with $\gamma = +$) transferred from the probe into the edge at given energy ϵ and $\vec{\theta} \equiv (\Phi, \phi)$. The scattering probabilities $P_{NN}^{\pm\pm}$ describe normal reflections, $P_{NN}^{\pm\mp}$ the Andreev ones and $N_N^{+(-)}$ the number of open channels for electrons (holes) at the probe. The quantity

$$\begin{aligned} Q^{\gamma}(\epsilon, \vec{\theta}) &= \left(P_{NL}^{++} + \gamma P_{NL}^{-+}\right) \\ &= (-1)^{\delta_{\gamma,-}} \left(P_{NR}^{+-} + \gamma P_{NR}^{--}\right). \end{aligned} \tag{A.16}$$

describes the strength of the charge (heat) $\gamma = -$ ($\gamma = +$) transferred into the probe N when a QP is injected from the left superconductor S_L. For $\gamma = -$, due to the gap symmetry and Eq. (A.12), it coincides with amount of QH (with opposite sign) transferred into the probe when a QH is injected from the right superconductor S_R. Similarly, when $\gamma = +$, Eq. (A.16) represents the amount of energy transferred into the probe when a QP(QH) is injected from $S_L(S_R)$. These quantities have been discussed in Chap. 8 in the case of the charge current (i. e. $\gamma = -$) and without the Doppler shift $\Phi = 0$. Here we generalized them also to the presence of the Doppler shift (namely $\vec{\theta} \neq 0$), in which case their analytical expressions read as:

$$A^{\gamma}(\epsilon, \vec{\theta}) = \begin{cases} \dfrac{2|t|^4 \cdot \delta_{\gamma,-}}{1 + |r|^4 + 2|r|^2 \cos\left(2\pi \frac{L\epsilon_+}{\xi\Delta} + \phi_u - 2\arccos\left(\frac{\epsilon_+}{\Delta}\right)\right)} & \text{for } \epsilon \in I \\[2ex] \dfrac{(g(\epsilon)^2 - \gamma)(g(\epsilon)^2 + \gamma|r|^2)|t|^2 \cdot \Theta(\epsilon_{DS})}{g(\epsilon)^4 + |r|^4 - 2g(\epsilon)^2|r|^2 \cos\left(2\pi \frac{L\epsilon_+}{\xi\Delta} + \phi_u\right)} + \dfrac{2|t|^4 \cdot \Theta(\epsilon_{DS})\, \delta_{\gamma,-}}{1 + |r|^4 + 2|r|^2 \cos\left(2\pi \frac{L\epsilon_+}{\xi\Delta} - \phi_u - 2\arccos\left(\frac{\epsilon_+}{\Delta}\right)\right)} & \text{for } \epsilon \in II \\[2ex] \dfrac{(g(\epsilon)^2 - \gamma)(g(\epsilon)^2 + \gamma|r|^2)|t|^2}{g(\epsilon)^4 + |r|^4 - 2g(\epsilon)^2|r|^2 \cos\left(2\pi \frac{L\epsilon_+}{\xi\Delta} + \phi_u\right)} & \text{for } \epsilon \in III \end{cases}$$

$$Q^{\gamma}(\epsilon, \vec{\theta}) = \begin{cases} 0 & \text{for } \epsilon \in I \\[2ex] \dfrac{(g(\epsilon)^2 - 1)(g(\epsilon)^2 + \gamma|r|^2)|t|^2}{g(\epsilon)^4 + |r|^4 - 2g(\epsilon)^2|r|^2 \cos\left(2\pi \frac{L\epsilon_+}{\xi\Delta} + \phi_u\right)} \cdot \Theta(\epsilon_{DS}) & \text{for } \epsilon \in II \\[2ex] \dfrac{(g(\epsilon)^2 - 1)(g(\epsilon)^2 + \gamma|r|^2)|t|^2}{g(\epsilon)^4 + |r|^4 - 2g(\epsilon)^2|r|^2 \cos\left(2\pi \frac{L\epsilon_+}{\xi\Delta} + \phi_u\right)} & \text{for } \epsilon \in III \end{cases} \tag{A.17}$$

where $g(\epsilon) = e^{\text{arcCosh}(\epsilon_+/\Delta)}$, $\epsilon_+ = \epsilon + \epsilon_{DS}$, $|r|^2 = 1 - |t|^2$ and $\phi_u = \phi + \frac{2L\epsilon_{DS}}{\pi\xi\Delta}$ is the phase difference along the edge which includes the contribution of the external magnetic flux. In the expressions of Eq. (A.17), we indicated the energy regions I, II and III, depicted in Fig. A.1, which represent, respectively, the contributions deriving from the sub-gap (region

I), the semi-continuum (region II) and the full continuum (regions III). We notice that in Eq. (A.17) the sub-gap contribution of the function $A^{\gamma}(\epsilon, \vec{\theta})$ is nonzero only in the case of charge current (for $\gamma = -$), while it is zero for the heat current (for $\gamma = +$). This is because the Andreev bound states cannot allow any thermal transport, while mediating only the charge transport.

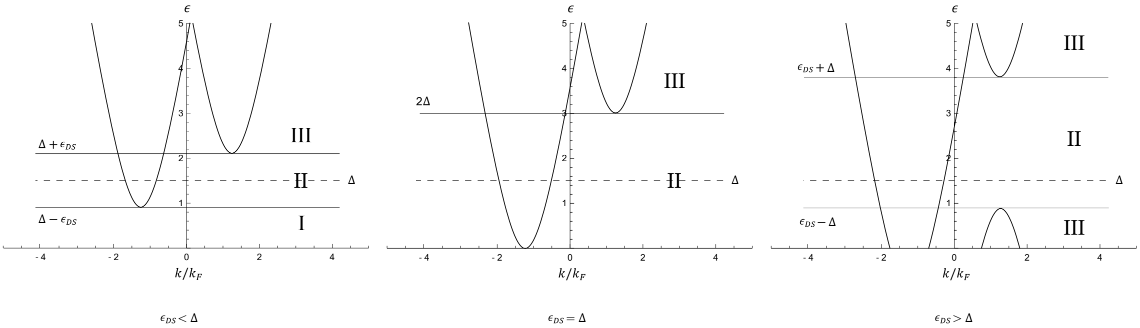

FIGURE A.1: Regions of validity in Eq. (A.17) for $\epsilon_{DS} > 0$: $\epsilon_{DS} < \Delta$ (left panel), $\epsilon_{DS} = \Delta$ (middle panel), $\epsilon_{DS} > \Delta$ (right panel).

From the previous analytical formulas we can deduce some general consequences for the probe's currents of Eqs. (A.13) and (A.14). Let us consider first the case of the charge current of Eq. (A.13). When $V_N = 0$, the function $F^{-}_{N} = 0$ (since $f^{+}_{N} = f^{-}_{N}$), so from the formula of Eq. (A.13) one can easily conclude that J^{c}_{N} is independent of the temperature T_N. This shows that no *local* thermoelectrical effect can be induced by means of a thermal bias between the TI and the probe. The only thermoelectric response in the probe is the *nonlocal* one when a thermal bias between the two superconductors δT is applied, i.e. $F^{-}_{LR} = f^{\pm}_{L} - f^{\mp}_{R} \neq 0$. This is particularly important at experimental level since the temperature of the probe does not need to be controlled during the measurement of nonlocal thermoelectricity. The strength of such nonlocal thermoelectric response (see Eq. (A.13)) is determined by the integral over the energies of the odd parity component in $\vec{\theta}$ of the function $Q^{-}(\epsilon, \vec{\theta})$, i. e. $Q^{-}(\epsilon, \vec{\theta}) - Q^{-}(\epsilon, -\vec{\theta})$, from which it follows that the Onsager nonlocal thermoelectrical linear coefficient L_{12} is an odd function of $\vec{\theta}$. Instead, when $\delta T = 0$, the function $F^{-}_{LR} = 0$ (since $f^{\pm}_{L} = f^{\mp}_{R}$), so from formula Eq. (A.13) it turns out that the charge current J^{c}_{N} is determined by the integral over the energies of the even parity component in $\vec{\theta}$ of the function $A^{-}(\epsilon, \vec{\theta})$, i. e. $A^{-}(\epsilon, \vec{\theta}) + A^{-}(\epsilon, -\vec{\theta})$, from which it follows that the Onsager local electrical coefficient L_{11} is an even function of $\vec{\theta}$

Furthermore, regarding the heat component of Eq.(A.14), it turns out that J^{h}_{N} is an even function of $\vec{\theta}$ since it depends only on the even components of the functions $A^{+}(\epsilon, \vec{\theta})$ and $Q^{+}(\epsilon, \vec{\theta})$. In the linear regime one can find that, for $T_{L/R} = T \pm \delta T/2$ and $T_N = T$, the heat current in the probe is proportional to the energy integral of the term

$$\sum_{\sigma=\pm} \left[A^{+}(\epsilon, \sigma\vec{\theta}) - Q^{+}(\epsilon, \sigma\vec{\theta}) \right], \tag{A.18}$$

which, using the expressions of Eq.(A.17), turns out to be zero. As a consequence, in the linear regime, the heat current at the probe $J^{h}_{N} = 0$.

A.4 Comparison with the tunneling approach

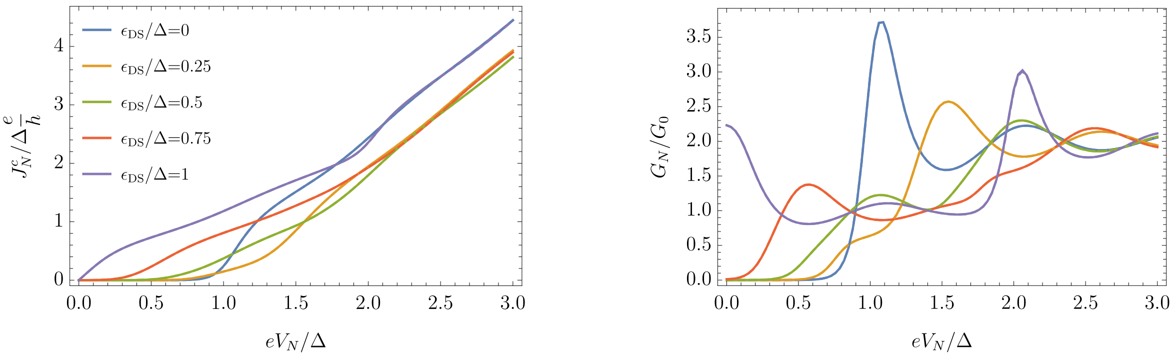

(a) (b)

Figure A.2: (a) - The charge current J_N^c at the metallic probe. Scattering results (solid lines) coincide with the tunneling ones (dashed lines), curves overlap. (b) - The differential conductance G_N at the metallic probe. Scattering results (solid lines) coincide with the tunneling ones (dashed lines), curves overlap. In both the plots we considered $L/\xi = 3$, $T/T_C = 1/10$ and $\phi = 0$.

In this section we compare the results obtained using the scattering approach with the results obtained using the tunneling approach [Sothmann2016, Bours2018, Bours2019]. For the sake of simplicity, here we consider the symmetric case of equal superconducting gaps, i. e. $\Delta_L = \Delta_R = \Delta$. Regarding the tunneling approach, we use the formulation presented in Ref. [Bours2018], but modifying the density of states (DOS) by adding an imaginary part γ to the energy in order to phenomenologically capture the contribution of Andreev bound states. Regarding the scattering approach we consider the analytical expression of the current J_N^c (derived in the Appendix Sec. A.3) at lowest order in $|t|^2$. In Figs. A.2(a) and A.2(b) we plot the current J_N^c and the differential conductance $G_N = dJ_N^c/dV_N$, respectively, as functions of the electrochemical potential eV_N for different values of ϵ_{DS} and setting $\gamma = 0$. As expected, on the scale of the plot the curves relative to the two approaches coincide for both quantities. The density plot of the differential conductance G_N is also shown in Figs. A.3(a) and A.3(b) for the two approaches, respectively, as a function of eV_N and ϵ_{DS}. Again, we see that the conductance G_N in the two approaches always coincides.

It is now important to notice that the expression for the current J_N^c in the scattering approach at lowest order in $|t|^2$ do not describe the results of the tunneling approach when a finite value of γ is taken. Indeed, in such a case G_N presents additional features produced by the ABSs (see Fig. A.4(b), to be compared with Fig. A.3(a)). This is expected because ABSs are accounted for by the scattering approach at the order $\mathcal{O}\left(|t|^4\right)$. By using the exact scattering approach one obtains the results reported in Fig. A.4(a) for $|t|^2 = 10^{-2}$. By comparing the two panels of Fig. A.4, we see that they show qualitatively the same behavior (highlighting the presence of the ABSs in the same positions inside the gap), but they do not exactly match. The difference is due to the effective description of the tunneling approach with respect to the exact scattering approach.

A more direct comparison between tunneling approach and exact scattering approach is given in Fig. A.5 where the linear-response conductance $\sigma = L_{11}/T$ is plotted as a function

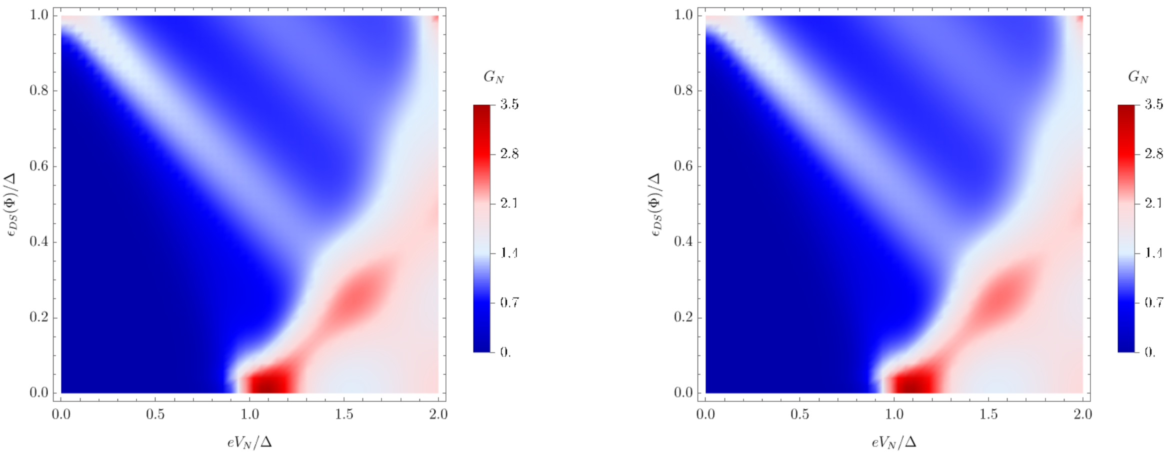

(a)

(b)

Figure A.3: (a) - Density plot of the differential conductivity G_N at the metallic probe obtained with the scattering approach in the leading order in $|t|^2$. (b) - Density plot of the differential conductivity G_N at the metallic probe obtained with the tunneling approach with $\gamma = 0$. In both the plots we considered $L/\xi = 3$, $T/T_C = 1/10$ and $\phi = 0$.

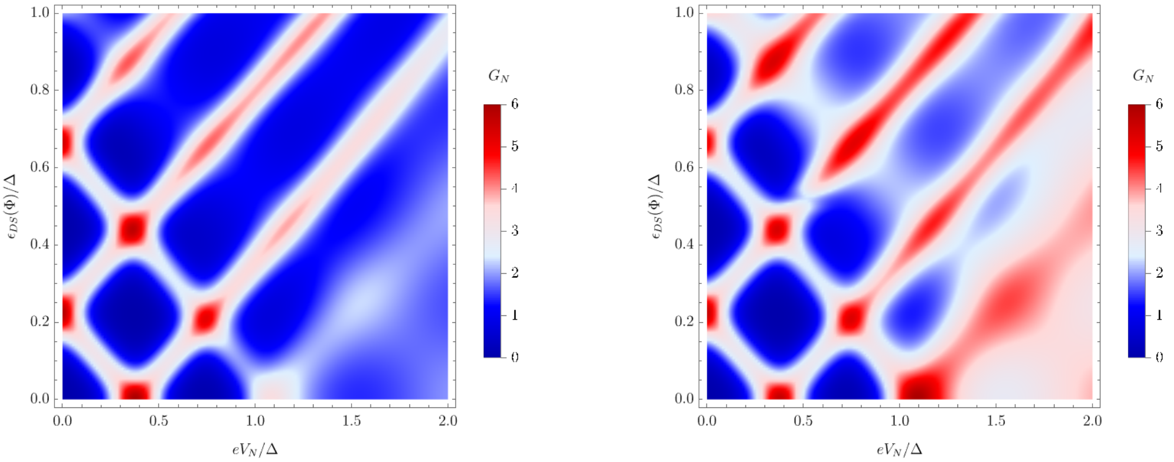

(a)

(b)

Figure A.4: (a) - Density plot of the differential conductance obtained in the scattering approach. G_N is normalized with respect to the transmittance of the probe $|t|^2 = 10^{-2}$. (b) - Density plot of the differential conductance obtained in the tunneling approach. Here $\gamma = \frac{\Delta}{100}$. In both the plots we considered $L/\xi = 3$, $T/T_C = 1/10$ and $\phi = 0$.

of ϵ_{DS} for various values of ϕ. The two approaches almost exactly coincide apart from a dip in the peak at $\phi = 0$ present in the tunneling curve (green dashed line).

We conclude the discussion by noting that only applying the full scattering formalism one can have a complete and consistent description of the transport in the three terminal setup which fully include the influence of ABSs. Similar considerations can be applied to the thermoelectrical current in the probe. In particular, we find that the scattering formalism shows,

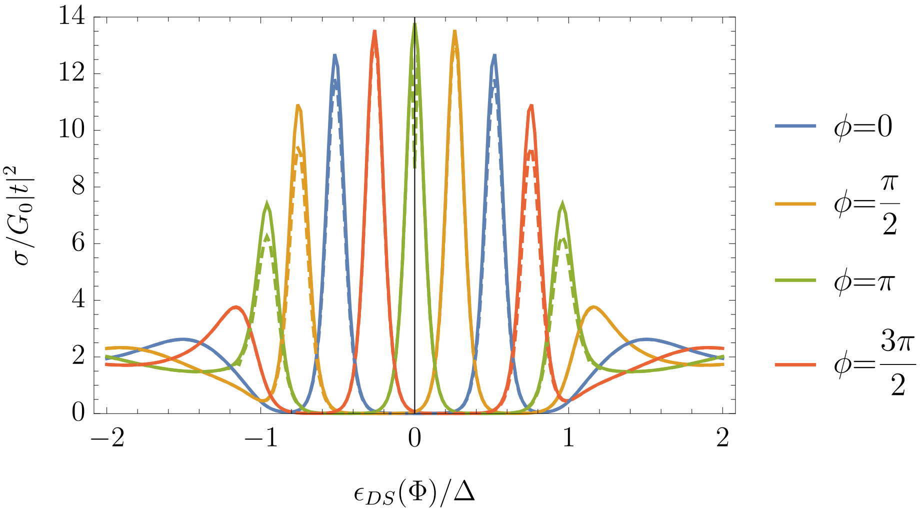

FIGURE A.5: Linear regime - Scattering-Tunneling Comparison - Electrical conductance σ in units of $G_0|t|^2$ (with $G_0 = \frac{2e^2}{h}$ the electrical conductance quantum), as a function of $\epsilon_{DS}(\Phi)/\Delta$. Different curves refer to different values of the phase difference ϕ between the two superconductors. Solid lines for the scattering approach (specifically $|t|^2 = 10^{-2}$), dashed lines for the tunneling approach ($\gamma = \frac{\Delta}{1000}$). The other parameters are: $L/\xi = 3$, $T/T_C = 1/10$ and $\phi = 0$.

as naively expected, that ABSs do not contribute neither to thermal or to thermoelectrical current in the probe. One can analytically show that, at $V_N = 0$, there is no contribution to the N probe thermoelectric current from ABSs for arbitrary values of $|t|^2$ (see the discussion in the Appendix Sec. A.3).

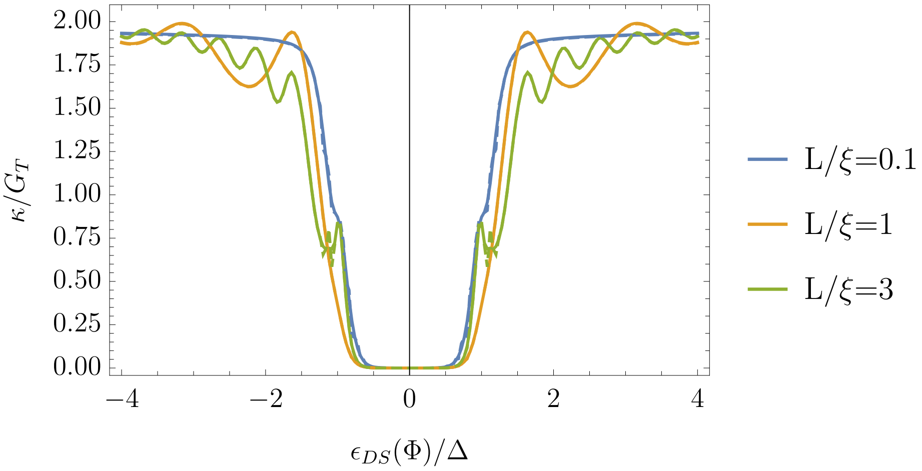

FIGURE A.6: Linear regime - Comparison between the scattering approach (without the probe) and the DOS method presented in Ref. [Sothmann2017] - Thermal conductance κ in units of the thermal conductance quantum $G_T = \frac{\pi^2}{3h}k_B^2 T$, as a function of $\epsilon_{DS}(\Phi)/\Delta$. Different curves refer to different values of $L/\xi = 0.1, 1, 3$. Solid lines for the scattering approach, dashed lines for the results obtained using the DOS [Sothmann2017]: curves exactly overlap. Other parameters: $T/T_C = 1/10$ and $\phi = 0$.

As a final remark, in Fig. A.6, we present the thermal conductance $\kappa = L_{22}/T^2$ calculated with the scattering approach by uncoupling the probe (i. e. setting $t = 0$) and compared with the results presented in Ref. [Sothmann2017] calculated using the DOS. As expected the two approaches are completely equivalent: curves overlap for all the parameters - see Fig. A.6.

B

Appendix:
Nonlocal thermoelectricity in a 3DTI based Andreev interferometer

In this appendix we generalize some of the calculations done in Chap. 8, obtained for a 2DTI Josephson junction, to the case of 3DTI Josephson junction in contact with a metallic probe.

B.1 The System

Here we consider a topological Josephson junction (TJJ) based on the 2D surface state of a 3DTI in contact with a metallic probe, as depicted in Fig. B.1, where the pairing in the superconducting regions is induced from a nearby s-wave superconductor. The surface state lies in the x-y plane, with the direction of the superconducting phase bias denoted as the x direction. We take the weak link to be infinite along the y direction and finite, of length L, along the x direction. We considered a 1D wire metallic probe in contact with the upper surface of the 3DTI, positioned in the middle of the junction (at $x = 0$) and extending all along the y direction (see Fig. B.1). Here, we study the regime where the Fermi level is situated inside the bulk gap and where only surface states exist. We assume that the surface considered is far enough away from the opposite surface so that there is no overlap between their states. Moreover, in the setup, a voltage bias V_N is applied between the probe N at the temperature T_N and the superconducting electrodes (grounded). A temperature gradient $\delta T = T_L - T_R$ is assumed between the left and the right superconducting leads.

The system is described by the following BdG Hamiltonian [Maistrenko2021]

$$H_{BdG} = \begin{pmatrix} H(x) & i\sigma_y \Delta(x) \\ -i\sigma_y \Delta(x)^* & -H(x)^* \end{pmatrix}, \tag{B.1}$$

expressed in the Nambu basis $(\psi_\uparrow, \psi_\downarrow, \psi^*_\uparrow, \psi^*_\downarrow)^T$, where

$$H(x) = v_F \left(\hat{p}_y \sigma_x - \hat{p}_x \sigma_y\right) - \mu\sigma_0 + \Lambda(x)\sigma_0 \tag{B.2}$$

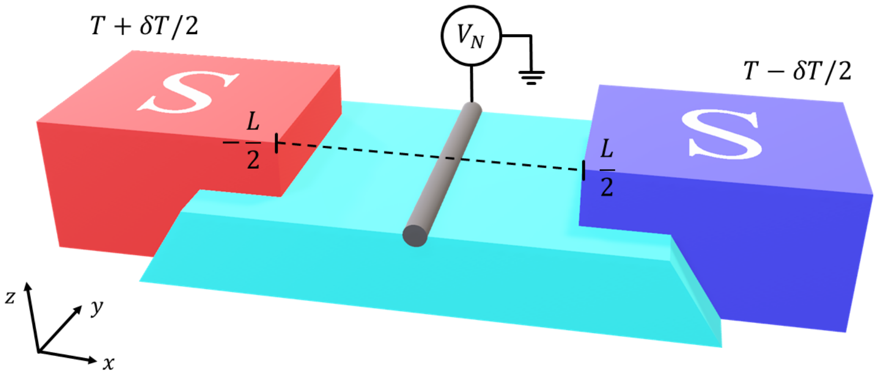

FIGURE B.1: Scheme of a Josephson junction based on a 3DTI: s-wave superconductors (S) on top of the TI proximity-induce pairing into the TI surface state. Superconductors have temperatures $T_L = T + \delta T/2$ and $T_R = T - \delta T/2$, and a phase difference $\phi \equiv \phi_L - \phi_R$. A bias voltage V_N is applied to the 1D wire metallic probe at temperature T_N and coupled to the upper surface state of the TI at the point $x = 0$. The length of the junction along the x direction is L, while the interfaces with the superconductors are placed at $x = \pm L/2$.

and $-H(x)^*$ being its time-reversal partner, with $\hat{p}_l = -i\partial_l$ (with $l = x, y$) the momentum operators. The Fermi velocity is v_F, μ is the chemical potential and σ_i are the Pauli matrices in the spin space. We consider rigid boundary conditions with order parameter $\Delta(x) = \Delta\left[\Theta(-x - L/2)e^{i\phi_L} + \Theta(x - L/2)e^{i\phi_R}\right]$, where $\Theta(x)$ is the step function, Δ is the proximity induced gap and $\phi \equiv \phi_L - \phi_R$ is the gauge invariant Josephson phase difference between the two superconductors. We include also a contact potential $\Lambda(x) = \Lambda\delta(x + L/2) + \Lambda\delta(x - L/2)$ at the boundaries.

To solve $H_{BdG}\Psi(\mathbf{r}) = E\Psi(\mathbf{r})$ and obtain the eigenspectrum of Eq.(B.1), we first make use of translational invariance along the y direction $[H_{BdG}, \hat{p}_y] = 0$ [Maistrenko2021]. Hence, we choose the ansatz $\Psi(\mathbf{r}) = e^{ip_y y}\psi(x)/\sqrt{W}$, where p_y is the momentum quantum number, $\psi(x)$ is a spinor in Nambu space, and W is a unit width of the system in y direction. The eigenenergies and $\psi(x)$ can then be obtained from the 1D BdG equation

$$H_{BdG}(p_y)\psi(x) = E\psi(x) \tag{B.3}$$

where $H_{BdG}(p_y)$ is given by Eq.(B.1) with the operator $\hat{p}_y$ replaced by the quantum number p_y. The ϵ-q relation in the both the superconducting regions is given by $q_\pm = \sqrt{(\mu \pm \Omega)^2/v_F^2 - p_y^2}$ with $\Omega = \sqrt{\epsilon^2 - \Delta^2}$. The solutions of Eq. (B.3) in the superconducting regions read as

$$\psi^j_{\xi,\alpha}(x) = \frac{1}{\sqrt{2}}\begin{pmatrix} e^{i\phi_j/2}u_\xi \\ -e^{i\phi_j/2}u_\xi \cdot \Gamma^S_{\xi,(\xi\alpha)} \\ e^{-i\phi_j/2}v_\xi \cdot \Gamma^S_{\xi,(\xi\alpha)} \\ e^{-i\phi_j/2}v_\xi \end{pmatrix} e^{i(\alpha\xi)q_\xi x} \tag{B.4}$$

where $j = L, R$ labels the left and right superconductor respectively, $\xi = \pm$ corresponds to quasi-particle (QP) and quasi-hole (QH) solutions and $\alpha = \pm$ selects the direction of motion along the x-axis. Here we defined

$$\Gamma^S_{\xi,\alpha} \equiv \frac{\alpha i\; q_\xi - p_y}{|\mu + \xi\Omega|} v_F; \qquad u_\xi \equiv \sqrt{\frac{1}{2}\left(1 + \frac{\xi\Omega}{\epsilon}\right)}; \qquad v_\xi \equiv \sqrt{\frac{1}{2}\left(1 - \frac{\xi\Omega}{\epsilon}\right)}. \tag{B.5}$$

In the weak link, the electron and hole states are given by

$$\psi^N_{\xi,\alpha}(x) = \frac{1}{\sqrt{2}}\begin{pmatrix}\frac{1+\xi}{2}\\ \frac{1-\xi}{2}\end{pmatrix} \otimes \begin{pmatrix}\Gamma^N_{\xi,(\xi\alpha)}\\ 1\end{pmatrix} e^{i(\alpha\xi)k_\xi x} \tag{B.6}$$

with

$$\Gamma^N_{\xi,\alpha} = \frac{\alpha i\; k_\xi + \xi p_y}{|\epsilon + \xi\mu|} v_F; \qquad k_\xi = \sqrt{\frac{(\epsilon + \xi\mu)^2}{v_F^2} - p_y^2}. \tag{B.7}$$

In Fig. B.2 are depicted the dispersion curves of the excitations in the superconductors (solid red curve for QPs and solid orange curve for QHs) and inside the weak link (blue solid curve for electrons and cyan solid curve for holes) respectively for different value of p_y.

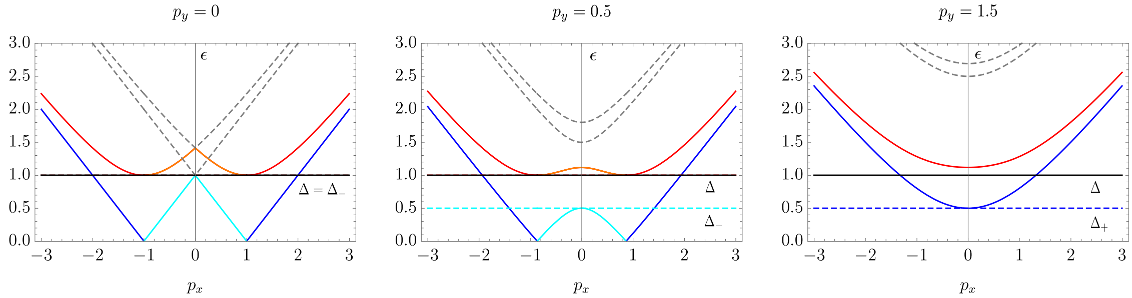

FIGURE B.2: Dispersion curves in the superconductors (solid red curve for QPs and solid orange curve for QHs) and inside the weak link (blue solid curve for electrons and cyan solid curve for holes). Gray dashed curves represent higher energy branches which do not contribute to the transport if $\epsilon, \Delta \ll \mu$. Different panels show the evolution of the dispersion curves for different values of $p_y = 0, 0.5, 1.5$ (expressed in arbitrary units). Horizontal lines label the position of the gap order parameter Δ (black solid line), the upper energy level Δ_- for holes (cyan dashed line) and the bottom energy level Δ_+ for electrons (blue dashed line).

B.2 Scattering matrix

We computed the full scattering matrix of the system

$$S = S_L \circ S_N \circ S_R \tag{B.8}$$

by combining the scattering matrices $S_{L/R}$ describing the left and right interfaces of the 3DTI with the superconductors, with the scattering matrix S_N describing the surface edge in contact with metallic probe N. More specifically, the scattering matrices at the interfaces $S_{L/R}$ have been obtained by exploiting the states solutions of Eqs.(B.4) and (B.6) and solving the wave function matching problem in the limit $k_B T \ll \Delta \ll \mu$. In this regime the higher energy branches of the dispersion curves (see gray dashed curves in Fig. B.2) do not contribute to the transport properties of the junction. The scattering matrices S_L and S_R take the following form

$$\begin{pmatrix} \tilde{c}_L^- \\ c_L^+ \\ \tilde{b}_L^- \\ b_L^+ \end{pmatrix}_{out} = \begin{pmatrix} r^L_{\tilde{e},\tilde{e}} & t^L_{\tilde{e},e} & r^L_{\tilde{e},\tilde{h}} & t^L_{\tilde{e},h} \\ t^L_{e,\tilde{e}} & r^L_{e,e} & t^L_{e,\tilde{h}} & r^L_{e,h} \\ r^L_{\tilde{h},\tilde{e}} & t^L_{\tilde{h},e} & r^L_{\tilde{h},\tilde{h}} & t^L_{\tilde{h},h} \\ t^L_{h,\tilde{e}} & r^L_{h,e} & t^L_{h,\tilde{h}} & r^L_{h,h} \end{pmatrix}_{S_L} \begin{pmatrix} \tilde{c}_L^+ \\ c_L^- \\ \tilde{b}_L^+ \\ b_L^- \end{pmatrix}_{in} \quad \begin{pmatrix} c_L^- \\ \tilde{c}_R^+ \\ b_L^- \\ \tilde{b}_L^+ \end{pmatrix}_{out} = \begin{pmatrix} r^R_{e,e} & t^R_{e,\tilde{e}} & r^R_{e,h} & t^R_{e,\tilde{h}} \\ t^R_{\tilde{e},e} & r^R_{\tilde{e},\tilde{e}} & t^R_{\tilde{e},h} & r^R_{\tilde{e},\tilde{h}} \\ r^R_{h,e} & t^R_{h,\tilde{e}} & r^R_{h,h} & t^R_{h,\tilde{h}} \\ t^L_{\tilde{h},e} & r^L_{\tilde{h},\tilde{e}} & t^L_{\tilde{h},h} & r^L_{\tilde{h},\tilde{h}} \end{pmatrix}_{S_R} \begin{pmatrix} c_R^+ \\ \tilde{c}_R^- \\ b_R^+ \\ \tilde{b}_R^- \end{pmatrix}_{in} \tag{B.9}$$

Here we indicated with $c_i^\pm/\tilde{c}_i^\pm$ and $b_i^\pm/\tilde{b}_i^\pm$ the incoming and outgoing electrons/QPs and holes/QHs respectively, with ± labeling the direction of propagation along the x-axis and $i = L, R$ indicating the interface with left or right superconductor. The obtained coefficients $r^i_{\alpha,\beta}$ and $t^i_{\alpha,\beta}$ represent the reflection and transmission amplitudes respectively of an incoming particle of type β to a particle of type α at the interface i. The explicit analytical expressions of such a scattering coefficients (obtained without any contact potential, i. e. $\Lambda = 0$) are cumbersome and therefore are not shown. The scattering matrix S_N, instead, can be written as

$$\begin{pmatrix} c_N^1 \\ c_N^2 \\ c_L^- \\ c_R^+ \\ b_N^1 \\ b_N^2 \\ b_L^- \\ b_R^+ \end{pmatrix}_{out} = \begin{pmatrix} S_N^+(\epsilon, p_y) & 0 \\ 0 & S_N^-(\epsilon, p_y) \end{pmatrix}_{S_N} \begin{pmatrix} c_N^1 \\ c_N^2 \\ c_L^+ \\ c_R^- \\ b_N^1 \\ b_N^2 \\ b_L^+ \\ b_R^- \end{pmatrix}_{in} \tag{B.10}$$

Here we indicated with c_N^n/b_N^n the incoming/outgoing electrons/holes respectively, with $n = 1, 2$ labeling the spin-degenerate transport channel inside the probe N. In Eq. (B.10), $S_N^+(\epsilon, p_y)$ and $S_N^-(\epsilon, p_y)$ represent the scattering matrices for particles and holes respectively. Is important to notice that, due to particle-hole symmetry, they satisfy the relation $S_N^-(\epsilon, p_y) = \left[S_N^+(-\epsilon, -p_y)\right]^*$. These matrices have been modeled as follows

$$S_N^\xi(\epsilon, p_y) = \begin{pmatrix} r \cdot R_N^\xi & t \cdot \mathbb{1} \\ -t \cdot \mathbb{1} & r \cdot R_S^\xi \end{pmatrix} \cdot \Theta\left[\xi\left(\epsilon - \Delta_\xi\right)\right] + \begin{pmatrix} \mathbb{1} & 0 \\ 0 & 0 \end{pmatrix} \cdot \Theta\left[\xi(\Delta_\xi - \epsilon)\right] \tag{B.11}$$

with $\xi = \pm$ and where we introduced the quantity

$$\Delta_\xi = \xi\left(|p_y| v_F - \mu\right) \tag{B.12}$$

labeling respectively the upper energy level Δ_- for holes (cyan horizontal dashed line of Fig. B.2) and the bottom energy level Δ_+ for electrons (blue horizontal dashed line of Fig. B.2). The latter quantities of Eq. (B.12) control, for different values of p_y, which types of particles are available for the transport inside the junction at a given energy. In this regard, the last term of Eq. (B.11) is needed in order to avoid particles, coming from the probe with energy ϵ, to propagate inside the junction if there are no available channels at that energy. In which case, such a particles are reflected back to the probe. In the first term of Eq. (B.11), without loss of generality, we considered real valued r and t scattering parameters, such that $|r|^2 + |t|^2 = 1$ which describe the coupling with the probe. Namely when $|t|^2 = 1$ the probe is fully coupled with surface edge of the 3DTI, instead when $|t|^2 = 0$ it is completely uncoupled. The matrix R^ξ_S takes the following form

$$R^\xi_S(\epsilon, p_y) = \begin{pmatrix} r^\xi_{LL} & i\ r^\xi_{RL} \\ i\ r^\xi_{LR} & r^\xi_{RR} \end{pmatrix}. \tag{B.13}$$

Here we introduced

$$r^\xi_{LL}(\epsilon, p_y) = r^\xi_{RR}(\epsilon, p_y) \equiv \left|(\psi^N_{\xi,\mp}(x_0), \psi^N_{\xi,\pm}(x_0))\right| = \left|\cos\left(\angle\Gamma^N_{\xi,\xi}\right)\right| \tag{B.14}$$

(where $\angle\Gamma^N_{\xi,\xi}$ represents the phase argument of the complex quantity $\Gamma^N_{\xi,\xi}$) which represent the reflection amplitude coefficients for an electron ($\xi = +$) or a hole ($\xi = -$) coming from the left/right (L/R) side of the weak link and reflected back. In Eq. (B.14), r^ξ_{ii} (with $i = L, R$) is constructed as the absolute value of the scalar product of the wave functions $\psi^N_{\xi,\pm}(x_0)$ associated to particles which move in opposite directions inside the junction at the point $x_0 = 0$. In this way, for example, when $p_y = 0$ states with opposite direction of motion are orthogonal, thus $r_{LL} = r_{RR} = 0$ (similarly to the 2DTI case). On the contrary, when $p_y \neq 0$ right (left) moving states have finite overlap with left (right) moving ones and this allow reflection processes toward the lead of origin (*i. e.* $r^\xi_{LL} = r^\xi_{RR} \neq 0$). The scattering coefficients which describe the reflection processes among the two superconductors can be written as

$$r^\xi_{RL}(\epsilon, p_y) = r^\xi_{LR}(\epsilon, p_y) \equiv \sqrt{1 - \left|r^\xi_{LL}(\epsilon, p_y)\right|^2} \tag{B.15}$$

such that $|r_{LL}|^2 + |r_{RL}|^2 = 1$ and $|r_{RR}|^2 + |r_{LR}|^2 = 1$. Notice that, because of the unitarity of the scattering matrix S^ξ_N of Eq. (B.11), $R^\xi_N = \left[R^\xi_S\right]^\dagger$.

B.3 Charge current at the probe

By using the scattering approach one can write the charge current J^c_N flowing in the probe as follows [Lambert1998, Blasi2020]:

$$J^c_N = \frac{1}{h}\sum_j \sum_{\alpha,\beta} \int_0^\infty d\epsilon\ \alpha e \left(f^\alpha_N(\epsilon) - f^\beta_j(\epsilon)\right) P^{\alpha,\beta}_{N,j}(\epsilon, \phi) \tag{B.16}$$

where $\alpha, \beta = +$ stand for quasi-particle (QP), $\alpha, \beta = -$ for quasi-hole (QH), and with j running over leads indices (L, R and N). In Eq. (*B*.16) we consider the chemical potentials of the grounded superconductors as reference for the energies. The current depends on the generalized Fermi distributions $f^\alpha_j(\epsilon) = \{e^{(\epsilon - \alpha e V_j)/k_B T_j} + 1\}^{-1}$, where T_j and V_j are respectively the temperature and the voltage at the lead j. In Eq. (*B*.16) the probability scattering coefficients

$$P^{\alpha,\beta}_{i,j} = \int_{-\infty}^{\infty} dp_y \sum_{\sigma,\sigma'} \left|S^{\alpha,\beta}_{(i,\sigma),(j,\sigma')}(p_y)\right|^2 \tag{B.17}$$

represent the reflection ($i = j$) or transmission ($i \neq j$) probabilities of a quasi-particle of type β in lead j to a quasi-particle of type α in lead i, and have been obtain by taking the trace of the scattering matrix S of the system (see Eq.(B.8)), where σ (σ') is a channel belonging to lead i (j) and p_y is the momentum quantum number [Lambert1998].

B.4 Linear response regime

As already discussed in the main text of Chap. 8, in the linear response regime, for $\delta T, V_N \to 0$, the temperature of the probe can be chosen as the average temperature of the superconducting leads, i. e. $T_N = (T_L + T_R)/2 = T$. With this choice Eq. (B.16) can be written in the following form [Benenti2017, Blasi2020]:

$$J_N^c = L_{11}(V_N/T) + L_{12}(\delta T/T^2) \tag{B.18}$$

where L_{11} is proportional to the charge conductance at the probe and L_{12} is the *nonlocal* thermoelectrical coefficient.

In the remaining part of this appendix we collect different results of the normalized nonlocal coefficient $L_{12}/(\sqrt{G_0 G_T T^3})$ (with $G_0 = 2e^2/h$ and $G_T = (\pi^2/3h)k_B^2 T$ being respectively the electrical conductance quantum and the thermal conductance quantum). In particular in Figs. B.3 we depict the nonlocal thermoelectric coefficient L_{12} as a function of the phase difference ϕ/π between the two superconductors versus the junction length L/ξ (Fig. B.3(a)) and the coupling parameter $|t|^2$ (Fig. B.3(b)) respectively. As already mentiond in Chap. 8, these results qualitatively match with those obtained in the case of a 2DTI Josephson junction (see Figs. 8.3 (c)-(d) with relative discussion in Sec. 8.5).

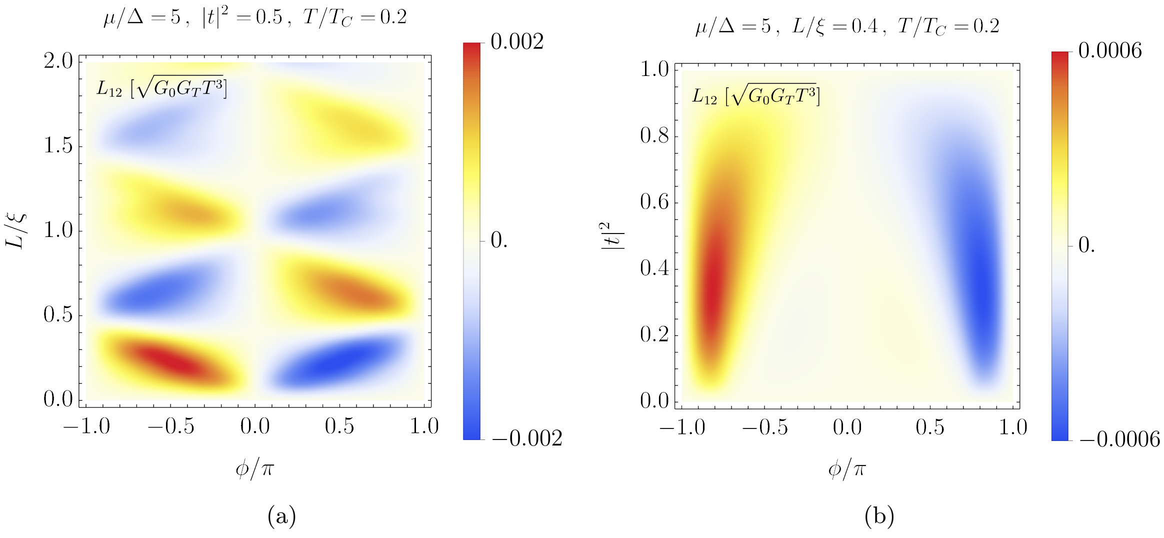

(a) (b)

Figure B.3: (a) - L_{12} as functions of ϕ/π and the junction length L/ξ for $|t|^2 = 0.5$. (b) - L_{12} as a function of ϕ/π and coupling parameter $|t|^2$ with the junction length $L/\xi = 0.4$. In both panels we considered a mean temperature of the junction $T/T_C = 0.2$ and a chemical potential $\mu/\Delta = 5$. Here we normalized the nonlocal thermoelectrical coefficient as follows: $L_{12}/(\sqrt{G_0 G_T T^3})$, with $G_0 = 2e^2/h$ and $G_T = (\pi^2/3h)k_B^2 T$ being respectively the electrical conductance quantum and the thermal conductance quantum.

To better quantify the nonlocal effect induced by the phase bias, in Fig. B.4, we depict the nonlocal Seebeck coefficient $S = (1/T)L_{12}/L_{11}$ expressed in units of $\mu V/K$ as a function of ϕ/π and the coupling with the probe $|t|^2$. Is important to notice that, even thou the behavior of the nonlocal Seebeck coefficient resembles that obtained in Sec. 8.7 for a 2DTI based Josephson junction, here (see Fig. B.4) S takes a maximum value which is one order of magnitude bigger ($\approx 20\ \mu V/K$) than the one obtained in Fig. 8.4 ($\approx 3\ \mu V/K$). The reason lies in the fact that, in the 3DTI case, the nonlocal Seebeck coefficient S results from an integration on different channels each labeled by the quantum number p_y (see Eq. B.17). In the 2DTI case only the mode with $p_y = 0$ contributes to the thermoelectric effect inside the probe.

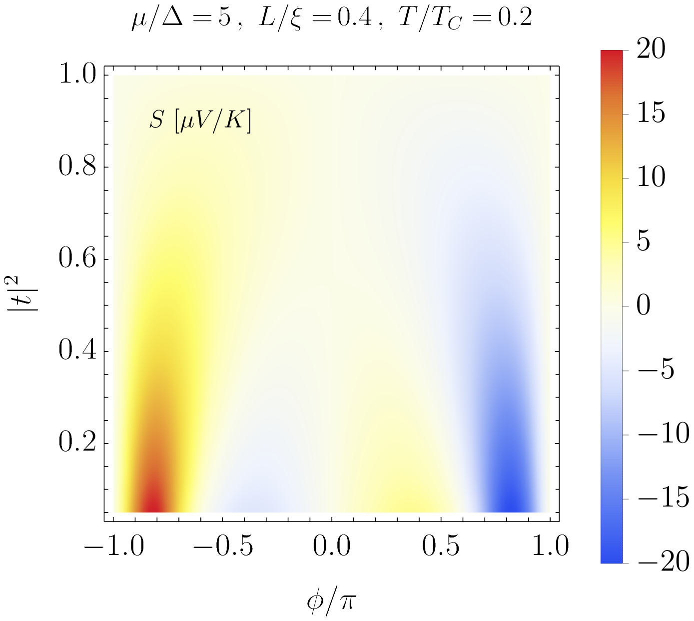

FIGURE B.4: Nonlocal Seebeck coefficient S in units of $\mu V/K$ as a function of ϕ/π and the coupling with the probe $|t|^2$. Other parameters in the heading.

B.5 Metallic pad probe

As a final remark, here we consider a probe which consists of a metallic pad modelled as a collection 1D metallic parallel wires centered in different positions x_0 along the junction. We take the metallic pad, centered in the middle of the junction, to be infinite along the y direction and finite, of length d, along the x direction, as depicted in Fig. B.5. The nonlocal thermoelectric coefficient L_{12} as a function of the Josephson phase difference ϕ/π has been computed by integrating the quantity $L_{12}(x_0)$ (depicted in Fig. B.6(a)), obtained for a single metallic wire centered at $-d/2 \leq x_0 \leq d/2$. The final result is shown in Fig. B.6(b).

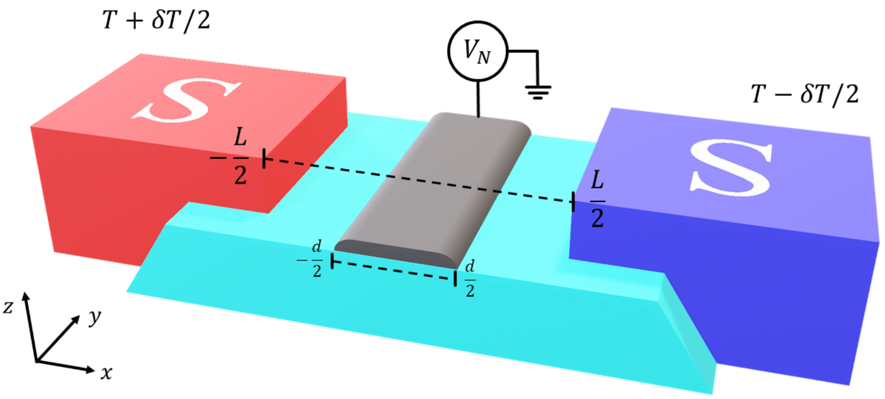

Figure B.5: Scheme of a Josephson junction based on a 3DTI with a normal metallic pad as a probe. The metallic pad is centered in the middle of the junction, is infinite along the y direction and finite, of length d, along the x direction

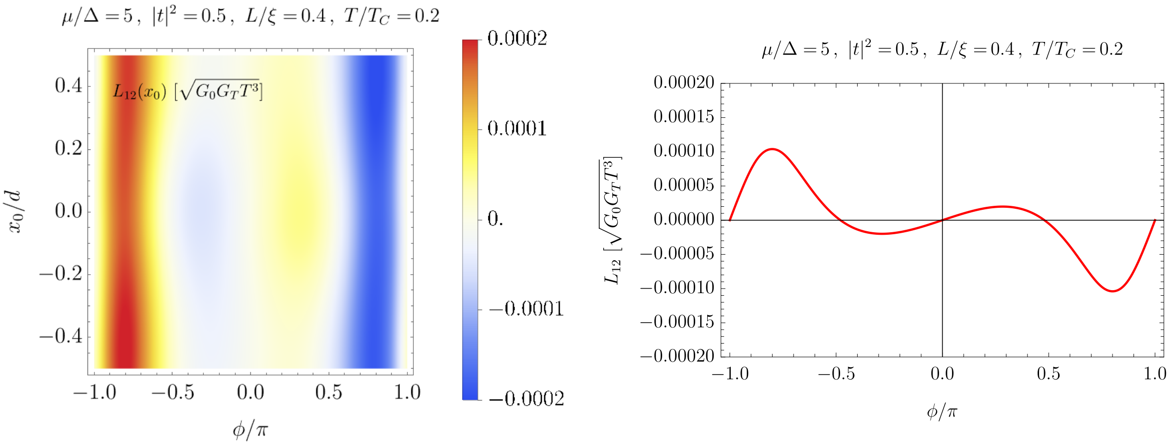

(a)

(b)

Figure B.6: (a) - Nonlocal thermoelectric coefficient $L_{12}(x_0)$ as function of ϕ/π and the position of a single metallic wire centered at $-d/2 \leq x_0 \leq d/2$. Here we used $d = L/2$. (b) - $L_{12} = \int_{-d/2}^{d/2} dx_0\ L_{12}(x_0)$. Both panels have been obtained for the same set of parameters (see headings). Both results are expressed in units of $\sqrt{G_0 G_T T^3}$, with $G_0 = 2e^2/h$ and $G_T = (\pi^2/3h)k_B^2 T$ being respectively the electrical conductance quantum and the thermal conductance quantum.

C

Appendix: Topological Josephson junctions with magnetic islands

In this appendix we present the details of the calculations for the different scattering matrices $S_{L,R}$ and S_M introduced in Eq. (10.8) of Chap. 10. We proceed by writing first the scattering matrices $S_{L,R}$ describing the left and right interfaces of the 2DTI with the superconductors (in Sec. C.1) and then the scattering matrix S_M describing the 2DTI edge in contract with the magnetic domain (in Sec. C.2). In section C.3 we combine them in order to get the full scattering matrix of the system.

C.1 Scattering matrix of the SC-2DTI interface

The scattering matrix equation for S_L, obtained by solving the wave function matching problem at the interface between the left superconducting lead and the edge state of the 2DTI, can be written as

$$\begin{pmatrix} \tilde{c}^{-}_L \\ \tilde{b}^{-}_L \\ c^{+}_L \\ b^{+}_L \end{pmatrix} = \begin{pmatrix} 0 & r^L_{\tilde{e},\tilde{h}} & t^L_{\tilde{e},e} & 0 \\ r^L_{\tilde{h},\tilde{e}} & 0 & 0 & t^L_{\tilde{h},h} \\ t^L_{e,\tilde{e}} & 0 & 0 & r^L_{e,h} \\ 0 & t^L_{h,\tilde{h}} & r^L_{h,e} & 0 \end{pmatrix} \begin{pmatrix} \tilde{c}^{+}_L \\ \tilde{b}^{+}_L \\ c^{-}_L \\ b^{-}_L \end{pmatrix}, \tag{C.1}$$

where we indicated with $c^{\mp}_L/b^{\mp}_L$ the incoming and outgoing electrons/holes in the TI region and with $\tilde{c}^{\pm}_L/\tilde{b}^{\pm}_L$ the incoming and outgoing quasiparticles/quasiholes in the superconductor. The index L labels the interface with left superconductor and $\pm$ indicate the direction of propagation of quasiparticles along the x-axis ($+$ for right movers and $-$ for left movers). Notice that with this basis the scattering matrix can be written as

$$S_L = \begin{pmatrix} r_L & t'_L \\ t_L & r'_L \end{pmatrix}, \tag{C.2}$$

where r_L and r'_L are blocks concerning particles reflected at the interface, whereas t_L and t'_L are blocks concerning particles transmitted through the interface. The obtained coefficients $r^L_{\alpha,\beta}$ and $t^L_{\alpha,\beta}$ represent the reflection and transmission amplitudes respectively of an incoming particle of type β to a particle of type α at the interface.

The coefficients of Eq. C.1 can be compactly written as

$$\begin{aligned} r^L_{\gamma,\bar{\gamma}} &= \gamma\frac{v}{u}e^{i\alpha}e^{i\frac{\phi}{2}}, \\ r^L_{\tilde{\gamma},\bar{\tilde{\gamma}}} &= -\frac{v}{u}e^{-i\beta}\Theta\left(\epsilon-\Delta\right), \\ t^L_{\gamma,\tilde{\gamma}} &= \frac{\sqrt{u^2-v^2}}{u}e^{\frac{i}{2}(\alpha-\beta)}e^{-i\gamma\frac{\phi}{4}}\Theta(\epsilon-\Delta), \\ t^L_{\tilde{\gamma},\gamma} &= \bar{\gamma}\frac{\sqrt{u^2-v^2}}{u}e^{\frac{i}{2}(\alpha-\beta)}e^{i\bar{\gamma}\frac{\phi}{4}}\Theta(\epsilon-\Delta), \end{aligned} \tag{C.3}$$

where the QP/QH index ($\gamma = e, h$) in the LHS is converted in a simple sign ($\gamma = +, -$) in the RHS and the bar represents the opposite element (for instance $\bar{e} = h$). In Eq. (C.3) we defined the functions

$$u = \sqrt{\frac{\Delta}{2\epsilon}}e^{\frac{1}{2}\operatorname{arccos}\frac{\epsilon}{\Delta}}; \quad v = \sqrt{\frac{\Delta}{2\epsilon}}e^{-\frac{1}{2}\operatorname{arccos}\frac{\epsilon}{\Delta}}, \tag{C.4}$$

and the phases

$$\alpha = 2\frac{\epsilon}{\Delta}\frac{l_S}{\xi_S}; \quad \beta = 2\frac{l_S}{\xi_S}\sqrt{\left(\frac{\epsilon}{\Delta}\right)^2-1}, \tag{C.5}$$

with $\xi_S = \hbar v_F/\Delta$ the coherence length, Δ the superconducting gap and l_S the length of the 2DTI measured from the superconductor as depicted in Fig. 10.1. A similar result for the scattering matrix S_R at the right interface can be obtained. The scattering coefficients can be obtained from Eqs. (C.3) by replacing $\left(r^L_{\alpha,\beta}, t^L_{\alpha,\beta}\right) \to \left(r^R_{\beta,\alpha}, t^R_{\beta,\alpha}\right)$ and $\phi \to -\phi$.

C.2 Scattering matrix of the magnetic island

Following Refs. [Bustos-Marun2013, Sternativo2014, Arrachea2015, Gresta2019], here we compute the scattering matrix S_M describing the edge of the 2DTI in contact with a magnetic island. In order to do this we start by writing the evolution operator $U^e(x_N, x_0) = \prod_{k=1}^{N} U^e(x_k, x_{k-1})$ where the superscript e makes reference to the electron part and N indicates the total number of magnetic domains, with

$$U^e(x_k, x_{k-1}) = \sigma_0 \cos\lambda_k + i\vec{n}_k \cdot \vec{\sigma}_k \sin\lambda_k, \tag{C.6}$$

where $L_k = x_k - x_{k-1}$ is the length of the corresponding magnetic domain. We have introduced $\lambda_k = L_k\sqrt{\epsilon^2-\epsilon_\perp^2}/(\hbar v_F)$, with $\vec{n}_k = \left(i\epsilon_{k\perp}\sin\theta_k, -i\epsilon_{k\perp}\cos\theta_k, \epsilon\right)/\sqrt{\epsilon^2-\epsilon_\perp^2}$ and θ_k is the orientation of the domain in the plane of the sample.

The inverse of the evolution operator is the transfer matrix

$$(U^e)^{-1} = T^e = \begin{pmatrix} T^e_{11} & T^e_{12} \\ T^e_{21} & T^e_{22} \end{pmatrix}, \tag{C.7}$$

which in turn is related to the scattering matrix as follows

$$S^e_M = \frac{1}{T^e_{22}}\begin{pmatrix} -T^e_{21} & 1 \\ 1 & T^e_{12} \end{pmatrix}, \tag{C.8}$$

satisfying the following scattering equation

$$\left(c_L^-, c_R^+\right)^T = S_M^e \left(c_L^+, c_R^-\right)^T. \tag{C.9}$$

A similar relation links the incoming and outgoing holes

$$\left(b_L^-, b_R^+\right) = S_M^h \left(b_L^+, b_R^-\right), \tag{C.10}$$

where $S_M^h(\epsilon) = -\sigma_z S_M^{e*}(-\epsilon)\sigma_z$ [Crepin2014]. By combining Eqs. (C.9) and (C.10), we obtain the scattering matrix for the magnetic island which reads

$$S_M = \begin{pmatrix} r_M & t'_M \\ t_M & r'_M \end{pmatrix} = \begin{pmatrix} S^e_{M,11} & 0 & S^e_{M,12} & 0 \\ 0 & S^h_{M,11} & 0 & S^h_{M,12} \\ S^e_{M,21} & 0 & S^e_{M,22} & 0 \\ 0 & S^h_{M,21} & 0 & S^h_{M,22} \end{pmatrix}, \tag{C.11}$$

satisfying the scattering equation

$$\left(c_L^-, b_L^-, c_R^+, b_R^+\right)^T = S_M \left(c_L^+, b_L^+, c_R^-, b_R^-\right)^T.$$

Here we can see that each sub-matrix takes a block diagonal form since in the magnetic domain an electron cannot be converted into a hole or vice versa in contrast to the case of the SC-2DTI interface which only allows an electron (hole) to be reflected as a hole (electron) or be transmitted as a QP (QH) - see Eq. (C.1) .

C.3 Combination of the scattering matrices

By following Ref. [Datta1997] we combine matrices S_L of Eq. (C.2) and S_M of Eq. (C.11) and obtain

$$S_L \circ S_M = \begin{pmatrix} r & t' \\ t & r' \end{pmatrix}, \tag{C.12}$$

in which

$$\begin{aligned} r &= r_L + t'_L r_M \left[\mathbb{1} - r'_L r_M\right]^{-1} t_L, \\ r' &= r'_M + t_M \left[\mathbb{1} - r'_L r_M\right]^{-1} r'_L t'_M, \\ t &= t_M \left[\mathbb{1} - r'_L r_M\right]^{-1} t_L, \\ t' &= t'_L \left[\mathbb{1} - r_M r'_L\right]^{-1} t'_M, \end{aligned} \tag{C.13}$$

where $\mathbb{1}$ stands for the 2×2 identity matrix. Finally, by applying the same procedure but adding S_R we obtain the full scattering matrix of the system

$$S = S_L \circ S_M \circ S_R. \tag{C.14}$$

D

Appendix: Manipulation of Cooper pair entanglement in hybrid topological Josephson junctions

In this appendix we present the details of some calculations relative to Chap. 11. We introduce the full scheme of the system that we used in the main text (explicitly accounting for the presence of the edge modes running in the backside par of the device), and consider the more general application of the local fields along the edge states.

D.1 Effective Hamiltonian

The helical edge states at boundaries of each TI of the system are described by a one-dimensional Dirac Hamiltonian

$$H_k = \sum_{\zeta=\pm} \int dx \times \left[\psi^\dagger_{\zeta k\downarrow}(\zeta i\hbar v_F \partial_x - \mu)\psi_{\zeta k\downarrow} - \psi^\dagger_{\zeta k\uparrow}(\zeta i\hbar v_F \partial_x + \mu)\psi_{\zeta k\uparrow}\right] \tag{D.1}$$

where $k = u, \ell$ labels the upper and lower TI plane, $\psi_\uparrow$ ($\psi_\downarrow$) is the field operator of $\uparrow(\downarrow)$ electrons, μ is the chemical potential and v_F is the propagation Fermi velocity. The index ζ is associated to the front-side ($\zeta = +$) or backside ($\zeta = +$) edges, see Fig. 11.2 of the main text. For the sake of simplicity we considered the same spin-quantization axis for both the TI planes edges along the $\hat{\mathbf{n}}$ direction [Qi2008, Maciejko2010]. In the case this condition is not realized one need to generalize our approach to the case of not collinear spin quantization axis. In this case some of the simple analytical results are not anymore valid, but numerically all the calculations can be repeated. Nonetheless the main results presented in Chap. 11, such as the selective action of the V-field over the entanglement symmetry, are still valid since they are based purely on general symmetry arguments. Furthermore not collinear natural spin quantization axis would potentially results also in a reduction of the CAR injection in favour of the LAR processes.

D.2 Gate potential

Let us consider the Schrödinger equation for the topological effective edge Hamiltonian

$$\begin{pmatrix} -i\hbar v_F \partial_x + eV(x) - \epsilon_F & 0 \\ 0 & i\hbar v_F \partial_x + eV(x) - \epsilon_F \end{pmatrix} \begin{pmatrix} u(x) \\ d(x) \end{pmatrix} = E \begin{pmatrix} u(x) \\ d(x) \end{pmatrix} \tag{D.2}$$

in which we considered the application of a constant gate potential

$$V(x) = \begin{cases} 0 & \text{for } |x| > \frac{L}{2} \\ V & \text{for } |x| \leq \frac{L}{2} \end{cases} .$$

In in Eq. (*D*.2) we expressed the wave function $\Psi = \begin{pmatrix} u(x) \\ d(x) \end{pmatrix}$ in spinorial notation for the spin-up and spin-down components (along the $\hat{\mathbf{n}}$ natural spin-quantization axis), while ϵ_F and v_F represent the Fermi energy and the Fermi velocity respectively. The general form of the solution is the following

$$\Psi(x) = \begin{cases} A \begin{pmatrix} 1 \\ 0 \end{pmatrix} e^{ikx} + B \begin{pmatrix} 0 \\ 1 \end{pmatrix} e^{-ikx} & \text{for } x < -\frac{L}{2} \ (I) \\ \\ C \begin{pmatrix} 1 \\ 0 \end{pmatrix} e^{ik'x} + D \begin{pmatrix} 0 \\ 1 \end{pmatrix} e^{-ik'x} & \text{for } |x| \leq \frac{L}{2} \ (II) \\ \\ F \begin{pmatrix} 1 \\ 0 \end{pmatrix} e^{ikx} + G \begin{pmatrix} 0 \\ 1 \end{pmatrix} e^{-ikx} & \text{for } x > \frac{L}{2} \ (III) \end{cases}$$

where, in the limit of low energies ($E \ll \epsilon_F$), $k \approx k_F$ and $k' \approx k_F - \frac{eV}{\hbar v_F}$. In order to obtain the relation between the coefficients A,B, . . . ,G, one uses the continuity requirements for the wave function Ψ and the current

$$\lim_{\delta\to 0} \Psi(x) \mid_{-L/2-\delta}^{-L/2+\delta} = 0, \qquad \lim_{\delta\to 0} \Psi(x) \mid_{L/2-\delta}^{L/2+\delta} = 0,$$

$$\lim_{\delta\to 0} \hat{J}\Psi(x) \mid_{-L/2-\delta}^{-L/2+\delta} = 0, \qquad \lim_{\delta\to 0} \hat{J}\Psi(x) \mid_{L/2-\delta}^{L/2+\delta} = 0, \tag{D.3}$$

where $\hat{J} \equiv \frac{\partial \hat{H}}{\partial \hat{p}} = v_F \sigma_z$ is the current operator for the Hamiltonian defined in Eq. (*D*.1) with σ_z the z-Pauli matrix. By following standard procedures [Schwabl2008] one can calculate the transmission t and reflection r amplitudes through the region **II**, in the following cases:

- A particle incident from the left (region **I**), i. e. $A = 1$, $G = 0$:

$$t_{I\to III} = \frac{F}{A} = e^{-iL\frac{eV}{\hbar v_F}}; \qquad r_{I\to I} = \frac{B}{A} = 0. \tag{D.4}$$

- A particle incident from the right (region **III**), i. e. $A = 0$, $G = 1$:

$$t_{III\to I} = \frac{B}{G} = e^{-iL\frac{eV}{\hbar v_F}}; \qquad r_{III\to III} = \frac{A}{G} = 0. \tag{D.5}$$

The only contribution of V is to generate a dynamical phase in the electron propagation. From Eqs. (D.4) and (D.5) is clear that the constant potential barrier acts by assigning to electrons the same phase factor independently from their propagation direction and spin, clarifying why the unitary operator of Eq. (11.1) takes the form $\mathcal{U}_V(\theta_V) = e^{i\ \theta_V \mathbb{1}/2}$, with $\mathbb{1}$ the identity operator in the spin space. In particular, in this case $\theta_V = 2eVL/(\hbar v_F)$. This phase indeed coincides with the dynamical phase acquired by an electron propagating along the edge under the electrical potential V for a time of flight $t = L/v_F$ [Xiao2016].

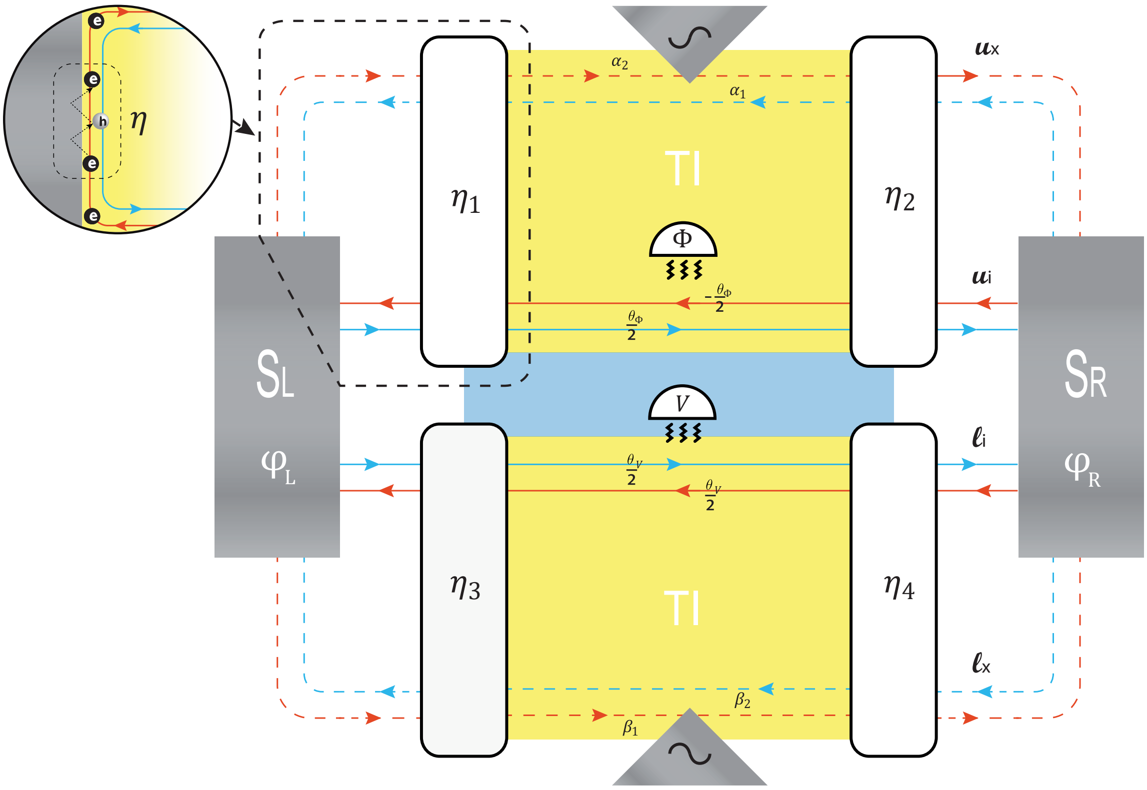

FIGURE D.1: The full scheme of the system is depicted here by unfolding the 3D model of Fig. 11.2 in the main text, keeping fixed the frontal side in the z-x-plane (cyan area) in between the two superconductors (S_L and S_R in gray), and tilting the upper TI-plane along the z-axis and the lower TI-plane in the opposite direction, such that the top of the first TI-plane and the bottom of the second one are coplanar. In this scheme, the edges in the z-x-plane (frontal side) are defined as internal and labeled with u_i and ℓ_i (blue/red solid lines) instead the edge modes running in the backside are referred to as external channels (blue/red dashed lines), and labeled with u_x and ℓ_x for the upper and lower TI-plane respectively. In the model the coherence of the branches is suppressed assuming to insert dephasing angles $\alpha_1, \alpha_2, \beta_1, \beta_2 \overset{i.i.d.}{\sim} U_{[0,2\pi]}$ and averaging over them. As in the main text, we considered the case in which the V-field is applied along the ℓ_i edge of the lower TI-plane and the Φ-field is applied along the u_i edge of the upper TI-plane. The white boxes at each interface between the TI-planes and the superconductors depict the beam splitters (BSs) which model the scattering of the particle among the internal and external channels of each TI respectively. Notice that, in case the beam splitters are purely transmitting, there is no coupling between the external and internal edges corresponding to the limit of $\eta = 0$ we used in the main text for the analytical derivation of the CPR. In the inset an incoming electron, impinging toward the left SC, emerges an another electron with the same spin on the opposite counter-propagating edge of the same TI-plane, after an even number of perfect Andreev reflections.

D.3 The scheme

Here we discuss in detail the model we use in the main text. The full scheme of the system is sketched in Fig. *D*.1 (details in the caption). Following the arrangement of the local fields discussed in the main text, here we considered the application of the V-field on the internal edge of the lower TI-plane together with the application of the Φ-field on the internal edge of the upper one (later we will discuss how to go beyond to this semplification). The internal (external) edges corresponds to the frontside (backside) edges of setup shown in Fig. 11.2 of the main text. The model consists of four beam-splitters (BSs) which describe effectively the contact interfaces between the superconductors and the TI-planes. This is needed - also in case of ideal interfaces - in order to take into account those scattering processes of particles which involve both the (internal and external) edges of a same TI-plane by means of ordinary reflection processes. Intriguingly those processes may be also mediated by multiple Andreev reflections. Indeed, for example, an incoming electron toward the SC, can emerges an another electron with the same spin on the opposite counter-propagating edge of the same TI-plane, after an even number of perfect Andreev reflections (see the inset in Fig. *D*.1) independently of their local or nonlocal nature. Anyway, we will see in a moment that if the edge modes running in the backside part of the device (hereinafter referred to as "external edges", namely the dashed lines depicted in Fig. *D*.1) are long enough with respect to ℓ_ϕ or properly dephased with a voltage probe their only action is to suppress the critical current not affecting the general conclusions discussed in the main text of Chap. 11. We modeled this mechanism by introducing a loss parameter $\eta_j \in [0,1]$ with $j = 1,2,3,4$; which describes the reflectance probability of the BS at each interface, such that:

$$\eta_j = |r_j|^2 = 1 - |t_j|^2 \tag{D.6}$$

where r_j and t_j represent respectively the reflectance and transmittance amplitudes of the j-th BS. In particular, if $\eta_j = 0$ there are no losses, namely the BS is perfectly transmissive and no electrons are reflected from internal to external modes of Fig. *D*.1. Conversely if $\eta_j = 1$ the BS is perfectly reflective and all the electrons reaching the superconductive contact from the internal edges will be reflected onto the external modes (and vice versa), no Andreev reflection are possible in that case and Josephson current is null. For the sake of simplicity, in our calculation, we considered all the beam splitters to be characterized by the same reflectance amplitude, such that $\eta_j = \eta \ \forall j = 1,2,3,4$ but all the results given can be easily generalized to a less symmetric case.

As discussed in Sec. 6.4, in order to derive the Josephson current of the model, we have to calculate the Andreev bound state energies ϵ_p, solving the following self-consistent secular problem [Beenakker1992]:

$$Det\Big[e^{i\arccos{(\epsilon_p/\Delta_0)}}\mathbb{1} - s_A s_N\Big] = 0. \tag{D.7}$$

Here s_A and s_N are respectively the Andreev scattering reflection matrix and the scattering matrix describing the weak-link in the short-junction limit with ideal interfaces; which in turn (according to the notation introduced in Sec. 6.4) take the following form:

$$s_N = \begin{pmatrix} s_0 & \emptyset \\ \emptyset & s_0^* \end{pmatrix}; \quad s_A = \begin{pmatrix} \emptyset & r_A \\ r_A^* & \emptyset \end{pmatrix}. \tag{D.8}$$

In Eq.(*D*.8), the scattering matrix component r_A^*, which relates the electrons impinging the

SCs to the respective Andreev-reflected holes, takes the following form:

$$\begin{pmatrix} b^{\downarrow}_{uxL} \\ b^{\uparrow}_{uiL} \\ b^{\uparrow}_{liL} \\ b^{\downarrow}_{lxL} \\ b^{\uparrow}_{uxR} \\ b^{\downarrow}_{uiR} \\ b^{\downarrow}_{liR} \\ b^{\uparrow}_{lxR} \end{pmatrix}_{in} = \begin{pmatrix} \begin{pmatrix} |\Lambda_{Lx}| & 0 & 0 & i|X_{Lx}| \\ 0 & |\Lambda_{Li}| & i|X_{Li}| & 0 \\ 0 & i|X_{Li}| & |\Lambda_{Li}| & 0 \\ i|X_{Lx}| & 0 & 0 & |\Lambda_{Lx}| \end{pmatrix} e^{i\phi_L} & \emptyset \\ \emptyset & \begin{pmatrix} |\Lambda_{Rx}| & 0 & 0 & i|X_{Rx}| \\ 0 & |\Lambda_{Ri}| & i|X_{Ri}| & 0 \\ 0 & i|X_{Ri}| & |\Lambda_{Ri}| & 0 \\ i|X_{Rx}| & 0 & 0 & |\Lambda_{Rx}| \end{pmatrix} e^{i\phi_R} \end{pmatrix}_{r_A^*} \begin{pmatrix} c^{\uparrow}_{uxL} \\ c^{\downarrow}_{uiL} \\ c^{\downarrow}_{liL} \\ c^{\uparrow}_{lxL} \\ c^{\downarrow}_{uxR} \\ c^{\uparrow}_{uiR} \\ c^{\uparrow}_{liR} \\ c^{\downarrow}_{lxR} \end{pmatrix}_{out} \tag{D.9}$$

It differs from the Andreev matrix of the main text because of the explicit presence of the edge modes running in the backside part of the device which add new scattering channels to the final structure (namely the external edges depicted in Fig. *D*.1 and labeled with u_x and ℓ_x respectively). For this reason we have to enlarge the set of the splitting parameters, i. e. $\{\Lambda_{Sn}, X_{Sn}\}$ as presented in Eq. (*D*.9), accounting for the local and non-local splitting of Cooper pairs on each side of the junction $S = L, R$, and along the specific set of internal and external channels $n = i, x$. One may have noticed, both from the scheme of Fig. *D*.1 and the structure itself of the scattering matrix of Eq. (*D*.9), that the splitting of CPs along the internal and external edges of the model are related to independent mechanisms, which are ruled by the set of constrain equations $|\Lambda_{Sn}|^2 + |X_{Sn}|^2 = 1$ for $S = L, R$ and $n = i, x$, imposed on the relative strength of the local and non-local splitting amplitudes because of unitarity. At microscopical level this competitive role of LAR vs CAR processes at each interface depends on the strength of the Coulomb interaction between the edges. Note also that the phase difference in the Josephson junction is defined as $\phi = \phi_L - \phi_R$.

The scattering matrix s_N, which describes the weak-link, does not couple electrons and holes, thus it takes a block-diagonal form in the electron-hole space as shown in Eq. (*D*.8). Specifically, the block-matrix component s_0, which relates incoming and outgoing electrons only, assumes the following structure:

$$\begin{pmatrix} c^{\uparrow}_{uxL} \\ c^{\downarrow}_{uiL} \\ c^{\downarrow}_{liL} \\ c^{\uparrow}_{lxL} \\ c^{\downarrow}_{uxR} \\ c^{\uparrow}_{uiR} \\ c^{\uparrow}_{liR} \\ c^{\downarrow}_{lxR} \end{pmatrix}_{out} = \begin{pmatrix} 0 & A_2 & 0 & 0 & D_1 & 0 & 0 & 0 \\ A_1 & 0 & 0 & 0 & 0 & D_2 & 0 & 0 \\ 0 & 0 & 0 & A_4 & 0 & 0 & D_3 & 0 \\ 0 & 0 & A_3 & 0 & 0 & 0 & 0 & D_4 \\ C_1 & 0 & 0 & 0 & 0 & B_2 & 0 & 0 \\ 0 & C_2 & 0 & 0 & B_1 & 0 & 0 & 0 \\ 0 & 0 & C_3 & 0 & 0 & 0 & 0 & B_4 \\ 0 & 0 & 0 & C_4 & 0 & 0 & B_3 & 0 \end{pmatrix}_{s_0} \begin{pmatrix} c^{\downarrow}_{uxL} \\ c^{\uparrow}_{uiL} \\ c^{\uparrow}_{liL} \\ c^{\downarrow}_{lxL} \\ c^{\uparrow}_{uxR} \\ c^{\downarrow}_{uiR} \\ c^{\downarrow}_{liR} \\ c^{\uparrow}_{lxR} \end{pmatrix}_{in} \tag{D.10}$$

In which

$$A_1 = r_1 + \frac{t_1^2 r_2 e^{i\alpha_2} e^{-i\theta_\Phi/2}}{1-r_1 r_2 e^{i\alpha_2} e^{-i\theta_\Phi/2}}; \quad A_2 = r_1 + \frac{t_1^2 r_2 e^{i\alpha_1} e^{i\theta_\Phi/2}}{1-r_1 r_2 e^{i\alpha_1} e^{i\theta_\Phi/2}}; \quad A_3 = r_3 + \frac{t_3^2 r_4 e^{i\beta_2} e^{-i\theta_V/2}}{1-r_3 r_4 e^{i\beta_2} e^{-i\theta_V/2}}; \quad A_4 = r_3 + \frac{t_3^2 r_4 e^{i\beta_1} e^{i\theta_V/2}}{1-r_3 r_4 e^{i\beta_1} e^{i\theta_V/2}}$$

$$B_1 = r_1 + \frac{t_2^2 r_1 e^{i\alpha_1} e^{i\theta_\Phi/2}}{1-r_1 r_2 e^{i\alpha_1} e^{i\theta_\Phi/2}}; \quad B_2 = r_1 + \frac{t_2^2 r_1 e^{i\alpha_2} e^{-i\theta_\Phi/2}}{1-r_1 r_2 e^{i\alpha_2} e^{-i\theta_\Phi/2}}; \quad B_3 = r_4 + \frac{t_4^2 r_3 e^{i\beta_1} e^{i\theta_V/2}}{1-r_3 r_4 e^{i\beta_1} e^{i\theta_V/2}}; \quad B_4 = r_4 + \frac{t_4^2 r_3 e^{i\beta_2} e^{-i\theta_V/2}}{1-r_3 r_4 e^{i\beta_2} e^{-i\theta_V/2}}$$

$$C_1 = \frac{t_1 t_2 e^{i\alpha_2}}{1-r_1 r_2 e^{i\alpha_2} e^{-i\theta_\Phi/2}}; \quad C_2 = \frac{t_1 t_2 e^{i\theta_\Phi/2}}{1-r_1 r_2 e^{i\alpha_1} e^{i\theta_\Phi/2}}; \quad C_3 = \frac{t_3 t_4 e^{-i\theta_V/2}}{1-r_3 r_4 e^{i\beta_2} e^{-i\theta_V/2}}; \quad C_4 = \frac{t_3 t_4 e^{i\beta_1}}{1-r_3 r_4 e^{i\beta_2} e^{i\theta_V/2}}$$

$$D_1 = \frac{t_1 t_2 e^{i\alpha_1}}{1-r_1 r_2 e^{i\alpha_1} e^{i\theta_\Phi/2}}; \quad D_2 = \frac{t_1 t_2 e^{-i\theta_\Phi/2}}{1-r_1 r_2 e^{i\alpha_2} e^{-i\theta_\Phi/2}}; \quad D_3 = \frac{t_3 t_4 e^{i\theta_V/2}}{1-r_3 r_4 e^{i\beta_1} e^{i\theta_V/2}}; \quad D_4 = \frac{t_3 t_4 e^{i\beta_1}}{1-r_3 r_4 e^{i\beta_2} e^{-i\theta_V/2}}$$

A similar relation links the incoming and outgoing holes through s_0^*. As an example of the derivation of the non-null entries of Eq. (*D*.10), let us explicit the calculation of the term A_1, which relates an incoming electron from the upper-external branch on the left side (labeled by uxL), with an outgoing electron with the same spin on the internal-upper edge, again at interface with S_L (labeled by uiL):

$$
\begin{aligned}
c^{\downarrow}_{uxL} \to c^{\downarrow}_{uiL}:& \\
A_1 &= r_1 + t_1 e^{i\alpha_2} r_2 e^{-i\theta_\Phi/2} t_1 + t_1 e^{i\alpha_2} \cdot r_2 e^{-i\theta_\Phi/2} r_1 e^{i\alpha_2} \cdot r_2 e^{-i\theta_\Phi/2} t_1 + \dots \\
&= r_1 + t_1^2 r_2 e^{i\alpha_2} e^{-i\theta_\Phi/2} \sum_{n=0}^{\infty} (r_2 r_1 e^{i\alpha_2} e^{-i\theta_\Phi/2})^n \\
&= r_1 + \frac{t_1^2 r_2 e^{i\alpha_2} e^{-i\theta_\Phi/2}}{1 - r_1 r_2 e^{i\alpha_2} e^{-i\theta_\Phi/2}}. \qquad \text{(D.11)}
\end{aligned}
$$

Multiple reflections between the different BSs have been taken into account, as results from the geometrical series in Eq. (*D.11*). In the previous equation we also introduce the phases acquired during the evolution along the external edges labeled as α_i and β_i. Those phases are introduced in order to effectively describe the dephasing processes since, in the end, we average the physical quantities over them (namely $\alpha_i, \beta_i \overset{i.i.d.}{\sim} U_{[0,2\pi]}$). So by the set of the previous equations we can calculate the Josephson current $J(\phi, \theta_\Phi, \theta_V, \alpha_1, \alpha_2, \beta_1, \beta_2)$ where the dependence over T and η is implicitly assumed. The final value of this quantity, in our results is obtained by the mentioned averaging procedure, i. e. $\bar{J}(\phi, \theta_\Phi, \theta_V) = \frac{1}{(2\pi)^4} \int_0^{2\pi} d\alpha_1 d\alpha_2 d\beta_1 d\beta_2 \; J(\phi, \theta_\Phi, \theta_V, \alpha_1, \alpha_2, \beta_1, \beta_2)$. In the main text we show the numerical results for the Josephson current at finite η and temperature T. In Sec. 11.4.1 we analytically derive, with the same method, the Josephson current as perturbative expansion in $(1-\eta)$.

D.4 Configuration of the fields

The most general scheme of the application of the local fields along the edge states of the system is depicted in Fig. *D.2*. We represents four local fields contributions divided among the different edge states such that each set of helical modes (belonging to the upper and lower TI-plane respectively) is interested by one V-type field (which describing the TRS terms) and one Φ-type field (describing TRS breaking terms). Here we labelled each manipulation angle, associated with the corresponding term, $\theta_{Vn}, \theta_{\Phi n}$ with the index $n = u, \ell$ to indicate the pertinent upper or lower edge (plane) of application.

Within this picture, by following the same procedure employed in the main text for the calculation of the Josephson current, we obtained - in case of no losses ($\eta = 0$) - the following result:

$$
\begin{aligned}
J(\phi) =& 4\frac{e\Delta_0}{\hbar} \sum_{\nu=\pm} \Bigg\{ \sin\left(\frac{\bar{\theta}_\Phi + \phi}{2} + \nu \tan^{-1}\left(\sqrt{\frac{1-\Gamma}{1+\Gamma}} \right) \right) \\
& \tanh\left[\frac{\Delta_0}{2k_B T} \cos\left(\frac{\bar{\theta}_\Phi + \phi}{2} + \nu \tan^{-1}\left(\sqrt{\frac{1-\Gamma}{1+\Gamma}} \right) \right) \right] \Bigg\} \qquad \text{(D.12)}
\end{aligned}
$$

which appears with the same functional form already presented in the main text. In particular, $\bar{\theta}_\Phi = \frac{\theta_{\Phi u} + \theta_{\Phi \ell}}{2}$ is given by the sum of the two separated Φ contributions. The quantity $\bar{\theta}_\Phi$ affect the CPR with a global phase shifting and one immediately see that for $\bar{\theta}_\Phi \neq 0$ one could find an anomalous current, i. e. Josephson current at $\phi = 0$. This is consistent with the fact that in general anomalous current can be generated by the breaking of TRS. Anyway if the TRS is broken, at local level, but in an exactly opposite way, such as $\theta_{\Phi u} = -\theta_{\Phi \ell}$, the anomalous current disappear since $\bar{\theta}_\Phi = 0$. At the same time also the function Γ is generalized:

$$\Gamma = \cos\left(\frac{\Delta\theta_V}{2}\right)|X_L||X_R| + \cos\left(\frac{\Delta\theta_\Phi}{2}\right)|\Lambda_L||\Lambda_R|, \tag{D.13}$$

where we note that the effective action of θ_{Vn} and $\theta_{\Phi n}$ is given by their differential mode $\Delta\theta_V = \theta_{Vu} - \theta_{V\ell}$ and $\Delta\theta_\Phi = \theta_{\Phi u} - \theta_{\Phi\ell}$. So only the difference between the local action in the upper and lower edges of both the V and Φ terms effectively contributes on the modification of the shape of the CPR. Intriguingly, the approaches suggested to generate the fields operate (by construction) on the *differential* mode which are the required terms which modify the Γ of Eq. (D.13). In this way we still preserve the selective action of the two different fields which operate in a targeted manner on the local and non-local components of the current as discussed in the main text.

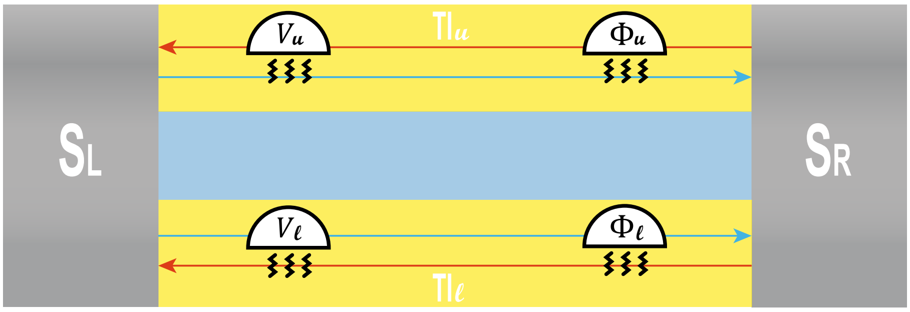

FIGURE D.2: General application of the fields along the edges states of the system.

References

[Akkermans1991] E. Akkermans, A. Auerbach, J. E. Avron, and B. Shapiro. *Relation between persistent currents and the scattering matrix.* Phys. Rev. Lett., **66**(1) 76–79, Jan. 1991.

[Altland-Zirnabauer1997] A. Altland and M. R. Zirnbauer. *Nonstandard symmetry classes in mesoscopic normal-superconducting hybrid structures.* Phys. Rev. B, **55**(2) 1142–1161, Jan. 1997.

[Anderson1958] P. W. Anderson. *Absence of Diffusion in Certain Random Lattices.* Phys. Rev., **109**(5) 1492–1505, Mar. 1958.

[Anderson1963] P. W. Anderson and J. M. Rowell. *Probable Observation of the Josephson Superconducting Tunneling Effect.* Phys. Rev. Lett., **10**(6) 230–232, Mar. 1963.

[Anderson1964] P. W. Anderson. *Special Effects in Superconductivity. In Lectures on the Manybody Problem*, volume 2. E. R. Caianiello, (1964).

[Ando2013] Y. Ando. *Topological Insulator Materials.* J. Phys. Soc. Jpn., **82**(10) 102001, Sept. 2013.

[Andreev1964] A. F. Andreev. *The thermal conductivity of the intermediate state in superconductors.* The thermal conductivity of the intermediate state in superconductors, **46**(5) 1823–1828, (1964).

[Arrachea2015] L. Arrachea and F. von Oppen. *Nanomagnet coupled to quantum spin Hall edge: An adiabatic quantum motor.* Physica E: Low-dimensional Systems and Nanostructures, **74** 596–602, Nov. 2015.

[Aspect1981] A. Aspect, P. Grangier, and G. Roger. *Experimental tests of realistic local theories via bell's theorem.* Phys. Rev. Lett., **47**(7) 460–463, Aug. 1981.

[Barash2002] Y. S. Barash and I. V. Bobkova. *Interplay of spin-discriminated Andreev bound states forming the $0-\pi$ transition in superconductor-ferromagnet-superconductor junctions.* Phys. Rev. B, **65**(14) 144502, Mar. 2002.

[Barbarino2013] S. Barbarino, R. Fazio, M. Sassetti, and F. Taddei. *Parity dependent Josephson current through a helical Luttinger liquid.* New J. Phys., **15**(8) 085025, Aug. 2013.

[Bardeen1969] J. Bardeen, R. Kümmel, A. E. Jacobs, and L. Tewordt. *Structure of Vortex Lines in Pure Superconductors.* Phys. Rev., **187**(2) 556–569, Nov. 1969.

[Barone1982] A. Barone and G. Paterno. *Physics and Applications of the Josephson Effect.* Wiley, (1982).

[BCS1957] J. Bardeen, L. N. Cooper, and J. R. Schrieffer. *Theory of Superconductivity.* Phys. Rev., **108**(5) 1175–1204, Dec. 1957.

[Beenakker1991] C. W. J. Beenakker. *Universal limit of critical-current fluctuations in mesoscopic Josephson junctions.* Phys. Rev. Lett., **67**(27) 3836–3839, Dec. 1991.

[Beenakker1992] C. Beenakker. Three "universal" mesoscopic Josephson effects. In *Transport Phenomena in Mesoscopic Systems*, pages 235–253. Springer, (1992).

[Beenakker2003] C. W. J. Beenakker, C. Emary, M. Kindermann, and J. L. van Velsen. *Proposal for production and detection of entangled electron-hole pairs in a degenerate electron gas.* Phys. Rev. Lett., **91**(14) 147901, Oct. 2003.

[Beenakker2005] C. W. J. Beenakker and H. Van Houten. *The superconducting quantum point contact.* arXiv:0512610, **[cond-mat.mes-hall]**, (2005).

[Beenakker2006] C. W. J. Beenakker. *Three "universal" mesoscopic Josephson effects.* arXiv:0406127, **[cond-mat.mes-hall]**, (2006).

[Behnia2016] K. Behnia and H. Aubin. *Nernst effect in metals and superconductors: A review of concepts and experiments.* Rep. Prog. Phys., **79**(4) 046502, Mar. 2016.

[Bekenstein1981] J. D. Bekenstein. *Energy Cost of Information Transfer.* Phys. Rev. Lett., **46**(10) 623–626, Mar. 1981.

[Bekenstein1984] J. D. Bekenstein. *Entropy content and information flow in systems with limited energy.* Phys. Rev. D, **30**(8) 1669–1679, Oct. 1984.

[Bell1966] J. S. Bell. *On the problem of hidden variables in quantum mechanics.* Rev. Mod. Phys., **38**(3) 447–452, July 1966.

[Bell2004] J. S. Bell and J. S. Bell. *Speakable and Unspeakable in Quantum Mechanics: Collected Papers on Quantum Philosophy.* Cambridge university press, (2004).

[Bena2002] C. Bena, S. Vishveshwara, L. Balents, and M. P. A. Fisher. *Quantum entanglement in carbon nanotubes.* Phys. Rev. Lett., **89**(3) 037901, June 2002.

[Benenti2017] G. Benenti, G. Casati, K. Saito, and R. S. Whitney. *Fundamental aspects of steady-state conversion of heat to work at the nanoscale*. Physics Reports, **694** 1–124, June 2017.

[Benoit1986] A. D. Benoit, S. Washburn, C. P. Umbach, R. B. Laibowitz, and R. A. Webb. *Asymmetry in the Magnetoconductance of Metal Wires and Loops*. Phys. Rev. Lett., **57**(14) 1765–1768, Oct. 1986.

[Bergeret2018] F. S. Bergeret, M. Silaev, P. Virtanen, and T. T. Heikkilä. *Colloquium: Nonequilibrium effects in superconductors with a spin-splitting field*. Rev. Mod. Phys., **90**(4) 041001, Oct. 2018.

[Bernevig2013] B. A. Bernevig and T. L. Hughes. *Topological Insulators and Topological Superconductors, Princeton University Press*. New Jersey, , (2013).

[Bernevig2013a] B. A. Bernevig. *Topological Insulators and Topological Superconductors*. Princeton University Press, Apr. 2013.

[Berry1984] M. V. Berry. *Quantal phase factors accompanying adiabatic changes*. Proceedings of the Royal Society of London. A. Mathematical and Physical Sciences, **392**(1802) 45–57, Mar. 1984.

[BHZ2006] B. A. Bernevig, T. L. Hughes, and S.-C. Zhang. *Quantum Spin Hall Effect and Topological Phase Transition in HgTe Quantum Wells*. Science, **314**(5806) 1757–1761, Dec. 2006.

[Binder2019] F. Binder, L. A. Correa, C. Gogolin, J. Anders, and G. Adesso. *Thermodynamics in the Quantum Regime: Fundamental Aspects and New Directions*, volume 195. Springer, (2019).

[Blanter2000] Y. M. Blanter and M. Büttiker. *Shot noise in mesoscopic conductors*. Physics Reports, **336**(1) 1–166, Sept. 2000.

[Blasi2019] G. Blasi, F. Taddei, V. Giovannetti, and A. Braggio. *Manipulation of Cooper pair entanglement in hybrid topological Josephson junctions*. Phys. Rev. B, **99**(6) 064514, Feb. 2019.

[Blasi2020] G. Blasi, F. Taddei, L. Arrachea, M. Carrega, and A. Braggio. *Nonlocal Thermoelectricity in a Superconductor–Topological-Insulator–Superconductor Junction in Contact with a Normal-Metal Probe: Evidence for Helical Edge States*. Phys. Rev. Lett., **124**(22) 227701, June 2020.

[Blasi2020a] G. Blasi, F. Taddei, L. Arrachea, M. Carrega, and A. Braggio. *Nonlocal thermoelectricity in a topological Andreev interferometer*. Phys. Rev. B, **102**(24) 241302, Dec. 2020.

[Blatt2012] R. Blatt and C. F. Roos. *Quantum simulations with trapped ions*. Nature Phys, **8**(4) 277–284, Apr. 2012.

[Bloch1929] F. Bloch. *Über die Quantenmechanik der Elektronen in Kristallgittern*. Z. Physik, **52**(7) 555–600, July 1929.

[Bocquillon2017] E. Bocquillon, R. S. Deacon, J. Wiedenmann, P. Leubner, T. M. Klapwijk, C. Brüne, K. Ishibashi, H. Buhmann, and L. W. Molenkamp. *Gapless Andreev bound states in the quantum spin Hall insulator HgTe*. Nature Nanotech, **12**(2) 137–143, Feb. 2017.

[Bocquillon2018] E. Bocquillon, J. Wiedenmann, R. S. Deacon, T. M. Klapwijk, H. Buhmann, and L. W. Molenkamp. Microwave Studies of the Fractional Josephson Effect in HgTe-Based Josephson Junctions. In D. Bercioux, J. Cayssol, M. G. Vergniory, and M. Reyes Calvo, editors, *Topological Matter: Lectures from the Topological Matter School 2017*, Springer Series in Solid-State Sciences, pages 115–148. Springer International Publishing, Cham, (2018).

[Bogoliubov1958] N. N. Bogoliubov. *Zetf 34 (1958) 65*. Sov. Phys. JETP, **34** 41, (1958).

[Bohling2018] S. Böhling, G. Engelhardt, G. Platero, and G. Schaller. *Thermoelectric performance of topological boundary modes*. Phys. Rev. B, **98**(3) 035132, July 2018.

[Bours2018] L. Bours, B. Sothmann, M. Carrega, E. Strambini, E. M. Hankiewicz, L. W. Molenkamp, and F. Giazotto. *Topological SQUIPT Based on Helical Edge States in Proximity to Superconductors*. Phys. Rev. Applied, **10**(1) 014027, July 2018.

[Bours2019] L. Bours, B. Sothmann, M. Carrega, E. Strambini, A. Braggio, E. M. Hankiewicz, L. W. Molenkamp, and F. Giazotto. *Phase-Tunable Thermal Rectification in the Topological SQUIPT*. Phys. Rev. Applied, **11**(4) 044073, Apr. 2019.

[Brandner2013] K. Brandner and U. Seifert. *Multi-terminal thermoelectric transport in a magnetic field: Bounds on Onsager coefficients and efficiency*. New J. Phys., **15**(10) 105003, Oct. 2013.

[Brune2012] C. Brüne, A. Roth, H. Buhmann, E. M. Hankiewicz, L. W. Molenkamp, J. Maciejko, X.-L. Qi, and S.-C. Zhang. *Spin polarization of the quantum spin Hall edge states*. Nature Phys, **8**(6) 485–490, June 2012.

[BTK1982] G. E. Blonder, M. Tinkham, and T. M. Klapwijk. *Transition from metallic to tunneling regimes in superconducting microconstrictions: Excess current, charge imbalance, and supercurrent conversion*. Phys. Rev. B, **25**(7) 4515–4532, Apr. 1982.

[Budich2012] J. C. Budich, F. Dolcini, P. Recher, and B. Trauzettel. *Phonon-Induced Backscattering in Helical Edge States*. Phys. Rev. Lett., **108**(8) 086602, Feb. 2012.

[Burkard2000] G. Burkard, D. Loss, and E. V. Sukhorukov. *Noise of entangled electrons: Bunching and antibunching*. Phys. Rev. B, **61**(24) R16303–R16306, June 2000.

[Bustos-Marun2013] R. Bustos-Marún, G. Refael, and F. von Oppen. *Adiabatic Quantum Motors*. Phys. Rev. Lett., **111**(6) 060802, Aug. 2013.

[Butcher1990] P. N. Butcher. *Thermal and electrical transport formalism for electronic microstructures with many terminals*. J. Phys.: Condens. Matter, **2**(22) 4869–4878, June 1990.

[Buttiker1986] M. Büttiker. *Four-Terminal Phase-Coherent Conductance*. Phys. Rev. Lett., **57**(14) 1761–1764, Oct. 1986.

[Buttiker1992] M. Büttiker. *Scattering theory of current and intensity noise correlations in conductors and wave guides*. Phys. Rev. B, **46**(19) 12485–12507, Nov. 1992.

[Callen1998] H. B. Callen. *Thermodynamics and an Introduction to Thermostatistics, 2nd ed.* American Journal of Physics, **66**(2) 164–167, Feb. 1998.

[Campagnano2015] G. Campagnano, P. Lucignano, D. Giuliano, and A. Tagliacozzo. *Spin–orbit coupling and anomalous Josephson effect in nanowires*. J. Phys. Condens. Matter, **27**(20) 205301, (2015).

[Casimir1945] H. B. G. Casimir. *On Onsager's Principle of Microscopic Reversibility*. Rev. Mod. Phys., **17**(2-3) 343–350, Apr. 1945.

[Chang2006] C. W. Chang, D. Okawa, A. Majumdar, and A. Zettl. *Solid-State Thermal Rectifier*. Science, **314**(5802) 1121–1124, Nov. 2006.

[Chen2012] W. Chen, R. Shen, L. Sheng, B. G. Wang, and D. Y. Xing. *Electron entanglement detected by quantum spin hall systems*. Phys. Rev. Lett., **109**(3) 036802, July 2012.

[Choi2014] M.-S. Choi. *Hanbury Brown and Twiss correlations of Cooper pairs in helical liquids*. Phys. Rev. B, **89**(4) 045137, Jan. 2014.

[Chubov1969] P. N. Chubov, V. V. Eremenko, and Y. A. Pilipenko. *Dependence of the critical temperature and energy gap on the thickness of superconducting aluminum films*. Sov. Phys. JETP, **28**(3) 389–395, (1969).

[Citro2011] R. Citro, F. Romeo, and N. Andrei. *Electrically controlled pumping of spin currents in topological insulators*. Phys. Rev. B, **84**(16) 161301, Oct. 2011.

[Claughton1996] N. R. Claughton and C. J. Lambert. *Thermoelectric properties of mesoscopic superconductors*. Phys. Rev. B, **53**(10) 6605–6612, Mar. 1996.

[Clauser1969] J. F. Clauser, M. A. Horne, A. Shimony, and R. A. Holt. *Proposed experiment to test local hidden-variable theories*. Phys. Rev. Lett., **23**(15) 880–884, Oct. 1969.

[Crepin2014] F. Crépin and B. Trauzettel. *Parity measurement in topological Josephson junctions*. Phys. Rev. lett., **112**(7) 077002, (2014).

[Crepin2015] F. Crépin, P. Burset, and B. Trauzettel. *Odd-frequency triplet superconductivity at the helical edge of a topological insulator*. Physical Review B, **92**(10) 100507, (2015).

[Das2011] S. Das and S. Rao. *Spin-Polarized Scanning-Tunneling Probe for Helical Luttinger Liquids*. Phys. Rev. Lett., **106**(23) 236403, June 2011.

[Datta1996] S. Datta, P. Bagwell, and M. Anantram. *Scattering Theory of Transport for Mesoscopic Superconductors*. Department of Electrical and Computer Engineering Technical Reports, , Jan. 1996.

[Datta1997] S. Datta. *Electronic Transport in Mesoscopic Systems*. Cambridge university press, (1997).

[Datta1999] S. Datta and P. F. Bagwell. *Can the bogoliubov–de gennes equation be interpreted as a 'one-particle' wave equation?* Superlattices and Microstructures, **25**(5) 1233–1250, May 1999.

[Deacon2017] R. S. Deacon, J. Wiedenmann, E. Bocquillon, F. Domínguez, T. M. Klapwijk, P. Leubner, C. Brüne, E. M. Hankiewicz, S. Tarucha, K. Ishibashi, H. Buhmann, and L. W. Molenkamp. *Josephson Radiation from Gapless Andreev Bound States in HgTe-Based Topological Junctions*. Phys. Rev. X, **7**(2) 021011, Apr. 2017.

[DeGennes1966] P. G. De Gennes. *Superconductivity of metals and alloys wa benjamin*. Inc., New York, , (1966).

[DiLorenzo2005] A. D. Lorenzo and Y. V. Nazarov. *Full counting statistics with spin-sensitive detectors reveals spin singlets*. Phys. Rev. Lett., **94**(21) 210601, June 2005.

[Dolcini2009] F. Dolcini. *Andreev reflection*. Lecture Notes for XXIII Physics GradDays, **5** 9, (2009).

[Dolcini2015] F. Dolcini, M. Houzet, and J. S. Meyer. *Topological Josephson ϕ_0 junctions*. Phys. Rev. B, **92**(3) 035428, July 2015.

[Dresselhaus2007] M. S. Dresselhaus, G. Chen, M. Y. Tang, R. G. Yang, H. Lee, D. Z. Wang, Z. F. Ren, J.-P. Fleurial, and P. Gogna. *New Directions for Low-Dimensional Thermoelectric Materials*. Advanced Materials, **19**(8) 1043–1053, (2007).

[Duan2015] X. Duan, X.-L. Li, Y. G. Semenov, and K. W. Kim. *Nonlinear magnetic dynamics in a nanomagnet–topological insulator heterostructure*. Phys. Rev. B, **92**(11) 115429, Sept. 2015.

[Dubi2011] Y. Dubi and M. Di Ventra. *Colloquium: Heat flow and thermoelectricity in atomic and molecular junctions.* Rev. Mod. Phys., **83**(1) 131–155, Mar. 2011.

[Dyson1962] F. J. Dyson. *The Threefold Way. Algebraic Structure of Symmetry Groups and Ensembles in Quantum Mechanics.* Journal of Mathematical Physics, **3**(6) 1199–1215, Nov. 1962.

[Einstein1935] A. Einstein, B. Podolsky, and N. Rosen. *Can quantum-mechanical description of physical reality be considered complete?* Phys. Rev., **47**(10) 777–780, May 1935.

[Ekert1991] A. K. Ekert. *Quantum cryptography based on Bell's theorem.* Phys. Rev. Lett., **67**(6) 661–663, Aug. 1991.

[Engl2011] T. Engl, J. Kuipers, and K. Richter. *Conductance and thermopower of ballistic Andreev cavities.* Phys. Rev. B, **83**(20) 205414, May 2011.

[Eom1998] J. Eom, C.-J. Chien, and V. Chandrasekhar. *Phase Dependent Thermopower in Andreev Interferometers.* Phys. Rev. Lett., **81**(2) 437–440, July 1998.

[Eto2014] T. Yokoyama, M. Eto, and Y. V. Nazarov. *Anomalous Josephson effect induced by spin-orbit interaction and Zeeman effect in semiconductor nanowires.* Phys. Rev. B, **89**(19) 195407, May 2014.

[Ettingshausen1886] A. V. Ettingshausen and W. Nernst. *Ueber das Auftreten electromotorischer Kr‰ fte in Metallplatten, welche von einem W‰ rmestrome durchflossen werden und sich im magnetischen Felde befinden.* Annalen der Physik, **265**(10) 343–347, (1886).

[Fagas2014] G. Fagas, L. Gammaitoni, D. Paul, and G. A. Berini. *ICT - Energy - Concepts Towards Zero - Power Information and Communication Technology.* Feb. 2014.

[Feynman1965] R. P. Feynman, R. B. Leighton, and M. Sands. *The feynman lectures on physics; vol. i.* American Journal of Physics, **33**(9) 750–752, (1965).

[Fisher1981] D. S. Fisher and P. A. Lee. *Relation between conductivity and transmission matrix.* Phys. Rev. B, **23**(12) 6851–6854, June 1981.

[Fleckenstein2016] C. Fleckenstein, N. Traverso Ziani, and B. Trauzettel. *Chiral anomaly in real space from stable fractional charges at the edge of a quantum spin Hall insulator.* Phys. Rev. B, **94**(24) 241406, Dec. 2016.

[Fleckenstein2018] C. Fleckenstein, N. T. Ziani, and B. Trauzettel. *Conductance signatures of odd-frequency superconductivity in quantum spin Hall systems using a quantum point contact.* Phys. Rev. B, **97**(13) 134523, (2018).

[Fornieri2016] A. Fornieri, C. Blanc, R. Bosisio, S. D'Ambrosio, and F. Giazotto. *Nanoscale phase engineering of thermal transport with a Josephson heat modulator.* Nature Nanotech, **11**(3) 258–262, Mar. 2016.

[Fornieri2017] A. Fornieri and F. Giazotto. *Towards phase-coherent caloritronics in superconducting circuits.* Nature Nanotech, **12**(10) 944–952, Oct. 2017.

[Franz2013] M. Franz and L. Molenkamp. *Topological Insulators.* Elsevier, (2013).

[Friedenauer2008] A. Friedenauer, H. Schmitz, J. T. Glueckert, D. Porras, and T. Schaetz. *Simulating a quantum magnet with trapped ions.* Nature Phys, **4**(10) 757–761, Oct. 2008.

[Fu2008] L. Fu and C. L. Kane. *Superconducting Proximity Effect and Majorana Fermions at the Surface of a Topological Insulator.* Phys. Rev. Lett., **100**(9) 096407, Mar. 2008.

[Fu2009] L. Fu and C. L. Kane. *Josephson current and noise at a superconductor/quantum-spin-Hall-insulator/superconductor junction.* Phys. Rev. B, **79**(16) 161408, Apr. 2009.

[Galperin1974] I. U. M. Galperin, V. L. Gurevich, and V. I. Kozub. *Thermoelectric effects in superconductors.* Zhurnal Eksperimental'noi i Teoreticheskoi Fiziki, **66** 1387–1397, (1974).

[Germanese2021] G. Germanese, F. Paolucci, G. Marchegiani, A. Braggio, and F. Giazotto. *Spontaneous symmetry breaking-induced thermospin effect in superconducting tunnel junctions.* arXiv:2105.01527, [**cond-mat.mes-hall**], (2021).

[Ghosh2017] B. Ghosh, R. Dey, L. F. Register, and S. K. Banerjee. *A simulation study of voltage-assisted low-energy switching of a perpendicular anisotropy ferromagnet on a topological insulator.* J Comput Electron, **16**(1) 120–126, Mar. 2017.

[Giazotto2006] F. Giazotto, T. T. Heikkilä, A. Luukanen, A. M. Savin, and J. P. Pekola. *Opportunities for mesoscopics in thermometry and refrigeration: Physics and applications.* Rev. Mod. Phys., **78**(1) 217–274, Mar. 2006.

[Giazotto2012] F. Giazotto and M. J. Martínez-Pérez. *The Josephson heat interferometer.* Nature, **492**(7429) 401–405, Dec. 2012.

[Giazotto2014] F. Giazotto, J. W. A. Robinson, J. S. Moodera, and F. S. Bergeret. *Proposal for a phase-coherent thermoelectric transistor.* Appl. Phys. Lett., **105**(6) 062602, Aug. 2014.

[Giazotto2015] F. Giazotto, P. Solinas, A. Braggio, and F. S. Bergeret. *Ferromagnetic-Insulator-Based Superconducting Junctions* *as Sensitive Electron Thermometers*. Phys. Rev. Applied, **4**(4) 044016, Oct. 2015.

[Ginzburg-Landau1950] V. L. Ginzburg and L. D. Landau. On the Theory of Superconductivity. In V. L. Ginzburg, editor, *On Superconductivity and Superfluidity: A Scientific Autobiography*, pages 113–137. Springer, Berlin, Heidelberg, (2009).

[Ginzburg1944] V. L. Ginzburg. *On thermoelectric phenomena in superconductors*. J. Phys. USSR, **8** 148, (1944).

[Gisin2002] N. Gisin, G. Ribordy, W. Tittel, and H. Zbinden. *Quantum cryptography*. Rev. Mod. Phys., **74**(1) 145–195, Mar. 2002.

[Goldsmid2010] H. J. Goldsmid. *Introduction to Thermoelectricity*, volume 121. Springer, (2010).

[Goldstone1981] J. Goldstone and F. Wilczek. *Fractional Quantum Numbers on Solitons*. Phys. Rev. Lett., **47**(14) 986–989, Oct. 1981.

[Gorkov1959] L. P. Gor'kov. *Microscopic derivation of the Ginzburg-Landau equations in the theory of superconductivity*. Sov. Phys. JETP, **9**(6) 1364–1367, (1959).

[Gresta-Blasi2021] D. Gresta, G. Blasi, F. Taddei, M. Carrega, A. Braggio, and L. Arrachea. *Signatures of Jackiw-Rebbi resonance in the thermal conductance of topological Josephson junctions with magnetic islands*. Phys. Rev. B, **103**(7) 075439, Feb. 2021.

[Gresta2019] D. Gresta, M. Real, and L. Arrachea. *Optimal Thermoelectricity with Quantum Spin Hall Edge States*. Phys. Rev. Lett., **123**(18) 186801, Oct. 2019.

[Groenendijk2018] S. Groenendijk, G. Dolcetto, and T. L. Schmidt. *Fundamental limits to helical edge conductivity due to spin-phonon scattering*. Phys. Rev. B, **97**(24) 241406, June 2018.

[Groot2013] S. R. D. Groot and P. Mazur. *Non-Equilibrium Thermodynamics*. Courier Corporation, Jan. 2013.

[Guarcello2018a] C. Guarcello, P. Solinas, A. Braggio, and F. Giazotto. *Solitonic Josephson Thermal Transport*. Phys. Rev. Applied, **9**(3) 034014, Mar. 2018.

[Guarcello2019] C. Guarcello, A. Braggio, P. Solinas, G. P. Pepe, and F. Giazotto. *Josephson-Threshold Calorimeter*. Phys. Rev. Applied, **11**(5) 054074, May 2019.

[Guarcello2019a] C. Guarcello, A. Braggio, P. Solinas, and F. Giazotto. *Nonlinear Critical-Current Thermal Response of an Asymmetric Josephson Tunnel Junction*. Phys. Rev. Applied, **11**(2) 024002, Feb. 2019.

[Guarcello2020] C. Guarcello, R. Citro, O. Durante, F. S. Bergeret, A. Iorio, C. Sanz-Fernández, E. Strambini, F. Giazotto, and A. Braggio. *Rf-SQUID measurements of anomalous Josephson effect.* Phys. Rev. Research, **2**(2) 023165, May 2020.

[Hajiloo2019] F. Hajiloo, F. Hassler, and J. Splettstoesser. *Mesoscopic effects in the heat conductance of superconducting-normal-superconducting and normal-superconducting junctions.* Phys. Rev. B, **99**(23) 235422, June 2019.

[Hajiloo2020] F. Hajiloo, P. T. Alonso, N. Dashti, L. Arrachea, and J. Splettstoesser. *Detailed study of nonlinear cooling with two-terminal configurations of topological edge states.* Phys. Rev. B, **102**(15) 155434, Oct. 2020.

[Haldane1988] F. D. M. Haldane. *Model for a Quantum Hall Effect without Landau Levels: Condensed-Matter Realization of the "Parity Anomaly".* Phys. Rev. Lett., **61**(18) 2015–2018, Oct. 1988.

[Halperin1982] B. I. Halperin. *Quantized Hall conductance, current-carrying edge states, and the existence of extended states in a two-dimensional disordered potential.* Phys. Rev. B, **25**(4) 2185–2190, Feb. 1982.

[Harman2000] T. C. Harman, P. J. Taylor, D. L. Spears, and M. P. Walsh. *Thermoelectric quantum-dot superlattices with high ZT.* Journal of Electronic Materials, **29**(1) 1–2, Jan. 2000.

[Hart2014] S. Hart, H. Ren, T. Wagner, P. Leubner, M. Mühlbauer, C. Brüne, H. Buhmann, L. W. Molenkamp, and A. Yacoby. *Induced superconductivity in the quantum spin Hall edge.* Nature Phys, **10**(9) 638–643, Sept. 2014.

[Hasan2010] M. Z. Hasan and C. L. Kane. *Colloquium: Topological insulators.* Rev. Mod. Phys., **82**(4) 3045–3067, Nov. 2010.

[Hegde2020] S. S. Hegde, G. Yue, Y. Wang, E. Huemiller, D. J. Van Harlingen, and S. Vishveshwara. *A topological Josephson junction platform for creating, manipulating, and braiding Majorana bound states.* Annals of Physics, **423** 168326, Dec. 2020.

[Heidrich2019] J. Heidrich and D. Beckmann. *Nonlocal thermoelectric effects in high-field superconductor-ferromagnet hybrid structures.* Phys. Rev. B, **100**(13) 134501, Oct. 2019.

[Heikkila2018] T. T. Heikkilä, R. Ojajärvi, I. J. Maasilta, E. Strambini, F. Giazotto, and F. S. Bergeret. *Thermoelectric Radiation Detector Based on Superconductor-Ferromagnet Systems.* Phys. Rev. Applied, **10**(3) 034053, Sept. 2018.

[Hicks1993] L. D. Hicks and M. S. Dresselhaus. *Thermoelectric figure of merit of a one-dimensional conductor.* Phys. Rev. B, **47**(24) 16631–16634, June 1993.

[Hicks1993a] L. D. Hicks, T. C. Harman, and M. S. Dresselhaus. *Use of quantum-well superlattices to obtain a high figure of merit from nonconventional thermoelectric materials.* Appl. Phys. Lett., **63**(23) 3230–3232, Dec. 1993.

[Hou2016] Z. Hou, Y. Xing, A.-M. Guo, and Q.-F. Sun. *Crossed Andreev effects in two-dimensional quantum Hall systems.* Phys. Rev. B, **94**(6) 064516, Aug. 2016.

[Houzet2013] M. Houzet, J. S. Meyer, D. M. Badiane, and L. I. Glazman. *Dynamics of Majorana States in a Topological Josephson Junction.* Phys. Rev. Lett., **111**(4) 046401, July 2013.

[Hus2017] S. M. Hus, X.-G. Zhang, G. D. Nguyen, W. Ko, A. P. Baddorf, Y. P. Chen, and A.-P. Li. *Detection of the Spin-Chemical Potential in Topological Insulators Using Spin-Polarized Four-Probe STM.* Phys. Rev. Lett., **119**(13) 137202, Sept. 2017.

[Hussein2016] R. Hussein, L. Jaurigue, M. Governale, and A. Braggio. *Double quantum dot Cooper-pair splitter at finite couplings.* Physical Review B, **94**(23) 235134, (2016).

[Hussein2017] R. Hussein, A. Braggio, and M. Governale. *Entanglement-symmetry control in a quantum-dot Cooper-pair splitter.* physica status solidi (b), **254**(3) 1600603, (2017).

[Hussein2019] R. Hussein, M. Governale, S. Kohler, W. Belzig, F. Giazotto, and A. Braggio. *Nonlocal thermoelectricity in a Cooper-pair splitter.* Phys. Rev. B, **99**(7) 075429, Feb. 2019.

[Hwang2020] S.-Y. Hwang and B. Sothmann. *Phase-coherent caloritronics with ordinary and topological Josephson junctions.* Eur. Phys. J. Spec. Top., **229**(4) 683–705, Feb. 2020.

[Ilin2004] K. S. Ilin, S. A. Vitusevich, B. B. Jin, A. I. Gubin, N. Klein, and M. Siegel. *Peculiarities of the thickness dependence of the superconducting properties of thin Nb films.* Physica C: Superconductivity, **408-410** 700–702, Aug. 2004.

[Imry1986] Y. Imry. *Directions in Condensed Matter Physics.* World Scientific, Singapore, (1986).

[Islam2017] S. F. Islam, P. Dutta, and A. Saha. *Enhancement of crossed Andreev reflection in a normal-superconductor-normal junction made of thin topological insulator.* Phys. Rev. B, **96**(15) 155429, Oct. 2017.

[Jackiw-Rebbi1976] R. Jackiw and C. Rebbi. *Solitons with fermion number* 1/2. Phys. Rev. D, **13**(12) 3398–3409, June 1976.

[Jacquet2019] R. Jacquet, J. Rech, T. Jonckheere, A. Zazunov, and T. Martin. *Unified scattering approach to Josephson current and thermal noise in BCS and topological superconducting junctions*. The European Physical Journal B, **92**(3) 59, Mar. 2019.

[Jacquod2010] P. Jacquod and R. S. Whitney. *Coherent thermoelectric effects in mesoscopic Andreev interferometers*. EPL, **91**(6) 67009, Sept. 2010.

[Jacquod2012] P. Jacquod, R. S. Whitney, J. Meair, and M. Büttiker. *Onsager relations in coupled electric, thermoelectric, and spin transport: The tenfold way*. Phys. Rev. B, **86**(15) 155118, Oct. 2012.

[Jia2017] Z.-Y. Jia, Y.-H. Song, X.-B. Li, K. Ran, P. Lu, H.-J. Zheng, X.-Y. Zhu, Z.-Q. Shi, J. Sun, J. Wen, D. Xing, and S.-C. Li. *Direct visualization of a two-dimensional topological insulator in the single-layer* $1T'$*-*WTe_2. Phys. Rev. B, **96**(4) 041108, July 2017.

[Jiang2005] Z. Jiang and V. Chandrasekhar. *Quantitative measurements of the thermal resistance of Andreev interferometers*. Phys. Rev. B, **72**(2) 020502, July 2005.

[Jiang2013] L. Jiang, D. Pekker, J. Alicea, G. Refael, Y. Oreg, A. Brataas, and F. von Oppen. *Magneto-Josephson effects in junctions with Majorana bound states*. Phys. Rev. B, **87**(7) 075438, Feb. 2013.

[Josefsson2018] M. Josefsson, A. Svilans, A. M. Burke, E. A. Hoffmann, S. Fahlvik, C. Thelander, M. Leijnse, and H. Linke. *A quantum-dot heat engine operating close to the thermodynamic efficiency limits*. Nature Nanotechnology, **13**(10) 920–924, Oct. 2018.

[Josephson1962] B. D. Josephson. *Possible new effects in superconductive tunnelling*. Physics letters, **1**(7) 251–253, (1962).

[Josephson1964] B. D. JOSEPHSON. *Coupled Superconductors*. Rev. Mod. Phys., **36**(1) 216–220, Jan. 1964.

[Kalenkov2017] M. S. Kalenkov and A. D. Zaikin. *Large thermoelectric effect in ballistic Andreev interferometers*. Phys. Rev. B, **95**(2) 024518, Jan. 2017.

[Kalenkov2020] M. S. Kalenkov, P. E. Dolgirev, and A. D. Zaikin. *Phase-sensitive thermoelectricity and long-range Josephson effect supported by thermal gradient*. Phys. Rev. B, **101**(18) 180505, May 2020.

[Kamp2019] M. Kamp and B. Sothmann. *Phase-dependent heat and charge transport through superconductor–quantum dot hybrids*. Phys. Rev. B, **99**(4) 045428, Jan. 2019.

[Kane2005] C. L. Kane and E. J. Mele. *Quantum Spin Hall Effect in Graphene*. Phys. Rev. Lett., **95**(22) 226801, Nov. 2005.

[Kane2005a] C. L. Kane and E. J. Mele. $\mathbb{Z}_2$ *Topological Order and the Quantum Spin Hall Effect*. Phys. Rev. Lett., **95**(14) 146802, Sept. 2005.

[Kastner1992] M. A. Kastner. *The single-electron transistor*. Rev. Mod. Phys., **64**(3) 849–858, July 1992.

[Keidel2020] F. Keidel, S.-Y. Hwang, B. Trauzettel, B. Sothmann, and P. Burset. *On-demand thermoelectric generation of equal-spin Cooper pairs*. Phys. Rev. Research, **2**(2) 022019, Apr. 2020.

[Ketterson1999] J. B. Ketterson and S. N. Song. *Superconductivity*. Cambridge University Press, Cambridge, (1999).

[Kheradsoud2019] S. Kheradsoud, N. Dashti, M. Misiorny, P. P. Potts, J. Splettstoesser, and P. Samuelsson. *Power, Efficiency and Fluctuations in a Quantum Point Contact as Steady-State Thermoelectric Heat Engine*. Entropy, **21**(8) 777, Aug. 2019.

[Kim2004] E.-A. Kim, S. Vishveshwara, and E. Fradkin. *Cooper-pair tunneling in junctions of singlet quantum hall states and superconductors*. Phys. Rev. Lett., **93**(26) 266803, Dec. 2004.

[Kirsanov2019] N. S. Kirsanov, Z. B. Tan, D. S. Golubev, P. J. Hakonen, and G. B. Lesovik. *Heat switch and thermoelectric effects based on Cooper-pair splitting and elastic cotunneling*. Phys. Rev. B, **99**(11) 115127, Mar. 2019.

[Kitaev2001] A. Y. Kitaev. *Unpaired Majorana fermions in quantum wires*. Physics-Uspekhi, **44**(10S) 131–136, Oct. 2001.

[Klapwijk1982] T. M. Klapwijk, G. E. Blonder, and M. Tinkham. *Explanation of subharmonic energy gap structure in superconducting contacts*. Physica B+C, **109-110** 1657–1664, July 1982.

[Klitzing1980] K. v. Klitzing, G. Dorda, and M. Pepper. *New Method for High-Accuracy Determination of the Fine-Structure Constant Based on Quantized Hall Resistance*. Phys. Rev. Lett., **45**(6) 494–497, Aug. 1980.

[Kolenda2017] S. Kolenda, C. Sürgers, G. Fischer, and D. Beckmann. *Thermoelectric effects in superconductor-ferromagnet tunnel junctions on europium sulfide*. Phys. Rev. B, **95**(22) 224505, June 2017.

[Konig2007] M. König, S. Wiedmann, C. Brüne, A. Roth, H. Buhmann, L. W. Molenkamp, X.-L. Qi, and S.-C. Zhang. *Quantum Spin Hall Insulator State in HgTe Quantum Wells*. Science, **318**(5851) 766–770, Nov. 2007.

[Konig2008] M. König, H. Buhmann, L. W. Molenkamp, T. Hughes, C.-X. Liu, X.-L. Qi, and S.-C. Zhang. *The Quantum Spin Hall Effect: Theory and Experiment*. J. Phys. Soc. Jpn., **77**(3) 031007, Mar. 2008.

[Kopnin2011] N. B. Kopnin and A. S. Melnikov. *Proximity-induced superconductivity in two-dimensional electronic systems*. Phys. Rev. B, **84**(6) 064524, Aug. 2011.

[Kupriyanov1982] M. Y. Kupriyanov and V. F. Lukichev. *Proximity effect in electrodes and the steady-state properties of yosephson SNS structures*. Fizika Nizkikh Temperatur, **8**(10) 1045–1052, (1982).

[Kurter2015] C. Kurter, A. D. K. Finck, Y. S. Hor, and D. J. Van Harlingen. *Evidence for an anomalous current–phase relation in topological insulator Josephson junctions*. Nat Commun, **6**(1) 7130, June 2015.

[Lambert1991] C. J. Lambert. *Generalized Landauer formulae for quasi-particle transport in disordered superconductors*. J. Phys.: Condens. Matter, **3**(34) 6579–6587, Aug. 1991.

[Lambert1993] C. J. Lambert, V. C. Hui, and S. J. Robinson. *Multi-probe conductance formulae for mesoscopic superconductors*. J. Phys.: Condens. Matter, **5**(25) 4187–4206, June 1993.

[Lambert1998] C. J. Lambert and R. Raimondi. *Phase-coherent transport in hybrid superconducting nanostructures*. J. Phys.: Condens. Matter, **10**(5) 901–941, Feb. 1998.

[Landauer1957] R. Landauer. *Spatial Variation of Currents and Fields Due to Localized Scatterers in Metallic Conduction*. IBM Journal of Research and Development, **1**(3) 223–231, July 1957.

[Landauer1989] R. Landauer. *Conductance determined by transmission: Probes and quantised constriction resistance*. J. Phys.: Condens. Matter, **1**(43) 8099–8110, Oct. 1989.

[Lee1985] P. A. Lee and T. V. Ramakrishnan. *Disordered electronic systems*. Rev. Mod. Phys., **57**(2) 287–337, Apr. 1985.

[Lee2014] S.-P. Lee, K. Michaeli, J. Alicea, and A. Yacoby. *Revealing Topological Superconductivity in Extended Quantum Spin Hall Josephson Junctions*. Phys. Rev. Lett., **113**(19) 197001, Nov. 2014.

[Lee2019] S. Lee, V. Stanev, X. Zhang, D. Stasak, J. Flowers, J. S. Higgins, S. Dai, T. Blum, X. Pan, V. M. Yakovenko, J. Paglione, R. L. Greene, V. Galitski, and I. Takeuchi. *Perfect Andreev reflection due to the Klein paradox in a topological superconducting state*. Nature, **570**(7761) 344–348, June 2019.

[Lesovik2011] G. B. Lesovik and I. A. Sadovskyy. *Scattering matrix approach to the description of quantum electron transport*. Phys.-Usp., **54**(10) 1007–1059, Oct. 2011.

[Li2012] N. Li, J. Ren, L. Wang, G. Zhang, P. Hänggi, and B. Li. *Colloquium: Phononics: Manipulating heat flow with electronic* *analogs and beyond*. Rev. Mod. Phys., **84**(3) 1045–1066, July 2012.

[Li2018] G. Li, W. Hanke, E. M. Hankiewicz, F. Reis, J. Schäfer, R. Claessen, C. Wu, and R. Thomale. *Theoretical paradigm for the quantum spin Hall effect at high temperatures*. Phys. Rev. B, **98**(16) 165146, Oct. 2018.

[Likharev1979] K. K. Likharev. *Superconducting weak links*. Rev. Mod. Phys., **51**(1) 101–159, Jan. 1979.

[Liu2015] L. Liu, A. Richardella, I. Garate, Y. Zhu, N. Samarth, and C.-T. Chen. *Spin-polarized tunneling study of spin-momentum locking in topological insulators*. Phys. Rev. B, **91**(23) 235437, June 2015.

[Liu2020] C. Liu, D. Culcer, Z. Wang, M. T. Edmonds, and M. S. Fuhrer. *Helical Edge Transport in Millimeter-Scale Thin Films of Na3Bi*. Nano Lett., **20**(9) 6306–6312, Sept. 2020.

[Locane2017] E. Locane and P. W. Brouwer. *Current-induced switching of magnetic molecules on topological insulator surfaces*. Phys. Rev. B, **95**(12) 125437, Mar. 2017.

[London1935] F. London, H. London, and F. A. Lindemann. *The electromagnetic equations of the supraconductor*. Proceedings of the Royal Society of London. Series A - Mathematical and Physical Sciences, **149**(866) 71–88, Mar. 1935.

[Loss1998] D. Loss and D. P. DiVincenzo. *Quantum computation with quantum dots*. Phys. Rev. A, **57**(1) 120–126, Jan. 1998.

[Lunczer2019] L. Lunczer, P. Leubner, M. Endres, V. L. Müller, C. Brüne, H. Buhmann, and L. W. Molenkamp. *Approaching Quantization in Macroscopic Quantum Spin Hall Devices through Gate Training*. Phys. Rev. Lett., **123**(4) 047701, July 2019.

[Lutchyn2010] R. M. Lutchyn, J. D. Sau, and S. Das Sarma. *Majorana Fermions and a Topological Phase Transition in Semiconductor-Superconductor Heterostructures*. Phys. Rev. Lett., **105**(7) 077001, Aug. 2010.

[MacFarlane2003] A. G. J. MacFarlane, J. P. Dowling, and G. J. Milburn. *Quantum technology: The second quantum revolution*. Philosophical Transactions of the Royal Society of London. Series A: Mathematical, Physical and Engineering Sciences, **361**(1809) 1655–1674, Aug. 2003.

[Machon2013] P. Machon, M. Eschrig, and W. Belzig. *Nonlocal Thermoelectric Effects and Nonlocal Onsager relations in a Three-Terminal Proximity-Coupled Superconductor-Ferromagnet Device*. Phys. Rev. Lett., **110**(4) 047002, Jan. 2013.

[Maciejko2009] J. Maciejko, C. Liu, Y. Oreg, X.-L. Qi, C. Wu, and S.-C. Zhang. *Kondo Effect in the Helical Edge Liquid of the Quantum Spin Hall State*. Phys. Rev. Lett., **102**(25) 256803, June 2009.

[Maciejko2010] J. Maciejko, X.-L. Qi, and S.-C. Zhang. *Magnetoconductance of the quantum spin Hall state*. Phys. Rev. B, **82**(15) 155310, Oct. 2010.

[Madsen2021] K. A. Madsen, P. W. Brouwer, P. Recher, and P. G. Silvestrov. *Interference effects induced by a precessing easy-plane magnet coupled to a helical edge state*. Phys. Rev. B, **103**(11) 115142, Mar. 2021.

[Mahan1996] G. D. Mahan and J. O. Sofo. *The best thermoelectric*. Proc. Natl. Acad. Sci. U.S.A., **93**(15) 7436–7439, (1996).

[Maier2012] L. Maier, J. B. Oostinga, D. Knott, C. Brüne, P. Virtanen, G. Tkachov, E. M. Hankiewicz, C. Gould, H. Buhmann, and L. W. Molenkamp. *Induced Superconductivity in the Three-Dimensional Topological Insulator HgTe*. Phys. Rev. Lett., **109**(18) 186806, Nov. 2012.

[Maistrenko2021] O. Maistrenko, B. Scharf, D. Manske, and E. M. Hankiewicz. *Planar Josephson Hall effect in topological Josephson junctions*. Phys. Rev. B, **103**(5) 054508, Feb. 2021.

[Majer2007] J. Majer, J. M. Chow, J. M. Gambetta, J. Koch, B. R. Johnson, J. A. Schreier, L. Frunzio, D. I. Schuster, A. A. Houck, A. Wallraff, A. Blais, M. H. Devoret, S. M. Girvin, and R. J. Schoelkopf. *Coupling superconducting qubits via a cavity bus*. Nature, **449**(7161) 443–447, Sept. 2007.

[Malciu2019] C. Malciu, L. Mazza, and C. Mora. *4π and 8π dual Josephson effects induced by symmetry defects*. Phys. Rev. B, **99**(12) 125153, Mar. 2019.

[Mani2017] A. Mani and C. Benjamin. *Probing helicity and the topological origins of helicity via non-local Hanbury-Brown and Twiss correlations*. Sci Rep, **7**(1) 6954, July 2017.

[Mani2018] A. Mani and C. Benjamin. *Helical thermoelectrics and refrigeration*. Phys. Rev. E, **97**(2) 022114, Feb. 2018.

[Marchegiani2020] G. Marchegiani, A. Braggio, and F. Giazotto. *Nonlinear Thermoelectricity with Electron-Hole Symmetric Systems*. Phys. Rev. Lett., **124**(10) 106801, Mar. 2020.

[Marchegiani2020a] G. Marchegiani, A. Braggio, and F. Giazotto. *Superconducting nonlinear thermoelectric heat engine*. Phys. Rev. B, **101**(21) 214509, June 2020.

[Marchegiani2020b] G. Marchegiani, A. Braggio, and F. Giazotto. *Noise effects in the nonlinear thermoelectricity of a Josephson junction*. Appl. Phys. Lett., **117**(21) 212601, Nov. 2020.

[Marchegiani2020c] G. Marchegiani, A. Braggio, and F. Giazotto. *Phase-tunable thermoelectricity in a Josephson junction*. Phys. Rev. Research, **2**(4) 043091, Oct. 2020.

[Marra2016] P. Marra, R. Citro, and A. Braggio. *Signatures of topological phase transitions in Josephson current-phase discontinuities*. Phys. Rev. B, **93**(22) 220507, June 2016.

[Martin-Rodero2011] A. Martín-Rodero and A. L. Yeyati. *Josephson and Andreev transport through quantum dots*. Advances in Physics, **60**(6) 899–958, Dec. 2011.

[Martinez-Perez2014] M. José Martínez-Pérez and F. Giazotto. *A quantum diffractor for thermal flux*. Nat Commun, **5**(1) 3579, Apr. 2014.

[Martinez-Perez2015] M. J. Martínez-Pérez, A. Fornieri, and F. Giazotto. *Rectification of electronic heat current by a hybrid thermal diode*. Nature Nanotech, **10**(4) 303–307, Apr. 2015.

[Matthews2014] J. Matthews, F. Battista, D. Sánchez, P. Samuelsson, and H. Linke. *Experimental verification of reciprocity relations in quantum thermoelectric transport*. Phys. Rev. B, **90**(16) 165428, Oct. 2014.

[Mazza2014] F. Mazza, R. Bosisio, G. Benenti, V. Giovannetti, R. Fazio, and F. Taddei. *Thermoelectric efficiency of three-terminal quantum thermal machines*. New J. Phys., **16**(8) 085001, Aug. 2014.

[Mazza2015] F. Mazza, S. Valentini, R. Bosisio, G. Benenti, V. Giovannetti, R. Fazio, and F. Taddei. *Separation of heat and charge currents for boosted thermoelectric conversion*. Phys. Rev. B, **91**(24) 245435, June 2015.

[McMillan1968] W. L. McMillan. *Tunneling Model of the Superconducting Proximity Effect*. Phys. Rev., **175**(2) 537–542, Nov. 1968.

[Mellars2016] E. Mellars and B. Béri. *Signatures of time-reversal-invariant topological superconductivity in the Josephson effect*. Phys. Rev. B, **94**(17) 174508, Nov. 2016.

[Meng2012] Q. Meng, V. Shivamoggi, T. L. Hughes, M. J. Gilbert, and S. Vishveshwara. *Fractional spin Josephson effect and electrically controlled magnetization in quantum spin Hall edges*. Phys. Rev. B, **86**(16) 165110, Oct. 2012.

[Meng2014] Q. Meng, S. Vishveshwara, and T. L. Hughes. *Spin-transfer torque and electric current in helical edge states in quantum spin Hall devices*. Phys. Rev. B, **90**(20) 205403, Nov. 2014.

[Meservey1971] R. Meservey and P. M. Tedrow. *Properties of Very Thin Aluminum Films*. Journal of Applied Physics, **42**(1) 51–53, Jan. 1971.

[Michelsen2020] A. B. Michelsen, T. L. Schmidt, and E. G. Idrisov. *Current correlations of Cooper-pair tunneling into a quantum Hall system*. Phys. Rev. B, **102**(12) 125402, Sept. 2020.

[Minutillo2018] M. Minutillo, D. Giuliano, P. Lucignano, A. Tagliacozzo, and G. Campagnano. *Anomalous josephson effect in S/SO/F/S heterostructures*. Physical Review B, **98**(14) 144510, (2018).

[Moore2009] J. Moore. *The next generation*. Nature Phys, **5**(6) 378–380, June 2009.

[Moskalets2011] M. V. Moskalets. *Scattering Matrix Approach to Non-Stationary Quantum Transport*. World Scientific, (2011).

[Nakahara2003] M. Nakahara. *Geometry, Topology and Physics, Second Edition*. CRC Press, June 2003.

[Nava2016] A. Nava, R. Giuliano, G. Campagnano, and D. Giuliano. *Transfer matrix approach to the persistent current in quantum rings: Application to hybrid normal-superconducting rings*. Phys. Rev. B, **94**(20) 205125, Nov. 2016.

[Nayak2008] C. Nayak, S. H. Simon, A. Stern, M. Freedman, and S. Das Sarma. *Non-Abelian anyons and topological quantum computation*. Rev. Mod. Phys., **80**(3) 1083–1159, Sept. 2008.

[Nesterov2016] K. N. Nesterov, M. Houzet, and J. S. Meyer. *Anomalous Josephson effect in semiconducting nanowires as a signature of the topologically nontrivial phase*. Phys. Rev. B, **93**(17) 174502, May 2016.

[Octavio1983] M. Octavio, M. Tinkham, G. E. Blonder, and T. M. Klapwijk. *Subharmonic energy-gap structure in superconducting constrictions*. Physical Review B, **27**(11) 6739, (1983).

[Onsager1931] L. Onsager. *Reciprocal Relations in Irreversible Processes. I*. Phys. Rev., **37**(4) 405–426, Feb. 1931.

[Oreg2010] Y. Oreg, G. Refael, and F. von Oppen. *Helical Liquids and Majorana Bound States in Quantum Wires*. Phys. Rev. Lett., **105**(17) 177002, Oct. 2010.

[Ozaeta2014] A. Ozaeta, P. Virtanen, F. S. Bergeret, and T. T. Heikkilä. *Predicted Very Large Thermoelectric Effect in Ferromagnet-Superconductor Junctions in the Presence of a Spin-Splitting Magnetic Field*. Phys. Rev. Lett., **112**(5) 057001, Feb. 2014.

[Parsons2003] A. Parsons, I. A. Sosnin, and V. T. Petrashov. *Reversal of thermopower oscillations in the mesoscopic Andreev interferometer*. Phys. Rev. B, **67**(14) 140502, Apr. 2003.

[Partanen2016] M. Partanen, K. Y. Tan, J. Govenius, R. E. Lake, M. K. Mäkelä, T. Tanttu, and M. Möttönen. *Quantum-limited heat conduction over macroscopic distances*. Nature Phys, **12**(5) 460–464, May 2016.

[Pekola2015] J. P. Pekola. *Towards quantum thermodynamics in electronic circuits*. Nature Phys, **11**(2) 118–123, Feb. 2015.

[Pendry1983] J. B. Pendry. *Quantum limits to the flow of information and entropy*. J. Phys. A: Math. Gen., **16**(10) 2161–2171, July 1983.

[Pershoguba2019] S. S. Pershoguba and L. I. Glazman. *Thermopower and thermal conductance of a superconducting quantum point contact*. Phys. Rev. B, **99**(13) 134514, Apr. 2019.

[Pretre1996] A. Prêtre, H. Thomas, and M. Büttiker. *Dynamic admittance of mesoscopic conductors: Discrete-potential model*. Phys. Rev. B, **54**(11) 8130–8143, Sept. 1996.

[Pribiag2015] V. S. Pribiag, A. J. A. Beukman, F. Qu, M. C. Cassidy, C. Charpentier, W. Wegscheider, and L. P. Kouwenhoven. *Edge-mode superconductivity in a two-dimensional topological insulator*. Nature Nanotech, **10**(7) 593–597, July 2015.

[Qi2008] X.-L. Qi, T. L. Hughes, and S.-C. Zhang. *Fractional charge and quantized current in the quantum spin Hall state*. Nature Physics, **4**(4) 273–276, (2008).

[Qi2011] X.-L. Qi and S.-C. Zhang. *Topological insulators and superconductors*. Rev. Mod. Phys., **83**(4) 1057–1110, Oct. 2011.

[Recher2001] P. Recher, E. V. Sukhorukov, and D. Loss. *Andreev tunneling, Coulomb blockade, and resonant transport of nonlocal spin-entangled electrons*. Phys. Rev. B, **63**(16) 165314, Apr. 2001.

[Reis2017] F. Reis, G. Li, L. Dudy, M. Bauernfeind, S. Glass, W. Hanke, R. Thomale, J. Schäfer, and R. Claessen. *Bismuthene on a SiC substrate: A candidate for a high-temperature quantum spin Hall material*. Science, **357**(6348) 287–290, July 2017.

[Ren2019] H. Ren, F. Pientka, S. Hart, A. T. Pierce, M. Kosowsky, L. Lunczer, R. Schlereth, B. Scharf, E. M. Hankiewicz, L. W. Molenkamp, B. I. Halperin, and A. Yacoby. *Topological superconductivity in a phase-controlled Josephson junction*. Nature, **569**(7754) 93–98, May 2019.

[Resta2020] R. Resta. *Geometry and topology in many-body physics*. arXiv:2006.15567, **[cond-mat.str-el]**, (2020).

[Ronetti2016] F. Ronetti, L. Vannucci, G. Dolcetto, M. Carrega, and M. Sassetti. *Spin-thermoelectric transport induced by interactions and spin-flip processes in two-dimensional topological insulators*. Phys. Rev. B, **93**(16) 165414, Apr. 2016.

[Ronetti2017] F. Ronetti, M. Carrega, D. Ferraro, J. Rech, T. Jonckheere, T. Martin, and M. Sassetti. *Polarized heat current generated by quantum pumping in two-dimensional topological insulators*. Phys. Rev. B, **95**(11) 115412, Mar. 2017.

[Ronetti2020] F. Ronetti, M. Carrega, and M. Sassetti. *Levitons in helical liquids with Rashba spin-orbit coupling probed by a superconducting contact*. Phys. Rev. Research, **2**(1) 013203, Feb. 2020.

[Roth2009] A. Roth, C. Brüne, H. Buhmann, L. W. Molenkamp, J. Maciejko, X.-L. Qi, and S.-C. Zhang. *Nonlocal Transport in the Quantum Spin Hall State*. Science, **325**(5938) 294–297, July 2009.

[Roura-Bas2018] P. Roura-Bas, L. Arrachea, and E. Fradkin. *Helical spin thermoelectrics controlled by a side-coupled magnetic quantum dot in the quantum spin Hall state*. Phys. Rev. B, **98**(19) 195429, Nov. 2018.

[Sacepe2011] B. Sacépé, J. B. Oostinga, J. Li, A. Ubaldini, N. J. G. Couto, E. Giannini, and A. F. Morpurgo. *Gate-tuned normal and superconducting transport at the surface of a topological insulator*. Nat Commun, **2**(1) 575, Dec. 2011.

[Sanchez2014] D. Sánchez and H. Linke. *Focus on thermoelectric effects in nanostructures*. New J. Phys., **16**(11) 110201, Nov. 2014.

[Sanchez2015] R. Sánchez, B. Sothmann, and A. N. Jordan. *Chiral Thermoelectrics with Quantum Hall Edge States*. Phys. Rev. Lett., **114**(14) 146801, Apr. 2015.

[Sanchez2016] D. Sánchez and R. López. *Nonlinear phenomena in quantum thermoelectrics and heat*. Comptes Rendus Physique, **17**(10) 1060–1071, Dec. 2016.

[Sanchez2018] R. Sánchez, P. Burset, and A. L. Yeyati. *Cooling by Cooper pair splitting*. Phys. Rev. B, **98**(24) 241414, Dec. 2018.

[Sato2010] K. Sato, D. Loss, and Y. Tserkovnyak. *Cooper-pair injection into quantum spin hall insulators*. Phys. Rev. Lett., **105**(22) 226401, Nov. 2010.

[Sato2014] K. Sato and Y. Tserkovnyak. *Detection of entanglement by helical Luttinger liquids*. Phys. Rev. B, **90**(4) 045419, July 2014.

[Scharf2020] B. Scharf, A. Braggio, E. Strambini, F. Giazotto, and E. M. Hankiewicz. *Topological Josephson heat engine*. Commun Phys, **3**(1) 1–6, Nov. 2020.

[Scharf2021] B. Scharf, A. Braggio, E. Strambini, F. Giazotto, and E. M. Hankiewicz. *Thermodynamics in topological Josephson junctions*. arXiv:2103.10923, **[cond-mat.mes-hall]**, (2021).

[Schnyder2008] A. P. Schnyder, S. Ryu, A. Furusaki, and A. W. W. Ludwig. *Classification of topological insulators and superconductors in three spatial dimensions*. Phys. Rev. B, **78**(19) 195125, Nov. 2008.

[Schrade2015] C. Schrade, A. A. Zyuzin, J. Klinovaja, and D. Loss. *Proximity-Induced π Josephson Junctions in Topological Insulators and Kramers Pairs of Majorana Fermions*. Phys. Rev. Lett., **115**(23) 237001, Dec. 2015.

[Schwabl2008] F. Schwabl. *Second Quantization*. Advanced Quantum Mechanics, pages 3–32, (2008).

[Sedlmayr2021] N. Sedlmayr and A. Levchenko. *Hybridization mechanism of the dual proximity effect in superconductor–topological insulator interfaces*. Solid State Communications, **327** 114221, Mar. 2021.

[Senior2020] J. Senior, A. Gubaydullin, B. Karimi, J. T. Peltonen, J. Ankerhold, and J. P. Pekola. *Heat rectification via a superconducting artificial atom*. Commun Phys, **3**(1) 1–5, Feb. 2020.

[Shapiro2017] D. S. Shapiro, D. E. Feldman, A. D. Mirlin, and A. Shnirman. *Thermoelectric transport in junctions of Majorana and Dirac channels*. Phys. Rev. B, **95**(19) 195425, May 2017.

[Shelly2016] C. D. Shelly, E. A. Matrozova, and V. T. Petrashov. *Resolving thermoelectric "paradox" in superconductors*. Science Advances, **2**(2) e1501250, Feb. 2016.

[Shen2012] S.-Q. Shen. *Topological Insulators*, volume 174. Springer, (2012).

[Shi2019] Y. Shi, J. Kahn, B. Niu, Z. Fei, B. Sun, X. Cai, B. A. Francisco, D. Wu, Z.-X. Shen, X. Xu, D. H. Cobden, and Y.-T. Cui. *Imaging quantum spin Hall edges in monolayer WTe2*. Science Advances, **5**(2) eaat8799, Feb. 2019.

[Silvestrov2016] P. G. Silvestrov, P. Recher, and P. W. Brouwer. *Noiseless manipulation of helical edge state transport by a quantum magnet*. Phys. Rev. B, **93**(20) 205130, May 2016.

[Snelder2013] M. Snelder, M. Veldhorst, A. A. Golubov, and A. Brinkman. *Andreev bound states and current-phase relations in three-dimensional topological insulators*. Phys. Rev. B, **87**(10) 104507, Mar. 2013.

[Sochnikov2015] I. Sochnikov, L. Maier, C. A. Watson, J. R. Kirtley, C. Gould, G. Tkachov, E. M. Hankiewicz, C. Brüne, H. Buhmann, L. W. Molenkamp, and K. A. Moler. *Nonsinusoidal Current-Phase Relationship in Josephson Junctions from the 3D Topological Insulator HgTe*. Phys. Rev. Lett., **114**(6) 066801, Feb. 2015.

[Sothmann2014] B. Sothmann, R. Sánchez, and A. N. Jordan. *Thermoelectric energy harvesting with quantum dots*. Nanotechnology, **26**(3) 032001, Dec. 2014.

[Sothmann2016] B. Sothmann and E. M. Hankiewicz. *Fingerprint of topological Andreev bound states in phase-dependent heat transport*. Phys. Rev. B, **94**(8) 081407, Aug. 2016.

[Sothmann2017] B. Sothmann, F. Giazotto, and E. M. Hankiewicz. *High-efficiency thermal switch based on topological Josephson junctions*. New J. Phys., **19**(2) 023056, Feb. 2017.

[SSH1980] W. P. Su, J. R. Schrieffer, and A. J. Heeger. *Soliton excitations in polyacetylene*. Phys. Rev. B, **22**(4) 2099–2111, Aug. 1980.

[Stanescu2010] T. D. Stanescu, J. D. Sau, R. M. Lutchyn, and S. Das Sarma. *Proximity effect at the superconductor–topological insulator interface*. Phys. Rev. B, **81**(24) 241310, June 2010.

[Stehno2016] M. P. Stehno, V. Orlyanchik, C. D. Nugroho, P. Ghaemi, M. Brahlek, N. Koirala, S. Oh, and D. J. Van Harlingen. *Signature of a topological phase transition in the Josephson supercurrent through a topological insulator*. Phys. Rev. B, **93**(3) 035307, Jan. 2016.

[Sternativo2014] P. Sternativo and F. Dolcini. *Tunnel junction of helical edge states: Determining and controlling spin-preserving and spin-flipping processes through transconductance*. Phys. Rev. B, **89**(3) 035415, Jan. 2014.

[Strom2015] A. Ström, H. Johannesson, and P. Recher. *Controllable spin entanglement production in a quantum spin Hall ring*. Phys. Rev. B, **91**(24) 245406, June 2015.

[Tan2021] Z. B. Tan, A. Laitinen, N. S. Kirsanov, A. Galda, V. M. Vinokur, M. Haque, A. Savin, D. S. Golubev, G. B. Lesovik, and P. J. Hakonen. *Thermoelectric current in a graphene Cooper pair splitter*. Nat Commun, **12**(1) 138, Jan. 2021.

[Tang2017] S. Tang, C. Zhang, D. Wong, Z. Pedramrazi, H.-Z. Tsai, C. Jia, B. Moritz, M. Claassen, H. Ryu, S. Kahn, J. Jiang, H. Yan, M. Hashimoto, D. Lu, R. G. Moore, C.-C. Hwang, C. Hwang, Z. Hussain, Y. Chen, M. M. Ugeda, Z. Liu, X. Xie, T. P. Devereaux, M. F. Crommie, S.-K. Mo, and Z.-X. Shen. *Quantum spin Hall state in monolayer 1T'-WTe 2*. Nature Phys, **13**(7) 683–687, July 2017.

[Timm2012] C. Timm. *Theory of superconductivity*. Institute of theoretical Physics Dresden, , (2012).

[Timossi2018] G. F. Timossi, A. Fornieri, F. Paolucci, C. Puglia, and F. Giazotto. *Phase-Tunable Josephson Thermal Router*. Nano Lett., **18**(3) 1764–1769, Mar. 2018.

[Tinkham1966] M. Tinkham. *Introduction to Superconductivity*. Mcgraw-hill, new york edition, (1966).

[Titov2008] M. Titov. *Thermopower oscillations in mesoscopic Andreev interferometers*. Phys. Rev. B, **78**(22) 224521, Dec. 2008.

[Tittel1998] W. Tittel, J. Brendel, H. Zbinden, and N. Gisin. *Violation of bell inequalities by photons more than 10 km apart*. Phys. Rev. Lett., **81**(17) 3563–3566, Oct. 1998.

[Tkachov2013] G. Tkachov and E. M. Hankiewicz. *Helical Andreev bound states and superconducting Klein tunneling in topological insulator Josephson junctions*. Phys. Rev. B, **88**(7) 075401, Aug. 2013.

[Tkachov2015] G. Tkachov, P. Burset, B. Trauzettel, and E. M. Hankiewicz. *Quantum interference of edge supercurrents in a two-dimensional topological insulator*. Physical Review B, **92**(4) 045408, (2015).

[Tkachov2015a] G. Tkachov. *Topological Insulators: The Physics of Spin Helicity in Quantum Transport*. CRC Press, (2015).

[Tkachov2017] G. Tkachov. *Giant spin splitting and 0-π Josephson transitions from the Edelstein effect in quantum spin Hall insulators*. Phys. Rev. B, **95**(24) 245407, June 2017.

[TKNN1982] D. J. Thouless, M. Kohmoto, M. P. Nightingale, and M. den Nijs. *Quantized Hall Conductance in a Two-Dimensional Periodic Potential*. Phys. Rev. Lett., **49**(6) 405–408, Aug. 1982.

[Valatin1958] J. G. Valatin and D. Butler. *On the collective properties of a boson system*. Il Nuovo Cimento (1955-1965), **10**(1) 37–54, (1958).

[Veldhorst2012] M. Veldhorst, M. Snelder, M. Hoek, T. Gang, V. K. Guduru, X. L. Wang, U. Zeitler, W. G. van der Wiel, A. A. Golubov, H. Hilgenkamp, and A. Brinkman. *Josephson supercurrent through a topological insulator surface state*. Nature Mater, **11**(5) 417–421, May 2012.

[Veldhorst2014] M. Veldhorst, M. Hoek, M. Snelder, H. Hilgenkamp, A. A. Golubov, and A. Brinkman. *Nonlocal spin-entangled Andreev reflection, fractional charge, and current-phase relations in topological bilayer-exciton-condensate junctions*. Phys. Rev. B, **90**(3) 035428, July 2014.

[Venkatasubramanian2001] R. Venkatasubramanian, E. Siivola, T. Colpitts, and B. O'Quinn. *Thin-film thermoelectric devices with high room-temperature figures of merit*. Nature, **413**(6856) 597–602, Oct. 2001.

[Virtanen2004] P. Virtanen and T. T. Heikkilä. *Thermopower in Andrew Interferometers*. Journal of Low Temperature Physics, **136**(5) 401–434, Sept. 2004.

[Virtanen2012] P. Virtanen and P. Recher. *Signatures of Rashba spin-orbit interaction in the superconducting proximity effect in helical Luttinger liquids*. Phys. Rev. B, **85**(3) 035310, Jan. 2012.

[Virtanen2018] P. Virtanen, F. S. Bergeret, E. Strambini, F. Giazotto, and A. Braggio. *Majorana bound states in hybrid two-dimensional Josephson junctions with ferromagnetic insulators*. Phys. Rev. B, **98**(2) 020501, July 2018.

[Vischi2019] F. Vischi, M. Carrega, P. Virtanen, E. Strambini, A. Braggio, and F. Giazotto. *Thermodynamic cycles in Josephson junctions*. Sci Rep, **9**(1) 3238, Mar. 2019.

[Voigtlander2018] B. Voigtländer, V. Cherepanov, S. Korte, A. Leis, D. Cuma, S. Just, and F. Lüpke. *Invited Review Article: Multi-tip scanning tunneling microscopy: Experimental techniques and data analysis*. Review of Scientific Instruments, **89**(10) 101101, Oct. 2018.

[Wallraff2004] A. Wallraff, D. I. Schuster, A. Blais, L. Frunzio, R.-S. Huang, J. Majer, S. Kumar, S. M. Girvin, and R. J. Schoelkopf. *Strong coupling of a single photon to a superconducting qubit using circuit quantum electrodynamics*. Nature, **431**(7005) 162–167, Sept. 2004.

[Wang2015] J. Wang, L. Hao, and K. S. Chan. *Quantized crossed-Andreev reflection in spin-valley topological insulators*. Phys. Rev. B, **91**(8) 085415, Feb. 2015.

[Wees1988] B. J. van Wees, L. P. Kouwenhoven, H. van Houten, C. W. J. Beenakker, J. E. Mooij, C. T. Foxon, and J. J. Harris. *Quantized conductance of magnetoelectric subbands in ballistic point contacts*. Phys. Rev. B, **38**(5) 3625–3627, Aug. 1988.

[Wen1995] X.-G. Wen. *Topological orders and edge excitations in fractional quantum Hall states*. Advances in Physics, **44**(5) 405–473, Oct. 1995.

[Wharam1988] D. A. Wharam, T. J. Thornton, R. Newbury, M. Pepper, H. Ahmed, J. E. F. Frost, D. G. Hasko, D. C. Peacock, D. A. Ritchie, and G. A. C. Jones. *One-dimensional transport and the quantisation of the ballistic resistance*. Journal of Physics C: Solid State Physics, **21**(8) L209–L214, Mar. 1988.

[Whitney2013] R. S. Whitney. *Thermodynamic and quantum bounds on nonlinear dc thermoelectric transport*. Phys. Rev. B, **87**(11) 115404, Mar. 2013.

[Whitney2014] R. S. Whitney. *Most Efficient Quantum Thermoelectric at Finite Power Output*. Phys. Rev. Lett., **112**(13) 130601, Apr. 2014.

[Wiedenmann2016] J. Wiedenmann, E. Bocquillon, R. S. Deacon, S. Hartinger, O. Herrmann, T. M. Klapwijk, L. Maier, C. Ames, C. Brüne,

C. Gould, et al. *4π-periodic Josephson supercurrent in HgTe-based topological Josephson junctions.* Nature communications, **7** 10303, (2016).

[Wigner1931] E. P. Wigner. *Gruppentheorie und ihre Anwendung auf die Quantenmechanik der Atomspektren*, , (1931).

[Wigner1951] E. P. Wigner. On the statistical distribution of the widths and spacings of nuclear resonance levels. In *Mathematical Proceedings of the Cambridge Philosophical Society*, volume 47, pages 790–798. Cambridge University Press, (1951).

[Wu2006] C. Wu, B. A. Bernevig, and S.-C. Zhang. *Helical Liquid and the Edge of Quantum Spin Hall Systems.* Phys. Rev. Lett., **96**(10) 106401, Mar. 2006.

[Wu2014] L.-H. Wu, Q.-F. Liang, and X. Hu. *New scheme for braiding Majorana fermions.* Sci. Technol. Adv. Mater., **15**(6) 064402, Dec. 2014.

[Wu2018] S. Wu, V. Fatemi, Q. D. Gibson, K. Watanabe, T. Taniguchi, R. J. Cava, and P. Jarillo-Herrero. *Observation of the quantum spin Hall effect up to 100 kelvin in a monolayer crystal.* Science, **359**(6371) 76–79, Jan. 2018.

[Xiao2010] D. Xiao, M.-C. Chang, and Q. Niu. *Berry phase effects on electronic properties.* Rev. Mod. Phys., **82**(3) 1959–2007, July 2010.

[Xiao2016] X. Xiao, Y. Liu, Z. Liu, G. Ai, S. A. Yang, and G. Zhou. *All-electric spin modulator based on a two-dimensional topological insulator.* Appl. Phys. Lett., **108**(3) 032403, (2016).

[Xie2011] R. Xie, C. T. Bui, B. Varghese, Q. Zhang, C. H. Sow, B. Li, and J. T. L. Thong. *An Electrically Tuned Solid-State Thermal Memory Based on Metal–Insulator Transition of Single-Crystalline VO2 Nanobeams.* Advanced Functional Materials, **21**(9) 1602–1607, (2011).

[Yamamoto2015] K. Yamamoto and N. Hatano. *Thermodynamics of the mesoscopic thermoelectric heat engine beyond the linear-response regime.* Phys. Rev. E, **92**(4) 042165, Oct. 2015.

[Yokoyama2013] T. Yokoyama, M. Eto, and Y. V. Nazarov. *Josephson current through semiconductor nanowire with Spin–Orbit interaction in magnetic field.* Journal of the Physical Society of Japan, **82**(5) 054703, (2013).

[Yuan2018] N. F. Q. Yuan and L. Fu. *Zeeman-induced gapless superconductivity with a partial Fermi surface.* Phys. Rev. B, **97**(11) 115139, Mar. 2018.

[Yukalov2009] V. I. Yukalov. *Cold bosons in optical lattices.* Laser Phys., **19**(1) 1–110, Jan. 2009.

[Zhang2014] F. Zhang and C. L. Kane. *Time-Reversal-Invariant $\mathbb{Z}_4$ Fractional Josephson Effect*. Phys. Rev. Lett., **113**(3) 036401, July 2014.

[Zhang2015] Y. Zhang, G. Lin, and J. Chen. *Three-terminal quantum-dot refrigerators*. Phys. Rev. E, **91**(5) 052118, May 2015.

[Zhang2017] X. Zhang and Y. Pei. *Manipulation of charge transport in thermoelectrics*. npj Quant Mater, **2**(1) 1–5, Dec. 2017.

[Zhang2019] S.-B. Zhang and B. Trauzettel. *Perfect Crossed Andreev Reflection in Dirac Hybrid Junctions in the Quantum Hall Regime*. Phys. Rev. Lett., **122**(25) 257701, June 2019.

[Zhu2010] Z. Zhu, H. Yang, B. Fauqué, Y. Kopelevich, and K. Behnia. *Nernst effect and dimensionality in the quantum limit*. Nature Phys, **6**(1) 26–29, Jan. 2010.

[Zhu2020] Z. Zhu, M. Papaj, X.-A. Nie, H.-K. Xu, Y.-S. Gu, X. Yang, D. Guan, S. Wang, Y. Li, C. Liu, J. Luo, Z.-A. Xu, H. Zheng, L. Fu, and J.-F. Jia. *Discovery of segmented Fermi surface induced by Cooper pair momentum*. arXiv:2010.02216, **[cond-mat.supr-con]**, (2020).

[Ziani2015] N. T. Ziani, F. Crépin, and B. Trauzettel. *Fractional Wigner Crystal in the Helical Luttinger Liquid*. Phys. Rev. Lett., **115**(20) 206402, Nov. 2015.

[Ziani2020] N. T. Ziani, C. Fleckenstein, L. Vigliotti, B. Trauzettel, and M. Sassetti. *From fractional solitons to Majorana fermions in a paradigmatic model of topological superconductivity*. Phys. Rev. B, **101**(19) 195303, May 2020.

[Zuev2009] Y. M. Zuev, W. Chang, and P. Kim. *Thermoelectric and Magnetothermoelectric Transport Measurements of Graphene*. Phys. Rev. Lett., **102**(9) 096807, Mar. 2009.